

Phenomenology of combustion in a jet-stabilized combustor

Sampat, R.P.

DOI

[10.4233/uuid:132eb207-492d-435f-9292-3bdae208b4de](https://doi.org/10.4233/uuid:132eb207-492d-435f-9292-3bdae208b4de)

Publication date

2025

Document Version

Final published version

Citation (APA)

Sampat, R. P. (2025). *Phenomenology of combustion in a jet-stabilized combustor*. [Dissertation (TU Delft), Delft University of Technology]. <https://doi.org/10.4233/uuid:132eb207-492d-435f-9292-3bdae208b4de>

Important note

To cite this publication, please use the final published version (if applicable).
Please check the document version above.

Copyright

Other than for strictly personal use, it is not permitted to download, forward or distribute the text or part of it, without the consent of the author(s) and/or copyright holder(s), unless the work is under an open content license such as Creative Commons.

Takedown policy

Please contact us and provide details if you believe this document breaches copyrights.
We will remove access to the work immediately and investigate your claim.

PHENOMENOLOGY OF COMBUSTION IN A JET-STABILIZED COMBUSTOR

Dissertation

for the purpose of obtaining the degree of doctor
at Delft University of Technology
by the authority of the Rector Magnificus, prof. dr. ir. T.H.J.J. van der Hagen,
chair of the Board for Doctorates
to be defended publicly on Monday 31, March 2025 at 15:00 o'clock

by

Rishikesh Pankaj SAMPAT

This dissertation has been approved by the promotors.

Composition of the doctoral committee:

Rector Magnificus,	chairperson
Prof. dr. A. Gangoli Rao,	Technische Universiteit Delft, <i>promotor</i>
Dr. ir. F.F.J. Schrijer,	Technische Universiteit Delft, <i>copromotor</i>

Independent members:

Prof. dr. A. Parente,	Université Libre de Bruxelles
Dr. D.C. Vaz	Universidade NOVA de Lisboa
Prof. dr. D.J.E.M. Roekaerts,	Technische Universiteit Delft
Prof. dr. J. van Oijen	Technische Universiteit Eindhoven
Dr. M. De Joannan	Consiglio Nazionale delle Ricerche
Prof. dr. S. Hickel,	Technische Universiteit Delft, reserve member



Keywords: Flameless Combustion, Autoignition, Turbulent jet-in-coflow, NO_x emissions, Internal recirculation

Printed by: ProefschriftMaken

Cover by: Rishikesh Sampat (Pyromaniac art captured during experiments).

Copyright © 2025 by R. Sampat

ISBN 978-94-6510-559-8

An electronic copy of this dissertation is available at
<https://resolver.tudelft.nl/uuid:132eb207-492d-435f-9292-3bdae208b4de>.

Dedicated to my Mother, Father and Sister.



*Nature is the source of all true knowledge.
She has her own logic, her own laws,
she has no effect without cause nor invention without necessity.*

Leonardo da Vinci



CONTENTS

Summary	xi
Samenvatting	xiii
1 Introduction	1
1.1 Role of Combustion in the green energy economy	3
1.2 NO _x Emissions from Combustion	5
1.3 Low NO _x combustion for gas turbine engines	7
1.4 Layout of Thesis	11
2 Flameless Combustion	13
2.1 Definition of Flameless Combustion	15
2.2 Laboratory-scale combustion setups	17
2.2.1 Internal recirculation systems	18
2.2.2 Two stream system	21
2.3 Flame structure and stabilization mechanism	23
2.3.1 Structure of Reaction zone	23
2.3.2 Stabilization mechanism from experiments	24
2.3.3 Indicators of Autoignition	26
2.4 Low NO _x by FC	27
2.5 Research Objectives and Questions	28
3 Experiment Setup	31
3.1 Jet Stabilized Combustor setup	32
3.1.1 Operation Principle	32
3.1.2 Design and layout of Flameless Combustor	32
3.1.3 Laboratory Infrastructure	35
3.2 Measurement techniques	40
3.2.1 Particle Image Velocimetry	40
3.2.2 Chemiluminescence	42
3.2.3 Image Processing Algorithms	44
3.2.4 Gas Analyser	46
3.2.5 Thermocouples	48
4 Autoignition of Methane-Air mixtures vitiated by exhaust gases	49
4.1 Introduction	50
4.2 Methodology	52
4.2.1 Numerical Setup	52
4.2.2 Ignition criteria	54

4.3	Results	55
4.3.1	Ignition parameters.	55
4.3.2	Emissions	57
4.3.3	Occurrence of Multi-ignition	58
4.4	Conclusions	66
5	Flow physics of turbulent jet-in-coflow	69
5.1	Introduction.	70
5.2	Experiment	73
5.2.1	Experimental Setup.	73
5.2.2	Flow Conditions	76
5.2.3	Interface detection	78
5.3	Results	81
5.3.1	Mean field.	81
5.3.2	Radial Profiles	85
5.3.3	Conditional Statistics along the interface	89
5.4	Discussion.	91
5.5	Conclusion	92
6	Characterization of a Jet-stabilized Combustor	95
6.1	Introduction.	96
6.2	Experiment Setup	99
6.2.1	Setup and operating conditions	99
6.2.2	Measurement Techniques.	102
6.2.3	Flame kernel detection	103
6.3	Results and Discussion	105
6.3.1	Flow Field.	105
6.3.2	Temperature measurements	108
6.3.3	Gas Composition measurement	110
6.3.4	DSLR results	115
6.4	Conclusion	119
7	Conclusions and Recommendations	121
7.1	Conclusions	123
7.1.1	Autoignition of CH ₄ /Air mixtures vitiated by exhaust gases.	123
7.1.2	Physics of the turbulent interface in a two-stream system	124
7.1.3	Reaction zone stabilization and emissions from a jet stabilized combustor with CH ₄ /H ₂ admixtures	125
7.2	Discussion.	126
7.3	Recommendations for future work.	127
	Bibliography	131
A	Emissions Pathway	145
A.1	Carbon Monoxide.	145
A.1.1	Formation.	145
A.2	Nitrogen Oxides.	146
A.2.1	Formation mechanisms	147

B	Multi-ignition ROP and mole fraction	151
C	Characterization of a Jet-stabilized Combustor	153
C.1	Combustion Setup and Operation Conditions.	153
C.1.1	Backflow from exhaust	153
C.2	Measurement Processing	155
C.2.1	Thermocouple correction.	155
C.3	Supplementary Data	155
C.3.1	Flow field Reynolds Stresses	155
C.3.2	Gas Composition Plots	156
C.3.3	Raw Temperature measurements	156
C.3.4	Chemiluminescence $H_2=100\%$	156
D	Combustor P&ID	161
	Acknowledgements	163
	Curriculum Vitæ	165
	List of Publications	167



SUMMARY

To meet the climate goals and reduce the negative effects of anthropogenic industrial activity, the human civilization must move toward sustainable energy sources. However, in hard-to-abate applications and to compensate for the intermittency of renewable energy sources, combustion will continue to be a crucial energy conversion mechanism. This requires modern combustion devices to have highly reduced emissions not only to abide by stringent regulations but also as a collective social responsibility. Usually, a reduction of NO_x requires a lowering of flame temperatures, which leads to an increase in CO. However, Flameless/MILD combustion is a technology that has the potential for low NO_x while attaining complete combustion. This is because of its unique requirements of having very high reactant temperatures (typically above autoignition temperatures) and having low oxygen concentration. The current work investigates the phenomenology of the combustion process in a jet-stabilized combustor, where this regime can be produced with fuel and oxidizer injected in a premixed manner. The work has three main components; the first deals with the autoignition chemistry of methane-air mixtures under exhaust gas vitiation conditions, the second investigates the flow field and turbulent interface of a turbulent-jet-in-coflow which is a canonical version of the flow conditions in a jet stabilized combustor and finally, experiments were done on a jet-stabilized combustor with methane-hydrogen blends to classify the flame stabilization mechanism and quantify emissions.

Autoignition characteristics of vitiated methane-air mixtures were studied by simulations in 0D reactor setup. Unlike most studies in literature, vitiation, in the context of flameless combustion, was generated as the hot combustion product of fresh reactants that also contained radicals that existed in equilibrium. Particularly, the effect of varying levels of vitiation and heat loss was studied on properties such as ignition delay time, reaction time scale, and the NO_x and CO emissions. This revealed the most suitable conditions to achieve low emissions and distributed reaction zones for premixed reactants that are vitiated by exhaust gases. Further, a regime of multi-ignition was discovered where prior to the main ignition event, there is a pre-ignition event attributed to the initial pool of radicals in a vitiated mixture. The conditions of occurrence were mapped out, as well as the mechanism behind it was explained.

The mixing at the interface of the jet and the recirculation zone in a jet-stabilized combustor has an important role in determining the composition of the hot-diluted mixtures. Thus, the fluid mechanics of the turbulent-turbulent interface were studied in a canonical configuration of a turbulent-jet-in-turbulent-coflow. This is also a common configuration used to produce Flameless/MILD combustion under laboratory conditions. Although there is vast research on free turbulent jets, combustors operating in the Flameless Combustion regime would reach flow conditions where the ratio of coflow to jet velocity would increase. This work elucidates the evolution of such a flow field through Particle Image Velocimetry (PIV) measurements done along the axis of the jet

in the range $0 < x/D < 42$. Further, the interface is detected using an algorithm developed based on other image processing algorithms using vorticity as a criterion. This enables the assembly of conditional statistics with respect to the interface. The results show that the cases with higher coflow have a lower jet centerline velocity decay rate and reduced jet spreading. The mean axial velocity shows a region of deficit compared to the free jet near the interface region. Further, the case with higher coflow shows higher turbulence intensity and Reynolds Shear Stress close to the interface. The detailed results are presented as both unconditional and conditional statistics and the mechanism behind this effect is deduced.

Experiments were done on a jet-stabilized combustor capable of producing the Flameless Combustion regime. It was operated using methane-hydrogen fuel admixtures at varying equivalence ratios. The combustor performance was analyzed based on the stabilization of the flame zone and the emissions. This work presents a unique, comprehensive measurement of temperature, gas composition, velocity field, and chemiluminescence signal in a jet-stabilized combustor. The recirculation regions are visualized through PIV measurements and the recirculation ratio is quantified. The instantaneous flame images are used to identify flame kernels and construct probability density functions of the aspect ratio, rotation angle, and location along the combustor axis. An increase in hydrogen content in the fuel mixture shifts the stabilization mechanism from autoignition to flame propagation. There is also an increase in NO emissions. A similar effect is seen with the increase in equivalence ratio from lean to stoichiometric condition. Distributed reaction regimes with ultra-low NO and moderate flame temperatures are achieved at very low equivalence ratios. Such mixtures are stabilized better with the addition of hydrogen to the fuel mixture.

This thesis provides fundamental information on the chemistry and flow physics of the phenomenon in a jet-stabilized combustor followed by measurements from the operation of one. The data and conclusions are a suitable reference for future engineers designing jet-stabilized combustors for low NO_x emissions and high combustion efficiency.

SAMENVATTING

Om de klimaatdoelen te halen en de negatieve effecten van door de mens veroorzaakte industriële activiteit te verminderen, moet de menselijke beschaving overstappen op duurzame energiebronnen. In moeilijk te verminderen toepassingen en om de intermitterende werking van hernieuwbare energiebronnen te compenseren, zal verbranding echter een cruciaal energieomzettingsmechanisme blijven. Dit vereist dat moderne verbrandingsapparaten sterk verminderde emissies hebben, niet alleen om te voldoen aan strenge regelgeving, maar ook als een collectieve maatschappelijke verantwoordelijkheid. Meestal vereist een reductie van NO_x een verlaging van de vlamtemperaturen, wat leidt tot een toename van CO. Vlamloze/MILD-verbranding is echter een technologie die het potentieel heeft voor lage NO_x terwijl volledige verbranding wordt bereikt. Dit komt door de unieke vereisten van zeer hoge reactanttemperaturen (meestal boven de zelfontbrandingstemperaturen) en een lage zuurstofconcentratie. Het huidige werk onderzoekt de fenomenologie van het verbrandingsproces in een straalgestabiliseerde verbrandingskamer, waar dit regime kan worden geproduceerd met brandstof en oxidatiemiddel die op een voorgemengde manier worden geïnjecteerd. Het werk heeft drie hoofdcomponenten; de eerste gaat over de zelfontbrandingschemie van methaan-luchtmengsels onder uitlaatgasvervuilende omstandigheden, de tweede onderzoekt het stromingsveld en de turbulente interface van een turbulente straal-in-costroom, wat een gangbare versie is van de stromingsomstandigheden in een straalgestabiliseerde verbrandingskamer en tot slot werden er experimenten uitgevoerd op een straalgestabiliseerde verbrandingskamer met methaan-waterstofmengsels om het vlamstabilisatiemechanisme te classificeren en emissies te kwantificeren.

Zelfontbrandingskarakteristieken van verdund methaan-luchtmengsels werden bestudeerd door simulaties in een 0D-reactoropstelling. In tegenstelling tot de meeste studies in de literatuur werd verontreinigende verbranding, in de context van vlamloze verbranding, gegenereerd als het hete verbrandingsproduct van verse reactanten die ook radicalen bevatten die in evenwicht bestonden. Met name het effect van verschillende niveaus van verontreinigende verbranding en warmteverlies werd bestudeerd op eigenschappen zoals ontstekingsvertraging, reactietijdschaal en de NO_x - en CO-emissies. Dit onthulde de meest geschikte omstandigheden om lage emissies en verdeelde reactiezones te bereiken voor voorgemengde reactanten die verontreinigd zijn door uitlaatgasen. Verder werd een regime van multi-ontsteking ontdekt waarbij er voorafgaand aan de hoofdontsteking een pre-ontstekingsgebeurtenis is die wordt toegeschreven aan de initiële pool van radicalen in een bedorven mengsel. De omstandigheden van voorkomen werden in kaart gebracht, evenals het mechanisme erachter werd uitgelegd.

Het mengen op het grensvlak van de straal en de recirculatiezone in een straalgestabiliseerde verbrander speelt een belangrijke rol bij het bepalen van de samenstelling van de heet verdunde mengsels. Zo werd de vloeistofmechanica van het turbulente-turbulente grensvlak bestudeerd in een canonieke configuratie van een turbulente straal-

in-turbulente coflow. Dit is ook een gebruikelijke configuratie die wordt gebruikt om Flameless/MILD verbranding te produceren onder laboratoriumomstandigheden. Hoewel er uitgebreid onderzoek is gedaan naar vrije turbulente jets, zouden branders die werken in het Flameless Combustion regime stromingsomstandigheden bereiken waarbij de verhouding tussen coflow en straalsnelheid zou toenemen. Dit werk verduidelijkt de evolutie van een dergelijk stromingsveld door middel van Particle Image Velocimetry (PIV) metingen uitgevoerd langs de as van de jet in het bereik $0 < x/D < 42$. Verder wordt de interface gedetecteerd met behulp van een algoritme dat is ontwikkeld op basis van andere beeldverwerkingsalgoritmen die vortciteit als criterium gebruiken. Dit maakt het mogelijk voorwaardelijke statistieken met betrekking tot de interface samen te stellen. De resultaten laten zien dat de gevallen met een hogere coflow een lagere snelheidsverval op de hartlijn van de straal hebben en een verminderde straalspreiding. De gemiddelde axiale snelheid vertoont een tekortgebied vergeleken met de vrije straal nabij het grensvlakgebied. Verder vertoont het geval met een hogere coflow een hogere turbulentie-intensiteit en Reynolds-schuifspanning dichtbij het grensvlak. De gedetailleerde resultaten worden gepresenteerd als zowel onvoorwaardelijke als voorwaardelijke statistieken en het mechanisme achter dit effect wordt afgeleid.

Er werden experimenten uitgevoerd met een jet-gestabiliseerde verbrander die in staat was het vlamloze verbrandingsregime te produceren. Het werd bedreven met behulp van methaan-waterstof mengsels met verschillende equivalentieverhoudingen. De prestaties van de brander werden geanalyseerd op basis van de stabilisatie van de vlamzone en de emissies. Dit werk presenteert een unieke uitgebreide meting van temperatuur, gassamenstelling, snelheidsveld en chemiluminescentiesignaal in een jet-gestabiliseerde verbrander. De recirculatiegebieden worden gevisualiseerd door middel van PIV metingen en de recirculatieverhouding wordt gekwantificeerd. De momentane vlambeelden worden gebruikt om vlamkernen te identificeren en waarschijnlijkheidsdichtheidsfuncties te construeren van de aspectverhouding, rotatiehoek en locatie langs de branderas. Een toename van het waterstofgehalte in het brandstofmengsel verschuift het stabilisatiemechanisme van zelfontbranding naar vlamvoortplanting. Ook de NO uitstoot neemt toe. Een soortgelijk effect wordt waargenomen bij de toename van de equivalentieverhouding van een magere naar een stoichiometrische toestand. Gedistribueerde reactieregimes met ultralage NO en gematigde vlamtemperaturen worden bereikt bij zeer lage equivalentieverhoudingen. Dergelijke mengsels worden beter gestabiliseerd door toevoeging van waterstof aan het brandstofmengsel.

Dit proefschrift biedt fundamentele informatie over de chemie en stromingsfysica van het fenomeen in een jet-gestabiliseerde verbrander, gevolgd door metingen van de werking ervan. De gegevens en conclusies zijn een geschikte referentie voor toekomstige ingenieurs die jet-gestabiliseerde verbranders ontwerpen voor lage NO_x emissies en een hoge verbrandings efficiëntie.

1

INTRODUCTION

*The philosophers have only interpreted the world in various ways.
The point, however, is to change it.*

Karl Marx

Climate change is a long-standing issue that requires immediate attention not only for environmental conservation but, more importantly, for the survival of human civilization. Anthropogenic activities, especially through emissions of greenhouse gases, have led to global surface temperature reaching $1.1\text{ }^{\circ}\text{C}$ above 1850-1900 in 2011-2020[1].

The synthesis report on climate change by the IPCC¹ in 2023[1] mentions with high confidence that human-caused climate change is already affecting weather and climate extremes around the world. This has led to adverse impacts and losses to nature and people; vulnerable communities who have historically contributed least to the current climate change are disproportionately affected. Increasing weather and climate extremes have subjected millions of people to acute food and water insecurity, with the largest impacts being observed in communities across Africa, Asia, Central and South America, LDCs², Small Islands and the Arctic and globally for Indigenous Peoples.

Addressing this issue is not only a matter of science and engineering but also politically driven. Nations of the world have come together to make pledges to drive action towards climate-neutral activities; however, the ground reality is far from ideal. In December 2015, 196 parties at the United Nations Climate Change Conference, Conference of Parties (COP) 21, signed a legally binding treaty on climate change, today known as the Paris Agreement [2]. The goal was to hold “the increase in the global average temperature to well below $2\text{ }^{\circ}\text{C}$ above pre-industrial levels” and pursue efforts “to limit the temperature increase to $1.5\text{ }^{\circ}\text{C}$ above pre-industrial levels”. However, at COP28, held in December 2023 in Dubai, it was underlined that despite overall progress on mitigation, adaptation, and means of implementation and support, Parties are not yet collectively on track toward achieving the purpose of the Paris Agreement and its long-term goals[3]. It was also noted with alarm and serious concern the following [3]:

1. emissions of greenhouse gases by human activities have unequivocally caused global warming of about $1.1\text{ }^{\circ}\text{C}$
2. human-caused climate change impacts are being felt across the globe, with those who have contributed the least being most vulnerable
3. most observed adaptations responses are fragmented, incremental, sector-specific, and unequally distributed across regions.

There are gaps between projected emissions from policies that have been implemented by nations and those from nationally determined contributions(NDCs). It is highly likely, based on current policies, implementation, and financial flow, that warming will exceed $1.5\text{ }^{\circ}\text{C}$ during the 21st century, making it harder to limit it below $2\text{ }^{\circ}\text{C}$. Without a strengthening of policies, global warming of $3.2\text{ }^{\circ}\text{C}$ is projected by 2100(Fig 1.1).

¹The Intergovernmental Panel on Climate Change (IPCC) is the United Nations body for assessing the science related to climate change

²Least Developed Countries, as classified by the United Nations, are low-income countries confronting severe structural impediments to sustainable development. They are highly vulnerable to economic and environmental shocks and have low levels of human assets

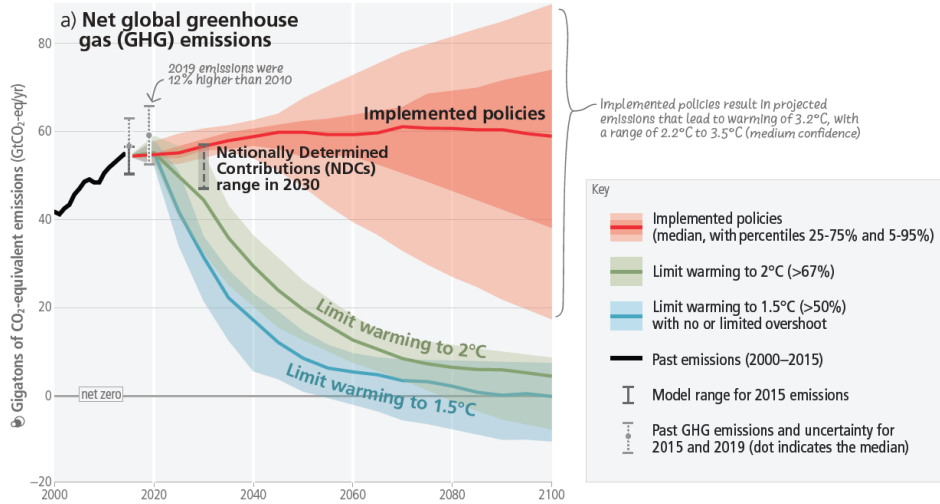


Figure 1.1: Net global greenhouse gas emissions and the projected scenarios of global warming they lead to [1].

1.1. ROLE OF COMBUSTION IN THE GREEN ENERGY ECONOMY

WE might be too late to achieve the Paris Climate goals and must now even strive for carbon-negative activities. Based on the trends in Fig 1.1, the timing of action is more critical in the near future. On the other hand, there is an urgent need to deploy technologies over the next two decades across several industry sectors to meet the energy requirements for the economic and social development of emerging economies as well as that of the rising global population. This poses as a challenge but also is a great opportunity to minimize the climate impact of new assets by employing the latest "green technologies". A large amount of research and development backed by large investments is being made toward transitioning to renewable energy and decarbonization across many sectors. However, the fact remains that there are still a lot of anthropogenic activities that remain hard to abate and make carbon-free, requiring some form of combustion to power them. These include process industries such as steelmaking, glass manufacturing, and chemical production, and transportation industries such as aviation, maritime, and land-based freight transport. Even for example, in the power generation industry, where renewable energy sources can be used, the intermittency of these sources requires either some form of storage or power generation that can be provided on demand, such as through gas turbines or thermal power plants. Thus, the need for clean combustion technologies is pertinent and required to curtail the effects of existing assets through retrofitting and provision of low emission/climate neutral technologies in assets to be installed in the near future. Contribution of various industries to climate change (IEA report)

According to the 2024 report by the International Energy Agency (IEA)³ [4], renew-

³The International Energy Agency is a Paris-based autonomous intergovernmental organization established

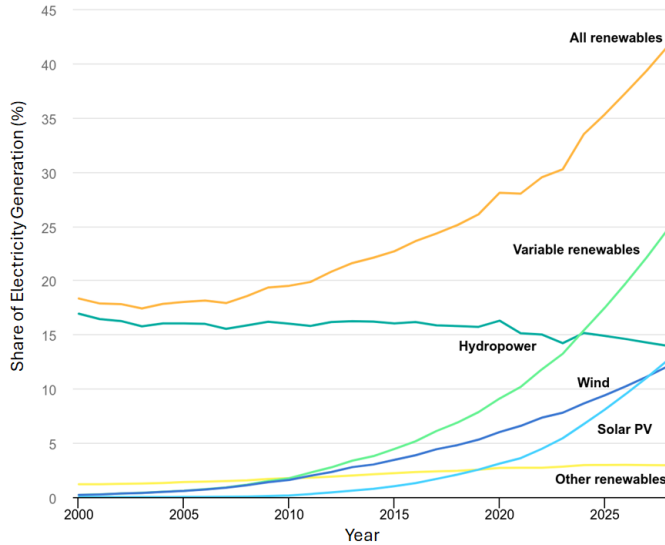


Figure 1.2: Share of renewable electricity generation by technology 2000-2028 [6]

ables contributed to 30% of global power demands. The remainder was still by fossil fuel and nuclear-based power plants. Coal and natural gas contributed to 35% and 20% of global electricity, respectively, while nuclear contributed to 10%. There is a healthy projection for the rise of wind and solar power plants in the future, as shown in Fig 1.2. However, they are considered variable sources, i.e., characterized by intermittency. Hydroelectricity is a clean source of energy that may fill the gap, but it is limited in the available sites worldwide. The rest of this intermittency may be fulfilled by thermal power plants[5]. The emissions from these sources may be improved by using low-carbon fuels such as hydrogen. The scenario is positive with the rise of renewable energy. However, the truth remains that there are still existing fossil fuel power plants that need to exist due to capital investment or just to provide sufficient energy for a population.

For transportation, Battery Electric Vehicles (BEVs) have proven to be a good fit for the urban sedan market (source); however, for heavy road vehicles, ships, and aviation, a dense energy carrier is required, and it is difficult to beat chemical energy storage. Shipping and aviation each contributed to 2% of the global CO₂ emission in 2022[7]. Fuel cells are emerging as a potential technology, but especially for aviation, where there is a high power demand during take-off, combustion be it of fossil fuels such as jet-A1, sustainable aviation fuels (SAFs), or carbon-free carriers such as hydrogen, will remain a cornerstone method for propulsion. This is especially important in the short term up to 2050, where a significant curtailment of CO₂ emissions must be made.

From the above-presented scenarios, it can be seen that combustion research will play an important role in not only retrofitting older power plants and propulsion sys-

in 1974 that provides policy recommendations, analysis, and data on the entire global energy sector. The 31 member countries and 13 association countries of the IEA represent 75% of global energy demand.

tems to reduce their emissions but also developing newer ones that have low emissions and are fuel-flexible, such that, in the long term they are capable of burning sustainable fuels produced from renewable energy. Even if "cleaner" fuels are adopted, the process of combustion is accompanied by so-called non-CO₂ emissions, which consist of carbon monoxide (CO), nitrogen oxides (NO_x), and water vapor. While these are emitted in small quantities, they can have a significant impact on the climate as well as human health.

1.2. NO_x EMISSIONS FROM COMBUSTION

The term NO_x stands for nitrogen oxides and is used to collectively refer to various compounds, typically NO, NO₂, and N₂O, as they are the most abundant species among the group. NO_x emissions in combustion are formed by the thermal, prompt, N₂O, NNH, and fuel-based pathways. A detailed description of the chemical equations can be found in Appendix A. Their emission in the atmosphere can have an impact on human health, plant and marine life as well as climate effects that directly or indirectly play a role in global warming.

Nitrogen oxides can dissolve in water and react to form nitric acid (HNO₃) or nitrous acid (HNO₂). NO is only slightly soluble in water, while NO₂ and N₂O are water soluble. This dissolution can occur in droplets in the atmosphere, which eventually fall as rain, leading to acid rain. Acid rain can adversely affect water quality in reservoirs, negatively affect forests and vegetation, cause soil acidification, damage structures and monuments made of rocks containing calcium carbonate, such as limestone and marble, and cause some skin irritation to humans.

Photochemical smog is produced when Volatile Organic Compounds (VOC) react with NO_x in the presence of sunlight. The reaction leads to the formation of particulate matter less than 2.5 μm in diameter (PM_{2.5}) through the formation of nitrates and nitrites. This usually appears as smog, smoke, white overcast, or haze, which does not vanish when the air warms up again. Nitric acid can react with ammonia in the air to form solid crystals, much smaller than 2.5 μm and can serve as nucleation sites for particle growth. Overall, the presence of such fine particles at ground level is toxic to humans and can cause damage to lung tissue, reduced lung function, and respiratory diseases such as bronchitis. Also, long-term exposure to large quantities of NO_x can lead to chronic lung disease.

NO_x in the atmosphere may also dissolve directly in water bodies. This can lead to elevated nitrogen levels (eutrophication) in the water, leading to excessive growth of algae ("algal bloom"). This can cut off sunlight from aquatic plants, leading to their death and subsequent oxygen depletion in the water. This can make the lower layers of the water body uninhabitable for aquatic animals and plants, thereby causing an imbalance in the ecosystem. It is estimated that anywhere between 12 and 44% of nitrogen loading of coastal water bodies can come from the air (cite EPA).

Nitrogen oxides (NO+NO₂) lead to ozone formation through a catalytic reaction. NO reacts with HO₂ to form ozone, which in turn undergoes photo-dissociation to form atomic oxygen (O). This reacts with diatomic oxygen to form ozone (O₃) [8]. NO_x also decreases the level of methane, stratospheric water vapor, and the amount of primary-mode ozone (PMO) [9]. Ozone, methane, and water vapor are all greenhouse gases, and

NO_x either produces or destroys them depending on the altitude of emission. Within the upper troposphere-low stratosphere, NO_x emissions lead to net ozone production. Slightly above, between 13-14 km altitude, there is an ozone-neutral region, and above this region, O_3 is consumed by NO to produce NO_2 and O_2 . [10]. Overall, the warming effect is dominant [9]. Although NO_x is not a direct greenhouse gas, in the troposphere, it can lead to the formation of ozone and the consumption of methane. Ozone has a net global warming effect at low altitudes. Direct inhalation of ozone is also toxic for humans.

Due to the aforementioned effects that NO_x can have, there are several regulations and advisory targets on the level of NO_x that may be emitted from combustion devices, especially those used for power generation, such as land-based gas turbines, ICE engines in road transport, and aircraft engines. The ACARE⁴ goal is to have a 90% reduction in NO_x emissions by 2050 from all intra-EU flights and those departing the EU, relative to the year 2000, while in the short term, it aims at a 30% reduction by 2035 relative to the baseline in 1990 (cite ACARE webpage). International bodies such as ICAO⁵ exist to coordinate regulations regarding these emissions as it is not a local phenomenon. For example, ICAO has set up the Committee on Aviation Environmental Protection (CAEP) to formulate policies and assist the council in adopting new standards and recommended practices to reduce emissions from aviation. The policy and standards are used as references for determining individual regional regulations updated to account for new technologies and goals.

The European Union's Directive 2010/75/EU [11] states the regulation for large gas turbine engines and combustion plants (>50MWth). For all gas turbines, across all fuel types (light and middle distillates as liquid fuel as well as gas-fired) and including combined cycle gas turbines, the NO_x ($\text{NO} + \text{NO}_2$) Emission Limit Value (ELV) is set at 50 mg/Nm^3 (25 ppm) and for CO at 100 mg/Nm^3 (82 ppm). However, for single-cycle gas-fired turbines having an efficiency greater than 35%, the ELV for NO_x is allowed to be determined based on the efficiency as $50 \times \eta / 35$, where η is the gas turbine efficiency at ISO base load conditions expressed as a percentage. The ELV, expressed in mg/Nm^3 is the mass of the emission divided by the volume of the flue gas. Further, all ELVs are calculated at a temperature of 273.15 K, pressure of 101.3 kPa, and after correction for water vapor of the flue gases at an O_2 standard of 15% for gas turbines. Directive 2015/2193/EU [12] for medium power plant (1-50 MWth), states NO_x ELV values of 150 mg/Nm^3 (75 ppm) and 200 mg/Nm^3 (100 ppm) for existing gas turbines operating on natural gas and other fuels respectively. New gas turbines need to have a NO_x ELV of 50 mg/Nm^3 (25 ppm) and 75 mg/Nm^3 (37.5 ppm) for natural gas and other fuels, respectively.

⁴ACARE provides strategic technical and institutional guidance based on an open forum for discussion and consensus-based decision-making process to the European Commission

⁵ICAO: A United Nations agency which helps 193 countries to cooperate and share their skies to their mutual benefit. Since it was established in 1944, ICAO's support and coordination has helped countries to diplomatically and technically realize a uniquely rapid and dependable network of global air mobility, connecting families, cultures, and businesses all over the world and promoting sustainable growth and socio-economic prosperity wherever aircraft fly.

1.3. LOW NO_x COMBUSTION FOR GAS TURBINE ENGINES

The context of this work is centered around low-emission combustion for gas turbine engines, which may pertain to either power or propulsion applications. This section aims to present some of the low NO_x combustion technologies implemented in both stationary and aviation gas turbines. Gas turbines, both stationary and aviation, must comply with very strict emissions regulations. In land-based gas turbines, low NO_x can be achieved by introducing aftertreatment systems such as scrubbers and catalytic converters. Aviation gas turbine engines cannot include those due to the weight penalty. Thus, the low target emission levels must be achieved by manipulating the combustor itself. Several strategies, such as RQL (Rich burn-Quick-quench-Lean burn), LPP (Lean Premixed Prevaporised), and LDI (Lean Direct Injection), have been used. Further, aviation gas turbines usually operate on liquid fuels such as Jet-A1, thereby including a phase change and mixing problem. Stationary gas turbine engines employ several NO_x reduction strategies, some of which involve additional equipment and raw material [13]. Some of the NO_x reduction techniques used in power plants are as follows:

- NO_x can be reduced by reducing peak temperatures to mitigate the thermal pathway. This is done by injection of water/steam or cooled flue gas. However, additional equipment and pumping power are required for this.
- The residence time at high temperatures can be restricted by the process of air staging. The high-temperature flame region is restricted by dilution with air. Sometimes, this is also done with cooled flue gas.
- Two common methods are used to chemically reduce NO_x back to molecular nitrogen: Selective Catalytic Reduction (SCR) and Selective Non-Catalytic Reduction (SNCR). In both techniques, reagents such as ammonia or urea are injected into the flue gas. The difference is that SCR uses a catalyst such as titanium dioxide (TiO₂) or vanadium-5 oxide (V₂O₅) to increase reaction rate at lower temperatures, whereas SNCR does not and hence has higher operational temperature requirements. In some applications, the process of fuel reburn is also used. In this, fuel is injected after the main combustion zone to create a fuel-rich region such that NO_x is reduced through the NO_x-reburn pathway [14] and CO is formed. This method required further air addition to oxidize the CO.
- The flue gas can be treated by sorbents (such as ammonia, powdered limestone, aluminium oxide, or carbon) to remove NO_x and other pollutants such as sulphur. Sorption can be either adsorption or absorption and often the resultant by-products are marketed as commodities. When solid particles are used, electrostatic precipitation is used to remove the sorbent and by-product from the exhaust stream.
- Most of the above-mentioned are either post-combustion treatment or mitigation by additional systems. There is also NO_x reduction by prevention at production. These are Dry LOW Emission technologies wherein the NO_x is controlled by optimal design of thermo-fluid behavior of the combustor. One example is lean premixed combustion.

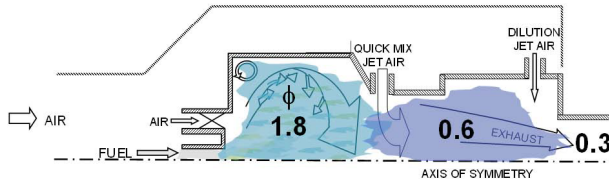


Figure 1.3: Rich burn Quick mix Lean burn (RQL) combustor [16].

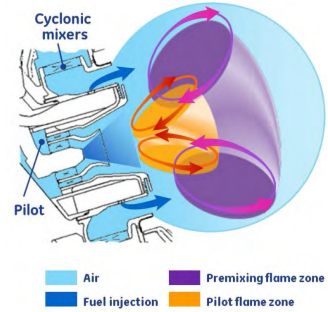


Figure 1.4: Twin Annular Premixing Swirler (TAPS) fuel injection concept [17].

In the case of aviation gas turbines, the weight of the system is critical for efficient flight performance. Thus, most strategies mitigate NO_x at source and would fall under the DLE category of stationary gas turbines. Some low NO_x configurations are listed here, but a comprehensive review has been done by Liu *et al.* [15]:

- Rich burn-Quick quench-Lean burn (RQL) is a concept used to obtain a stable flame while reducing NO_x . The primary zone is fuel rich, which enhances combustion stability. This is further diluted to become fuel lean but must go past the stoichiometric region around which high temperatures and, hence, high NO_x may be produced. Thus, this is done "quickly" by minimizing the residence time under these conditions. Finally, after dilution, there is a lean burn phase to consume the remaining CO and UHC while producing negligible NO_x . This is currently used on Pratt and Whitney TALON combustors powering several engines such as PW1500, PW1133G1-JM, etc. This concept is also used in the Rolls Royce Trent 1000 and GE's CFM56 series.
- TAPS (Twin Annular Premixing Swirler) consists of a partially premixed configuration with a pilot and main stage arranged coaxially. The pilot fuel is injected through a simplex atomizer such that a film is produced and atomized in air-blast mode upon the interaction between the two axial air streams. The swirling stream generates the pilot recirculation zone which stabilizes the pilot flame. This is a rich burn system that ensures its stability under varying operating conditions. At high power, the main burner is also turned on wherein air is introduced through cyclone swirlers. There is a premixing channel where liquid jets of fuel are injected radially. The main flame stabilizes in the mixing layer between the pilot and the main burners. The smaller recirculation zones produced are crucial for stabilization due to the supply of radicals and hot products. The TAPS combustors' premixed nature ensures operation at lean equivalence ratios without local hot spots, ensuring low NO_x . Thus, the low-power, fuel-rich pilot flame is used to stabilize the high-power fuel-lean, premixed main flame. This has been used on the GE GENx series of engines and the LEAP engine.

- LDI (Lean Direct Injection), as the name suggests, injects the liquid fuel directly into the combustor without premixing with the air. The concept relies on quick mixing of fuel and air after injection, such that a lean mixture is obtained before combustion initiates, thereby leading to low NO_x. This concept is extended to multiple injectors, thereby leading to Multipoint lean direct injection (MLDI). This increases the mixing surface area for the same fuel flow, increasing mixing efficiency. The injector comprises a central fuel injector surrounded by an air swirler. The swirler helps generate a flow field with a recirculation, which enables the stabilization of a lean flame.
- LPP (Lean Premixed Prevaporised) is a concept in which the liquid fuel is given enough residence time to first completely vaporize and mix with the air stream in a premixing section. This mixture then enters the combustor, typically at lean equivalence ratios such that low NO_x is produced due to low adiabatic flame temperatures. The flame is stabilized by the presence of a recirculation zone. Such a combustor has challenges with lean blowout and a higher risk of autoignition and flashback.

Next-generation gas turbine combustors would have to be fuel-flexible to accommodate varying amounts of renewable fuels such as hydrogen, ammonia, and SAFs, as it is possible that due to the scale-up time required, these fuels would be introduced as admixtures. Further, gas turbines will have to meet even more stringent emission regulations, which will become challenging as OPR and TIT would increase to increase thermodynamic efficiency. Thus, the combustors need to produce low NO_x while also producing low CO.

Flameless/Mild combustion is a technology that gives very low NO_x emissions while achieving nearly 100% combustion efficiency. This has been extensively used in industrial furnaces over the last 2 decades, and its unique properties make it suitable for use in gas turbines. It is characterized by dilution of reactants to achieve reduced O₂% (vitiation) while the reactants have a high temperature above the autoignition temperature. Counterintuitively, this leads to low peak temperatures in the combustion chamber, hence the suppression of thermal NO_x. It also offers a fuel-flexible combustion option, making it suitable for combusting blends of fuels depending on their availability, thereby aiding in the energy transition in land and aviation gas turbines.

This concept has been studied by DLR in their high-pressure combustor (Fig 1.5). This used a modified FLOX burner head with 12 nozzles and was operated with admixtures of methane and hydrogen. The reactants were injected through high-velocity jets in the combustion chamber, which undergo internal recirculation. The configuration relies on this recirculation of hot combusted gases to produce conditions suited for flameless combustion. The combustor was reported to output NO_x of the order <10 ppm.

Sequential combustors such as Ansaldo Energia's GT26 and GT36 engines have a reheat concept where combustion staging is applied to stationary gas turbines. The first stage is stabilized by flame propagation through a vortex breakdown mechanism, while the second stage is autoignition stabilized [20][21]. The principle involves a heat addition in two stages such that the peak temperature is limited to reduce NO_x production. In the GT24/26, a high-pressure turbine is located between the two combustors such

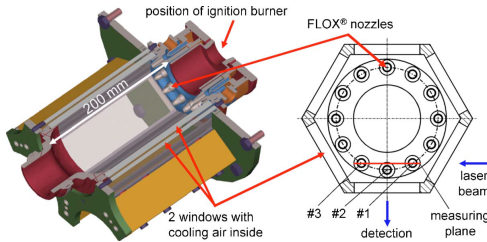


Figure 1.5: DLR jet stabilized combustor [18]

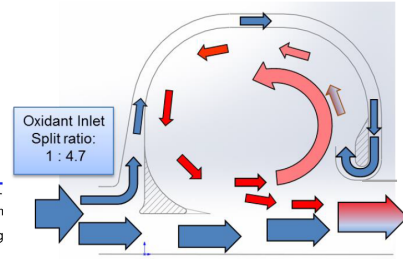


Figure 1.6: Schematic of Flameless combustor for sequential combustion turbofan engine [19].

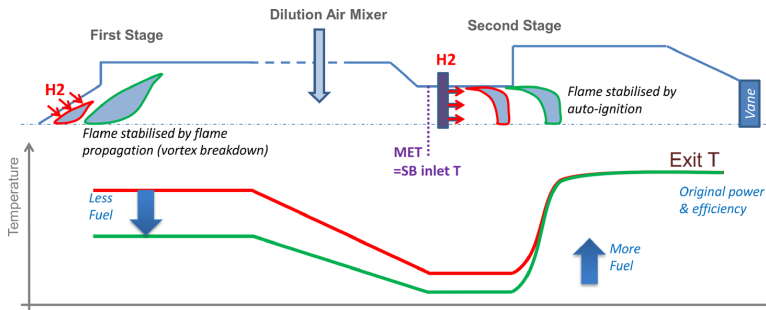


Figure 1.7: Ansaldo GT36 combustor schematic highlighting fuel flexibility [21].

that after the first heat addition, the temperature is reduced by expansion in the turbine, and then the second stage follows. In the newer GT36, there is no inter-burner turbine, but instead, dilution air is added to reduce the temperature between the first and second stages. The technology allows for stable lean premixed combustion, efficiently using the available oxygen, thereby reducing soot and CO at the exhaust. Further, stabilization by autoignition in the second stage leads to enhanced fuel flexibility, allowing for an easy switch to low-carbon fuels such as hydrogen. The concept of heat addition in stages with an intermediate step of temperature reduction through expansion in a turbine or dilution by air allows for the complete combustion of fuel while limiting peak temperatures. Further, due to low O₂ levels in the second stage, the sequential combustor can operate at high firing temperatures with low NO_x production. Although the developers never mention it as a flameless/mild combustor, it has all the elements befitting this regime.

A similar concept was developed for aeronautical engines under the AHEAD (Advanced Hybrid Engines for Aircraft Development) project. This involved a dual combustor configuration wherein the first combustor was designed to work with cryogenic LH₂/LNG fuel and the second combustor, located between the high-pressure and low-pressure turbine and also called the inter turbine burner (ITB), was designed to work on Jet-A1/biofuel in the flameless combustion regime. The hot products from the first combustor would help to achieve a low O₂% and high-temperature environment in the second one. The ITB also had a dome structure to promote internal recirculation as shown in Fig 1.6. This was done to increase residence time for complete combustion as well as

promote recirculation for further vitiation. Thus, in addition to dilution from hot products of the first combustor, the second combustor had a geometry that promoted high internal recirculation, thereby producing further dilution of $O_2\%$. Experiments showed that NO_x levels < 8.5 ppm could be achieved [22] for overall equivalence ratios ranging from 0.12 to 0.22, which included non-combustion air that is diverted from the combustor and remixed downstream as shown in Fig 1.6.

1.4. LAYOUT OF THESIS

The discussion above motivates the need for low NO_x combustors that can work on low-carbon fuels, such as hydrogen, to aid in the energy transition. The flameless combustion regime, which occurs in hot vitiated environments, emerges as a potential candidate for combustion strategy in future gas turbine engines. This thesis investigates the phenomenology of combustion in a jet-stabilized combustor capable of producing the flameless combustion regime. The structure of the thesis is shown in Fig 1.8, with the arrows indicating prerequisite chapters. Chapter 2 explains the concept of Flameless combustion and the state-of-the-art literature on the subject. This is followed by the research objective and the resulting research questions addressed in this dissertation. The Flameless Combustor experimental facility, along with experiment and data processing methods, are described in Chapter 3. This chapter also describes some of the engineering design decisions and calculations that were done to design and commission the combustion test rig. Chapter 4 investigates the autoignition chemistry of CH_4 -Air mixtures with exhaust gas vitiation and the resulting NO_x and CO emissions. Chapter 5 is an experimental study of flow physics and mixing at the interface of a turbulent-jet-in-turbulent coflow, a typical configuration used to produce the flameless combustion regime. This is also a canonical representation of the turbulent interaction of the jet and recirculation zone in a jet-stabilized combustor. Chapter 6 presents experimental results on the operation of a jet-stabilized combustor with varying CH_4 - H_2 fuel mixture conditions. The flame stabilization mechanism and emissions are analyzed. Finally, Chapter 7 presents the main conclusions and recommendations derived from a synthesis of results.

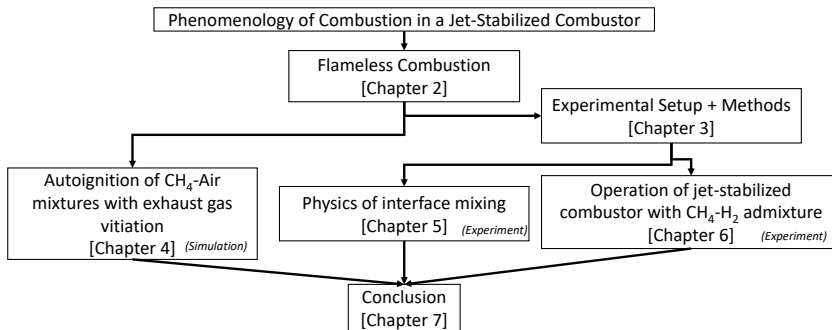


Figure 1.8: Layout of this dissertation



2

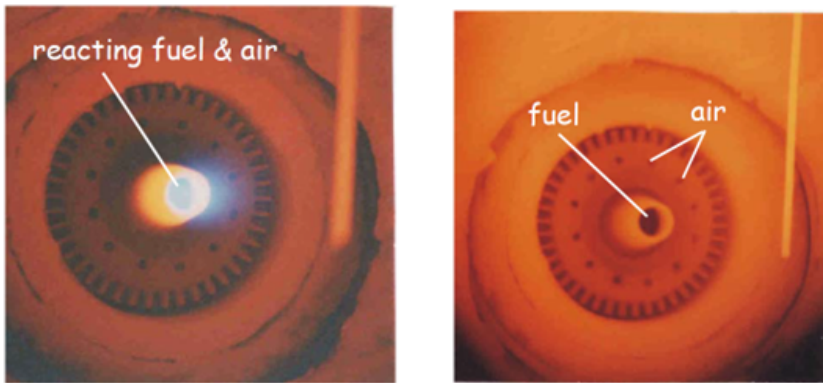
FLAMELESS COMBUSTION

Any intelligent fool can make things bigger, more complex, and more violent. It takes a touch of genius and a lot of courage to move in the opposite direction.

Albert Einstein

This chapter provides an overview of the concept of Flameless combustion and the body of knowledge on its characteristics. Various laboratory scale setups are introduced, along with a brief description of the working principle and major findings regarding stabilization and emissions. Further, the knowledge of the structure and stabilization of the reaction zone is summarized, which is primarily obtained from DNS simulations and jet-in-hot-coflow experiments. Finally, a commentary is provided on the capability of Flameless Combustion to generate low NO_x followed by the research objectives of this dissertation.

Flameless Combustion was a chance discovery made during the operation of a furnace by a German company called W S Warmeprozessestechnik GmbH. In 1989, during experiments on a self-recuperative burner, at furnace temperatures of 1000 °C and air preheat temperature of 650 °C, no flame was visible to the naked eye, while the fuel was completely burnt [23]. The CO content in the exhaust was below 1 ppm and the NO_x emissions were close to zero. At first, it was thought to be a defect of the NO analyzer, but upon further observation and analysis, it was determined that there was indeed a stable and smooth reaction zone which came to be known as flameless oxidation or FLOX. Over the years, this regime of combustion has been known by several names, such as flameless combustion (FC), MILD (Moderate or Intense Low-oxygen Dilution), mild combustion, etc. One of the first technical descriptions of Flameless Combustion can be found in [24], where the inspiration comes from the technology of exhaust gas recirculation, where the exhaust gas is tapped from the exhaust duct, cooled and re-injected with the combustion air. This requires a compressor/blower to increase the pressure of the exhaust gas back to that of the inlet reactants. However, in Flameless Combustion technology, the recirculation occurs internally within the chamber, reducing the complexity of equipment required to handle different hot gas streams. FC is proposed to reduce NO_x by lowering peak temperatures. This shall be further discussed in the context of premixed and non-premixed combustion in this chapter. This chapter aims to give a description of the definition of Flameless Combustion, as it has evolved since its discovery, present some common configurations used in laboratories to study this phenomenon, highlight features of flame stabilization, reaction zone structure, and differences from conventional premixed/non-premixed combustion. Finally, some open research aspects are mentioned, which also form the basis of the research done in this thesis.



(a) Conventional flame

(b) FLOX mode

Figure 2.1: Visual appearance of flame under conventional and flameless conditions [25]

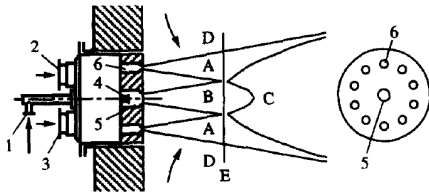


Figure 2.2: Flameless Combustion burner [24]

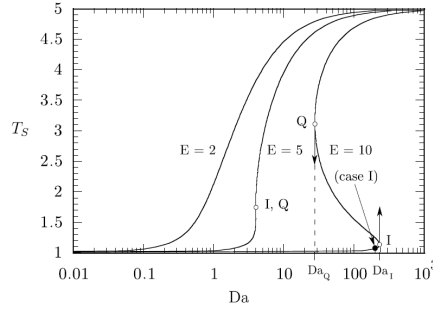


Figure 2.3: Ignition-extinction curve for varying conditions of initial reactant mixture[26]

2.1. DEFINITION OF FLAMELESS COMBUSTION

Flameless Combustion is characterized by high reactant inlet temperature combined with the addition of diluents, which is referred to as dilution/vitiation. The combustion research community has defined Flameless Combustion in several ways. Wüning [24] defined Flameless Oxidation as the conditions when there is no visual flame. This was observed in a furnace where exhaust gases were recirculated and mixed with the fuel/air stream before injection into the chamber, by physical piping and valves. Flue gas entrained within the chamber was not considered as part of this recirculation. The conditions to achieve this are shown to be those with a high recirculation ratio ($K_v > 2$) and high furnace temperature ($> 700^\circ\text{C}$). High recirculation with insufficient furnace temperature results in unstable flames that lift off and blow out and stable flames may be achieved with low recirculation ratio ($K_v < 0.5$) for almost any furnace temperature. This was seen to be possible in both non-adiabatic and adiabatic furnaces, i.e., with and without cooling of exhaust gases before recirculation; however, in the adiabatic case, the temperature needs to be controlled by the equivalence ratio. The working principle can be better understood through the sketch of the burner, shown in Fig 2.2. In 'flame mode', fuel and air are supplied through '1' and '2', respectively, and they enter the chamber through '4'. Once the chamber is hot enough, the air supply is redirected from '2' to go through '3' such that it is directly injected into the chamber through nozzles '6'. The air jet 'A' entrains recirculated exhaust gas 'D' as well as the fuel jet 'B'. The reaction zone 'C' occurs when the fuel and air jets meet but by then the jets have already mixed with large amounts of exhaust gas, thereby creating a hot diluted environment for combustion.

One of the explanations for the colourless or flameless appearance of this regime is given by Cavaliere and de Joannon [27]. The authors mention the work of De Joannon *et al.* [28] in which, through numerical analysis, it was shown that the 'kinetic' fluxes of methane oxidation yield light-emitting radicals, like CH and C_2 , only at relatively high temperatures. In vitiated rich conditions, typical of the first stage of Mild Combustion, the maximum temperature is relatively low, and this is particularly suitable for pyrolytic or reforming stages leading to H_2 and CO. Even very high temperatures in the oxidative region are not capable of producing CH and C_2 , which are among the main light-emitting species in traditional flames. Thus, the lack of visible radiation renders the flameless

effect. Another explanation is provided by Zhou *et al.* [29]. The authors claim that in the FC mode, a significant increase in the Continuous Background (CBG) emission is seen. The CBG is supposed to be the light emitted due to CO_2^* . This reduces the contrast of the CH^* and C_2^* light emissions, which are the emissions that conventionally make a flame visible, compared to the background, and hence, the flame appears to be invisible to the naked eye.

Oberlack *et al.* [26] studied the effect of Damköhler number variation in a 0-D, homogeneous reactor by numerical modeling of the system of ordinary differential equations. The variation of the steady-state temperature with Damköhler number for different values of E ($E = \frac{E_{activation}}{RT_u}$) is shown in Fig 2.3. Above a certain activation energy, the 'S'-shaped curve occurs, where two attractor solutions exist, depending on whether the state is on the I or Q branch, leading to ignition or extinction, respectively. As Damköhler number increases, for a low initial temperature, one reaches a point where ignition occurs, and the state of the gas jumps from the lower branch to the upper branch. This is because the intermediate state is not a stable one. Similarly, as one reduces Damköhler number, for gases at a high temperature, it reaches a quenching point where the state jumps down to the lower branch for the same reason. Thus, the ignition and extinction points of the mixture are defined. In contrast, for lower values of E , the curve has a monotonic shape, i.e. points along the entire curve are stable states in which the gas may exist, thus there isn't a distinctive ignition or extinction point. This condition is mathematically represented as

$$\frac{E_{activation}/R}{T_{in}} \leq 4\left(1 + \frac{C_p W_f T_{in}}{Q Y_f}\right) \quad (2.1)$$

where R is the universal gas constant, C_p the specific heat at constant pressure, W_f the molecular weight of the fuel, Q the heat of combustion of the mixture, Y_f the inlet fuel mass fraction and $E_{activation}$ is the activation energy of a one-step reaction. Thus, the authors define Eqn 2.1 as a quantitative definition of flameless combustion. In this case, it was observed that stochastic variation of Damköhler number leads to a monomodal PDF of temperature around the steady state solution in contrast to a bimodal solution seen for conventional combustion. A bimodal PDF has two peaks, one at the low-temperature unburned state and the other at the high-temperature burned state. On the other hand, a monomodal PDF has a single peak for an intermediate temperature. Therefore, both the monotonic ignition curve and monomodal PDF of temperature indicate the flameless combustion regime.

Cavaliere and de Joannon [27] define a combustion process as Mild when the inlet temperature of the reactant mixture is higher than the mixture self-ignition temperature ($T_{in} > T_{si}$) while the maximum allowable increase in temperature during the process is lower than the mixture self-ignition temperature ($\Delta T < T_{si}$), in Kelvin. This definition is derived from analyzing a well-stirred reactor with a mixture of $\text{CH}_4/\text{O}_2/\text{N}_2$. The operating conditions are varied by changing the dilution level by increasing N_2 for a constant CH_4/O_2 ratio, thereby leading to lower temperatures during oxidation. For various combinations of inlet temperature and temperature rise, the authors identify three regimes: Feedback Combustion ($T_{in} < T_{si}$, $\Delta T > T_{si}$), High-Temperature Combustion ($T_{in} > T_{si}$, $\Delta T > T_{si}$) and Mild combustion ($T_{in} > T_{si}$, $\Delta T < T_{si}$). In the cases of feedback

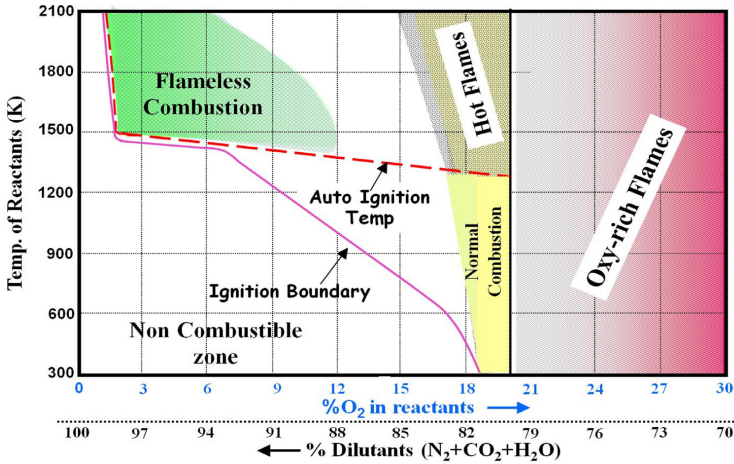


Figure 2.4: Flameless Combustion regime diagram[30]

and high-temperature combustion, the heat released from the process provides a sufficient temperature rise to sustain the process. In contrast, mild combustion requires the preheating of reactants to progress. However, the authors acknowledge that Mild combustion may be considered a subset of High Temperature Air Combustion (HiTAC) and High temperature Combustion (HiCOT) which were earlier introduced technologies that exploited high-temperature reactants. It must be noted here that this definition does not put any constraint on the level of oxygen.

A comprehensive overview of definitions and state of the art of Flameless Combustion can be found in [30]. The authors present a modified form of a regime diagram to indicate the conditions of reactant temperature and oxygen content in the reactant mixture required to achieve Flameless combustion, as shown in Fig 2.4. The Flameless regime was identified to be in a low O₂% regime ranging from 2%-12% with the reactant temperature above the autoignition temperature of the inlet mixture, which in their case was 1400 K.

2.2. LABORATORY-SCALE COMBUSTION SETUPS

Since its discovery and recognition for low NO_x potential, flameless/mild combustion has been studied by various research groups worldwide. This section lists some laboratory setups developed to produce and, hence, study this regime. Broadly, there are two strategies used: the first is internal recirculation of hot products of combustion within the chamber, and the second is having two separate streams, one of hot combustion products and the other containing fuel/fuel+air such that they mix at the interface. A more detailed list can be found in review articles such as [30], while only a few are described here.

2.2.1. INTERNAL RECIRCULATION SYSTEMS

These systems rely on the internal recirculation of hot products of combustion to vitiate the incoming fuel/oxidizer streams. Usually, the fuel and oxidizer are injected through jets that are confined by the combustor walls, and the entrainment of the surrounding fluid by the jet leads to the establishment of recirculation zones. The oxygen content may also be manipulated by adding inert gases such as N_2/CO_2 to the inlet streams.

LUCY NAPLES

A cyclonic lab scale burner, called LUCY (Laboratory Unit CYclonic), was developed by Sorrentino *et al.* [31] at the University of Naples Federico II, Italy, which has a non-premixed configuration such that there is a diluent+ O_2 stream and a separate fuel stream. As shown in Fig 2.5, two sets of fuel/oxidizer inlets are located asymmetrically on opposite corners of the chamber such that the injected flow streams generate a cyclonic vortex flow in the chamber. The outlet of the chamber is located in the middle, at the bottom of the chamber. The combustor was designed to have enhanced mixing of the streams in a short time after injection while allowing for long enough residence times to achieve complete oxidation [32]. The combustor operates at a nominal thermal power of 2-10 kW, and the oxidizer stream can be preheated. The chamber was made from vermiculite, a refractory material that can be machined and has a high insulating capacity. In addition, the chamber is insulated externally with refractory ceramic fiber boards and electric trace heating. There is one quartz window on the top that gives optical access to the ensuing combustion process[33]. This burner shows high fuel flexibility, having been operated on a variety of fuels such as propane [34], methane, biogas [35], and ammonia [36]. Measurements are done with N-type thermocouples, a gas analyzer, and direct imaging of the flame. The residence time (τ) is varied by varying the input thermal power supplied by the massflow rate of fuel. The system shows a strong decrease in maximum temperature with large τ due to the combination of lower input power and heat loss variation [32]. This leads to lower NO_x for higher τ . Experiments with C_3H_8 -Air [33] showed very low NO_x , specifically less than 10 ppm for $\tau=1.5$ s, less than 14 ppm for $\tau=1$ s and less than 34 ppm for $\tau=0.5$ s. Low NO_x values corresponded to temperatures less than 1400 K in the chamber; thus, the thermal NO_x route was suppressed. For varying equivalence ratios from ultra-lean (0.17) to stoichiometric, NO_x first increases, peaks, and then decreases. The burner was also operated with CH_4 -Air [35], and NO_x levels between 5 and 20 ppm were obtained with similar variation with ϕ at 4 kW, as the previous case. However, for a higher thermal load of 10 kW, the NO_x was almost constant at 20 ppm for all ϕ .

DLR FLOX COMBUSTOR

A high-pressure combustor (20 bar) was developed at the German Aerospace Center(DLR), Stuttgart, Germany, based on the FLOX burner design with 12 nozzles, and the chamber had optical access to perform optical diagnostics [18], as shown in Fig 1.5. Each nozzle is comprised of a 1 mm fuel nozzle surrounded by an air nozzle of 4.5 mm diameter. The fuel nozzle was located upstream of the air nozzle, and the relative position could be adjusted to obtain different mixing levels before injection into the chamber [37]. Due to the injection location of the reactant mixture through high-velocity jets(90-140 m/s), a strong central recirculation zone is formed that comprises hot burnt products. This

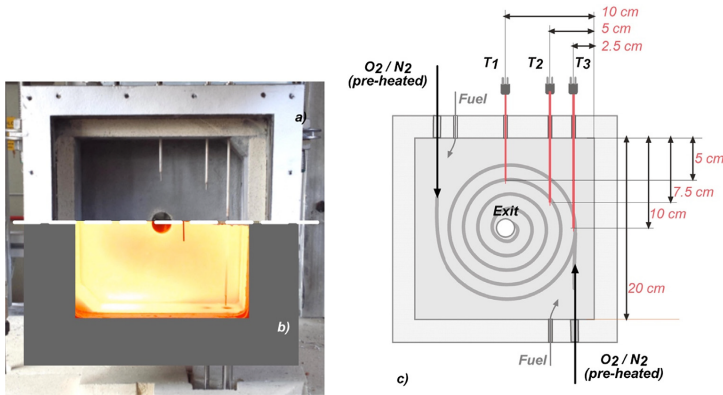


Figure 2.5: Laboratory Unit CYclonic(LUCY) burner (a) burner front view, (b) burner in flameless mode, (c) mid-plane sketch of the chamber with geometrical features. [33]

mixes with the fresh reactants and creates conditions suitable for Flameless combustion. Experiments were done using several diagnostic techniques such as PIV, OH* chemiluminescence, OH-LIF, CARS, and exhaust gas analysis. This combustor has been operated with natural gas-hydrogen admixtures ranging from 0-100% H₂, and sensitivity of emissions to jet velocity, equivalence ratio, and admixture composition was tested. Increasing jet velocity from 40-160 m/s led to reduced NO_x emissions and widened the low emission range (where NO_x and CO, both are less than 10 ppm) of equivalence ratios, which was depicted as a range of adiabatic flame temperature. The addition of H₂ to the fuel mixture increased the NO_x emissions, but from the CO emissions, it was seen that the extinction limit was extended to leaner ϕ . The sensitivity to ϕ is measured for the range 0.38-0.54, and NO_x is seen to vary from < 1 ppm to 37 ppm. Thus, higher NO_x at higher ϕ . Low NO_x regimes were also accompanied by homogeneously distributed reaction zones as seen by OH* chemiluminescence images.

Sadanandan *et al.* [37] investigated the effect of the level of premixedness by varying the position of the fuel nozzle axially with respect to the exit plane of the air nozzle in the chamber. A well-premixed configuration led to the flame stabilizing upstream, closer to the nozzle, and provided less time for mixing with recirculated products before heat release. Non-premixed provided an advantage by stabilizing the reaction zone downstream, thus having a more uniformly distributed reaction zone and temperature field. This enabled lower NO_x. However, the NO_x could be matched irrespective of premixedness if higher jet velocities were used, as that pushed the reaction zone further downstream and made it more distributed.

The combustor was hexagonal with quartz windows. Hence, the velocity field measured by PIV[38] was in limited regions, particularly available only close to the centerline of the combustor, which only covers a section of the recirculation zone. The main jet and interactions with the recirculation are not captured. The complete visualization of the flow field was done by supplementing with CFD simulations. The NO_x values are reported at the exhaust for operations with natural gas, natural gas + propane, and natural gas + hydrogen. With natural gas, NO_x<10 ppm was achieved even at adiabatic tempera-

tures of 2000 K, while the addition of propane and hydrogen increased the NO_x levels for the same adiabatic flame temperature. The temperature measured by CARS and compared with CFD showed a uniform distribution along the combustor centerline.

A simpler, single off-center nozzle combustor was developed later to study the dynamic processes and the stabilization mechanism of the reaction zone in greater detail [39], at atmospheric conditions. Diagnostics such as high-speed PIV and OH-LIF were used to analyze the temporal development of the flow field and track flame kernels.

ULB MILD FURNACE

A MILD combustion furnace was built and studied at the Universite Libre de Bruxelles (ULB), Brussels, Belgium; however, this was a non-adiabatic furnace with an active heat removal circuit, such as in a furnace used to provide process heat [40]. As shown in Fig 2.6, the combustion chamber is a cube of 700 mm made of stainless steel and is insulated with 200 mm thick ceramic fiberboard, which limit the heat loss. Fuel and air are fed through separate jets, such that they mix in the chamber. The exhaust of the furnace is on the same side of the inlet. This allows for an integrated finned heat exchanger to preheat the inlet combustion air using the flue gases. There is an air cooling system with cooling tubes inside the furnace, which serve the purpose of heat extraction to simulate a process load and facilitate operation at different load conditions by varying the the air flow. Measurements were done using OH^* chemiluminescence, a gas analyzer, and a suction pyrometer equipped with an N-type thermocouple for flame temperature. The furnace was operated with methane as well as methane-hydrogen mixtures[41]. NO_x increased with increasing $\text{H}_2\%$ from 0-100%. Decreasing the fuel injector diameter from 25 to 16 mm led to a reduction of NO_x from 175 ppm at 3% O_2 to 60 ppm at 3% O_2 for 100% H_2 . By increasing the length of the fuel lance protruding into the chamber from 0 to 50 mm, the NO_x could be further reduced from 60 to 30 ppm for 100% H_2 . This was attributed to the extra residence time available for the air to mix with the exhaust gases before interacting with the fuel stream. The pure CH_4 case showed negligible levels of NO_x .

IST LISBON COMBUSTOR

A small-scale combustor was developed at the Instituto Superior Técnico (IST), Lisbon, Portugal [42]. The combustion chamber is a cylinder (100 mm diameter, 340 mm long) made of quartz. The burner head has a central air nozzle of 10 mm diameter surrounded by 16 fuel nozzles of 2 mm diameter each. During operations, the quartz cylinder was insulated with a 30 mm thick ceramic fiber blanket. The inlet air can be preheated up to 700 °C by an electric heater. Across the various works, the system has been operated for a fuel thermal input of 7-13 kW and an overall equivalence ratio of 0.43-1.0 with CH_4 as the fuel. Measurements were done by OH^* chemiluminescence, LDA, intrusive gas analyzer, and thermocouple measurements at various locations in the combustor. The operational characteristics of a small-scale combustor were studied by Verissimo *et al.* [42]. The combustor was non-premixed, with a central air nozzle surrounded by fuel nozzles. Emissions were measured for $\phi \leq 1.0$, and NO_x first increased, peaked at $\phi=0.5$ with a value of 9 ppm, and then decreased. On the other hand, CO first decreases and then increases below this value of ϕ . Further studies were done to assess the effect of inlet air velocity [43], thermal power input [44] and air preheat temperature [45]. The

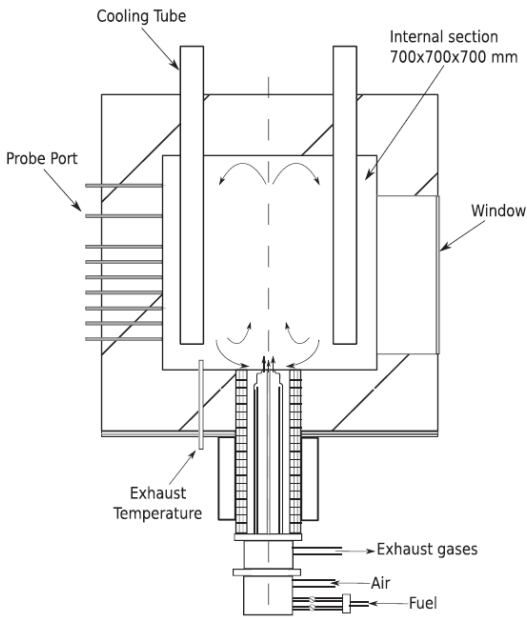


Figure 2.6: MILD combustion furnace at ULB, Belgium [41]

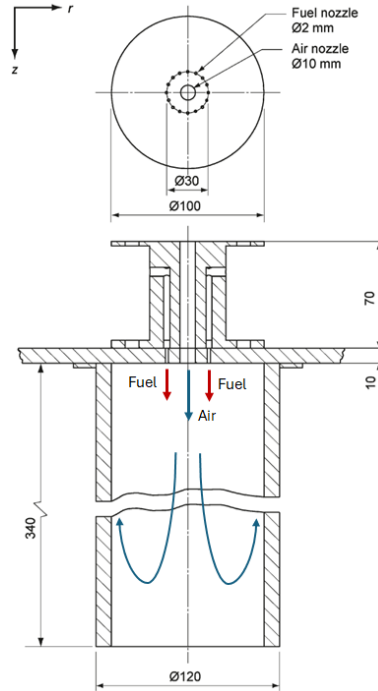


Figure 2.7: Schematic of small-scale MILD combustor, TU Lisbon. Adapted from [42].

effect of increasing air velocity by changing nozzle diameter, i.e., keeping all mass flows constant, resulted in lowering of NO_x and increasing CO. This is attributed to higher entrainment of fuel and recirculating product gases into the air jet, which helps in the onset of flameless combustion. Increasing thermal power implied increasing velocity of all inlet streams while keeping the equivalence ratio constant. This had a significant effect on residence time, thus higher thermal power cases had lower residence time. This led to higher CO at the exit; however, the NO_x remained constant. This was attributed to the suppression of the thermal NO_x pathway under FC regime and it is stipulated that the N_2O pathway may have a more important role.

2.2.2. TWO STREAM SYSTEM

The jet-in-hot-coflow (JHC) has emerged as a popular choice to emulate conditions created locally in a flameless/mild combustor in the laboratory while allowing for high-fidelity laser diagnostics. This is mainly due to the open nature of the flame, which allows for setting up laser beams with minimal reflections. The system consists of a central jet, usually fuel+inert(N_2), and a hot vitiated coflow provided by a coflow burner. The oxygen required to burn the central jet fuel is usually provided by excess O_2 in the burnt products of the hot coflow. This has been adopted by several groups resulting in the Cabra burner[46](14% O_2 in coflow), the Adelaide burner[47] (3-9% O_2 in coflow), and

the Delft Jet in Hot Coflow (DJHC) [48] (7-10% O₂ in coflow), to name a few. These setups have been used to study the variation of lift-off heights with operating conditions and diagnostics such as laser raman, rayleigh, and OH-PLIF have been used to observe the formation and evolution of ignition kernels and the mechanism behind the stabilization of reaction zone under flameless conditions. The JHC configuration offers advantages over enclosed furnaces/combustors operating on the principle of internal recirculation, as the O₂ composition and temperature of diluents can be well controlled and are not inherently coupled with the reactants fed to the main jet through the recirculation zone[49]. Further, the unconfined nature of this setup allows for better optical access for diagnostics, making this configuration suitable for investigating the mechanism of flame initiation and stabilization from a fundamental perspective.

The lift-off height is often used to parameterize turbulent non-premixed flames. For conventional jet flames, it is usually quantified by the average height of the flame interface. This is also used in jet-in-hot-coflow flames where average values of either temperature, OH concentrations, or luminescence are used. However, this would require defining a threshold value to identify the interface, but as the gradients in this combustion regime are expected to be low, the location can be very sensitive to threshold selection [50]. There can also be some differences based on which quantity is chosen. For example, Medwell *et al.* [51] note that for higher O₂ in the coflow (9%), the flames appeared lifted based on visual luminescence, but the OH-PLIF signal suggested that the reaction front extended upstream, up to the jet exit. The authors observed that the lift-off height decreased with an increase in the Reynolds number. The lift-off height is also sensitive to the temperature of the coflow and coflow velocity. A non-monotonic behavior is observed [49] such that lift-off height first increases with an increase in coflow temperature and then decreases. It is hypothesized that the variation of coflow temperature impacts the chemical kinetics and mixing rate between the coflow and fuel jet in a critical manner. Oldenhof *et al.* [50] devised probabilistic criteria based on the occurrence of flame kernels such that the lift-off height was defined as the location where the probability of observing kernels was greater than 50%. The lift-off height showed a non-monotonic variation with Reynolds number where it first decreases for Re increasing from 3000 to \approx 5000 and then increasing as Re increases up to 9500. In contrast, Cabra *et al.* [46] observed a monotonic increase in lift-off height with an increase in Re, although the coflow temperature profile, in this case, is flat and the Re is higher.

Oldenhof *et al.* [48] tracked ignition kernels in the Delft jet-in-hot-coflow and analyzed the lift-off behavior. The trends for the sensitivity of lift-off height to jet Reynolds number were completely different for hot and diluted coflow compared to conventional lifted flames. The addition of higher alkanes and increasing the coflow temperature had similar effects of leading to lower axial location where ignitions first occur, higher ignition frequencies, and reduced lift-off height. A quantitative analysis of entrainment of coflow gases into the central [52] revealed that the rate at which oxidizer is transported to the shear layer between the jet and the coflow, where mixing occurs, is critical to flame stabilization. Specifically, in the case of the DJHC, there is a positive radial temperature gradient, and an increase in jet velocity leads to increased entrainment of hot coflow, which leads to the initial drop in lift-off height with jet velocity.

Entrainment of cold laboratory air is observed in jet-in-hot-coflow setups [52] and is

seen to cause localized extinction events [53] at downstream locations. The entrained excess O_2 leads to local premixing, showing high CH_2O along with a rupture in OH surface and a decrease in temperature at that point. However, in the premixed pocket further downstream, OH and temperature are higher than in a non-premixed case due to higher O_2 . This entrainment and undefined boundaries of the setup make it impractical and inconsequential to measure emissions such as NO_x .

2.3. FLAME STRUCTURE AND STABILIZATION MECHANISM

Since flameless combustion lies in an unconventional regime of temperature and reactant conditions, it may be expected that the reaction zone may have a different structure and also stabilize differently compared to a conventional flame. FC can be achieved in both non-premixed and premixed combustion systems. In both cases, the reactants mix rapidly with diluents before the reactions progress, leading to a new mixture state that reacts. Thus, a comparison is made between autoignition-based stabilization and conventional flame propagation, as that of a premixed flame front where diffusion of heat and radicals from the flame front to the reactants plays a major role.

2.3.1. STRUCTURE OF REACTION ZONE

Minamoto *et al.* [54] studied the structure of the reaction zone under conventional premixed flame regime vs MILD regime using DNS simulations. The temperature distribution of a conventional premixed flame is compared to that of mild combustion in Fig 2.8. The conventional flame has a large temperature gradient across the flame front, which allows one to identify thin flame fronts. The Mild case, on the other hand, seems to have very low gradients and thus appears to have a uniform temperature distribution. Upon closer inspection by visualizing the isosurface of the normalized reaction rate, as shown in Fig 2.9 for the premixed case and MILD case, it was observed that the structure in the Mild case consisted of several flamelets that were interacting albeit with a small gradient, giving an overall distributed appearance. The zones are highly convoluted, increasing the probability of interaction. The level of flamelet interaction increased with increasing dilution and turbulence levels.

Minamoto *et al.* [55] studied the morphology of reaction zone structures through DNS of a premixed and premixed MILD combustion region to understand if they were sheet-like, thin, or distributed. Based on the parameters of thickness, width, and length of the structure, two parameters, Planarity(P) and Filamentarity(F), were defined. Depending on their combination, there can be structures that are blobs or ribbons, tubes or sheets, and in the middle, there are pancakes. The analysis revealed that the premixed conventional flame had sheet-like structures concentrated in a small region. On the other hand, in the MILD case, reaction structures are distributed all over the domain and take on a variety of shapes, such as blobs, pancakes, small ribbons, etc. However, it was seen that the pancake-like structure was the most probable. This may arise from several types of reaction zones, such as autoigniting, propagating flames of mixtures of reactants, products with radicals and intermediates, and interaction of these flames.

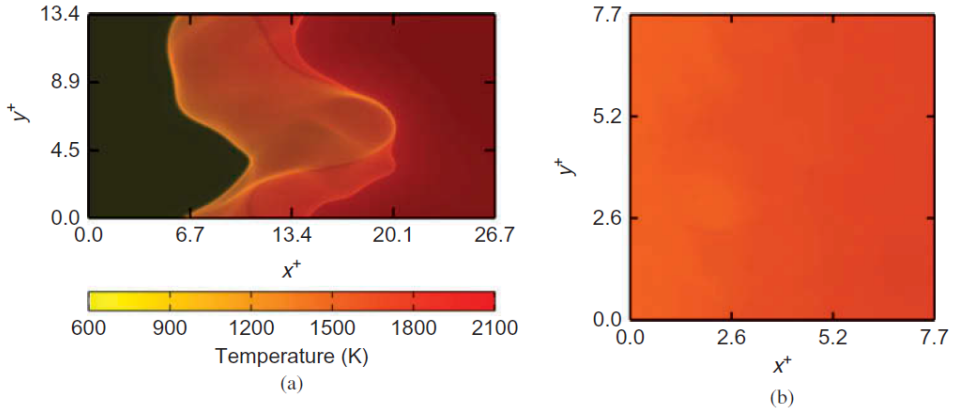


Figure 2.8: Comparison of typical volume rendered temperature field(a) Premixed (b) Mild case[54]

2.3.2. STABILIZATION MECHANISM FROM EXPERIMENTS

Medwell *et al.* [51] observed that for cases with hot coflow, high levels of formaldehyde (CH_2O) were also seen in the preignition zone, i.e., much upstream of the actual lift-off height. This suggested that MILD combustion conditions lead to a different flame stabilization mechanism. The addition of formaldehyde in low oxygen conditions of the coflow had a significant influence on reducing the ignition delay [56]. The addition of formaldehyde to the fuel stream also led to reduced lift-off height. In contrast, for higher oxygen content in the coflow, the addition of formaldehyde has less influence on ignition delay and is consumed only ahead of the reaction zone. Thus, CH_2O was proposed as a precursor species, indicative of FC.

Gordon *et al.* [57] identified a series of temporally successive phenomena based on previous experiments and numerical simulations that indicated the existence of autoignition. The events are:

1. Build up of precursor pool: where the mole fraction of CH_2O increases significantly and that of OH remains low.
2. Initiation of reaction: CH_2O and OH mole fractions reach a maximum in a very short period of time.
3. Formation of a steady flame: CH_2O peak decreases while the OH peak mole fraction does not change.

The authors took simultaneous OH, CH_2O PLIF, and Rayleigh temperature measurements in a flame of methane in vitiated coflow and identified the existence of these events as shown in Fig 2.10. They concluded that they observed a high percentage of autoignition events at the base of the lifted flame, and thus, it was highly likely to be the stabilization mechanism for such a flame. The corresponding author R.L.Gordon in his thesis [58] mentions that one of the future works may be to collect temporally resolved data to further strengthen proof of the hypothesis that lifted flames in a vitiated

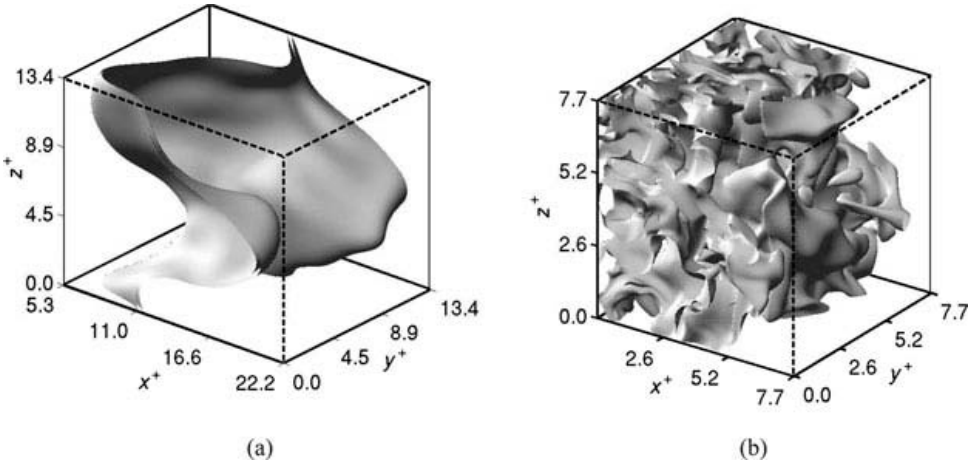


Figure 2.9: Iso surface of reaction rate in (a) conventional premixed flame (b) Flameless/Mild Combustion regime[54]

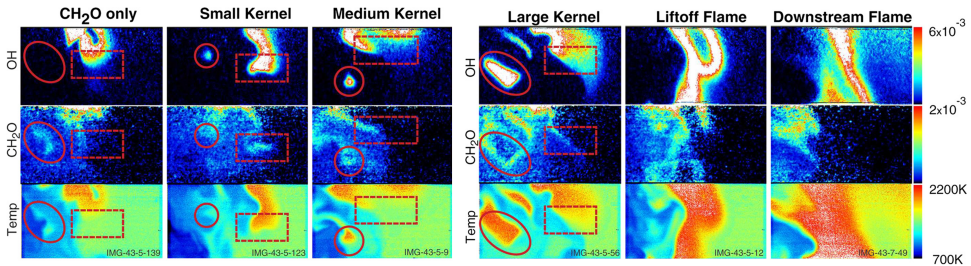


Figure 2.10: Flame features based on CH₂O and OH from PLIF and Temperature from Rayleigh scattering [57]

coflow are stabilised by autoignition. Another recommendation at the end of the thesis is to study the transition regime of stabilization mechanisms. The author mentions that 'clearly', lifted flames in cold flow are not stabilized by autoignition, while his research found heavy evidence that it might be the dominant mechanism in lifted flames in hot coflow. Thus, there may be a point of conditions where the stabilization mechanism transitions, and studying that phenomenon may yield better insight into the occurrence of lifted flames in hot coflow.

Huang [59] studied the stabilization mechanism of flameless combustion by tracking the 'flame base' using OH* chemiluminescence in a MILD furnace with recirculation similar to the one shown in Fig 2.6, but without the cooling tubes. The author visually observed a higher occurrence of autoignition kernels than flame propagation and asserted that autoignition may be the dominant mechanism of stabilization of the flameless zone. The autoignition kernel was recognized as a packet with a high OH* signal. According to the document, such a furnace cannot have stable flame propagation due to the flame stretching due to large-scale vortices in the studied furnace and the mixing is too dynamic to allow a stabilized flame fed continuously by fuel and air mixture. Hence,

the reactions are hypothesized to be started by autoignition.

Severin *et al.* [60] investigated the flame stabilization mechanism in a single jet stabilized combustor, operating on a CH₄ air mixture at $\phi=1$, $T_{in}=473\text{K}$, $Re=5640$. This resulted in a visible, lifted flame which was measured by OH-LIF, PIV, and OH* chemiluminescence, all at 5 kHz, thus yielding time-resolved information of the phenomenon. Vortices were generated in the shear layer, but only on the side where there was enough distance between the jet and the wall. These vortices induce the mixing of the recirculated hot products and fresh reactant stream, leading to a series of events in which the mixture ignites, there is a flame wrap-up, flame expansion, and finally, a merger into the main flame body. While flame propagation was attributed to cause most of the flame expansion, autoignition could not be ruled out. Autoignition was seen to occur through isolated flame kernels at the bottom of the flame body at high frequency, which had a significant effect on the lift-off height. Although the relative weightage of autoignition and flame propagation was difficult to quantify based on these diagnostics, it was clear that the mixing of hot products of combustion and fresh reactants led to the formation of flame precursors, which may enable both flame propagation and autoignition further downstream.

2.3.3. INDICATORS OF AUTOIGNITION

To study autoignition, one must be able to identify and distinguish it from flame propagation, which is the stabilization mechanism for a conventional flame. In conventional flame propagation, heat and radical species diffuse back from the flame front towards the reactants, thereby preheating and eventually igniting them. This heat and mass diffusion process is critical for the continued existence of a flame front. Autoignition, on the other hand, is the process where the reactants are already at an elevated temperature such that they spontaneously react and lead to a heat-release reaction. Several researchers have worked on developing criteria for the same.

Gordon *et al.* [61] have developed two indicators based on numerical modeling. The first one is a budget of convection, diffusion, and reaction of key species wherein it was shown that for a conventional flame, diffusion plays an important role whereas, for autoignition, the convection and reaction terms mostly balance out each other. The second is the build-up of HO₂ before autoignition followed by the creation of H, O, and OH, whereas in conventional premixed flame propagation, all radicals would build up simultaneously.

Schulz *et al.* [62] derived an autoignition index solely based on the chemistry. HO₂ was denoted as a critical intermediate species in the heat release reactions and it was found that the consumption occurs through two main reactions: $HO_2 + H \rightleftharpoons OH + OH$ (R6) and $HO_2 + OH \rightleftharpoons H_2O + O_2$ (R8). The relative extent of each reaction turns out to be a good indicator of whether the reaction is stabilized by flame propagation (R6>R8) or autoignition (R8>R6). This criterion was used to identify autoignition events in a turbulent lifted methane-air flame and to show that premixing and opposed mixing mode autoignition are the prominent mechanisms of stabilization in the outer shear layer and at the flame base.

Aditya *et al.* [63] extended the Chemical Explosive Mode Analysis (CEMA) to distinguish between autoignition and flame propagation. The ratio of the non-chemical to

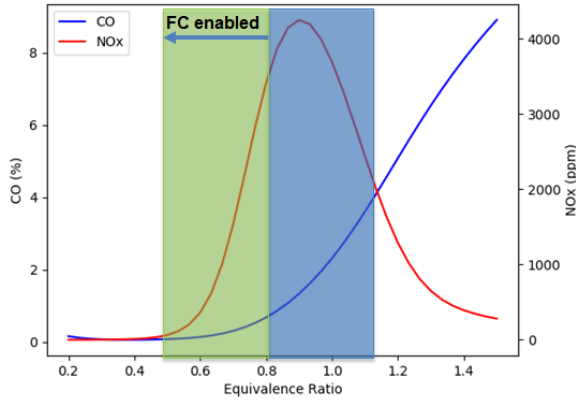


Figure 2.11: NO_x and CO evaluated in a 0D reactor comprising of a mixture of CH₄-Air and products of combustion

the chemical source term ($\alpha = \phi_s / \phi_\omega$), projected to the left eigenvector of the Chemical Explosive Mode, indicates the relative importance of diffusion to chemical kinetics. The value of this parameter is used to denote assisted ignition, i.e. flame propagation where diffusion plays a significant role, autoignition, and local flame extinction. This indicator is used to identify in the DNS of a reheat combustor that most of the fuel is consumed via the autoignition process.

2.4. LOW NO_x BY FC

The advantages of Flameless combustion are usually seen for a non-premixed combustion configuration. In conventional non-premixed combustion, the flame occurs where the equivalence ratio is unity. This is not favorable as the flame temperatures are high (> 1800 K for most gaseous fuels), because even if the overall equivalence ratio is lower, the heat release reaction occurs at these conditions, leading to high NO_x. The concept of FC allows hot product gases to mix with the air stream, thereby diluting the O₂ level, slowing down the chemistry and delaying its reaction with the fuel stream to the point where enhanced mixing of fuel and air occurs before the reaction progresses. This allows combustion at a lower equivalence ratio than stoichiometric, thus making it possible to have complete combustion with very low NO_x emissions. Joannon *et al.* [64] through 1D counterflow diffusion flame simulations show the difference in reactive structure between conventional high-temperature combustion and MILD. In conventional, the global heat release rate peak occurs at a mixture fraction very close to the stoichiometric mixture fraction (on the lean side) followed by an endothermic pyrolytic stage (on the rich side) where species such as C₂H₂ are broken down in methane combustion. In the case of MILD, where the fuel stream of CH₄ is diluted with N₂, the global heat release rate peak occurs at a mixture fraction significantly lower than the stoichiometric mixture fraction, indicating better mixing with the air stream at the point of heat release. Further, the pyrolytic region completely vanishes giving a more uniform structure that is different from the high-temperature conventional flame.

In the case of premixed combustion, as the reactants are well mixed before injection into the chamber, the equivalence ratio cannot be further reduced. This can be shown by a simple 0D PSR analysis where the reactants are mixed with their products of combustion to realize FC conditions. Figure 2.11 shows that NO_x still follows the same trend and magnitude with varying equivalence ratios. However, the hot diluted environment of FC provides a high enough temperature to stabilize a flame in an extremely locally lean condition which would have otherwise not been possible. Thus, under premixed combustion, FC allows one to go leaner than usual where flame temperatures are lower and thereby achieve very low NO_x emissions.

2.5. RESEARCH OBJECTIVES AND QUESTIONS

The objective of this research is to understand the phenomenology of combustion occurring in a jet-stabilized premixed combustor. As hot product gases recirculate and mix with the fresh reactants in this combustor, the regime is expected to have a strong semblance to Flameless/MILD Combustion. In this context, this work addresses three aspects: first, the fundamental chemistry of autoignition; second, the mixing characteristics at the interface of two turbulent streams; and finally, the performance characteristics of a jet-stabilized combustor using $\text{CH}_4\text{-H}_2$ fuel admixtures.

Premixed combustion can be leveraged for low NO_x operations by reducing the equivalence ratio. However, the lean blow-off limit prevents a further reduction. Flameless Combustion, typically governed by autoignition rather than conventional flame propagation, is well suited to stabilize a wide range of lean mixtures. Thus, to design a jet-stabilized combustor, it is essential to know the autoignition properties and emissions for premixed reactants under varying degrees of vitiation (produced by recirculated hot products) and heat loss (produced by the interaction of the recirculation zone with the wall). In most studies, these hot diluents are considered as a mixture of $\text{N}_2/\text{CO}_2/\text{H}_2\text{O}$ and termed largely inert. However, in the case of internal recirculation in a combustor, the product gases after combustion have a composition correlated to the inlet mixture and may also contain radicals existing in equilibrium. Thus, these factors need to be considered while determining the autoignition features and NO_x emissions of these mixtures in a combustor.

From several previous studies, it is evident that in multi-stream flow configurations, the mixing between these streams is the defining factor for the ensuing composition and state of the mixture. This affects the ignition delay and, thus, the lift-off height. For a jet-stabilized combustor, the influence of the surrounding flow on the interface and evolution of the jet can be systematically studied in a canonical flow configuration such as a turbulent-jet-in-turbulent-coflow. This is also commonly used to produce flameless combustion conditions in a controllable manner. A systematic study of a jet in coflow with a focus on the evolution of the interface could enhance the flame zone's prediction while designing a combustor operating on this principle.

Finally, for a FLOX type combustor, characterization of the stabilization mechanism under varying conditions of $\text{CH}_4\text{-H}_2$ fuel mixtures and the corresponding emissions could provide better proof of concept for low-emission combustors for gas turbines as well as predictive capabilities for operation of such a combustor. While there are some limited studies, there is a lack of comprehensive temperature and composition measurements

of such a combustor that also correlate with optical measurements such as chemiluminescence and PIV.

The above aspects give rise to the following research questions:

- What is the effect of vitiation and heat loss on autoignition properties and emissions of CH_4/Air mixtures in a combustor with internal recirculation?
- Can low NO_x and distributed reaction zone be achieved for premixed reactants vitiated with hot products of combustion?
- How different is the evolution of a turbulent-jet-in-turbulent-coflow compared to a turbulent free jet?
- How does the existence of a turbulent coflow affect the turbulent interface between a turbulent jet and its surroundings and the velocity statistics across it?
- How do the emissions from a jet-stabilized combustor vary when operated with varying $\text{CH}_4\text{-H}_2$ admixtures?
- Does the stabilization mechanism change when a jet-stabilized combustor is operated with varying $\text{CH}_4\text{-H}_2$ admixtures at varying equivalence ratios?

These questions are answered through simulations and experiments presented in the forthcoming chapters.



3

EXPERIMENT SETUP

*What we observe is not nature itself,
but nature exposed to our method of questioning.*

Werner Heisenberg

This chapter describes the experimental facility of the jet-stabilized combustor. The design and layout of the combustor, along with adjoining infrastructure such as the air/gas supply, heater, pilot burner, ventilation system, and some safety measures, are presented. Further, some major measurement techniques and post-processing methods used in this thesis have been described.

3.1. JET STABILIZED COMBUSTOR SETUP

3.1.1. OPERATION PRINCIPLE

The combustor is designed to produce the Flameless/MILD Combustion regime through intense internal recirculation zones. The air and fuel are injected through a burner head as shown in Fig 3.1. The two gases are injected coaxially in a partially premixed state through 12 nozzles positioned in a circular distribution on the face of the burner head. The combustion chamber is a cylindrical pipe that provides a means to confine the flames and sufficient residence time for combustion to occur before the product gases are exhausted through an exhaust duct. This design relies on the production of internal recirculation zones due to the high momentum of the fresh reactant jets. The high velocity jet leads to a lower pressure near the jet centerline, causing an entrainment of surrounding fluid. As this is a confined chamber, there is no other external source of fluid for entrainment. Thus, recirculation zones are established to supply this. This causes hot combustion products to mix with fresh reactants, leading to hot diluted mixtures. The advantage of this design is that the high-velocity jets prevent flashback, and the intense recirculation supplies heat and radicals, which prevents lean blow-off. Thus, this design is suitable for firing a wide variety of fuels.

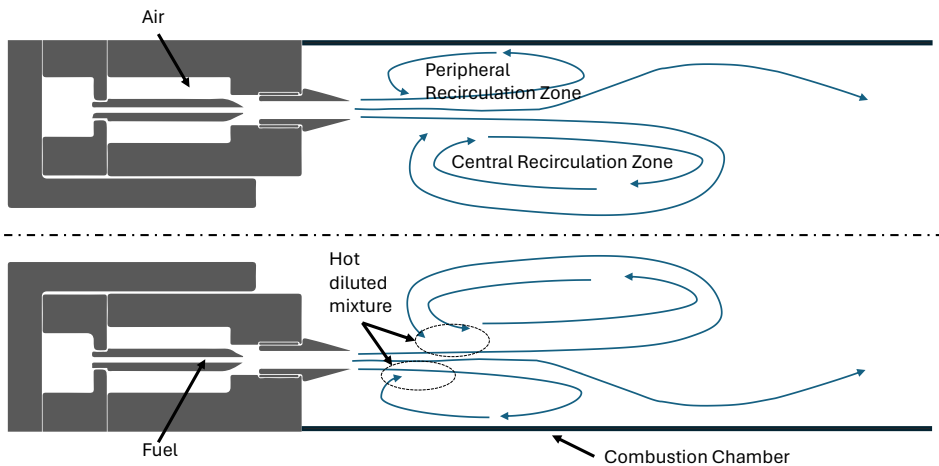


Figure 3.1: Flameless Combustion chamber schematic

3.1.2. DESIGN AND LAYOUT OF FLAMELESS COMBUSTOR

The engineering design of the combustor is shown in Fig 3.2. It consists of a burner head, a combustion chamber, and an exhaust system. The burner head was originally designed and developed at the Faculty of Mechanical Engineering by Vaz [65], with a steel combustor assembly for high-pressure testing with quartz windows which provided limited optical access to the combustion phenomenon. The burner head was modified from a FLOX burner and scaled up to operate between 60-500 kW. In the current facility

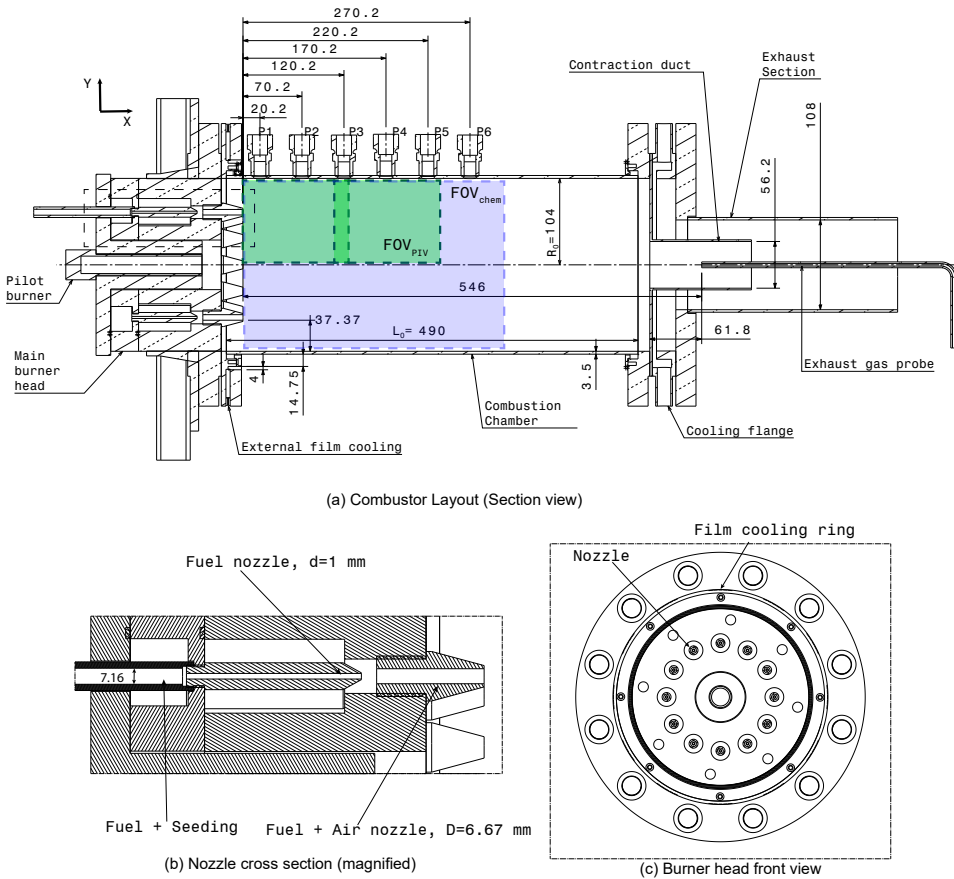


Figure 3.2: Combustor Setup where access ports are indicated as P1-6. All dimensions in mm.

at the Faculty of Aerospace Engineering, a decision was made to operate at atmospheric pressure, to reduce the engineering complexity, as well as facilitate easier optical access without worrying about structural integrity under pressure.

The burner head has two separate inputs, namely a fuel inlet and a gas inlet. The gas inlet is connected to the pipe coming from the heater and the mixer. The fuel inlet is connected to the hydrogen and methane pipes coming from the gas conditioning system. Fig 3.3 shows the partially disassembled burner head, indicating the air inlet, fuel inlet, fuel nozzle, and air plenum. The jets of the fuel inlet fit right into the concentric set of holes in the air plenum part of the burner head. These holes lead to nozzles on the face of the burner head, as can be seen in Fig 3.4. The burner head was modified to have a mating section such that a cylindrical combustion chamber could be fit and sealed without the use of a bolted flange, as seen in Fig 3.6. Compressing the rope gasket

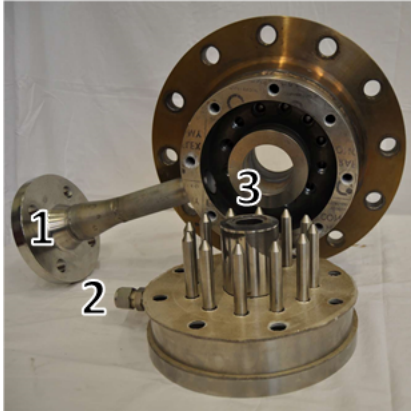


Figure 3.3: Burner head layout. 1: Air supply, 2: Fuel supply, 3: central hole for pilot burner.



Figure 3.4: Front of Burner head

in the axial direction leads to an expansion in the radial direction. This provides a gas-tight seal around the cylindrical quartz pipe without damaging it. Further, an external cooling stream was added, also seen in Fig 3.6, to cool the chamber through a wall offset jet configuration[66]. The air is supplied through 12 slots that combine into an annulus which is concentric with the combustion chamber, as shown in the figure. The jet leads to the formation of a recirculation zone near the wall and forms a boundary layer downstream of the impingement point. This leads to a convective cooling mechanism. Also, a modification was done to seed the 12 o'clock fuel nozzles for PIV measurements by introducing a pipe through the backplate and supplying fuel directly, while blocking access to the fuel plenum, as shown in Fig 3.2.

There were two combustion chambers, one was a quartz cylinder that provided complete optical access and the other was a steel chamber of the same dimensions, but it had six steel ports as shown in Fig 3.2, which allowed for the insertion of probes into the chamber. A suction probe to measure the gas composition and an S-type thermocouple were inserted through these Ports, while mounted on a Zaber traverse system, as shown in Fig 3.5

A cooling section is installed at the end of the combustion chamber, as shown in Fig 3.7. A flange with an internal groove is placed at the end of the quartz combustor. Cooling air is fed into the system through 12 holes on the circumference of the flange, which direct air through an annular channel in the flange, creating a sheet of air perpendicular to the direction of flow of exhaust gases. Thus the exhaust gases are cooled before they reach the exhaust duct. The exhaust system contained a cooling flange through which air was injected. This is done around the exhaust nozzle, such that the cold air is not injected directly into the combustor. This air mixes with the hot exhaust gases downstream to thermally dilute them such that the temperature in the exhaust duct does not exceed a set value. This helps to maintain the integrity of the system over time. The exhaust nozzle provides a contraction after the chamber to accelerate the flow as well as provide a pressure drop to prevent flow reversal. There is a gas probe in the contraction, the ex-

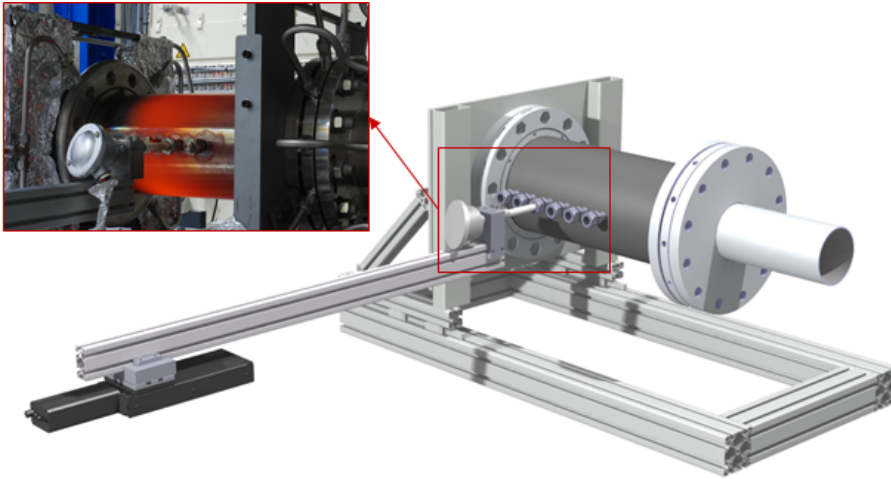


Figure 3.5: Probe traversal arrangement

act location is indicated in Fig 3.2, used to extract exhaust gas samples for composition analysis. There are four N-type thermocouples located 235 mm from the surface of the flange of the external exhaust pipe, and they serve as feedback for the cooling control system. The thermocouples are inserted to a depth of $1/3^{\text{rd}}$ the diameter from the wall. The exhaust pipe is connected to the exhaust duct fixed to the building infrastructure, the outlet of which is to the outside environment.

A pilot burner is used to ignite the system and aid in sustaining a flame when the main flow cannot sustain one by itself, such as in cases of lean blow-off. It is manufactured by Kromschroder and is of the ZMI 16B200R type (Fig 3.8). It has a 1-2kW capacity and runs on methane and air. There is a spark plug for ignition, and the electrode doubles up as an ionization current sensor, which gives a μA level DC current in the presence of flame radicals. This is used to determine a successful ignition by the controller (IFD 258-5/1W automatic burner controller). The pilot burner is turned off once a stable flame is established in the main burner. However, a small amount of airflow needs to be maintained to prevent overheating of sections closer to the flame zone.

The air is regulated by a mass flow controller, the setpoint of which may be electronically specified. The fuel line to the pilot burner has a manual regulator(J125) to regulate the supply. This must be pre-set to a particular pressure value based on the power requirement. This can be done by referring to the flow curves in Fig 3.9. The pilot air line also has a pressure reducer and mass flow controller. The reducer can be set to the required range, and the software controls the mass flow controller to deliver a specified flow rate. The mixing of air and fuel takes place within the pilot burner device.

3.1.3. LABORATORY INFRASTRUCTURE

The lab facilities are designed for 200kW input thermal capacity using CH_4 as fuel while being able to operate at the leanest condition of equivalence ratio=0.3. The mass flow

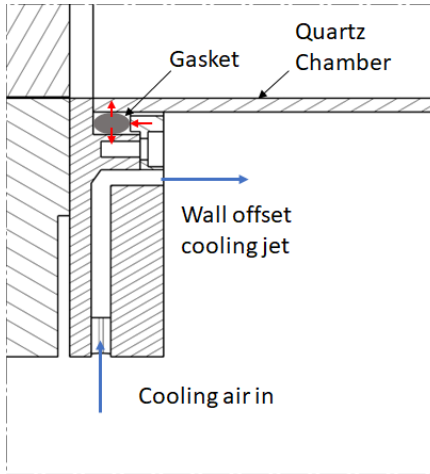


Figure 3.6: Wall offset cooling jet at the burner head.

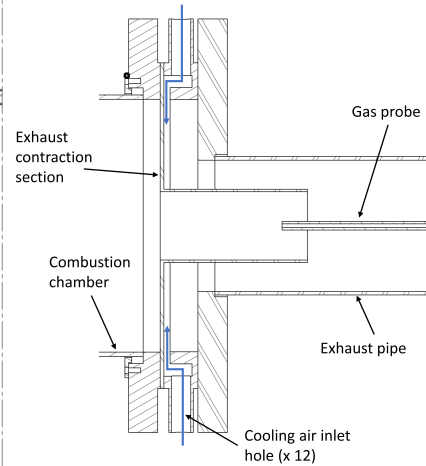


Figure 3.7: Cooling Section at the exhaust of the Combustor.

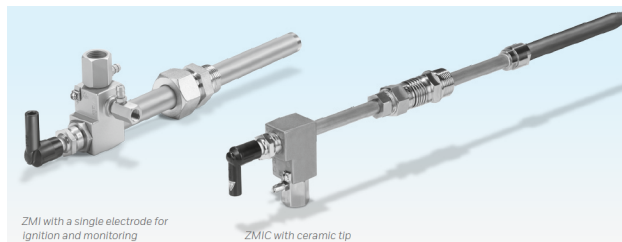


Figure 3.8: Pilot burner

controllers, solenoids, and pressure reducers of all gases except for air are located in a ventilated gas rack, mounted along a wall in the lab. The source of these gases is gas bottles, located in a gas storage facility outside the lab. The pressure of each gas is conditioned to 12 bar from the bottle pressure, through a pressure reducer located in the gas storage and is then directed through welded pipes into the gas rack. The gas rack contains a fuel manifold, where multiple fuel gases such as CH_4/H_2 can be mixed. This manifold then supplies one pipeline towards the Combustor. Some of the main parameters used to size the system were:

- Maximum main combustion air required: $0.3 \text{ kg/s} = 15000 \text{ lpm}$
- Maximum CH_4 required: $14.5 \text{ kg/h} = 338.5 \text{ lpm}$
- Cooling flow required: $0.3 \text{ kg/s} = 15000 \text{ lpm}$
- Electrical heating of main air by 48kW heater. The heater is expected to preheat the air up to 700°C when the air flow is limited to 0.1 kg/s . In practice, this was seen to be limited by the amount of insulation that could be fit around the pipes to reduce heat losses, and a maximum of 400°C was achievable at the burner head.

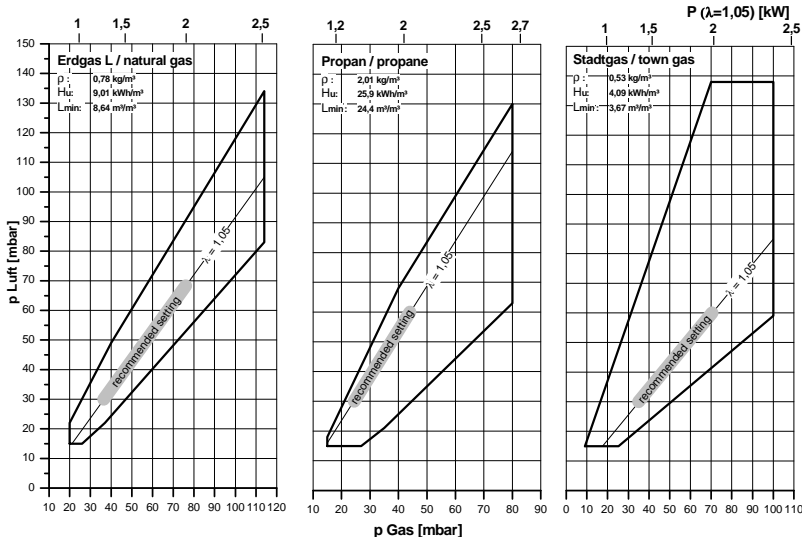


Figure 3.9: Pilot burner flow curves

A detailed layout of the infrastructure is given in a P&ID diagram in Appendix D. The labels in this diagram for certain parts are referred to in the upcoming sections.

AIR SYSTEM

Compressed air is sourced from the main tank of the High-Speed Lab, which is pressurized between 20 and 42 bars and has a volume of 300 m³. There is a drying unit in the compressor system that reduces the moisture such that a dewpoint of -40 °C is achieved at 45 bar. A dedicated airline was constructed to direct air toward the Combustion lab as the existing piping infrastructure is directed toward other high-speed wind tunnel facilities. The P&ID of this section is shown in Fig 3.10. This airline contains a strainer to filter any particulate matter in the flow. Next, the air goes through a pressure conditioning system which reduces the pressure of air coming from the storage vessel to acceptable operating pressures. The system consists of 2 pressure reducers (PCV-001/2) in parallel with different volume flow capacity ranges. This is required as the larger device becomes unstable while operating under low flow conditions. The pipe size on the low-pressure side of both pressure reducers is designed to be DN40, i.e. larger than the size of the devices, DN25 and DN15 because else the flow velocities reach unacceptably high values, which may lead to vibration in the moving parts of the device as well as high levels of noise in the system. There is an adjustable pressure relief valve near the end of this section which is set to open if the pressure inside the system exceeds 12 bar. There is also a vent line with a ball valve that can be used to manually vent the air pipe during maintenance activities.

There is a normally closed solenoid valve(V-006) downstream, which may be con-

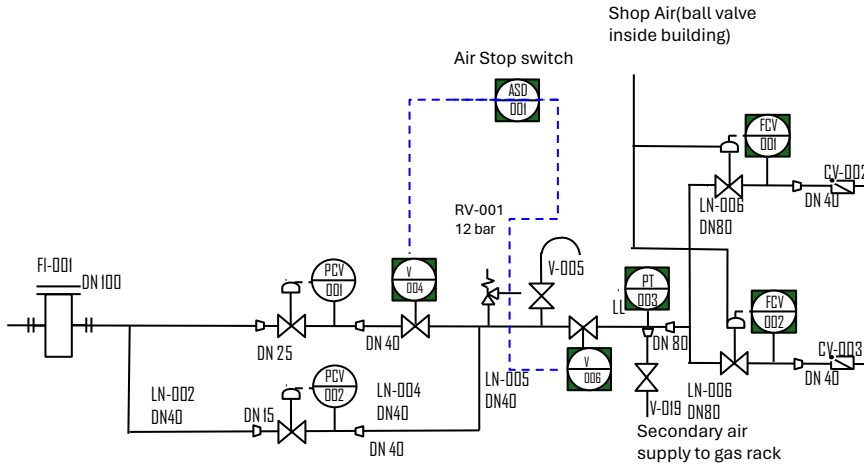


Figure 3.10: Air supply system

sidered the primary valve to be opened by the control system to allow airflow through the system. There is a pressure sensor (PT-003) and manual gauge just downstream of the solenoid valve, which provides the system pressure. There is a secondary air supply tapped from this point which goes through ball valve V-019 and serves as the input supply to smaller air mass flow controllers located in the gas rack in the lab. Further downstream, the air supply is split into two equal branches with a mass flow controller on each (FCV-001/2).

The mass flow control unit comprises a mass flow meter (F-107CI-RGD-13-V Digital Mass Flow Meter), which works on the principle of thermal mass flow measurement, and a valve (2" Badger RCV Control Valve type OR900 (ORION 9000)), the opening of which is based on the measurement by the mass flow meter. The valves are pneumatically actuated by shop air from the lab. The mass flow controllers are each able to handle air flow in the range of 300-15000 lpm with 1% FS accuracy.

Each branch ends with a DN40 check valve, which prevents hot air and combustion products from flowing back into the devices upstream.

FUEL MIXTURE

The fuel supply in this system is such that CH_4 and H_2 can be premixed upstream and supplied as a homogeneous mixture to the combustor. Both gases have an independent line with their massflow controller, and the mixing is done in a manifold, after which there is a pipe about 500 inner diameters long that connects to the fuel inlet port on the burner head. Increasing the hydrogen content increases the laminar burning velocity such that there is a greater rise beyond 60% volume fraction in the fuel mixture as shown in Fig 3.11a. For $\phi=1.0$, the S_L of 100% H_2 is about 7 times of a pure CH_4 fuel mixture. The adiabatic flame temperature, shown in Fig 3.11b, on the other hand, rises by only 100-200 K with variation in $\text{H}_2\%$ depending on ϕ .

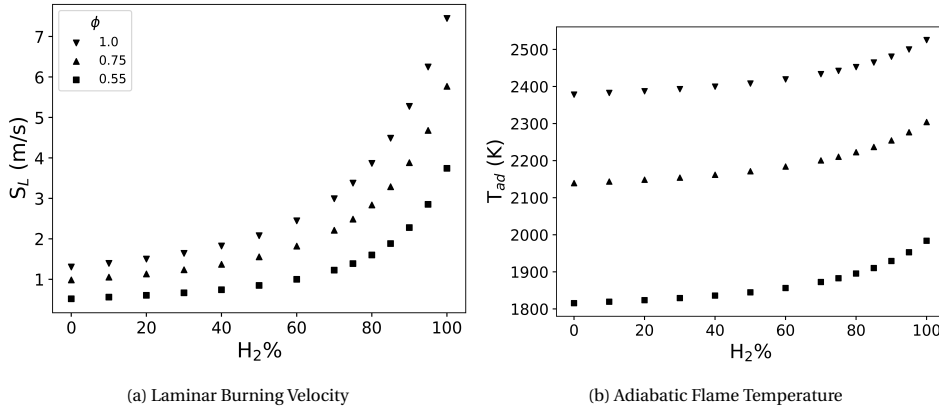


Figure 3.11: Properties of CH₄-H₂ admixtures, calculated from 1D laminar flamelet simulation using the FreeFlame model in Cantera.

ELECTRIC HEATER

A 48kW 3-phase AC electric heater is used to pre-heat the air to the required temperature before it enters the combustion chamber. There is a separate heater control cabinet which has a high-voltage 3-phase supply. The heater has 3 thermocouples at the outlet. Two of them are connected directly to the heater control cabinet and are used as feedback by the controller. The third thermocouple is connected to the main system controller and is used to log the temperature and provide feedback to the operator to monitor the process. The set point of the heater is specified by the operator in the Lab-View console and is communicated by a 0-5 V signal via the main system controller to the control cabinet. The power supply is interfaced with a set of relays that can be disengaged when the emergency stop button is pressed.

VENTILATION

The lab is ventilated by a fume hood, which, as part of the safety protocol, needs to be running before any requests for experiments can be made electronically to the Building Management System (BMS). This ensures that there is no build-up of explosive gases in the lab. This makes the zone ATEX compliant before the startup of the combustion chamber such that the high level of ventilation renders it a negligible ATEX-II zone. The system also extends to the gas rack to prevent a build-up of explosive gases due to leakage from the mass flow controller by constantly circulating air through it. The exhaust of the ventilation system is to the outside of the building. The system is designed such that the volume flow rate through the gas rack = 1650 m³/h and through the ventilation hood = 4600 m³/h. There is a contact switch connected to the beam of the fume hood, such that it registers a high signal when the fume hood is swung in place. This signal is necessary to start an experiment. The hood can be released by pressing a green button located at the front of the frame. If the necessary conditions are not met, a request for an experiment cannot be made to the control system, and the solenoids of the gases in the gas rack will not open.

NITROGEN PURGE LINE

All gas lines (except for air) are connected to a Nitrogen purge line. This is to be able to vent out the pipes around the lab of any combustible gases. The venting can take place in either one of the two directions, through the main combustor or in the opposite direction towards the gas bottles outside the lab. In the latter case, the gases vent out to the atmosphere through venting lines just outside the gas bottle storage shed. This process is controlled by 2 solenoids on each line, one located in the gas rack and the other located at the gas storage.

3

EXHAUST DUCT

The exhaust duct directs the gases from the combustion chamber and the cooling system outside the lab through a fully open channel. It is designed for a maximum temperature of 1400K. It is insulated to prevent the outer surface from getting hot and to prevent the cooling of gases due to heat loss which could cause water vapor condensation. The outlet is shielded on the outside to prevent rain from coming in. The duct is supported by a steel structure located near the base but is free to slide on it to allow its expansion upon heating.

3.2. MEASUREMENT TECHNIQUES

3.2.1. PARTICLE IMAGE VELOCIMETRY

Particle Image Velocimetry (PIV) is a commonly used technique to measure flow fields in laboratory-scale setups. The method includes introducing particles in the flow and illuminating them with a light source such as a laser. The particle size relative to the light wavelength used is such that they typically scatter by the Mie-scattering principle, and in most setups, the side-scattered light is used for imaging. The laser light is formed into a sheet using a series of optics located in the plane of interest. Thus, to the minimum, it provides a 2D field of view. The schematic of a PIV setup is shown in Fig 3.12. There are more advanced versions, such as Tomo PIV, where a 3D field of view is reconstructed by illuminating a volume instead of a plane and using three or more cameras for imaging. The displacement of the particles is tracked by taking two successive images with a predefined time interval and this results in the evaluation of the velocity. The particle displacement is evaluated using the concept of interrogation windows. An interrogation window size, much smaller than the image size, is chosen, and cross-correlations are done between the two successive images to determine the displacement. For example, a window size of 24x24 pixels is chosen. A region in the first image is chosen where this window is centered. A spatial cross-correlation of this window is done with the second image by translating this window in several directions. The displacement that gives the highest correlation corresponds to the displacement. It is assumed that all the particles in the window travel along the same displacement, hence PIV has an inherent averaging over the window. In practice, the cross-correlation is done by taking a Fourier transform and then multiplying as it is computationally faster. For a more detailed explanation of the PIV process, the reader is encouraged to refer to Raffel *et al.* [67].

The number density of particles is crucial for a good PIV acquisition. If there are too few particles, the average motion of the window does not reliably represent the average particle displacement, and it is instead more suitable for another method called Particle

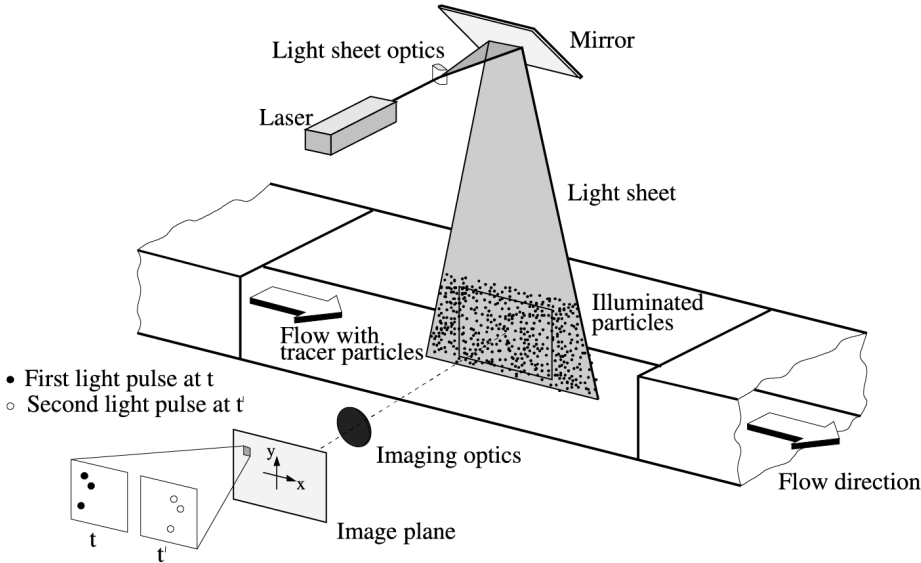


Figure 3.12: Particle image velocimetry arrangement in a wind tunnel[67].

Tracking Velocimetry (PTV), where the motion of individual particles is tracked. On the other hand, if there are too many particles, there is a reduction of contrast in correlation that may not represent the real displacement. A rule of thumb is to have 5-10 particles per window.

PIV inherently suffers from a limited dynamic range, given by the maximum to minimum perceived displacement. This proves to be a challenge when imaging shear flows such as a turbulent free jet, where the experimenter needs to make an informed decision and choose a Δt value depending on the smallest displacement acceptable for their application.

In the case of combustion flows there are several added complexities. First, the particles should survive the high temperatures. For this, TiO_2 particles are used. Next, the particles should reliably follow the flow field. This typically requires a reliable supply of particles of small sizes, which in this case is $0.5 \mu\text{m}$. The traceability is characterized by the Stokes number, which is the ratio of the characteristic particle response time to the flow characteristic time. This is expressed as,

$$St = \frac{d_p^2 \frac{\rho_p}{18\mu}}{\frac{L_f}{\Delta U}}, \quad (3.1)$$

where d_p is the particle diameter, ρ_p is the particle density, μ is the dynamic viscosity of the fluid, L_f is the characteristic length scale in the flow field, and U is the velocity. The higher temperature of a combustion environment leads to a higher dynamic viscosity of the gas within the working conditions of typical gas turbine combustors and furnaces. This works favorably for reliable flow tracing by reducing the Stokes number. Finally, the

particles in a confined chamber with optical access tend to stick/ deposit on the walls, thereby fouling them and degrading optical access over time. This drastically reduces the testing time and can also permanently damage the transparent surface. The latter can be prolonged by applying wall cooling to keep the wall temperature low enough such that the particles do not embed deep into the surface and remain on the outer surface. However, after several runs, the only method of cleaning the walls was to polish them using a polishing machine and a ceramic paste with fine particles that would essentially strip off the top layer of the glass to remove the embedded particles.

The PIV technique was tested on a confined laminar CH_4 -Air bunsen flame to identify the challenges that may be faced in combustion environments and the optical effects of cylindrical confinement. It was identified that the laser sheet needs to be carefully aligned such that it has a zero incidence angle at the cylinder, else there may be a secondary sheet formed due to internal reflection. The remaining reflections from the walls of the quartz cylinder could be mitigated by using a polarization filter, as shown in Fig 3.13a and 3.13b. Further, it was imperative to maintain a high enough laser power to overcome the luminosity of the flame, as well as that of the particles. The particles heat up across the flame front and radiate in a wide spectrum. Thus, despite using a band-pass filter around the 532 nm region, this light can pass through. As the second frame can have a longer exposure time due to the electronic build of the camera and data transfer, there can be significant streaklines formed, as shown in Fig 3.13c. The only way to avoid them was to have a sufficiently high laser power such that a much higher signal is obtained from Mie-scattering.

In the jet-stabilized combustor, the most efficient seeding technique was to seed a single fuel nozzle. This allowed for seeding the stream that was being visualized while allowing for an optimized acquisition time. This was limited by the particles embedded in the walls of the chamber, causing fouling and a loss of optical access.

The flow stream was seeded by bypassing a section of the flow into a seeder and recombining it with the flow. There are several types of particle seeders available commercially. The two most common ones are the fluidized bed and cyclonic seeder. The current seeder was developed in-house, originally for measurements in a hypersonic wind tunnel facility, and modified for use on the combustor. It uses a high-velocity jet in a confined chamber such that it would entrain and pick up particles. A valve located at the exit of the seeder generates a high shear flow such that only the smallest particles can be carried forward, and the rest would drop-down or deposit in the valve/piping. For the non-reacting flow experiments, a Laskin nozzle-type seeder was used where DEHS oil droplets would be formed.

3.2.2. CHEMILUMINESCENCE

Chemiluminescence is the emission of electromagnetic radiation as a result of a chemical reaction. In the context of combustion, this occurs when flame radicals are excited by absorbing energy from the heat released during combustion. When they de-excite, a light emission is released. Depending on the species being observed, this can indicate the reaction zone front. However, as these reactions occur in a volume and the light collected is from spontaneous emission, the images obtained are Line-of-sight integrated [68]. In hydrocarbon combustion, typically, the most luminescent radicals are OH, CH,

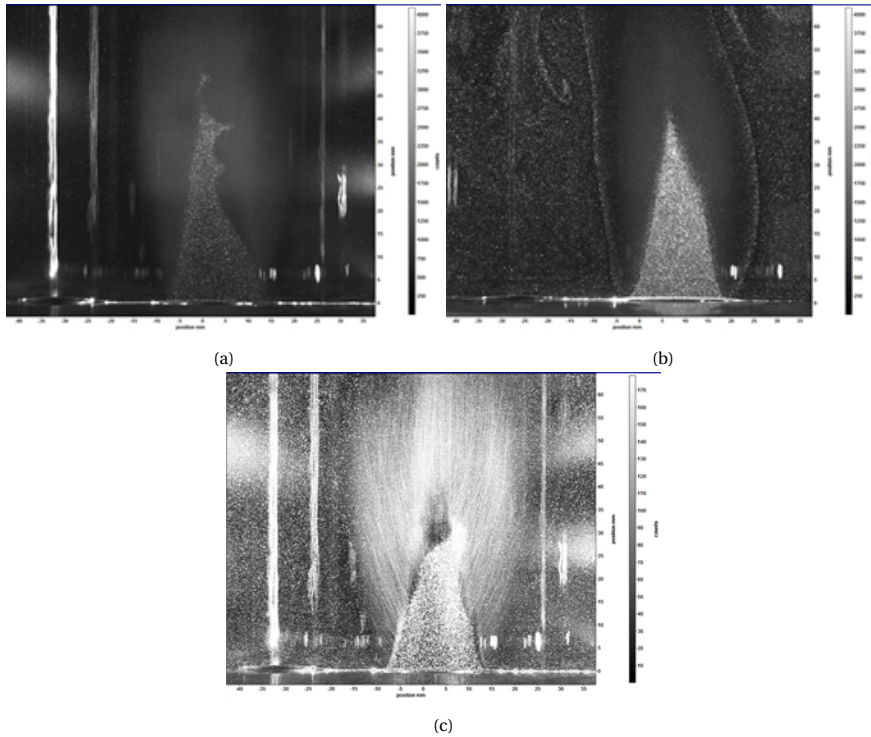


Figure 3.13: Examples of Mie-scattering images for a laminar CH_4/Air bunsen flame (a) without polarization filter, (b) with polarization filter and (c) streaklines formed by hot particles.

C_2 , and CO_2 , where the excited forms are represented with a '*' suffix. C_2^* is usually more dominant under rich combustion conditions, thus for lean-premixed combustion, CH^* (430 nm) and OH^* (306 nm) are tracked.

In most cases, an intensifier is used to boost the signal, which reduces as a function of $1/r^2$ with distance from the source. The intensifier is usually based on generating a stream of electrons from a photocathode, which are then accelerated through a micro-channel plate by applying a voltage such that the multiplication of electrons takes place in the channels. These electrons impinge on a phosphor screen that releases photons of a fixed wavelength ($\approx 532\text{nm}$) that are captured on an image sensor such as a CCD or sCMOS camera. The device provides signal multiplication as well as wavelength conversion such that if the luminescence signal is in the UV range, a sensor in the visible spectrum may still be used as the final signal is from the phosphor screen.

The above intensifier-camera setup was not available in the lab at the time. Hence, a simpler approach using a DSLR camera was used. The main disadvantage was that longer exposure time was required, but the advantage was higher resolution. A bandpass filter was not used. However, the DSLR camera has an RGB sensor of which the blue sensor spectrum intersects with the CH^* emission but has some broadening around the peak. The red spectrum was seen to be a good indication of background radiation from

H₂O. Further details about this technique and some limitations are discussed in Chapter 6.

3.2.3. IMAGE PROCESSING ALGORITHMS

Images obtained from various optical techniques were processed to extract features to study the underlying phenomenon. This was primarily done using the OpenCV library in a Python environment. This section describes the Otsu algorithm and the DBSCAN algorithm, which were used in this work.

3

OTSU ALGORITHM

Several image processing applications require distinguishing between an object and its surroundings. Ideally, for a gray image, this can be done from its histogram, where two distinct peaks are seen, and the bottom of the valley between them can be chosen as the threshold value. However, in most real images, this is not the case as there may be noise, the valley may be flat and broad, or even sometimes, the peaks may be of very different heights, often making it difficult to detect a valley. The Otsu method provides a solution by automatically selecting an optimal threshold through the means of evaluation of the "goodness" of the threshold. The method was first proposed by Otsu *et al.* [69], and the methodology from this article is described further.

The data is represented as a 2D image in grayscale, where there are L gray levels [1,2,3...L]. There are n_i number of pixels at level i and the total number of pixels is denoted by $N = n_1 + n_2 + \dots + n_L$. Thus, the probability of occurrence of the i^{th} level is

$$p_i = \frac{n_i}{N}, \quad p_i \geq 0, \quad \sum_{i=1}^L p_i = 1 \quad (3.2)$$

The pixels are segregated into two classes, C_0 and C_1 (background and object or vice versa), using a threshold level k , such that C_0 is a class consisting of pixels with levels [1,...,k] and C_1 consists of pixels with levels [k+1,...L]. Then, the probability of occurrence of each class is

$$\omega_0 = Pr(C_0) = \sum_{i=1}^k p_i = \omega(k) \quad (3.3)$$

$$\omega_1 = Pr(C_1) = \sum_{i=k+1}^L p_i = 1 - \omega(k) \quad (3.4)$$

and the class mean levels are

$$\mu_0 = \sum_{i=1}^k i Pr(i|C_0) = \sum_{i=1}^k i \frac{p_i}{\omega_0} = \frac{\mu(k)}{\omega(k)} \quad (3.5)$$

$$\mu_1 = \sum_{i=k+1}^L i Pr(i|C_1) = \sum_{i=k+1}^L i \frac{p_i}{\omega_1} = \frac{\mu_T - \mu(k)}{1 - \omega(k)} \quad (3.6)$$

where,

$$\omega(k) = \sum_{i=1}^k p_i \quad \text{and} \quad \mu(k) = \sum_{i=1}^k i p_i \quad (3.7)$$

are the zeroth and the first-order cumulative moments of the histogram up to the k^{th} level, respectively. $\mu_T = \mu(L)$ is the total mean level of the entire image. The class variances are given by

$$\sigma_0^2 = \sum_{i=1}^k (i - \mu_0)^2 Pr(i|C_0) = \sum_{i=1}^k (i - \mu_0)^2 \frac{p_i}{\omega_0} \quad (3.8)$$

$$\sigma_1^2 = \sum_{i=k+1}^L (i - \mu_1)^2 Pr(i|C_1) = \sum_{i=k+1}^L (i - \mu_1)^2 \frac{p_i}{\omega_1} \quad (3.9)$$

The "goodness" of the threshold, k , is tested by the following measures of class separability:

$$\lambda = \frac{\sigma_B^2}{\sigma_W^2}, \quad \kappa = \frac{\sigma_T^2}{\sigma_W^2}, \quad \eta = \frac{\sigma_B^2}{\sigma_T^2} \quad (3.10)$$

where,

$$\sigma_W^2 = \omega_0 \sigma_0^2 + \omega_1 \sigma_1^2 \quad (3.11)$$

$$\sigma_B^2 = \omega_0 (\mu_0 - \mu_T)^2 + \omega_1 (\mu_1 - \mu_T)^2 = \omega_0 \omega_1 (\mu_1 - \mu_0)^2 \quad (3.12)$$

$$\sigma_T^2 = \sum_{i=1}^L (i - \mu_T)^2 p_i \quad (3.13)$$

are the within-class variance, between-class variance, and the total variance of levels, respectively. Then, the problem is reduced to searching for a threshold, k , such that one of the objective functions in Eqn 3.10 is maximized. This stems from the assertion that well-thresholded classes should be separated by gray levels.

However, the objective functions λ, κ and η are equivalent; $\kappa = \lambda + 1$ and $\eta = \lambda / (\lambda + 1)$ in terms of λ because of the following relations that always holds true:

$$\sigma_W^2 + \sigma_B^2 = \sigma_T^2 \quad (3.14)$$

It must be noted that while σ_W^2 and σ_B^2 are functions of k , σ_T^2 is independent of k . The Otsu algorithm implementation in OpenCV solves the optimization by minimizing σ_W^2 , while traversing over the range of k .

DBSCAN ALGORITHM

Clustering similar regions on a 2D image in an automated manner requires the algorithm to work with inputs that do not rely on domain knowledge because the appropriate values may not be known in advance in large databases, furthermore, it should be able to discover clusters of arbitrary shapes. Density-Based Spatial Clustering of Applications with Noise (DBSCAN) is one such algorithm that satisfies this condition. As humans, we identify clusters by eye by recognizing regions with a density of points that is higher than outside of the cluster. Further, the density in noise regions is lower than within the cluster.

The DBSCAN algorithm is formalized by a series of definitions that lead up to identifying a cluster and noise[70]:

- Eps-neighborhood of a point p ($N_{Eps}(p)$): $N_{Eps}(p) = \{q \in D | dist(p, q) \leq Eps\}$
- Directly density-reachable: A point p is directly density-reachable from a point q if $p \in N_{Eps}(q)$ and $|N_{Eps}(q)| \geq MinPts$.
- Density-reachable: A point p is density-reachable from a point q if there is a set of points p_1, \dots, p_n , $p_1 = q$ and $p_n = p$ such that p_{i+1} is directly density reachable from p_i .
- Density-connected: A point p is density-connected to a point q if there is a point o such that both p and q are density reachable from o .
- Cluster: A cluster C is a non-empty set of points satisfying the conditions:
 - $\forall p, q$: if $p \in C$ and q is density reachable from p , then $q \in C$ (Maximality)
 - $\forall p, q \in C$: p is density connected to q (Connectivity)
- Noise: Let $C_1 \dots C_k$ be the cluster of the database D . Then, the noise is defined as the set of points in D not belonging to any cluster C_i

Points lying inside a cluster are termed core points, and those on the border are called border points. An Eps-neighborhood of a core point will contain more points than that of a border point. Thus, the algorithm cannot simply specify the MinPts for a general Eps-neighborhood and whether or not to include a point in a cluster. However, every border point would lie within the Eps-neighbourhood of at least one core point. Two border points of the same cluster may not be density-reachable from each other as they are not core points, but for them to be in a common cluster, they should satisfy the connectivity criteria, i.e., there should exist one core point from which both border points are density-reachable.

Thus, the DBSCAN algorithm allows for the identification of randomly shaped clusters, even in a noisy domain with minimal inputs from the user. This facilitates highly automated identification of coherent structures in large image datasets such as those obtained from PIV and chemiluminescence measurements.

3.2.4. GAS ANALYSER

An ABB gas analyzer unit is used for gas composition measurement and a schematic is shown in Fig 3.14. The unit has a suction pump that generates a suction flow to extract gas samples from the region of interest and pass them through three types of analyzers: the Uras (CO, CO₂, CH₄), Limas (NO, NO₂), and Magnos (O₂). The Uras and Limas work on Non-dispersive IR/UV photometry principle. The basic principle is that light is shown at one end of a sample cell, also called a cuvette. The sample gas is passed through the cuvette and the light is absorbed based on the Beer-Lambert law,

$$I_1 = I_0 e^{-\epsilon(\lambda)pL} \quad (3.15)$$

, where p is the density of the absorbing gas, L is the optical path length and $\epsilon(\lambda)$ is the extinction coefficient at wavelength λ . The remaining light exits the other end of the cuvette and reaches an opto-pneumatic detector. To improve sensitivity, the detector is

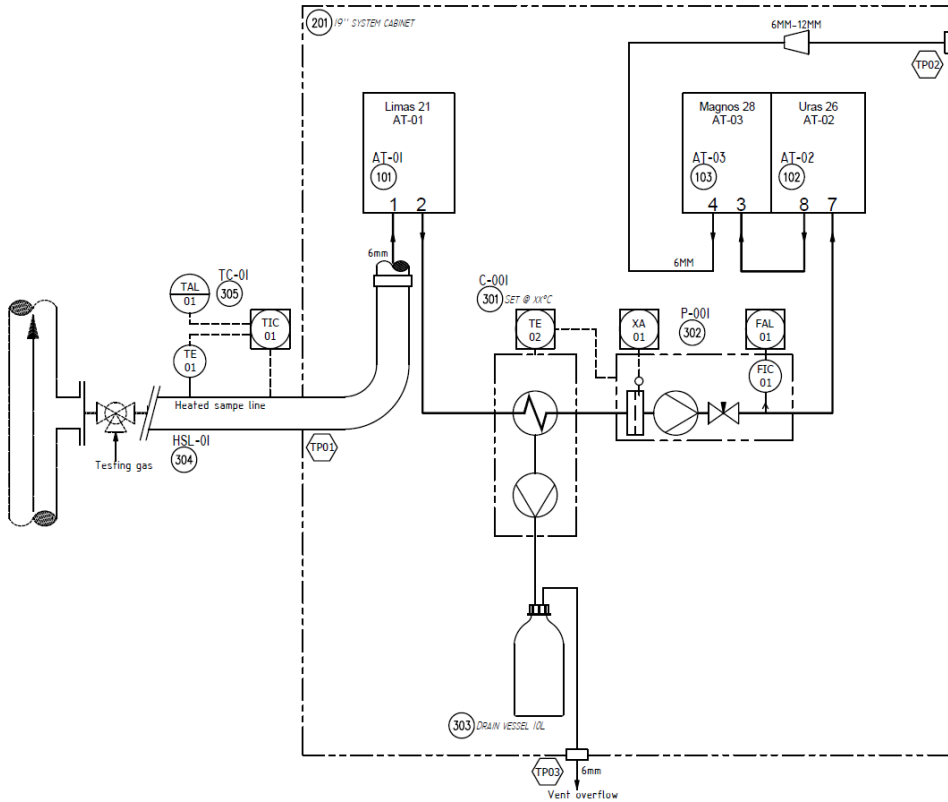


Figure 3.14: Schematic diagram of the gas analyzer unit

filled with the gas to be measured, for example, CO_2 . The sample gas absorbs the incoming radiation and heats up, thereby leading to an increase in pressure. This pressure is measured and is used as an indication of the concentration of the species[71].

The Limas11 HW uses the UV-RAS (Ultra Violet Resonant Absorption Spectroscopy) method[72]. An electrodeless discharge lamp (EDL) generates the UV light in the 200-500 nm range. The EDL contains a gas mixture of 10% O_2 and 90% N_2 at around 10 mbar. The radiation is generated by a gas discharge which is maintained by a high-frequency oscillator circuit. N_2 and O_2 dissociate and form excited NO . When the electrons go from excited to ground state, light is emitted of $\lambda \approx 226.5$ nm from $\text{NO}(A^2\Sigma^+ - X^2\Pi) - \gamma(0,0)$ transition. The emission spectrum contains numerous lines divided into 'cold' and 'hot' lines. The 'cold' lines are absorbed by NO molecules according to the Beer-Lambert law, and the 'hot' lines pass through unchanged. Thus, the 'hot' lines are used as a reference measurement. The gas filter correlation method is used for NO . This is done by using a selectivity cell filled with 100% NO , which is thick enough to absorb all of the 'cold' lines. This cell and an opening appear alternately in the beam path to produce a reference phase and a measurement phase. During the reference phase, only the 'hot' lines reach

the sample cell. NO_2 is measured by the wavelength comparison method. This is done by using two narrow-band interference filters such that one has a central wavelength whose absorption is maximal and the other's is minimal to produce a measurement and reference phase. The wavelengths are chosen to minimize cross-sensitivity with other species[73]. NO_x measurement is done hot-wet, i.e., the water is not allowed to condense by maintaining the heated suction line at 180°C and the analyzer is at 80°C .

The Magnos28 measures oxygen based on its paramagnetic properties. This device incorporates ABB's patent-pending microwing technology which is an advancement over the traditional glass dumbbell mechanism[74]. A high aspect ratio silicon etched wafer is suspended using a platinum wire in a magnetic field. When gas containing oxygen passes across it, the paramagnetic nature tends to make the O_2 accumulate in the magnetic field, which is along the plane of the wafer. This leads to a buoyancy effect[75] that deflects the "microwing". This deflection is detected and converted to an oxygen concentration.

3.2.5. THERMOCOUPLES

A thermocouple works on the thermoelectric effect, also known as the Seebeck effect. This is the phenomenon where two wires of dissimilar metals, when connected at both ends, produce an electromotive force (e.m.f) proportional to the temperature difference between the two junctions. The thermocouples used in this work were all sheathed, insulated type, where the sheath was made of Inconel except for the flame temperature thermocouple which had a sheath of 10% Platinum to endure higher temperatures in an oxidative environment. The sheath protects the junction but can also introduce a delay in the time response. K-type thermocouples are used to measure the temperature of all gas streams up to the combustor inlet. K-type thermocouples used to monitor and control the electric heater are bare at the tip, i.e. the sheath and insulation were stripped for faster time response. The thermocouples in the exhaust duct are N-type. The thermocouple used for flame temperature measurement is of S-type as was also the one used to measure the external wall cooling flow.

As the temperature difference of the two junctions influences the measurement, it is important to know the temperature of the cold junction. One of the methods is to insert the cold junction in an ice bath to maintain it at 0°C . However, this is not very convenient in a practical combustion lab. Thus, we use the National Instruments thermocouple module NI-9213, which has internal cold junction compensation that accounts for the deviation of the cold junction from the reference temperature and evaluates the measured e.m.f as an absolute hot junction temperature by correcting for this.

4

AUTOIGNITION OF METHANE-AIR MIXTURES VITIATED BY EXHAUST GASES

It is a profound and necessary truth that the deep things in science are not found because they are useful; they are found because it was possible to find them.

J. Robert Oppenheimer

Low NO_x combustion may be achieved by the Flameless/MILD regime, wherein reactants react at high initial temperatures under diluted oxygen environments and is characterized by autoignition. This may be achieved by combustors with internal recirculation, where hot combustion products are recirculated back to the fresh reactants. In this work, we look at the autoignition properties of such lean methane-air mixtures through simulations in a 0-D reactor and study the effects of vitiation fraction (ζ) and heat loss (χ). Further, NO_x and CO emissions under these conditions are also compared. It is found that radicals in hot products can reduce the autoignition time significantly, even under significant heat loss conditions. Further, simultaneous reduction of NO_x and CO can be achieved by moderate vitiation and a certain level of heat loss. Finally, the occurrence of multiple ignition peaks was observed under certain combinations of vitiation and heat loss. The regime of occurrence is mapped, and the mechanism behind this is explained. This observation has implications for the interpretation of the reaction zone tracked by this criteria under such hot-product-vitiated conditions.

4.1. INTRODUCTION

Low NO_x characteristics are an essential feature required for future combustion devices. This can be achieved by premixed combustion at lean equivalence ratio conditions where the adiabatic temperature is less than 1800 K, thereby reducing the thermal NO_x production [76]. However, in practical combustion systems, lean premixed combustion can be associated with instabilities leading to lean blow-off as well as incomplete combustion leading to high CO. Flameless/ Mild combustion is a regime that occurs at high reactant inlet temperature (above autoignition temperature) in a low oxygen environment, facilitating low NO_x while having a stable and complete combustion reaction zone [77, 24, 27]. Flameless combustion in a premixed configuration can be achieved in jet-stabilized combustors such that the fuel/air mixture is injected through high-velocity jets in a chamber, establishing strong internal recirculation zones [78, 37, 18]. This feeds back hot products of combustion to the reactants, thereby raising the temperature as well as diluting the mixture, leading to autoignition kernels that stabilize the reaction zone, even for very lean mixtures. Thus, it is important to understand the properties of such autoigniting mixtures, including the variation of emissions produced.

Exhaust gases consist of inert species such as CO_2 , N_2 , H_2O as well as radicals such as OH, H, CH_2O , etc. In general, it is understood that inert vitiation components might act towards slowing down the chemistry while radicals may increase the rate of reaction. This provides competing mechanisms in the mixture. The effect of the addition of inert diluents such as N_2 and CO_2 on hot fuel-oxidizer mixtures has shown several interesting chemical kinetic phenomena [79, 31]. Autoignition of $\text{CH}_4/\text{O}_2/\text{N}_2$ mixtures have been simulated [80], where the O_2 fraction was varied by diluting with N_2 . The autoignition delay time, determined using a homogeneous reactor model, was seen to increase with higher dilution and decrease with higher pressure and temperature of reactants. Autoignition delay for MILD combustion conditions [27] was measured in a tubular flow reactor and simulated using a plug flow reactor model in [81], for methane in O_2/N_2 mixtures at atmospheric pressure, elevated temperatures, and high dilution levels, varied by increasing N_2 content. It was observed that the combination of high N_2 dilution and heat loss to the surrounding slowed down chemical kinetic pathways typically promoted by high temperature such that there was significant competition between the oxidation and recombination channels. This is usually suppressed in conventional combustion characterized by high-temperature gradients. Under MILD conditions, it gives way to interesting kinetics allowing for regimes of slow combustion, pyrolysis, dynamic behavior, and transitional combustion [81]. The oxidation of methane, highly diluted with CO_2 , was investigated in [82], and the authors discovered a dynamic behavior. Unlike previous studies, this one was done under adiabatic conditions, thereby attributing the dynamics entirely to the chemical kinetics. For lean mixtures, temperature oscillations were attributed to the H_2/O_2 mechanism and were independent of dilution, initial temperature, and composition. The rich mixtures, on the other hand, had their dynamic behavior controlled by CO_2 reactions. CO_2 has a higher third body efficiency for CH_3 recombination-oxidation reactions and thus promotes the formation of C_2 , thereby lowering system reactivity, however, this reaction also releases heat thereby providing energy for branching reactions. CO_2 also inhibits the H_2/O_2 branching reactions by consuming H radicals to form CO and OH. This provides competing effects, leading to dy-

namic behavior. The authors in [83] observed a reduction in NO for sufficiently long residence times with the addition of exhaust gases in the form of $N_2/CO_2/H_2O$ combination.

The addition of radicals can have a significant effect on the autoignition properties. The authors in [84] investigated the influence of radicals on methane/air mixtures and found that H, CH_3 and C_2H_5 have similar effects of lowering autoignition delay time; however, CH_3 had the least promoting effect. The role of precursors in the stabilization of jet flames undergoing autoignition by mixing with a hot, diluted coflow, was examined in [56]. The sensitivity of ignition delay to intermediate species such as CH_2O , HO_2 , OH, and O was analyzed numerically through 0D reactor simulations. These species were seen to dramatically reduce the ignition delay with halving occurring with as little as 0.1% concentration addition.

In internal exhaust gas recirculation systems, the thermodynamic state and composition of recirculated product gases are uniquely correlated to the incoming fresh reactant stream. Further, heat losses to the combustor wall during recirculation and quenching of radicals may alter the assumed state of burnt products. Thus, it is important to take into account these factors while predicting the autoignition behavior of the incoming fuel-air mixture in a flameless/mild combustor. The authors in [85] simulated the reaction of methane-air mixtures with products of its combustion under adiabatic conditions in a plug flow reactor model. Different levels of dilution were explored along with different equivalence ratios. It was observed that mixtures containing all the species, including radicals, ignited faster than only those that included molecular major species, referred to as reduced. Thus, minor species in the mixture influenced the ignition. The fresh reactants were used at a constant inlet temperature of 298K. The authors in [86] performed a similar study while taking into account variations in levels of burntness of the hot diluent mixed with the fresh reactants to obtain the initial mixture. Lower burntness levels resulted in a lower temperature of the mixture while having a higher mole fraction of radical species. In general, increasing recirculation/level of hot diluent in a mixture enhanced the autoignition process. Both of the aforementioned studies were done using GRI Mech 3.0, which has its limitations in the low-temperature region ($T < 1200K$). In fact, ref. [87], has shown that GRI Mech 3.0 can give erroneous values of the autoignition delay time.

Most of the research on autoignition properties under Flameless/MILD combustion conditions consider diluents that consist of arbitrarily enforced concentrations of inert species such as N_2 , CO_2 , and H_2O . However, in combustors with internal recirculation, the composition is coupled to the input gases, and the burnt products also contain radical species that may exist in a steady state in the recirculation zones. More recently, some studies have looked at this [80, 86] in the context of gas turbine conditions. While they look at vitiation with radicals and composition derived from inlet gas products, they do not look at the effect of heat losses. This can affect the thermodynamic state of the mixture and, hence, the autoignition characteristics. This study aims to understand the autoignition characteristics of premixed methane-air mixtures diluted with hot exhaust gases and the resulting NO_x and CO formed while varying the extent of vitiation and heat loss.

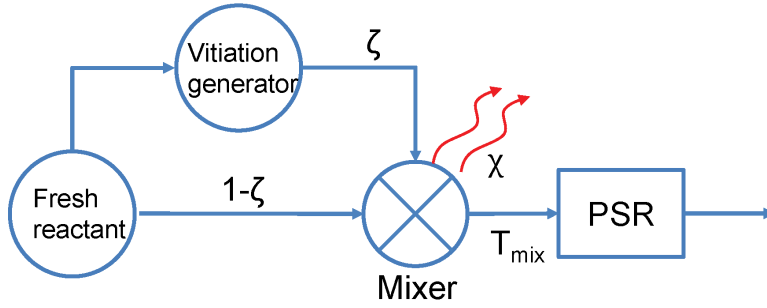


Figure 4.1: Schematic of setup for perfectly stirred reactor simulation.

4.2. METHODOLOGY

4.2.1. NUMERICAL SETUP

A zero-dimensional steady flow reactor system is set up to simulate the cases. A schematic is shown in Fig 5.1, where the fresh reactants (CH_4/Air mixture) are initialized with varying equivalence ratios, $\phi = 0.3, 0.55$ and 0.75 , at a fixed temperature of 1200K in a reservoir. The cases of $\phi=0.75$ and 0.55 represent typical lean methane-air mixtures within the ignition limit [88], while $\phi=0.3$ represents an ultra-lean case where a pure mixture without vitiator and radicals would not be ignitable. The composition of this reservoir is used to initialize a reactor ("Vitiator Generator"), which is solved to a steady state to obtain the burnt products. The hot products and fresh reactants are mixed based on the definition of vitiator fraction(ζ), such that

$$\zeta = \frac{N_{\text{hot products}}}{N_{\text{fresh}} + N_{\text{hot products}}} \quad (4.1)$$

, where N is the moles of substance. The net mole fraction and enthalpy of the mixture are determined on a mole basis. Further, a heat loss factor, χ , is defined where

$$\chi = \frac{T_{\text{adiabatic}} - T_{\text{mix}}}{T_{\text{adiabatic}} - T_{\text{fresh}}} \quad (4.2)$$

χ is varied such that T_{mix} , the resulting temperature of fresh reactant+vitiator mixture achieves a temperature between that of the fresh reactants (T_{fresh} at $\chi=1$) and adiabatic temperature of the hot products obtained by combustion of the fresh reactants ($T_{\text{adiabatic}}$ at $\chi=0$). The values of T_{fresh} , ϕ , ζ and χ used in the simulations are tabulated in Table 4.1.

The system was simulated in Cantera [89]. The hot products are generated by an "Ideal Gas Constant Pressure Reactor" object, simulated to steady state. They consist of not only stable species such as CO_2 , N_2 , H_2O and CO , but also radicals such as OH and H existing in equilibrium. The PSR is an "Ideal Gas Reactor" object that represents a Perfectly Stirred Reactor (PSR) of fixed volume and has an inlet from the "Mixer" with a fixed volume flow rate across all cases such that a constant residence time is maintained.

Table 4.1: Simulation conditions

Parameter	Values
T_{fresh}	1200 K
ϕ	0.3, 0.55, 0.75
ζ	0.1, 0.3, 0.5, 0.7, 0.9
χ	0, 0.25, 0.5, 0.75, 0.9

The outlet is defined by a similar flow controller with flow rate equal to the inlet flow rate. The generalized governing equations for a reactor are:

$$\frac{dm}{dt} = \sum_{\text{in}} \dot{m}_{\text{in}} - \sum_{\text{out}} \dot{m}_{\text{out}} \quad (4.3)$$

$$mC_v \frac{dT}{dt} = -p \frac{dV}{dt} + \sum_{\text{in}} \dot{m}_{\text{in}} \left(h_{\text{in}} - \sum_k u_k Y_{k,\text{in}} \right) - \frac{pV}{m} \sum_{\text{out}} \dot{m}_{\text{out}} - \sum_k V \dot{\omega}_k W_k u_k \quad (4.4)$$

$$m \frac{dY_k}{dt} = \sum_{\text{in}} \dot{m}_{\text{in}} (Y_{k,\text{in}} - Y_k) + V \dot{\omega}_k W_k \quad (4.5)$$

The NO_x related species are set to zero in the "Mixer" as we would like to study the NO_x formation that occurs in these vitiated mixtures without it being influenced by the pathway used to generate the hot products. The PSR is initialized to the same state and composition as the "Mixer" at $t=0$.

The POLIMI_C1C3_HT_NO_x_1412 chemical kinetic mechanism [90, 91] was used (referred to as C1C3 in this article), which is a detailed mechanism of the pyrolysis, partial oxidation, and combustion of hydrocarbon fuels up to 3 C atoms with NO_x . It accounts for 115 species and 2141 reactions. This choice was based on the work in [87], wherein the authors demonstrated that the C1C3 mechanism (also called the Ranzi mechanism in the literature [90, 91]) and Zhukov mechanism [92] captured the low-temperature chemistry and Negative Temperature Coefficient (NTC) region of methane-air combustion the best amongst the openly available mechanisms compared in the study.

An adaptive time-stepping approach was used to advance the simulation such that a finer increment is done at locations where there is a steep temperature/species gradient. This allows for overall simulation time economy as coarser steps can be used elsewhere. The simulation was initially solved with a uniform time step. The time steps were refined uniformly (if required) to reach a final state where the change in temperature and methane mole fraction was insignificant. Next, the time mesh was locally refined around points of high-temperature gradient and also specifically around a peak detected below 10-time steps from the start. This allowed for an optimal time marching where larger time steps were taken for smaller temperature gradients and vice-versa.

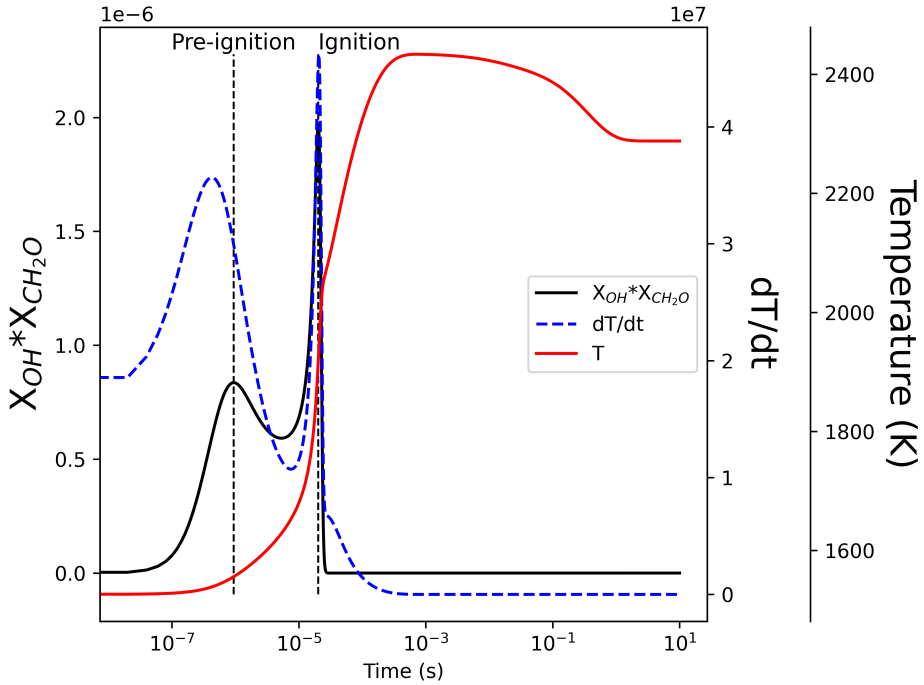


Figure 4.2: Time profile of quantities at $\phi=0.75$, $\zeta=0.5$, $\chi=0.5$.

4.2.2. IGNITION CRITERIA

One of the motivations of this work is to provide information on chemistry that may also be compared with experiments. Heat release rate (HRR) is difficult to measure directly in combustion, hence, it can be indirectly measured from the product of the PLIF signal of OH and CH₂O [93, 94, 95, 96]. Further, in the context of autoignition, it has been shown in [97] that a peak in the product of OH and CH₂O mole fractions is a good marker of heat release rate under autoignition conditions. Thus, in this study, an ignition event was detected based on the occurrence of a peak of Heat Release Rate (HRR) represented by the product of mole fractions of OH and CH₂O, as shown in an example in Fig 4.2 for $\phi=0.75$, $\zeta=0.5$, $\chi=0.5$. This figure also validates the use of the current ignition location identification criteria. The ignition peak corresponding to rapid temperature rise (T) indicated by a peak in dT/dt, matches well with the HRR ($X_{OH} * X_{CH_2O}$) peak. It is also seen that another 'pre-ignition' peak occurs in the timeline before the main ignition event. A similar preignition event is also reported in [85]. The occurrence of this is explained in Section 4.3.3 along with verification by comparing different chemical-kinetic mechanisms and simulating the mixture in a 1D flamelet model.

4.3. RESULTS

4.3.1. IGNITION PARAMETERS

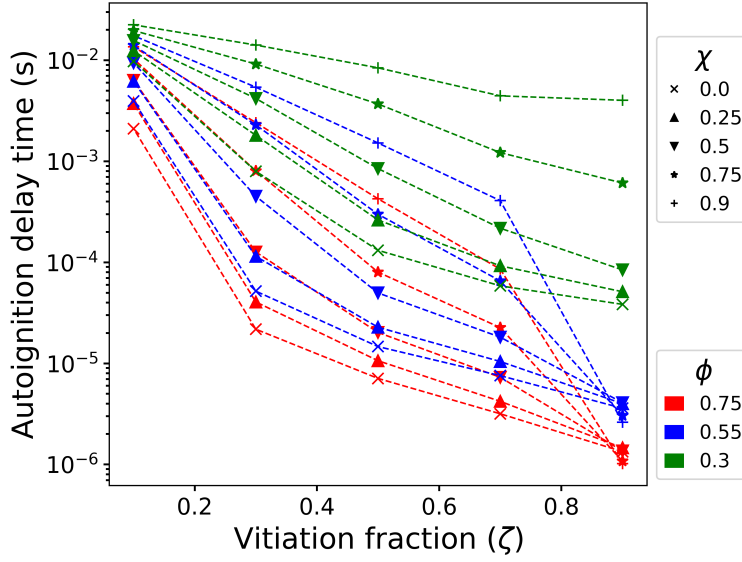
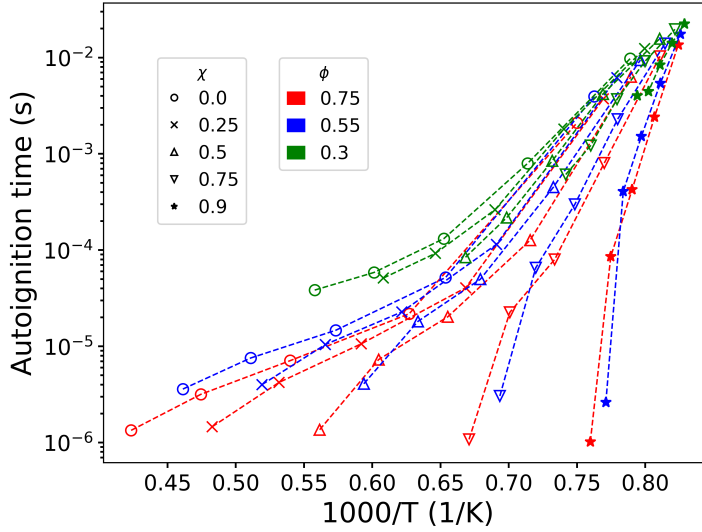
Numerical simulations of methane-air mixtures were carried out for $0.1 \leq \zeta \leq 0.9$, $0 \leq \chi \leq 0.9$, and $\phi=0.3, 0.55$ and 0.75 . These were done at a constant fresh reactant initial temperature of 1200 K, and the residence time was kept constant at ≈ 0.5 s across all cases by maintaining the same PSR volume and volume flow rate through it. The autoignition delay time decreases with increasing vitiation fraction, ζ , as shown in Fig 4.3. Increasing heat loss, indicated by increasing χ , increases autoignition delay time; however, for $\zeta=0.9$, $\phi=0.55$ and 0.75 , for $\chi \geq 0.75$, the autoignition delay time reduces. This is in contrast to cases in the literature [98] where dilution by inert components such as CO_2 and H_2O always leads to a longer delay. However, in this case, the presence of radicals pushes the reactions in a favorable direction. The variation of autoignition time with the inverse of temperature, for the same variation of ζ and χ , is shown in Fig 4.4. The various cases of ζ are not shown explicitly, but for every curve associated with a particular χ value, the rising temperature, i.e., is correlated to increasing ζ . Thus, the variation of the curve from right to left along the x-axis indicates the correlation to increasing ζ . The reduction is strongly correlated to an increase in temperature. The rise in vitiation, ζ , leads to a flattening tendency of the curve seen very well for $\chi=0$ cases. Increasing χ causes the curve to drop steeply with higher temperature (lower $1000/T$), such that significantly lower autoignition time is achieved without much temperature rise. This indicates that the presence of radicals introduced through the vitiation stream is a prominent driver of the autoignition delay and governs the onset of the reaction. This is also seen in Fig 4.3 where at $\zeta > 0.7$, the various χ curves converge towards a similar autoignition delay time.

It can also be seen that the ignition delay time for ultra-lean mixture, $\phi=0.3$, is significantly reduced with vitiation, even under conditions of heat loss. This occurs to the extent that the delay is comparable to lean conditions. Thus, this is promising to combust such ultra-lean mixtures to achieve low emissions.

The peak-width of the HRR peak at the ignition point is used as an indicator of the reaction timescale at this point. This can also serve as an indicator of the reaction zone thickness, for example, in a PLIF/chemiluminescence image. The peak width is calculated as a sum of the half-width evaluated on either side of the peak. The half-width point is chosen as the location along the time scale where

$$\text{HRR}_{\text{half-width}} = \frac{1}{e^2} (\text{HRR}_{\text{peak}} - \text{HRR}_{\text{min}}) + \text{HRR}_{\text{min}}, \quad (4.6)$$

where e is the exponential constant. Figure 4.5a shows the variation of peak width with ζ and χ . For adiabatic conditions, $\chi=0$, increasing ζ results in a slight increase and then decrease of peak-width. This occurs as increasing hot vitiation fraction leads to higher initial mixture temperature, as seen in Fig 4.5b, as well as a higher radical fraction that enhances the rates of reactions associated with ignition while countering the effects of inert, stable species that are also present in the vitiation. However, under ultra-lean conditions, $\phi=0.3$, there is an increase at $\zeta=0.9$, possibly due to the low radical fraction at such a large fraction of excess air. Now, when heat loss is introduced, i.e. increasing χ , one can observe that increasing ζ leads to larger peak-width, indicating longer reaction time scale. There is a ζ value beyond which peak-width starts decreasing. This is due to

Figure 4.3: Ignition delay time vs ζ Figure 4.4: Ignition delay time vs $1000/T$

the radicals present in the vitiation products that accelerate the reactions. For ultra-lean ($\phi=0.3$), this decrease doesn't occur at very high ζ . This shows that distributed combustion is not very prominent just by increasing vitiation at adiabatic conditions but is favored with a certain degree of heat loss.

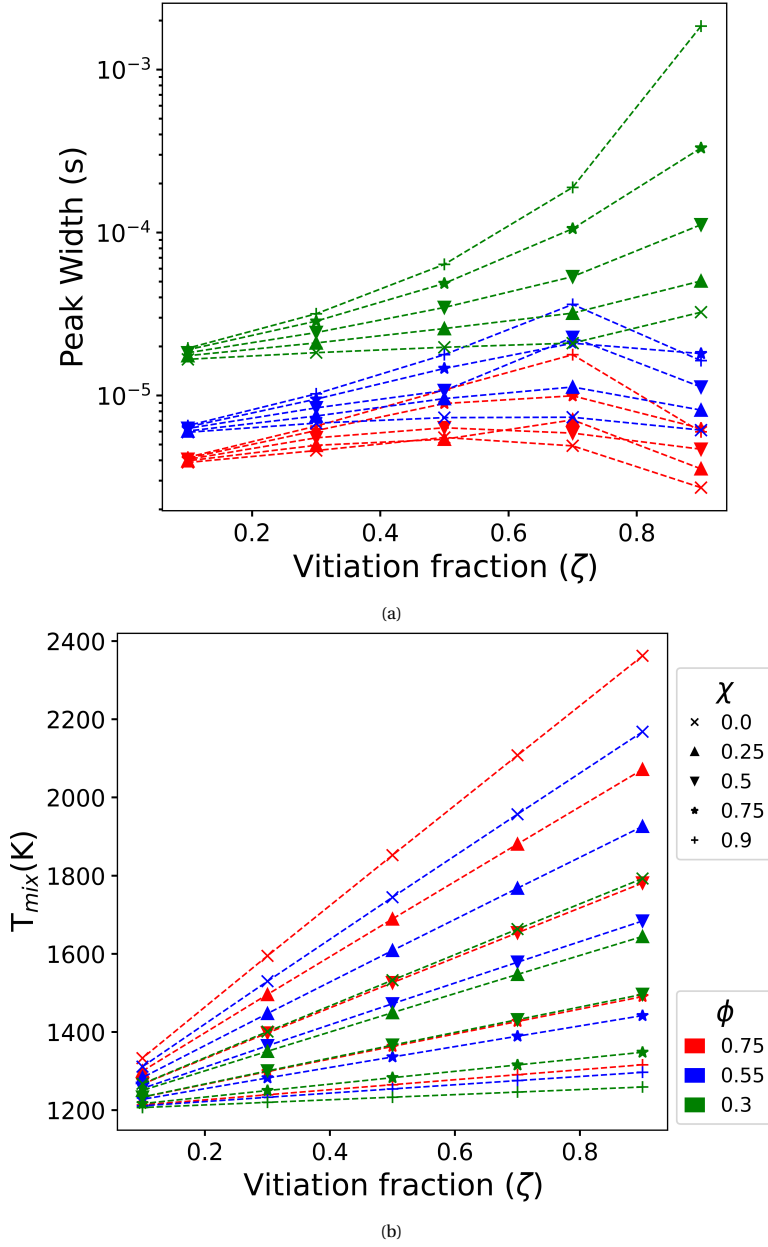


Figure 4.5: (a) Peak-width (b) T_{mix} vs ζ for varying ϕ and χ .

4.3.2. EMISSIONS

Emissions at steady state of the PSR are compared for different conditions of ζ and χ in Fig 4.6a (NO_x) and Fig 4.6b (CO). NO_x is evaluated as a sum of NO, NO_2 and N_2O . At lean

conditions ($\phi=0.75$ and 0.55), under adiabatic conditions ($\chi=0$), NO_x remains almost constant with a slight increase for increasing ζ while CO increases. The temperature at steady state, as shown in Fig 4.7a, is nearly constant at $\chi=0$, while the unburnt CH_4 at the exhaust decreases (Fig 4.7b). Further, CO increases as the CO- CO_2 equilibrium shifts in the reverse direction due to excess CO_2 introduced by vitiation. For ultra-lean conditions ($\phi=0.3$) and $\chi=0$, increasing ζ leads to a slight decrease in NO_x and CO. This corresponds to an increase in steady-state temperature and drop in CH_4 ; thus, the additional radicals and higher initial mixture temperature due to vitiation (Fig 4.5b) aids in completing the oxidation process, which otherwise would have been significantly slower without vitiation for ultra-lean conditions as also seen from the autoignition delay time in Fig 4.3.

This trend of NO_x and CO is in contrast to the typical philosophy for applying Flameless/MILD combustion, as no significant advantage is observed in the case of premixed combustion vitiated with its own products of combustion under adiabatic conditions. This strategy may work for non-premixed conditions where dilution by hot products containing the oxidizer required for oxidation delays the reaction such that optimal fuel-air mixture is achieved and combustion doesn't simply occur around stoichiometric conditions. In the case of premixed, there is no such advantage as the fuel and oxidizer are already mixed.

However, if heat loss is factored in, this can reduce the temperature of the mixture (while still containing radicals, theoretically) and cause a shift in the reaction pathway. For cases of $\chi>0$, increasing ζ leads to a reduction in NO_x for all ϕ . However, the curvature of the lines for $\phi=0.3$ (ultra-lean) differs from the lean cases. Simultaneously, increasing ζ with non-zero χ leads to a reduction in CO. For $\phi=0.3$, for higher ζ (>0.6) and higher χ (>0.5), it leads to slight increase in CO emissions. The reduction in NO_x can largely be attributed to a reduction in temperature (Fig 4.7a). This does lead to a minor rise in CH_4 , but it must be noted that the CH_4 scale is in ppm, and the maximum is less than 10 ppm. Hence, the unburnt fuel is considered to be negligible at steady-state. The increase in vitiation also leads to a lower O_2 concentration in the initial mixture, which contributes to suppressing NO_x production.

These observations show that under premixed adiabatic conditions, i.e., $\chi=0$, simply adding hot vitiation, i.e., increasing ζ , leads to higher NO_x and higher CO. CO reduces under ultra-lean conditions and $\chi=0$. However, if a certain amount of heat loss is factored in ($\chi > 0.25$), a system can achieve a reduction of NO_x and CO simultaneously. This can be possible in a combustor with intense recirculation zones such that the recirculating hot products lose heat through the walls before mixing back with the fresh reactants.

4.3.3. OCCURRENCE OF MULTI-IGNITION

Under certain conditions of ζ and χ , two peaks in HRR ($X_{\text{H}_2\text{O}} * X_{\text{CH}_2\text{O}}$) were observed. This is termed as 'multi-ignition' here, where there is a main ignition peak associated with major heat release and a pre-ignition peak, which may not necessarily lead to a huge temperature rise but leads to an atypical species pool before the main ignition event. An example of this phenomenon is shown in Fig 4.2, which shows the time profile of HRR, Temperature and dT/dt for $\phi=0.75$, $\zeta=0.5$ and $\chi=0.75$. The pre-ignition peak is also seen in the dT/dt profile. Figure 4.8 shows the combination of ζ and χ for which multi-ignition occurs for various lean equivalence ratios ($\phi=0.3, 0.55, 0.75$). This phenomenon is seen

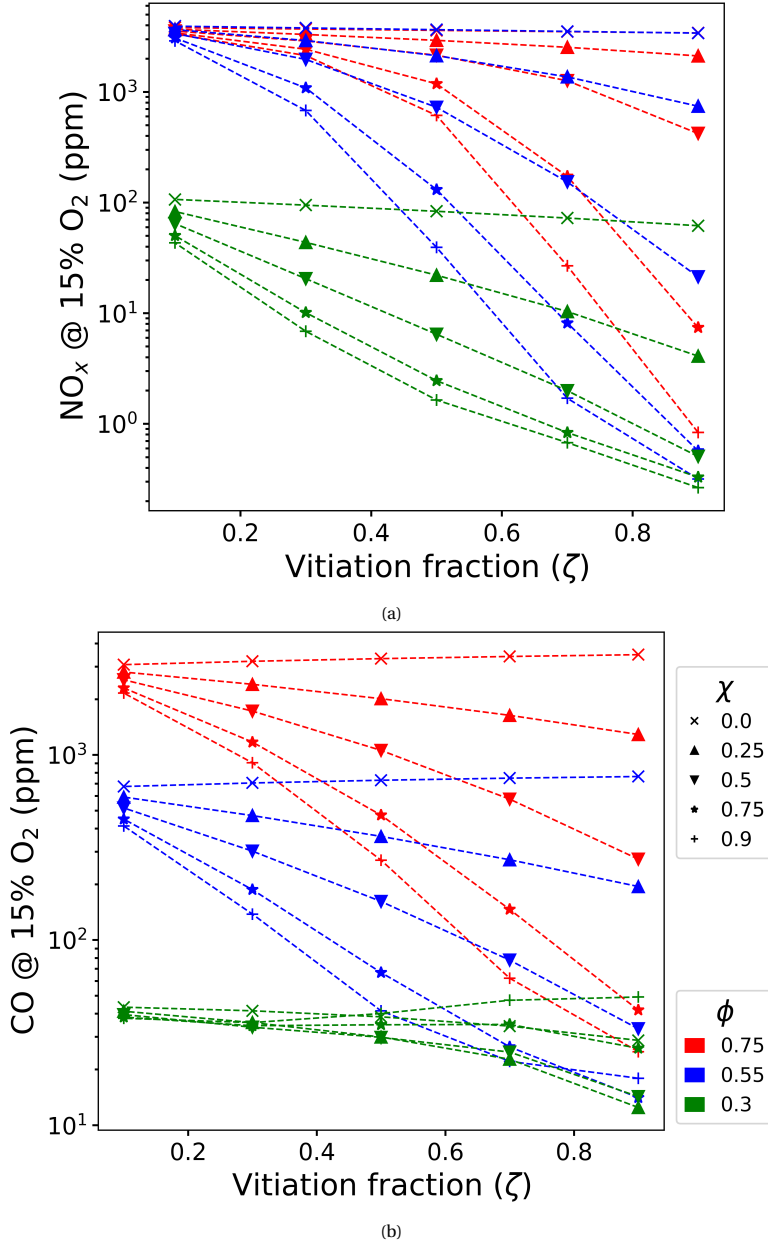


Figure 4.6: (a)NO_x and (b)CO at steady-state vs ζ for varying φ and χ.

only for moderate to high levels of vitiatio and is more prominent in cases of heat loss. However, for lean conditions, φ=0.55, 0.75, there is an intermediate ζ where this occurs under adiabatic conditions, χ=0, whereas for ultra-lean conditions, φ=0.3, a higher heat

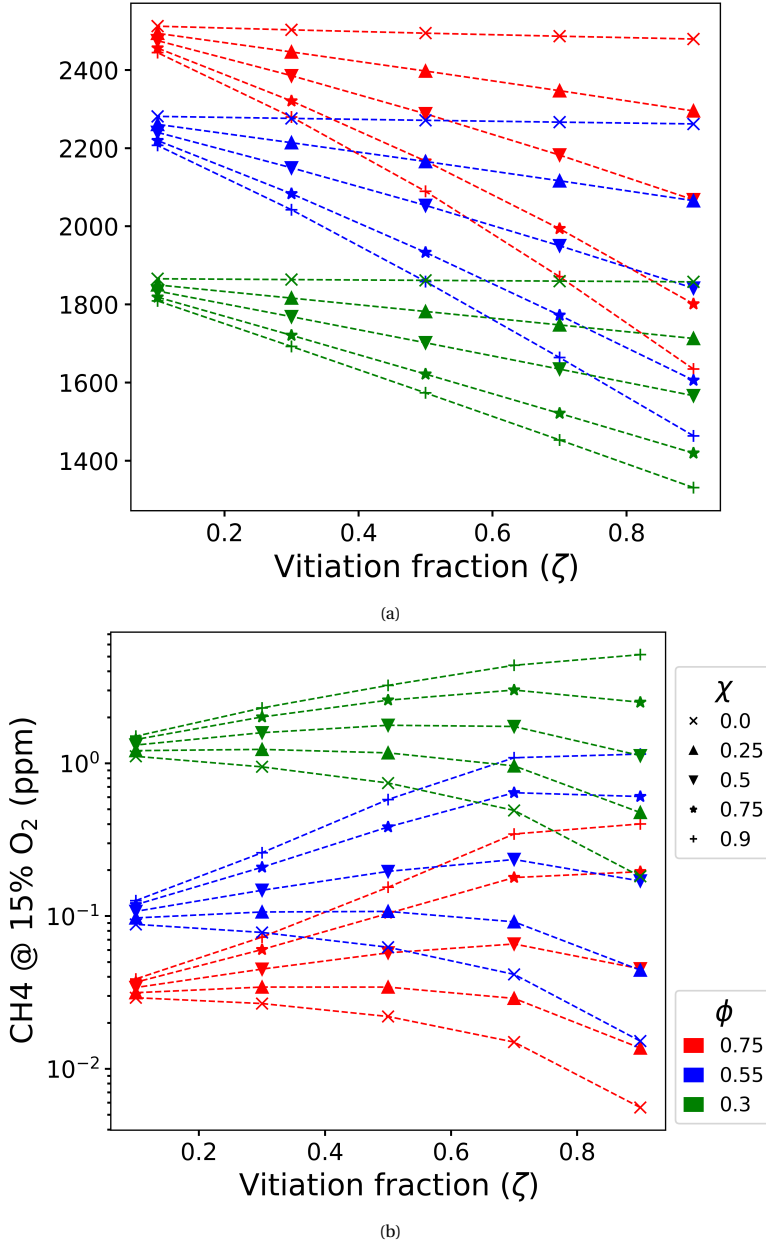


Figure 4.7: (a) Temperature and (b) CH₄ at steady-state vs ζ for varying ϕ and χ .

loss factor $\chi \geq 0.5$ is required to observe this.

The significance of the phenomenon can be seen through the ratio of preignition to ignition peak height in Fig 4.9. Under low χ and moderate ζ values, the ratio is much

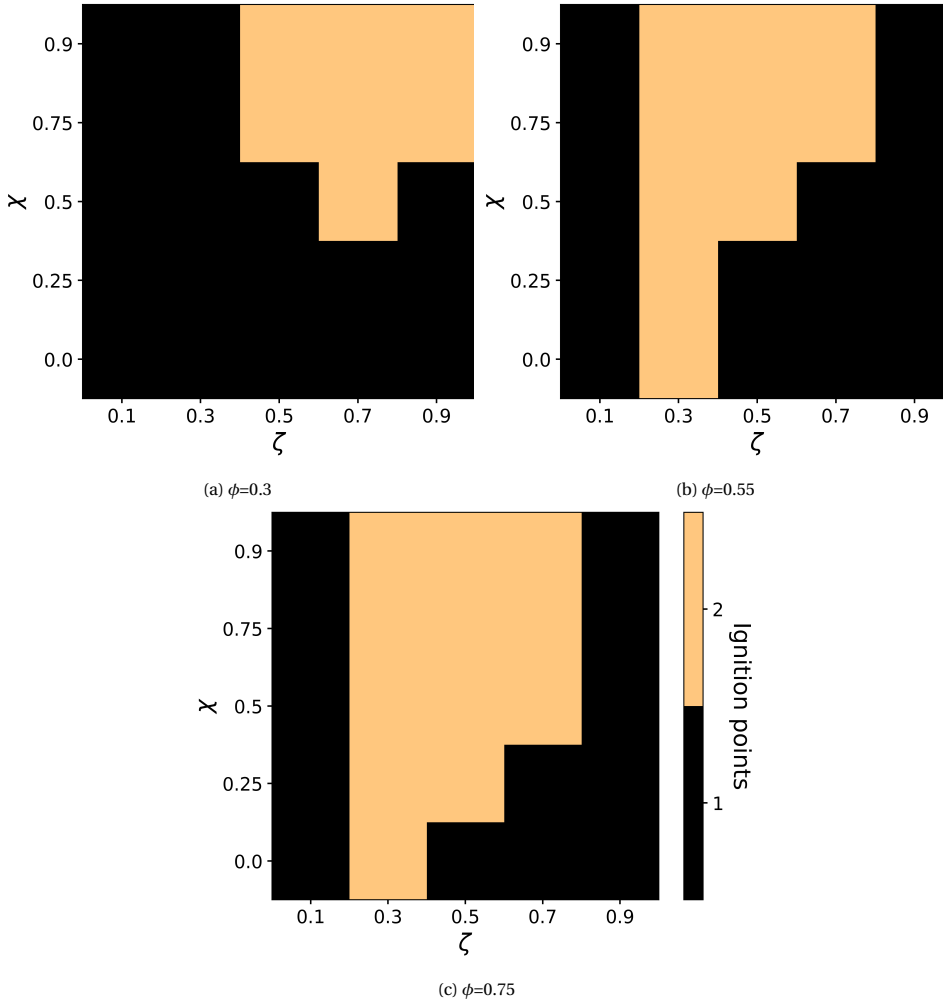


Figure 4.8: Number of ignition points.

smaller than 1. However, for higher ζ and χ values, the ratio can get close to and higher than 1, indicating that the pre-ignition peak magnitude is comparable to that of the ignition peak. This shows that a significant reaction front can occur at the pre-ignition point, which can be picked up as a significant measurement on a probe, either experimentally or numerically. This can have implications in flame front detection through OH/CH₂O tracking by chemiluminescence imaging or PLIF, as well as the interpretation of flame front detected in simulations using this criterion.

The occurrence of multi-ignition is verified by comparing simulations done with C1C3 mechanism with those of the Konnov [99] and SanDiego [100] chemical kinetic mechanisms in the PSR model and a 1-D flamelet model. As can be seen in Fig 4.10, the

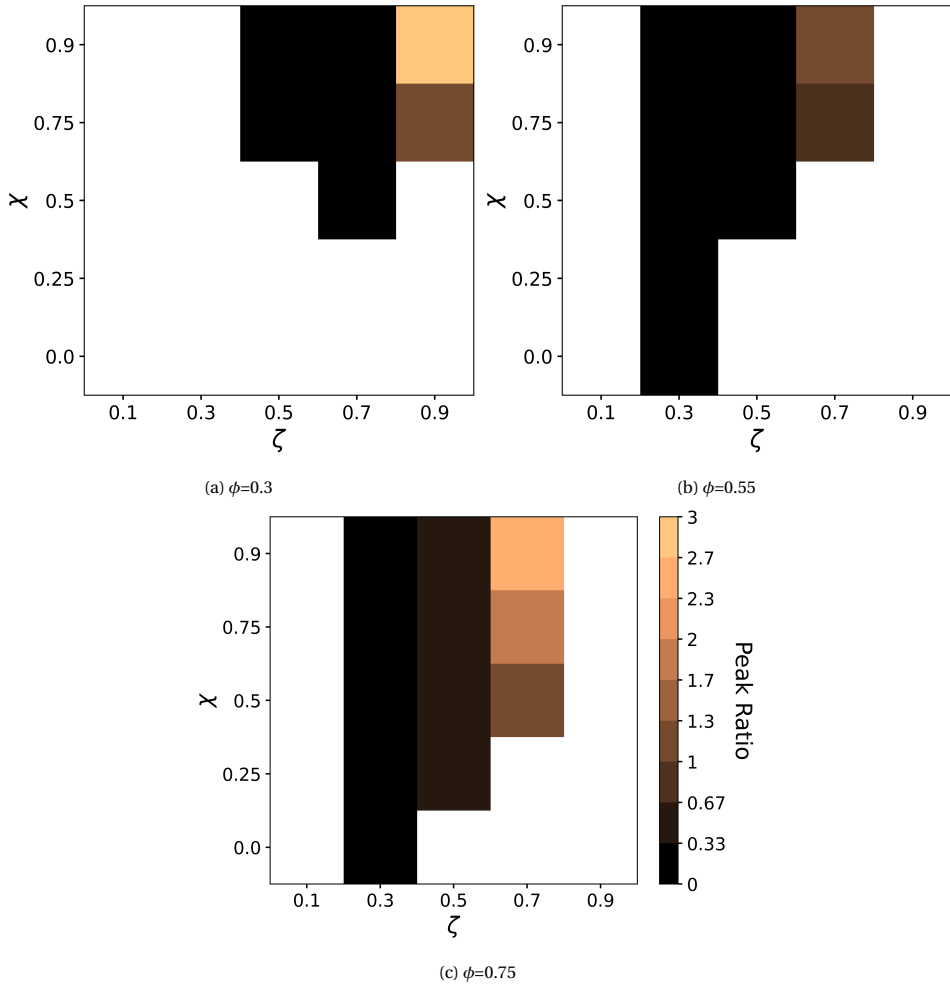
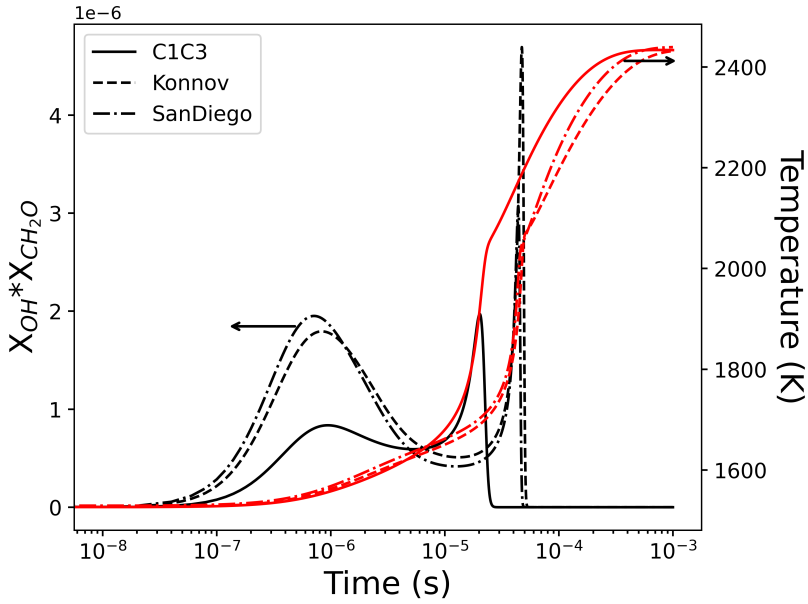


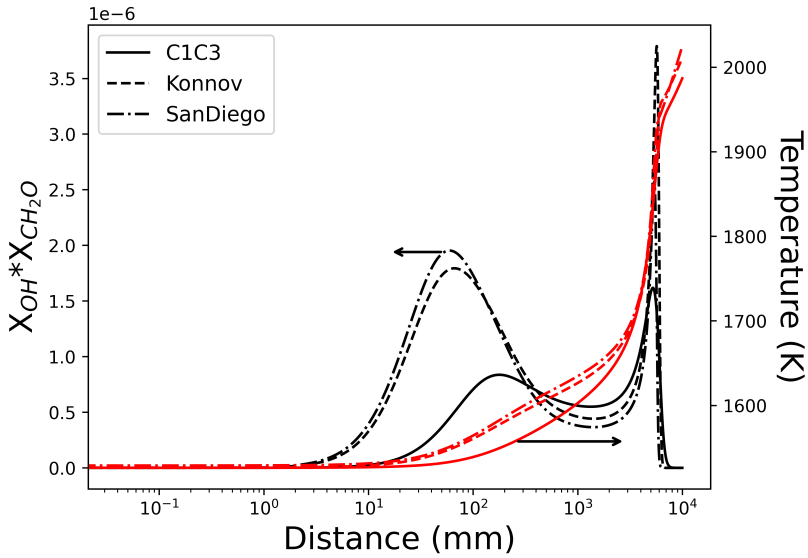
Figure 4.9: Ratio of preignition peak to ignition peak height.

pre-ignition and ignition peaks are seen in both the PSR and 1D flamelet cases for all three mechanisms, on the HRR curve ($X_{H_2O} * X_{CH_2O}$). However, the location of the ignition and pre-ignition peaks vary depending on the mechanism and the reactor model. A difference in ignition delay time was also observed between these mechanisms in [82]. The authors in [82] also observed dynamic behaviour for diluted methane-air mixtures in the post-ignition region for the mechanisms mentioned here.

The mechanism behind the multi-ignition points is closely examined by analyzing the reactions which influence CH_2O and OH . This is done by performing a sensitivity analysis for CH_2O and OH at the ignition and pre-ignition points. The normalized sen-



(a) PSR



(b) 1-D Flamelet

Figure 4.10: Verification of multi-ignition by simulating with other chemical kinetic mechanisms and 1-D flamelet model at $\phi=0.75, \zeta=0.5, \chi=0.5$.

sitivity coefficient was defined as

$$S_{ki} = \frac{p_i}{y_k} \frac{\partial y_k}{\partial p_i}, \tag{4.7}$$

where y_k is the solution variable, i.e. mass fraction of species, p_i is a multiplier on the rate constant. Further, the analysis was done by presenting reactions that were chosen based on their normalized sensitivity coefficient being greater than 10% of the maximum value detected amongst all the reactions.

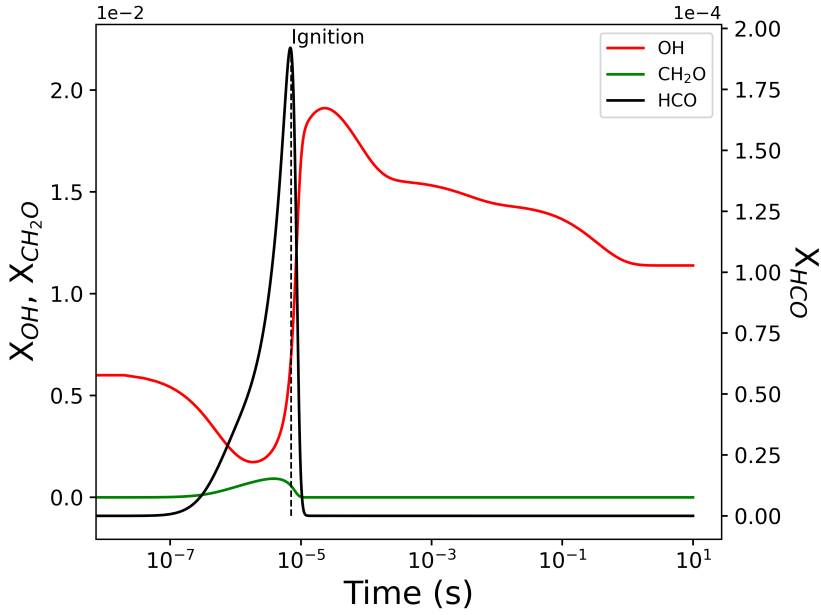
Comparing the cases of $\phi=0.75$, $\zeta=0.5$, $\chi=0$ (Fig 4.11a) and $\chi=0.5$ (Fig 4.11b), we observe that the pre-ignition peak is caused by the rising mole fraction of CH_2O and the falling mole fraction of OH. This is in contrast to the ignition point where OH is rising and CH_2O is dropping. There is also a distinct difference in the HCO profile in the multi-ignition case, where there is a peak just after the pre-ignition point, and then the mole fraction drops and rises again at the ignition point. Further, in the case of pre-ignition (Fig 4.11b), the CH_2O peak is wider and flatter as it starts rising just before the pre-ignition point. This indicates that the mechanism that leads to the pre-ignition point is driven by the conversion path of $\text{CH}_2\text{O} \rightarrow \text{HCO} \rightarrow \text{CO}$.

4

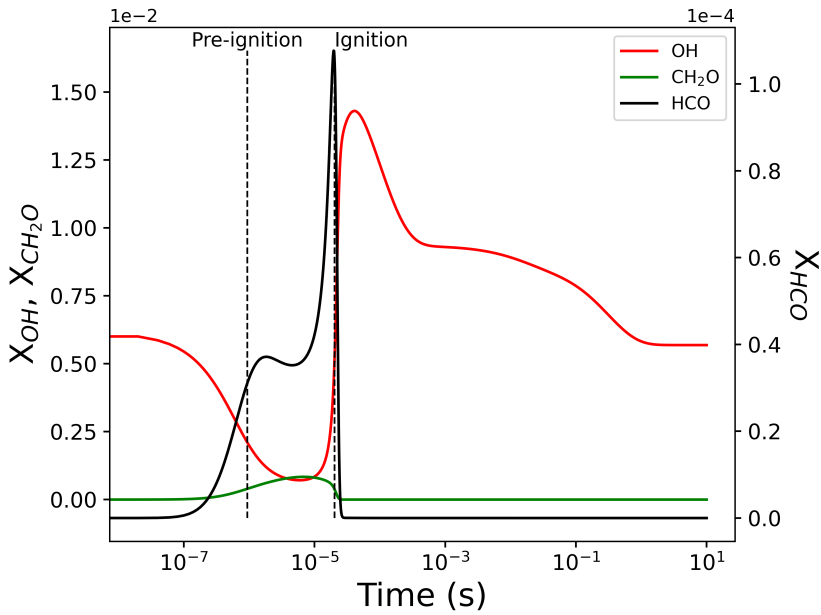
The Rate of Progress (ROP) of the reactions related to OH, CH_2O , and HCO, along with their mole fractions, for a case with multi-ignition ($\phi=0.75$, $\zeta=0.5$, $\chi=0.5$) are shown in Fig 4.12, 4.13 and 4.14. Similar plots for the case of a single ignition peak ($\phi=0.75$, $\zeta=0.5$, $\chi=0.0$) can be found in the Appendix (Fig B.2, B.1). Initially, there is a significant amount of OH radicals from the vitiation produced by combustion. This causes the initial breakdown of CH_4 into CH_3 and CH_2 through reactions such as R874 ($\text{CH}_4 + \text{OH} \rightleftharpoons \text{CH}_3 + \text{H}_2\text{O}$) and R312 ($\text{CH}_3 + \text{OH} \rightleftharpoons \text{CH}_2(\text{S}) + \text{H}_2\text{O}$) (Fig 4.12a). This resulting radical pool leads to significant CH_2O production through reactions R256 ($\text{CH}_3 + \text{OH} \rightleftharpoons \text{CH}_2\text{O} + \text{H}_2$) and R325 ($\text{CH}_2 + \text{O}_2 \rightleftharpoons \text{CH}_2\text{O} + \text{O}$), shown in Fig 4.13a.

In the case of pre-ignition, R256 has a higher peak ROP just before the pre-ignition point than at the ignition point (Fig 4.13a). The radical pool consisting of rising CH_2O levels establishes a rise in HCO through reactions R393 ($\text{CH}_2\text{O} + \text{H} \rightleftharpoons \text{H}_2 + \text{HCO}$), R1357 ($\text{CH}_2\text{O} + \text{OH} \rightleftharpoons \text{H}_2\text{O} + \text{HCO}$) and R1358 ($\text{CH}_2\text{O} + \text{O} \rightleftharpoons \text{HCO} + \text{OH}$), shown in Fig 4.14a. Thus, there are several reactions through which OH radicals are consumed to generate intermediates, CH_2O and HCO. In the case of heat loss ($\chi=0.5$), just after the pre-ignition point, HCO reaches a peak and then drops because consumption reactions such as R15, R173, R277, and R278 dominate, whereas there is insufficient HCO production from CH_2O due to lack of radicals which have been consumed. The effect of heat loss is thus to slow down the OH radical production just enough such that the initial radical pool is consumed to generate an intermediate level of CH_2O and HCO, leading to a rising CH_2O and falling OH profile causing the pre-ignition peak. After this peak, the OH levels are regenerated cumulatively over time to lead up to the main ignition event. In the case of low or no vitiation, this initial radical pool would be too low to generate CH_2O and HCO to a level that can lead to a significant peak in the HRR profile.

This process transitions into the main ignition peak when a sufficient radical level is re-established. Primarily OH levels increase back through R6 ($2\text{OH} \rightleftharpoons \text{H}_2\text{O} + \text{O}$) and R257 ($\text{CH}_3 + \text{OH} \rightleftharpoons \text{CH}_4 + \text{O}$) (Fig 4.12a) and CH_2O is converted to HCO through R393, R1357 and R1358 which is then rapidly converted to CO. This establishes the $\text{CH}_2\text{O} \rightarrow \text{HCO} \rightarrow \text{CO}$ conversion pathway which leads to heat release at the ignition point.



(a) $\phi=0.75, \zeta=0.5, \chi=0.0$



(b) $\phi=0.75, \zeta=0.5, \chi=0.5$

Figure 4.11: Time profiles of mole fractions of OH, CH₂O and HCO for (a) single ignition point and (b) multi-ignition points.

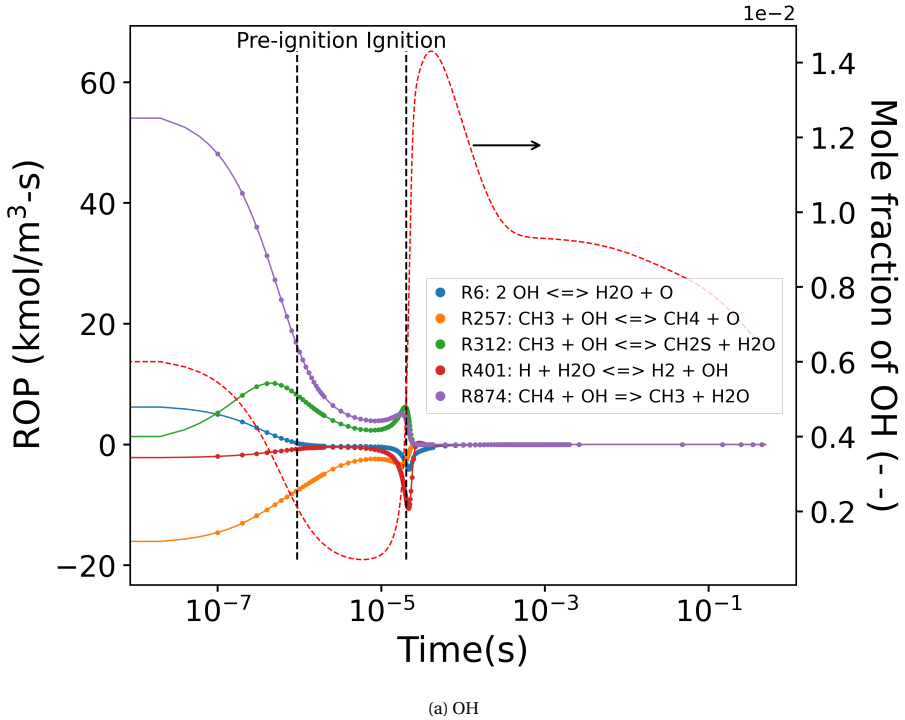


Figure 4.12: Rate of Progress of reactions related to OH and their mole fractions at $\phi=0.75$, $\zeta=0.5$, $\chi=0.5$

4.4. CONCLUSIONS

Methane-air mixtures vitiated with hot products of combustion from the same mixture were simulated in a PSR model to emulate chemical kinetic effects seen in Flameless/MILD combustion systems working on the principle of internal recirculation. This results in vitiation at elevated temperatures containing not only inert species as diluents but also radicals that occur at the end of steady-state combustion. Under these conditions, the effect of vitiation fraction (ζ) and heat loss factor (χ) are studied. The effects are:

- Increasing ζ leads to lower autoignition delay time while increasing χ increases it. However, even at higher values of χ , comparable values of autoignition delay to $\chi=0$ could be achieved at high ζ due to the presence of radicals.
- Under adiabatic conditions $\chi=0$, increasing ζ led to almost similar ignition peak-width of HRR ($X_{H_2O} \cdot X_{CH_2O}$) which decreases for $\zeta > 0.5$; however, for higher χ an increase in peak-width was achieved and a decrease only at $\zeta > 0.7$. For ultra-lean ($\phi=0.3$), a monotonic increase was seen. Considering the ignition peak-width as an indicator of reaction time scale and, hence, reaction zone thickness, a thickened reaction zone is achieved only with finite heat-loss for lean vitiated mixtures. This shows that the notion of a distributed reaction zone under Flameless/MILD

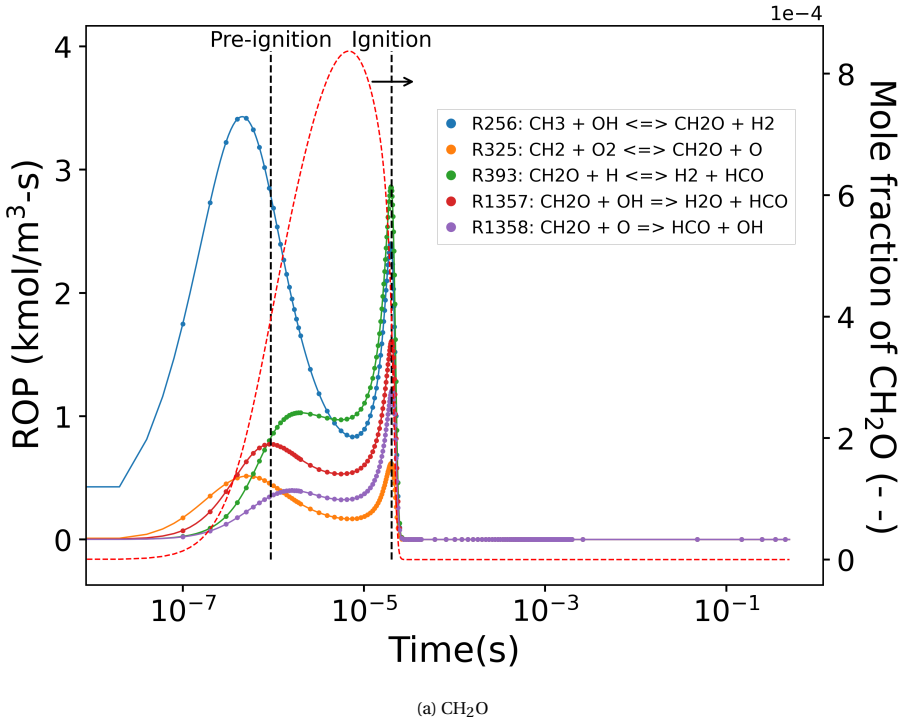


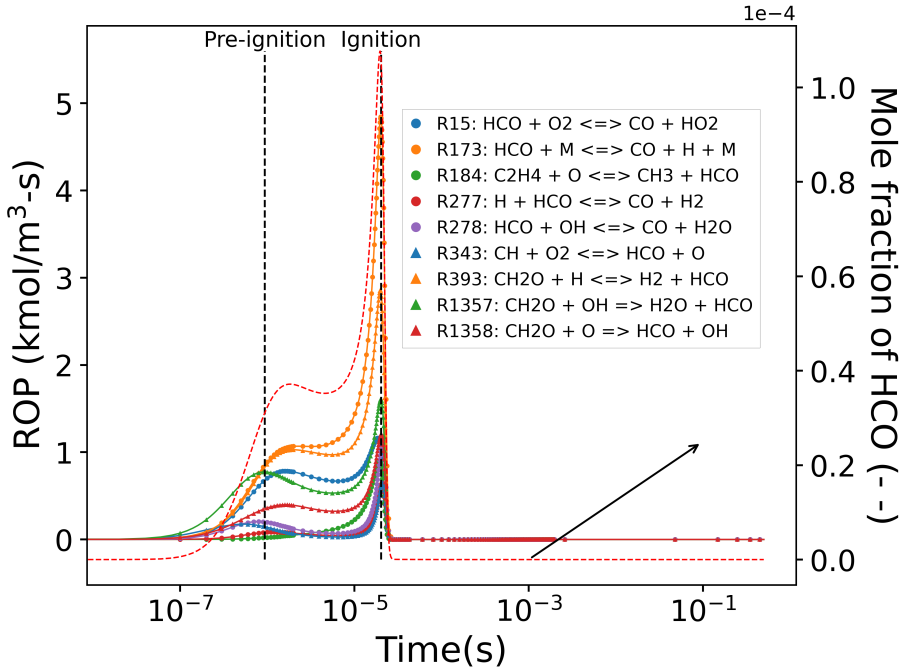
Figure 4.13: Rate of Progress of reactions related to CH₂O and their mole fractions at $\phi=0.75$, $\zeta=0.5$, $\chi=0.5$

conditions for premixed fuel-oxidizer may more likely occur when heat loss occurs.

- Significant reduction in NO_x and CO can occur with increasing vitiation (ζ) if a certain amount of heat loss (χ) is factored in.

Thus, the properties of lower emission and distributed reaction zones associated with Flameless/MILD combustion do not seem to be prominent for premixed mixtures vitiated by recirculated products under adiabatic conditions. However, these properties become significant when heat loss occurs.

The phenomenon of multi-ignition was seen to occur where the timeprofile of Heat Release rate indicated by product of OH and CH₂O mole fraction showed two peaks, one called the pre-ignition peak and the second the main ignition peak, associated with major temperature rise. The occurrence of the pre-ignition event was found at conditions with significant vitiation and heat loss. This was attributed to a peak caused by falling OH and rising CH₂O levels. The combination of sufficient vitiation and heat loss led to an initial consumption of OH radicals to generate CH₂O and HCO while the reduced temperature due to heat loss slowed down the OH production pathway. After the pre-ignition peak, the radical pool is re-established by a slow cumulative process, after which the main ignition event occurs. This observation has implications on the way ex-



(a) HCO

Figure 4.14: Rate of Progress of reactions related to HCO and its mole fraction at $\phi=0.75$, $\zeta=0.5$, $\chi=0.5$

perimental and numerical data on flame front detection by this criteria is interpreted for such mixtures with vitiation by hot products.

5

FLOW PHYSICS OF TURBULENT JET-IN-COFLOW

Real knowledge is to know the extent of one's ignorance.

Confucius

The jet-in-coflow is a two-stream configuration having engineering applications in combustors and gas turbine engine exhausts. In practical systems, the coflow generates a boundary layer of the outer wall of the jet pipe and may also have a certain level of turbulence. In the current work, the evolution of this flow configuration is studied using an air-air turbulent jet in a low turbulence coflow (turbulence intensity < 6%), and the 2D velocity field is measured by planar Particle Image Velocimetry. Cases of varying coflow ratio (ratio of coflow velocity to jet velocity) of 0 (turbulent free jet), 0.09, 0.15, and 0.33 are generated by keeping a constant velocity jet ($Re=14000$) and varying the coflow velocity. The trends of jet centerline properties such as velocity decay, jet spread, and jet momentum of jet-in-coflow cases, scaled to represent an equivalent free jet, show deviations from that of the turbulent free jet. The radial profile of mean velocity shows a region of velocity deficit, compared to a turbulent free jet, on the coflow side in the jet-in-coflow cases. In contrast, the turbulence intensity and Reynolds shear stress profiles show an enhanced peak near the interface for the jet-in-coflow cases. Further, conditional statistics were extracted by detecting the interface between the jet and the surroundings, wherein the same trends are observed. The low turbulence levels of the coflow have little effect on the jet/coflow interface, as seen by the conditional enstrophy diffusion and tortuosity compared to a turbulent free jet. The differences at the jet/coflow interface of a jet-in-coflow with respect to a turbulent free jet are attributed to the boundary layer initially developed by the turbulent coflow over the pipe generating the jet, and these are seen throughout the near-to-intermediate field ($0 \leq x/D \leq 40$).

5.1. INTRODUCTION

The turbulent-jet-in-turbulent-coflow is a configuration in which a turbulent jet is surrounded by a turbulent coflow. Studying the flow physics can help in understanding the nature of mixing between the two streams. This finds application in combustion devices, such as those used to create Flameless/MILD combustion conditions for low NO_x emission production. The Delft Jet in hot coflow [52] and Cabra flame [101] are examples where this configuration is used with a coflow ratio (ratio of coflow velocity, U_{coflow} , to jet bulk velocity at nozzle exit, U_{jet}) of ≈ 0.14 and ≈ 0.04 respectively. The interaction between the jet and coflow in the near-to-intermediate field determines the combustion regime downstream due to the resulting gas mixtures formed. Understanding the influence of the coflow on the evolution of the jet can improve understanding of the flame stabilization mechanism and provide parametric guidelines for engineers designing combustion systems working on similar principles.

The development of a free jet may be divided between the near ($0 \leq x/D \leq 7$), intermediate, and far-field ($x/D \geq 70$). In practical systems, most of the interactive phenomenon occurs in the near-to-intermediate field ($0 \leq x/D \leq 30$) where the upstream conditions can have an influence [102]. The profiles of various order statistics achieve self-similarity in the far field. [103] made hot-wire measurements of a turbulent jet from the near to far field, providing data on mean velocities, second and third-order single-point correlations, energy balances, and length scales. The mean velocity achieved self-similarity at an earlier axial location than other turbulence statistics, and overall self-similarity of properties occurred at $x/D > 70$. [104] measured the velocity field of a turbulent jet using hot wire anemometry and [105] did similar measurements using hot wire anemometry and laser doppler anemometry (LDA). The data was further used to evaluate transport budgets of Reynolds stress, mean kinetic energy, and turbulent kinetic energy. These are one of the many pioneering datasets on turbulent free jets that led to the characterization of this configuration. [106] compared a jet produced from a contraction nozzle and that from a long pipe with a fully developed turbulent pipe flow, both at Reynolds number ≈ 86000 , to study the effects of initial conditions. The contraction jet developed self-similarity faster than the pipe jet. The pipe jet had a thicker shear layer and higher turbulence intensity. This was seen to disrupt the streamwise vortex formation and pairing, which is typically associated with enhancing entrainment.

While a free jet flows into a quiescent surrounding, the presence of a turbulent coflow may influence the evolution of the turbulent jet through interactions at the interface. Several studies have also been performed on turbulent jet-in-coflow. [107] showed hot-wire measurements in a jet in coflow for $U_{\text{coflow}}/U_{\text{jet}} = 0.22, 0.33$. Based on the results, the authors concluded that self-similarity may not exist for this configuration and that the flow far downstream would still be affected by the initial conditions and not simply be a function of local conditions. [108] measured the jet in coflow by hot-wire anemometry for $U_{\text{coflow}}/U_{\text{jet}} = 0.045, 0.09, 0.33$. The mean flow and stresses were further analyzed such that a similarity was drawn with a double roller vortex model. It must be noted here that in both the aforementioned studies, the free stream turbulence was kept low, 0.1% [107] and 0.6% [108] respectively. [109] introduced the theory on entrainment wherein the entrainment is directly proportional to the excess axial velocity. [110] presented a modification to the entrainment function to account for the jet-in-coflow as

a weaker jet due to the reduction in excess velocity by allowing an ambient mean axial velocity. [111] measured the flow field using PIV and LIF to obtain velocity vectors and concentration fields in the first 15D of the jet to study its development under the influence of a coflow for $0.05 < U_{\text{coflow}}/U_{\text{jet}} < 0.5$. A higher coflow ratio resulted in slow decay of jet velocity and resulted in the virtual origin shifting upstream of the nozzle in several cases. The potential core length while affected to a lesser degree, was found to be shortened under a strong coflow environment. [112] measured scalar concentration and velocity field in a turbulent jet-in-coflow using LIF and LDA, respectively. They obtained mean field radial profiles and instantaneous cross-sections of the jet. [113] provided data on the effective jet spreading rate and centreline velocity obtained by Large Eddy Simulation of a jet-in-coflow with a coflow ratio of 0.09. The data showed that the turbulence intensity distribution at the orifice does not significantly affect the virtual origin or the axial spread of the jet. The turbulence intensity of the coflow is a critical parameter that might influence the evolution of the jet in coflow system. [114] have performed a systematic study to understand the effect of low and high turbulence intensity in the coflow on the jet in the intermediate-to-far-field ($45 \leq x/D \leq 95$), where the turbulence intensities were 3.2 and 7% and the coflow ratios, $U_{\text{coflow}}/U_{\text{jet}}$, effectively used were between 0.058 and 0.0344. Conclusions from their results show that coflow turbulence increases jet spreading and entrainment rates; however, the relative turbulence of the coflow is very low compared to the jet at these locations ($\approx O(0.01)$). Further, the variances in velocity are also seen to increase. [115] measured the properties of a plane jet ($Re=1200$) in the presence of a shallow coflow in a water tunnel. The background turbulence was varied by placing a series of submerged walls perpendicular to the direction of the flow. Higher background turbulence caused an increased rate of velocity decay. In the near field, background turbulence, at levels large enough to disrupt the jet structure, decreased dilution as the turbulent diffusion transport was less than the jet-induced entrainment. At higher turbulence levels, jet width growth reached that of jet-induced entrainment; however, the reduction in excess jet velocity due to jet structure disruption resulted in lower dilution. In the far-field, the dilution increased with background turbulence.

Researchers have studied the effect of background turbulence with zero mean flow on a jet. [116] studied the influence of homogeneous isotropic turbulence in the background produced by a random jet array on a turbulent jet ($Re=10600, 5800, 5300$). Velocity measurements showed that background turbulence reduced the mean axial velocity and enhanced the decay rate. Further, the radial profiles of velocity are no longer self-similar. [117] performed PLIF measurements to observe the dispersion of a passive scalar in the same configuration ($Re=10600, 5800$). The results showed a distinct behaviour when the turbulence ratio between the surroundings and the jet was greater than 0.5. This condition was achieved for the lower Re jet of 5800, wherein the downstream region, the half-width stopped growing, indicating a lack of entrainment. The shear layer was found to be preserved before the jet breakup region, as evidenced by the maintained Gaussian shape of the concentration profiles.

The entrainment of surrounding fluid in a turbulent jet is governed by the activity at the Turbulent/Non-Turbulent Interface (TNTI). This was postulated by [118] and has been investigated in detail over the years. The TNTI is characterized by a marked

jump in quantities such as mean axial velocity, vorticity and enstrophy from the rotational surroundings to the turbulent jet [119][120]. Entrainment can occur through either small-scale 'nibbling' or large-scale 'engulfment'. [119] showed that although both mechanisms occur and are responsible for mixing, 'nibbling' is more dominant. [121], on the other hand, demonstrate that the net entrainment is scale-independent. The coherent vorticity region comprises of Large-scale Vorticity Structures (LVS) produced by the mean shear at the interface and the Intense Vorticity Structures (IVS) produced by the background turbulent fluctuations[122]. The TNTI thickness is governed by the LVS [123] and is of the order of the Taylor microscale (λ) in turbulent jets [119][124]. The TNTI is also theorized to be a thin region consisting of a Viscous Superlayer (VSL) and a Turbulent Sublayer (TSL)[125]. The VSL is adjacent to the quiescent surroundings and governs the entrainment by viscous diffusion as evidenced by the significantly larger value of the enstrophy viscous diffusion transport over the turbulence production (vortex stretching) term, observed in DNS data [126]. This layer has been shown to be of a thickness $\approx 5\eta$ [127]. The TSL is adjacent to the turbulent core and is where the vorticity profile matching between the VSL and turbulent core occurs [125].

5

For a long time, the general consensus was that for rising background turbulence, there would be a limit beyond which an interface, consisting of a vorticity jump, would no longer exist[125]. [128] showed the existence of a Turbulent/Turbulent interface (TTI) through measurement in a turbulent wake with turbulent background flow. Increasing background turbulence lead to higher convolution of the interface. Unlike the TNTI, the TTI has a very low value of viscous diffusion of enstrophy compared to the inertial vorticity stretching term, indicating that, in this case, entrainment is not constrained by diffusion [129]. [130] show that large-scale eddy effects affect the entrainment in the near-wake and postulate that scale matching of background turbulence to wake influences the effectiveness of the turbulence on manipulating the entrainment.

Several researchers have used interface detection to determine conditional statistics to study the Turbulent/Non-Turbulent interface of a free jet. This reduces the effect of smearing of statistics due to the spatial fluctuation of the interface in the ground frame. [119] used Laser Induced Fluorescence (LIF) to detect the dispersion of a dye to identify the interface by thresholding the intensity of the LIF signal obtained from this passive scalar. Conditional velocity statistics were obtained by sampling velocity vectors, obtained from PIV, with respect to this interface. [117] and [131] similarly detected the TTI for a jet with a homogeneous turbulent surrounding with zero velocity. On the other hand, [128] used a gradient of the LIF signal intensity and determined the edge of a turbulent wake in turbulent surroundings by identifying a contour of a given threshold value. They studied the interaction of a turbulent wake behind a cylinder with a turbulent background flow and proved the existence of the turbulent-turbulent interface (TTI). The interface can also be detected based on velocity derived criteria. [132] and [133] detected the interface in DNS simulations using vorticity norm as a parameter to differentiate between the irrotational, quiescent, surroundings and the rotational turbulent jet. [134] performed 2D2C PIV in the developing region of a free jet. They use velocity as a criteria to detect the interface such that the local velocity should be 3% of the jet exit velocity. The reasoning is that only two components of velocity are measured, hence it is better to use that as a criterion rather than a vorticity vector which would require all three

components. [127] performed high resolution 2D2C PIV measurements of a turbulent mixing layer and used vorticity as a criteria to determine the TNTI. [135] compared different criteria for the detection of turbulent fluids from intermittent flows, in a turbulent boundary layer. Although they use three components of the vorticity vector for detection from their DNS, they acknowledge that in the case of experiments, often, obtaining all components is difficult. Thus, they compare the 3 component vorticity magnitude, the out-of-plane vorticity magnitude, local turbulent kinetic energy, and a passive scalar as detector functions. They find that with the turbulent kinetic energy function, the isosurface of the edge is very different from the others. Further, the conditional vorticity across the interface does not have as strong of a jump in the profile.

In a jet-in-coflow, the coflow can have two effects: the first is due to the boundary layer it forms upstream over the exterior of the jet pipe, which interacts with the shear layer downstream of the nozzle exit; the second is the turbulent fluctuations in the coflow which convert the TNTI to a TTI. The aforementioned body of literature had a gap in studies with comprehensive 2D velocity measurements ranging from the near field to the intermediate field of the turbulent jet in turbulent coflow and a direct comparison to a free jet. It is especially interesting to see if this configuration, when scaled appropriately as an effective free jet, yields statistical profiles similar to those of a turbulent free jet. There is also a lack of data and analysis of velocity-based quantities conditioned to the interface between a turbulent jet and turbulent coflow, leaving much to be known on the effects of a turbulent coflow on the evolution of a turbulent jet.

The current study looks at the phenomenological effects of a turbulent coflow on a turbulent jet by varying the coflow conditions from zero velocity (free jet) to higher coflow ratios. The flow field was measured using planar PIV ranging from the near-to-intermediate field ($0 < x/D < 42$) in a non-reacting air-air jet-in-coflow. The quantities are scaled taking into account the coflow to express the jet-in-coflow as an equivalent free jet and then analyzed for any differences. These differences should originate from the presence of turbulence in the coflow and the boundary layer formed by the coflow over the jet pipe. These observations are verified and explained by analyzing conditional statistics evaluated along the interface between the jet and the surroundings. To the authors' best knowledge, this is the first study that extracts conditional velocity statistics for a turbulent jet-in-coflow entirely from PIV data. This knowledge allows us to better understand the evolution of the flow field along the axis of a turbulent-jet-in-turbulent-coflow thereby enabling a more accurate prediction of this configuration for engineering design.

5.2. EXPERIMENT

5.2.1. EXPERIMENTAL SETUP

An experiment was set up to measure velocities in a turbulent-jet-in-turbulent-coflow by 2D2C Particle Imaging Velocimetry (PIV), as shown in Fig 5.1. The jet was generated by passing compressed air through a pipe about 3 m long with an inner diameter (D) of 11 mm and a wall thickness of 0.5 mm. This ensured that the jet had a fully developed pipe flow at the nozzle exit. The flow rate was controlled by a Bronkhorst EL-FLOW massflow controller with a range of 10-500 lpm and accuracy of +/- 0.5% of reading plus +/-0.1%

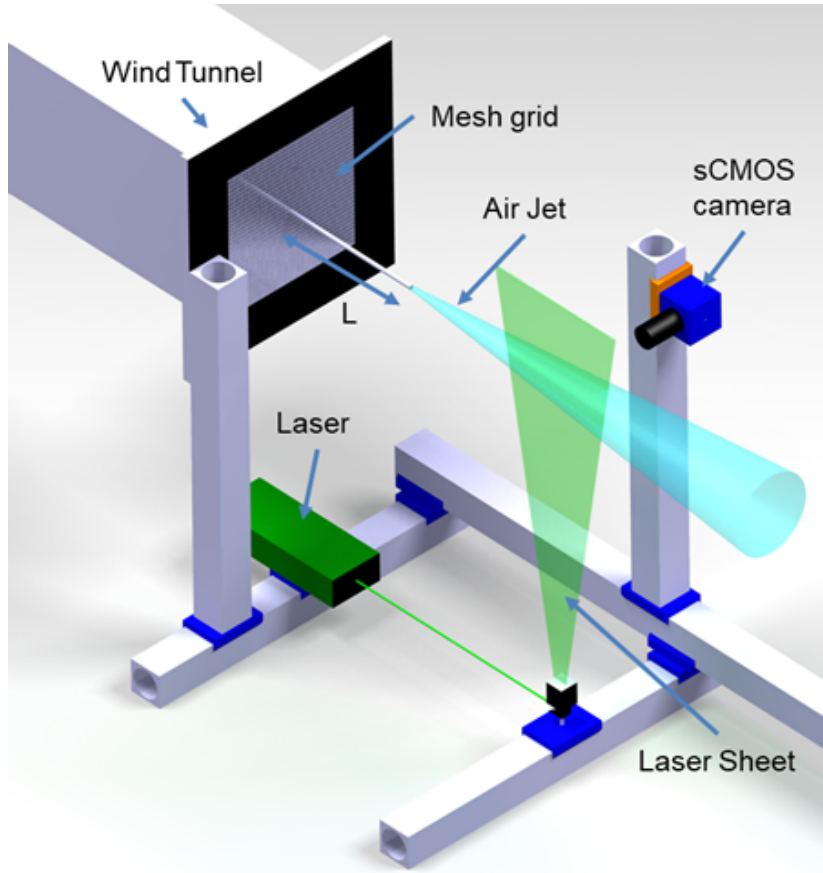


Figure 5.1: Schematic of experiment

of full scale. The coflow was produced by an open circuit low-speed wind tunnel. The jet pipe was coaxially positioned along the axis of the wind tunnel and was supported by a structure in the settling chamber and a strut closer to the exit. A wire mesh grid made of 0.5 mm diameter wires, forming square slots of 12x12 mm, was used at the tunnel exit. It served the purpose of breaking up any flow structures emanating due to the upstream support structures as well as introducing homogeneous turbulence in the coflow.

Both streams of air were seeded with particles of 1 μm diameter for PIV measurements. The coflow was seeded with a SAFEX fog generator placed near the suction side of the fan of the wind tunnel. The jet was seeded by bypassing a portion of the air through a PIVTEC aerosol generator containing DEHS oil and a manual ball valve was placed in the non-seeded branch to provide resistance to the flow to control the amount of air passing through the seeder. The PIV setup consisted of an Evergreen 200mJ laser at 532 nm and a LaVision sCMOS camera with 6.5 μm pixel size, with an acquisition frequency of 10Hz. The laser sheet was created such that a maximum of 1mm thickness was maintained in the region of interest. The camera and laser sheet locations were shifted to image differ-

Table 5.1: PIV Experiment Conditions

Field of View	100 mm
Laser sheet thickness	1 mm
dt	1 μ s
Pixel size	6.5 μ m
Interrogation window size in final pass	24x24 pixel
Window overlap in final pass	75%
Vector Spacing (mm)	0.16 ($x/D < 26$), 0.35 ($26 < x/D < 40$)

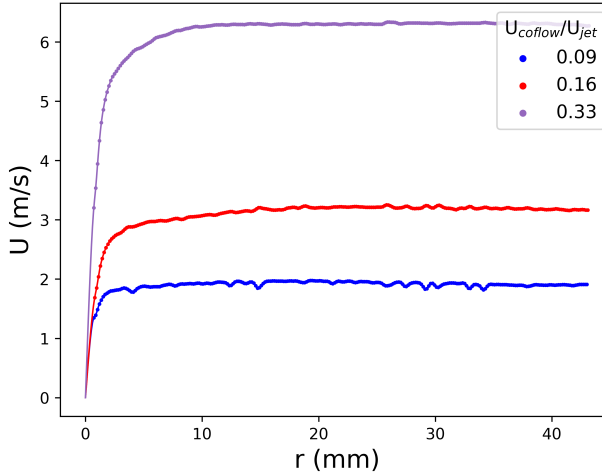


Figure 5.2: Boundary Layer profile around pipe extracted from PIV measurements.

ent axial sections of the jet. Measurements were done for axial locations varying from $0D$ to $35D$, where D is the inner diameter of the nozzle, while each frame spans about $5D$. The laser sheet and pipe nozzle were carefully aligned with the central axis of the wind tunnel by using a construction laser marker.

The experiments were conducted for 4 cases, one free jet (i.e., no coflow so the wind tunnel was idle) and coflow velocities of 1.9, 3.2, and 6.3 m/s, adjusted by the wind tunnel set point. During the measurements, it was ensured that the jet, coflow, and quiescent surroundings were uniformly seeded. PIV processing was done in DaVis 8.4. Interrogation windows of 24×24 pixel with 75% overlap in the final pass were used for the PIV correlation. This results in a vector spacing, Δx , of 0.16 mm, which was maintained for $x/D < 26$ and $\Delta x = 0.35$ mm for $26 < x/D < 40$. The ratio of PIV window size to local jet halfwidth at different axial locations along the jet is always less than 0.15, indicating that the window is small compared to the characteristic length of the flow, thereby ensuring a sufficient number of vectors for analysis. The Kolmogorov length scale (η) is approximated as $\eta = (\frac{\nu}{\epsilon})^{0.25}$, where ν is the kinematic viscosity of the fluid and ϵ is the dissipation rate. The value of ϵ is calculated from, $\epsilon = 0.015 \frac{(U_c - U_{\text{coflow}})^3}{b_u}$, where U_c is the local jet cen-

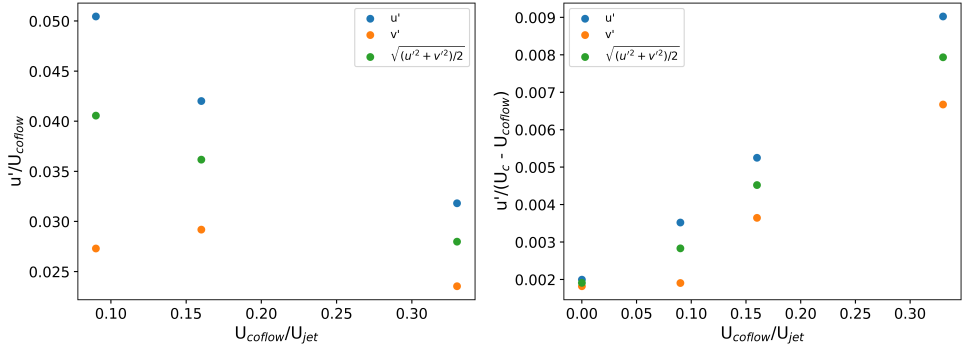


Figure 5.3: Velocity RMS vs Coflow ratio scaled to Figure 5.4: Velocity RMS vs Coflow ratio scaled to relative jet velocity

5

terline velocity, b_u is the local jet half-width and U_{coflow} is the coflow velocity. This is a modified form of $\epsilon = 0.015 \frac{(U_c)^3}{b_u}$ as suggested by [104] for a freejet. As U_c , U_{coflow} and b_u vary along the axis of the jet the exact value of the Kolmogorov length scale also varies. The values estimated for each coflow ratio case at the jet exit are listed in Table 5.2. In general, the vector spacing (Δx) achieved is such that $\Delta x < 10\eta$ and beyond $x/D > 15$, $\Delta x < 6\eta$. The detailed conditional statistics are analyzed in the region $20 < x/D < 25$ where $\Delta x \leq 3\eta$.

5.2.2. FLOW CONDITIONS

We investigated different coflow velocity conditions while keeping a constant jet exit bulk velocity, $U_{\text{jet}} = 20$ m/s, by maintaining a constant mass flow rate of air using the flow controller. This ensured that the jet Reynolds number based on bulk velocity and nozzle diameter remained constant ($Re = 14000$), between different cases. The cases were characterized using the concept of momentum radius (θ_{coflow}), which may be defined as the equivalent radius required of a stream flowing at the velocity of the coflow to have the same momentum as the jet. Thus, for lower coflow velocity, a larger radius is required. It is defined as:

$$\theta_{\text{coflow}} = \sqrt{\frac{J_0}{\pi \rho U_{\text{coflow}}^2}}, \quad (5.1)$$

$$J_0 = \frac{\pi}{4} D^2 \rho_0 U_{\text{jet}}^2,$$

where U_{coflow} is the coflow velocity, U_{jet} is the bulk jet exit velocity, D is the nozzle diameter, and J_0 is the source momentum flux. This definition has been used in the literature on free jets. [136] define a ratio x/θ_{coflow} , where x is the distance along the jet axis, such that for values of $x/\theta_{\text{coflow}} \leq 2$ the flow can be considered to be negligibly affected by the coflow and hence be treated as a free turbulent jet. Thus, a higher coflow ratio results in an earlier transition to an effective jet-in-coflow along the jet axis, listed as x/D_{trans} in Table 5.2. It should be noted that this threshold is an approximation as is seen in the case of [137] where at $x/D = 32$ a value of $x/\theta_{\text{coflow}} = 3$ was still considered a free jet.

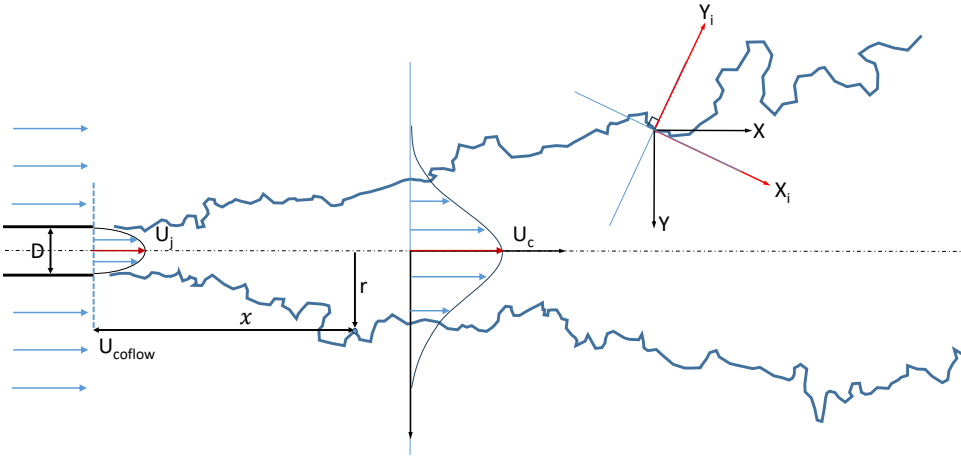


Figure 5.5: Representative sketch of the flow configuration. X_i, Y_i is the transformed coordinate system in the frame of the local interface.

Table 5.2: Coflow conditions of operation

U_{coflow} (m/s)	U_{jet} (m/s)	U_{coflow}/U_{jet}	x/D_{trans}	Re_d	η (μm)
0	20	0	∞	0	41.94
1.9	20	0.09	10	63	45.19
3.2	20	0.16	5.5	107	47.79
6.3	20	0.33	3	210	55.69

The coflow forms a boundary layer over the exterior of the central jet pipe. This is characterised by extracting the axial velocity profile at the first station closest to the nozzle exit from the PIV data. As this is not measured over the wall of the pipe but downstream where the wall just ends, the velocity measured does not achieve an absolute zero value. However, for the sake of characterization, all the coflow conditions are measured in the same way, hence a good comparison can be obtained. The boundary layer properties (displacement thickness (δ^*), momentum thickness (θ) and shape factor (H)), tabulated in Table 5.3, are calculated by fitting a cubic spline to the measured points and extrapolating it to the point where zero velocity is achieved, as shown in Fig 5.2. The Reynolds number based on momentum-thickness (Re_θ), tabulated in Table 5.3, increases with increasing coflow ratio.

The turbulence level of the coflow is also expected to influence the evolution of the flow field. Turbulence in the coflow was enhanced by a grid composed of cylindrical elements. For the given set of coflow conditions, the Re_d , where d is the diameter of the rod of the mesh grid on the coflow outlet, ranges from 63 to 210, as listed in Table 5.2. As mentioned by [138], vortex shedding for a cylinder is stable and laminar for $40 < Re < 150$ and transitions to turbulent between $150 < Re < 300$. Thus, in the current study, there is vortex shedding under both stable and transitioning regimes depending on the case.

Table 5.3: Coflow conditions of operation (Boundary Layer)

U_{coflow} (m/s)	δ^* (mm)	θ (mm)	Re_θ	H
0	-	-	-	-
1.9	2.55	1.78	235	1.43
3.2	4.48	3.2	693	1.40
6.3	2.93	1.82	769	1.61

According to the design recommendation of [139], after a distance $x/M > 10$, where M is the spacing between adjacent grid elements, well-developed turbulence behind a grid is obtained where the statistics are driven by dissipation and the turbulence intensity decays as a power law. However, a distance of the order of $x/M=50-100$ is required to achieve acceptable homogeneity and isotropy[140]. Thus, a trade-off is made to achieve a significant level of turbulence intensity in the region of interest and the distance of the pipe exit from the grid plane, L , is set such that $L > 120$ mm (shown in Fig 5.1).

The turbulence intensities of the coflow in the current study are shown in Fig 5.3, and the total magnitude is between 3-4%, with a slight decrease with coflow ratio. However, when the velocity fluctuations are scaled by the jet excess velocity ($U_c - U_{coflow}$), as shown in Fig 5.4, there is a clear increase in turbulence intensity with coflow ratio. This indicates that the jet perceives the coflow fluctuations as effectively increasing with coflow velocity.

5.2.3. INTERFACE DETECTION

The interface is defined as a thin region separating the high turbulence region (jet interior) from the low turbulence region (surrounding coflow). For a turbulent free jet, this has been shown through DNS studies to be well represented by a surface of thresholded vorticity or a passive scalar [133][123][141]. In most experimental studies, interface detection is done by introducing a dye (as a scalar) in one of the streams and the interface is said to be located at a certain defined dye concentration limit as detected by PLIF [119][128][121][120]. In this work, interface detection is done purely through the vector field due to the high resolution as also done by [127]. The criterion used for detection is vorticity magnitude ($|\Omega|$) based on the assumption that it is higher within the turbulent jet than in the turbulent coflow and quiescent surroundings. The quantity is calculated for an instantaneous vector field, where the gradients are evaluated after processing with a 2D Savitsky-Golay filter with a window size of 5x5 and a 2nd order polynomial of the form:

$$z = a_0 + a_1x + a_2y + a_3xy + a_4x^2 + a_5y^2 \quad (5.2)$$

, where x and y are the distances with respect to the center point of the window. Thus, the filtered value of 'z' is a_0 at $x=y=0$, and the derivatives with respect to x and y are the coefficients a_1 and a_2 , respectively. This filter provides the advantage of noise reduction while retaining the relevant flow features. A detailed analysis of the sensitivity to window size is derived by [142], where it is shown that spatial frequency response of the PIV cross-correlation and Savitsky-Golay regression are similar and, therefore, the noise reduction does not lead to spatial resolution loss. Finally, the value is normalized as

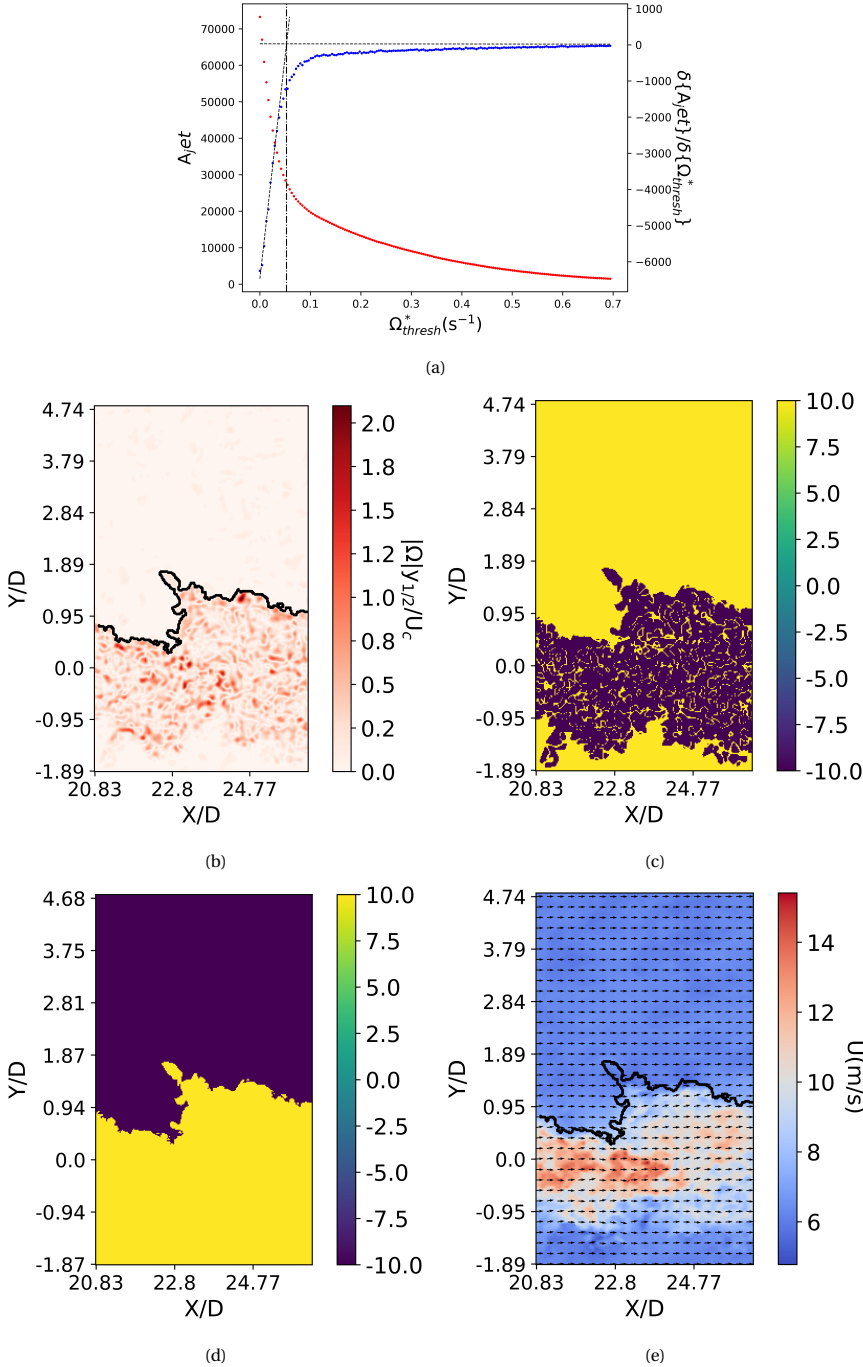


Figure 5.6: Interface detection methodology demonstrated on an instantaneous image of $U_{coflow}/U_{jet}=0.33$
 (a) Area method demonstrated by the area detected within the turbulent jet, A_{jet} (red points), for varying threshold values (Ω_{thresh}^*) and the corresponding derivative curve (blue points). (b) Instantaneous interface overlaid on vorticity contour. (c) First DBSCAN clustering. (d) Second DBSCAN clustering. (e) Instantaneous interface overlaid on axial velocity contour along with velocity vectors.

$\Omega^* = |\Omega|y_{1/2}(x)/(U_c(x))$, where $y_{1/2}(x)$ is the jet half-width and $U_c(x)$ is the axial velocity at the centerline at a given x distance from the nozzle. This is done locally, by taking the normalization values from the unconditioned average for each axial location.

A threshold value for the normalized vorticity (Ω_{thresh}^*) is used to distinguish the region within the jet from the surroundings which is determined using a method similar to [127], which in turn is based on threshold determination methods proposed by [121] and [143]. As the surroundings have a low/moderate level of turbulence, the higher level of vorticity within the jet should be distinguishable. This is done by plotting the area in the image (A_{jet} , in pixels) above a certain threshold, which is effectively the area within the turbulent jet, against varying threshold values (Ω_{thresh}^*). This results in a monotonically decreasing curve, shown in Fig 5.6a that finally reaches a constant value. The derivative of this curve is taken, where there is an initial rising part, and it ends with a nearly zero value. Two lines are fit to these regions (Fig 5.6a), and their intersection location is used as the threshold value. Applying this thresholding process results in several disjointed regions, as can be seen by the vorticity contours in Fig 5.6b; however, to obtain a continuous interface, the most intense vorticity regions need to be clustered together.

The Density Based Spatial Clustering for Applications with Noise (DBSCAN) [144] algorithm is applied to the thresholded data to determine clusters. It is an image-processing algorithm that clusters closely spaced points and marks outliers that lie separated in low-density regions as noise. The algorithm takes two input parameters, epsilon, which is the distance of search from a point for neighbors, and Minpts, which is the minimum number of points that should lie within a radius of epsilon from a point to classify it as a core point. The value of epsilon and Minpts were fixed to 3 and 20, respectively. The values were selected based on a manual sensitivity analysis. The values imply that within a radial distance of epsilon=3 pixels at least Minpts=20 pixels should be found in the thresholded image for the point to be considered to be part of a cluster. This means that in a 7x7 pixel square (area=49 pixels), 20 pixels should be found, i.e ~41% filled. This was found to provide a good balance between identifying filled points and leaving enough distance to exclude islands/ noise points. Small variations of these values did not impact the edge detection significantly. This results in the detection of the most intense vorticity structures. The clustering algorithm is applied in the following steps:

1. DBSCAN algorithm is applied on the thresholded image such that only pixels above a threshold are considered for the clustering process.
2. The largest cluster is chosen
3. Image is binarized by setting the value of the pixels of the largest cluster to 10 and the remaining pixels to -10.
4. The binarized image is inverted such that the largest cluster pixels now have a value of -10

The first clustering step is applied to the image thresholded by the value of $|\Omega|y_{1/2}(x)/(U_c(x))$ obtained from the area method, resulting in an image such as Fig 5.6c. The clustering algorithm is applied a second time on the resulting image thresholded by zero, such that only pixels with positive values are considered. This results in an image such as Fig 5.6d.

Finally, the interface is identified as the edge of the region with a positive value, using contour detection in OpenCV [145], which is overlaid on the vorticity field in Fig 5.6b and on the axial velocity contour in Fig 5.6e.

Statistics are collected in a relative coordinate frame oriented perpendicular to the local edge. The slope of the edge is obtained by fitting a 3rd order polynomial in a region of 5 edge points around the point of interest. The velocity in the conditional frame is obtained by projecting the ground frame velocity vector in the rotated coordinate system. Thus, the "axial component" in the rotated frame is parallel to the interface and the "radial component" is perpendicular to the interface as shown in Fig 5.5.

5.3. RESULTS

5.3.1. MEAN FIELD

The jet was imaged at different axial locations in the near and intermediate field (up to $x/D = 42$). We first explore the overall evolution by tabulating the average axial velocity field in Fig 5.7. The images are presented as U/U_j , where U_j is the velocity at the centerline at the jet exit, which is kept constant across all cases of varying coflow. Thus, it can be seen that cases with a higher coflow ratio have a higher coflow velocity. At first glance, it seems that the free jet decays faster in the streamwise direction and has a larger width compared to cases with higher coflow. The turbulence intensity distribution is shown in Fig 5.8. The qualitative evolution is as expected, where high turbulent fluctuations originate in the shear layers starting close to the nozzle exit and the region of turbulent fluctuations expands radially as the jet evolves further downstream. The turbulence intensity is higher further downstream in all cases, due to mean axial velocity decay at a rate that is faster than turbulence fluctuation dissipation along the axis. Also, it can be seen that an increase in the coflow ratio results in a higher turbulence intensity, especially for $19.6 < x/D < 40$.

The jet centerline axial mean velocity is shown in Fig 5.9a. In the self-similar region, the axial velocity decays as

$$\frac{U_j}{U_c(x)} = \frac{1}{b} \left(\frac{x}{D} - \frac{x_0}{D} \right) \quad (5.3)$$

where $U_c(x)$ is the jet centerline velocity at axial location x , b is the decay constant and x_0 is the virtual origin. Typically, this linear fit is done for $x/D > 15$. The velocity decays along the axis, as is expected for a round turbulent jet, where the value of $b = 5.30$ (Table 5.4), which is comparable to 5.6 from [106]. One can notice that the decay line deviates from a linear fit as the coflow ratio increases. To correct this and represent the case as a free jet relative to the coflow, appropriate scaling of $\frac{U_j - U_{coflow}(x)}{U_c(x) - U_{coflow}(x)}$ is applied, where $U_{coflow}(x)$ is the coflow axial velocity at that axial location. This results in scaled decay constant and virtual origin represented as b^* and x_0^* , respectively. The scaled jet decay profiles are re-linearized as seen in Fig 5.9b; however, the slopes are still different, as listed in Table 5.4. The maximum value of the decay constant, b , is 21.21 and after scaling b^* is 6.59 for the highest coflow case. The virtual origin location, x_0/D is negative for non-zero coflow, indicating a location behind the nozzle exit, and after scaling, $x_0^*/D = 3.16$ for the free jet and reduces to 2.06 for the case with the highest coflow. In

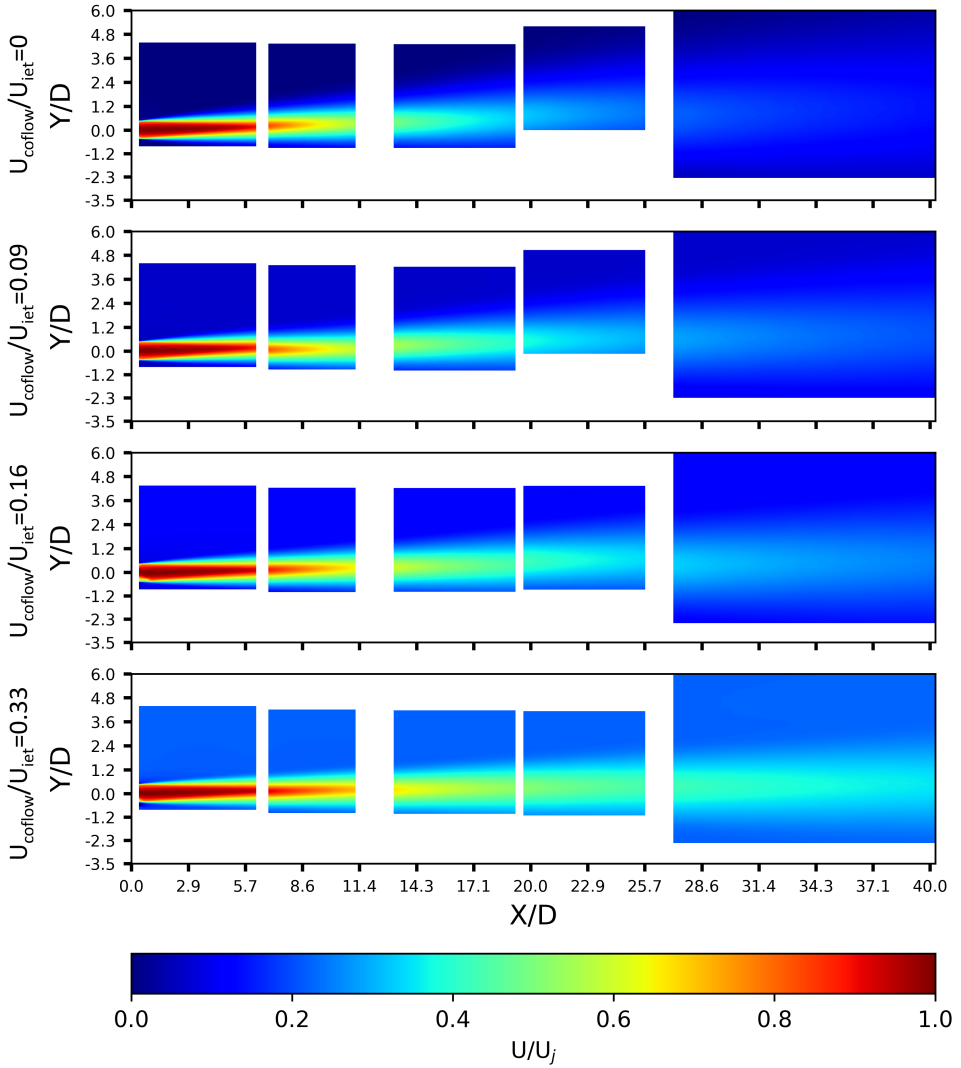


Figure 5.7: Axial velocity distribution over the measured domain, compared across cases of varying coflow ratio.

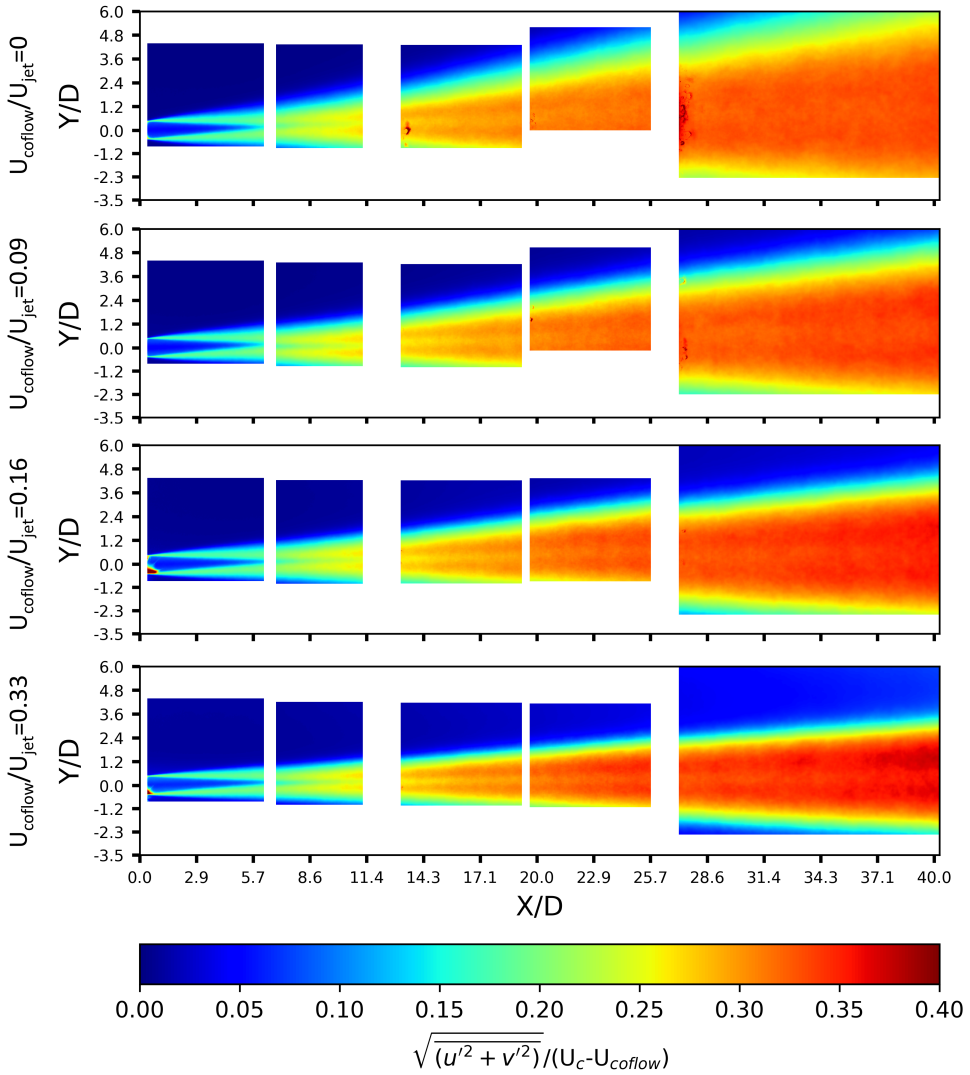


Figure 5.8: Turbulence intensity distribution over the measured domain, compared across cases of varying coflow ratio.

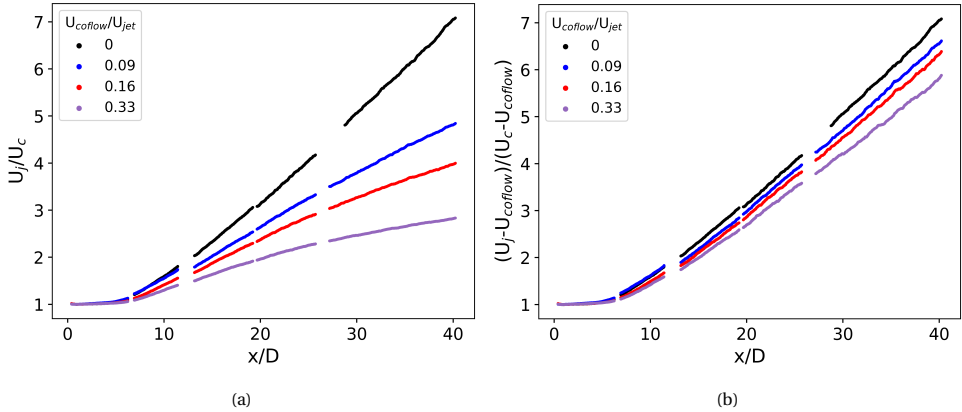


Figure 5.9: Jet centerline velocity decay expressed as (a) U_j/U_c (b) $(U_j - U_{c}) / (U_c - U_{c})$

5

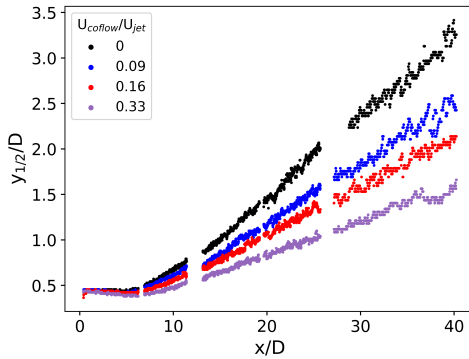


Figure 5.10: Jet half width ($y_{1/2}$) v/s x/D

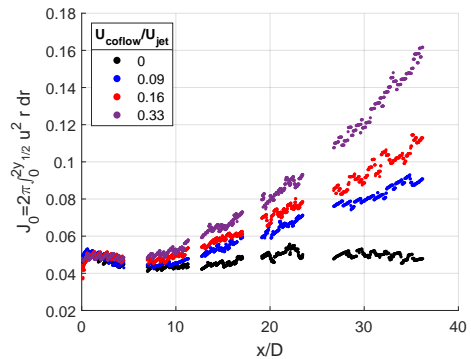


Figure 5.11: Jet momentum (J_0) v/s x/D

comparison, [106] obtained a value of 3.7 for a free jet. It must be noted that cases with a higher coflow ratio have higher turbulence when scaled with the relative velocity of the jet to the coflow, which seems to influence the velocity decay rate. Further, the establishment of linearity with scaling shows its importance to correctly represent the jet in coflow as a 'slower moving jet' in the frame of reference of the coflow and comparing it to a free jet.

The evolution of the half-width, $y_{1/2}$, is shown in Fig 5.10, where the half-width for a free jet is defined as the distance from the centerline to the radial location where the axial velocity is half that of the local centerline axial velocity. The mean spread rate (A) of $y_{1/2}$ beyond $x/D > 15$ is given by

$$\frac{y_{1/2}}{D} = A \frac{x}{D} - B \tag{5.4}$$

For a turbulent-jet-in-turbulent-coflow, the point is redefined to be along the radial direction where the axial velocity is the average of the maximum and coflow velocity at

Table 5.4: Jet halfwidth and spreading characteristics

$\frac{U_{\text{coflow}}}{U_{\text{jet}}}$	b	b^*	x_0/D	x_0^*/D	A	B
0	5.30	5.30	3.16	3.16	0.089	0.307
0.09	8.88	5.70	-3.50	2.92	0.066	0.127
0.16	11.81	5.92	-8.12	2.87	0.054	0.017
0.33	21.21	6.59	-21.62	2.06	0.037	-0.092

that axial station. The halfwidth remains approximately constant, with a slight decay, in the first 5D but then increases further downstream. The halfwidth of the free jet has a higher mean spread rate than the cases with a higher coflow ratio, which is also tabulated in Table 5.4. The decay constant, A, is 0.089 for the free jet and drops to 0.037 for the case with the highest coflow. In comparison, [106] obtained a value of 0.086 for a free jet.

Fig 5.11 shows jet momentum flux ($J_0 = 2\pi \int_0^{y_{1/2}} u^2 r dr$) variation along the axis. It is calculated by integrating momentum flux from the jet centerline to a radial distance twice that of the jet halfwidth. In $0 < x/D < 5$, all 4 cases of coflow ratio have almost the same momentum, which should also be the case as the same mass flow rate of the jet was maintained. As we go further downstream, the free jet maintains this level of momentum, while for increasing coflow values, the momentum increases in the downstream direction. This is caused by the additional momentum present in the coflow which is entrained by the jet.

5.3.2. RADIAL PROFILES

Radial profiles are presented at various axial distances from the jet nozzle. The radial distance is represented as a ratio of distance (r) to the local jet half width ($y_{1/2}$). The data is normalized as $\frac{U(x) - U_{\text{coflow}}(x)}{U_c(x) - U_{\text{coflow}}(x)}$ relative to the coflow such that a jet-in-coflow would represent a "slower moving" turbulent jet in a zero mean velocity, turbulent environment. This results in a value of 1 at the jet centerline and 0 in the coflow for all cases. A similar normalization has been used by [146] where they analyzed cases for $U_{\text{coflow}}/U_{\text{jet}} = 0, 0.0833, 0.166, \text{ and } 0.333$. Other works such as that by [108] and [107] also scale their data similarly. Ideally, the scaled profiles from different cases would overlap; however, the presence of a boundary layer generated by the coflow over the jet pipe and the turbulence of the coflow can lead to some differences.

The mean axial velocity profiles are shown in Fig 5.12 at $x/D = 5, 10, 22$ and 30 , for 4 different conditions of coflow velocity ratio, $U_{\text{coflow}}/U_{\text{jet}} = 0, 0.09, 0.16$ and 0.33 . The profiles show a significant overlap between the different cases; however, a difference is seen at the interface between the jet and coflow ($r/y_{1/2} = 2$), in the form of a separation of profiles for the different coflow ratios. For cases with higher coflow ratios, the profile decreases faster in the radial direction leading to region of "velocity deficit" compared to the free jet.

The normalized axial turbulence fluctuation profiles are plotted in Fig 5.13 at $x/D = 5, 10, 22, 30$. The profiles have an 'M' shape with turbulence intensity peaks around $r/y_{1/2} = \pm 0.5$. There is an intersection between the profiles of the free jet and coflowing jets located between $r/y_{1/2} \approx 1.8$ and $r/y_{1/2} \approx 2.5$, which also corresponds to the inflection

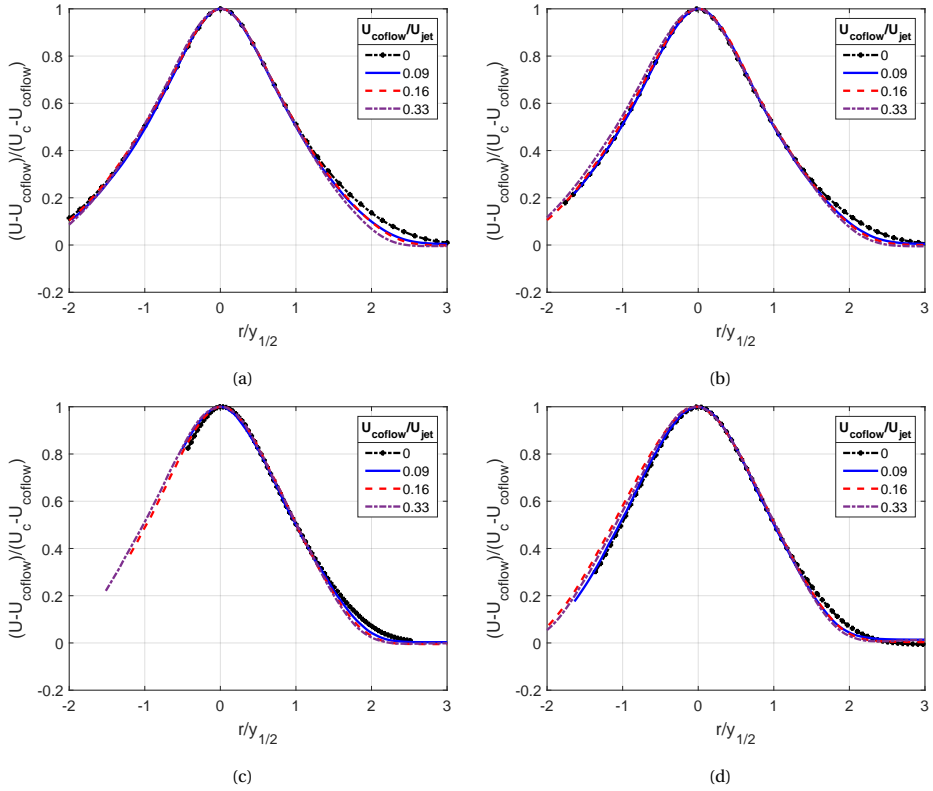


Figure 5.12: Axial velocity profile at (a) $x/D=5$, (b) $x/D=10$, (c) $x/D=22$, (d) $x/D = 30$.

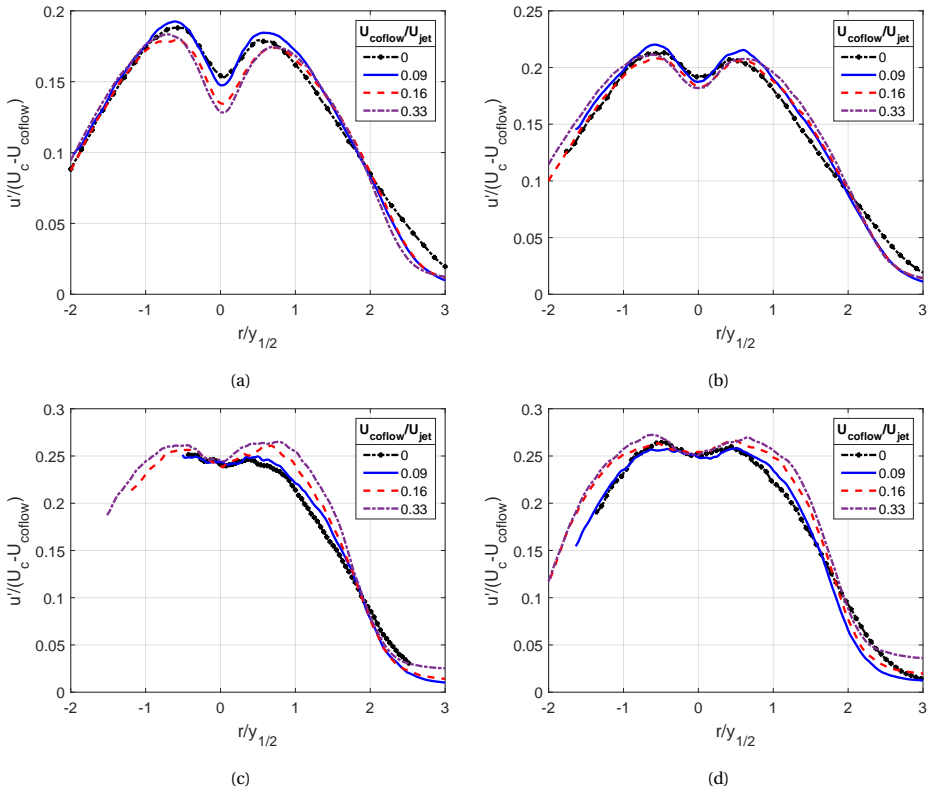


Figure 5.13: Axial turbulence intensity profile at (a) $x/D=5$, (b) $x/D=10$, (c) $x/D=22$, (d) $x/D=30$.

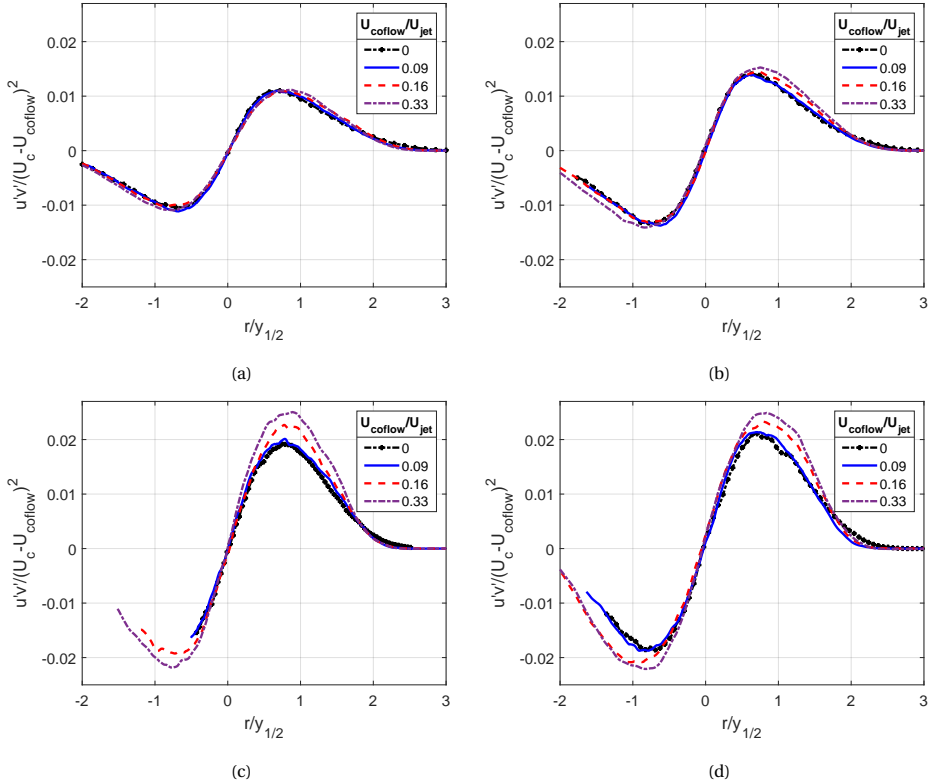


Figure 5.14: Reynolds shear stress profile at (a) $x/D=5$, (b) $x/D=10$, (c) $x/D=22$, (d) $x/D=30$.

point of the profiles. At $x/D=5$ cases with lower coflow have a higher relative turbulence intensity ($\Delta \approx 0.025$) at the centerline but this difference reduces further downstream to nearly zero. In the radial vicinity of the inflection point ($r/y_{1/2} \approx 1.8$), the coflowing jets have a higher value towards the centerline whereas in $2.25 < r/y_{1/2} < 3$, the free jet has a higher turbulence intensity. At $x/D=22$ and 30 , the trend is similar but the higher turbulence intensity of free jet is up to $r/y_{1/2}=2.5$ beyond which it starts dropping under the highest coflow ratio cases. This shows that there is a higher turbulence region for the free jet compared to a turbulent-jet-in-turbulent-coflow, which is located between the inflection point and the far surroundings. This indicates a higher propagation of turbulence from the turbulent jet to the surroundings in the case of a free jet than that of a jet-in-coflow. This is supported by higher entrainment rates for a free jet seen through faster centerline velocity decay and larger half-width seen in Section 5.3.1. Also, there is a higher turbulence intensity peak as the coflow ratio increases.

The normalized Reynolds shear stress (RSS) profiles, shown in Fig 5.14, indicate momentum transport due to turbulence. It achieves a peak in a region, $0.7 < r/y_{1/2} < 1.0$, between the turbulent jet and the turbulent coflow, and has a value of zero in the surrounding far field. The peak shifts radially outward for higher coflow ratios.

The one-point statistics reveal that the higher coflow cases exhibit a deficit in the mean axial velocity profile near the interface region with respect to the free jet. Furthermore, the turbulence intensity and Reynolds Shear Stress reach higher peak values compared to a free jet at $x/D=22$ and 30 . The velocity deficit identified in the axial velocity profiles is caused by the boundary layer over the external wall of the pipe that produces the central jet. The wake originating from this boundary layer shields the jet from the coflow, thereby reducing the amount of turbulent interaction and retaining a large velocity gradient at the interface as far as $x/D=30$. This shielding also dampens the turbulence exchange due to which the jet and coflow sides retain their respective turbulence intensity levels. As the coflow has a low turbulence intensity, this is not sufficient to disrupt the interface and enhance entrainment as was observed in higher background turbulence cases [117][115]. This leads to a larger radial gradient in the turbulence intensity profile for higher coflow velocity.

5.3.3. CONDITIONAL STATISTICS ALONG THE INTERFACE

Mean field statistics, when observed from the ground frame of reference, may lead to the smearing of gradients. Conditional statistics are assembled by sampling data at fixed locations with respect to the local interface. Therefore, they provide more accurate information about phenomena near the interface. The interface is detected using the methodology explained in Section 5.2.3. Conditional statistics are assembled by sampling points along a line perpendicular to the local interface. The slope of the tangent is determined by fitting a 3rd order polynomial in a region of 5 points along the detected interface around the point of interest. The points along the perpendicular are equispaced and the velocity data at these points are obtained by bilinear interpolation of the underlying original PIV data. Finally, the vectors are projected onto the rotated local frame of reference of the interface such that the conditional axial velocity is tangent to the interface and conditional radial velocity is perpendicular to the interface. The conditional data is presented in Fig 5.15 where the turbulent jet interior is at the negative x-axis location and the coflow/surroundings are located at the positive x-axis locations. To improve statistical conversion, samples are collected over a window, 20 vectors wide, along the frame centered at the point of interest on the interface.

The conditional axial velocity, shown in Fig 5.15a, shows that the cases with coflow have a visible velocity deficit close to the interface compared to the free jet. However, the profiles of the three cases with coflow collapse over each other and deviate towards the centerline. The deficit region clearly shows the influence of the boundary layer, originally generated over the external surface of the jet pipe by the coflow, in the vicinity of the interface, creating a larger velocity jump across the interface than a free turbulent jet ($U_{\text{coflow}}/U_{\text{jet}=0}$).

Enstrophy is an indicator of small-scale turbulence activity, and there is a strong jump of enstrophy across the interface of a free jet [119]. The conditional enstrophy profile in Fig 5.15b captures this jump across the interface, validating the interface detection based on vorticity. While the profiles collapse over each other in the coflow region, the cases of higher coflow show a higher enstrophy within the jet. This shows a higher level of small-scale turbulence. Evidence of large-scale turbulent activity is seen in Fig 5.15c, through a higher peak for a higher coflow ratio, around the interface. This also corre-

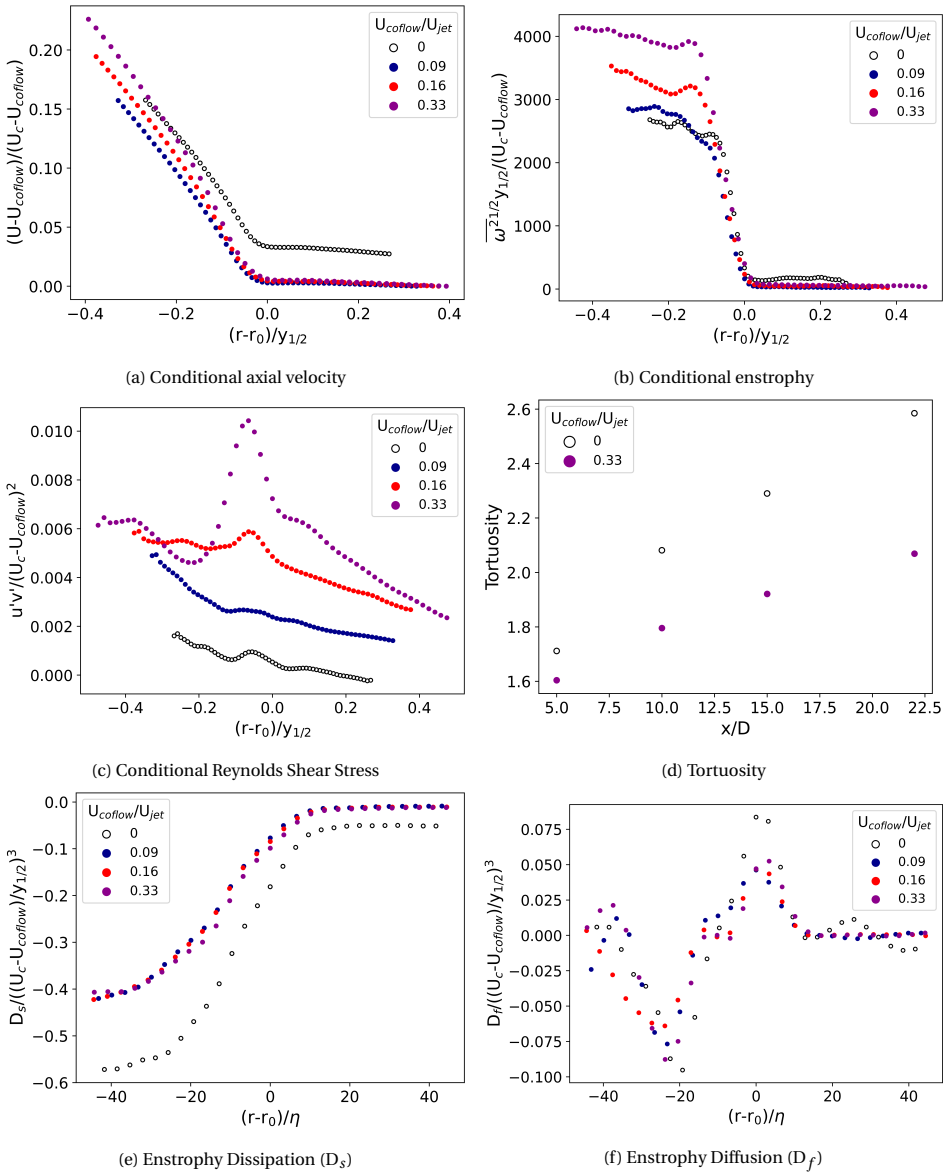


Figure 5.15: Conditional radial profiles at $x/D=22$ (a,b,c,e,f). Tortuosity variation along the jet axis (d).

sponds well with higher peaks seen in the mean RSS radial profiles in Section 5.3.2.

The turbulent interface is highly convoluted. This would cause a spatial variation of the collection point for the conditional statistics. Thus, quantifying the degree of convolution would give an objective parameter to help appreciate the significance of conditional statistics and also differentiate between an interface formed in a free jet and that of a turbulent-jet-in-turbulent-coflow. Tortuosity is a parameter used to quantify the level of contortion of a surface. In this work, the tortuosity of the interface is defined as the ratio of the length of the curve to the shortest distance between the two extreme ends, similar to that by [128]. The tortuosity, as shown in Fig 5.15d, of the interface along the axial stations increases in the downstream direction. It is also lower in magnitude for higher coflow velocity.

The viscous super layer (VSL) is known to be a feature of the TNTI where viscous diffusion dominates over the production of enstrophy[118][125]. The enstrophy transport equation is expressed as

$$\frac{D}{Dt} \left(\frac{1}{2} \omega_i \omega_i \right) = \underbrace{\omega_i \omega_j S_{ij}}_{\text{Production}} + \underbrace{\nu \frac{\partial^2}{\partial x_j \partial x_j} \left(\frac{1}{2} \omega_i \omega_i \right)}_{\text{Diffusion}} - \underbrace{\nu \frac{\partial \omega_i}{\partial x_j} \frac{\partial \omega_i}{\partial x_j}}_{\text{Dissipation}} \quad (5.5)$$

As 2D data is available in the current experiment, only the out-of-plane component of vorticity ($\omega_z(x, y)$) can be evaluated. Therefore, the 2D surrogates of dissipation ($D_s = -\nu \frac{\partial \omega_z}{\partial x} \frac{\partial \omega_z}{\partial y}$) and diffusion ($D_f = \nu \left[\frac{\partial^2}{\partial x^2} \left(\frac{1}{2} \omega_z \omega_z \right) + \frac{\partial^2}{\partial y^2} \left(\frac{1}{2} \omega_z \omega_z \right) \right]$) can be obtained and the production term cannot be evaluated. The diffusion term in Fig 5.15f shows a positive peak, where the VSL is located at the interface and has a peak-width of $\approx 10\eta$. Given that the vector spacing is $\approx 3\eta$ in this region and the VSL for a TNTI is shown to be $\approx 5\eta$ in previous works[125][127], the structure of the VSL may not be fully resolved, however, the extents should be fairly captured. The dissipation term in Fig 5.15e indicates higher diffusion towards the jet centerline and reduced magnitude of dissipation for cases with coflow. Further interpretation of these terms and their impact are discussed in Section 5.4. [129] found that for a TTI with high outer turbulence (greater than levels achieved in this study), the vorticity stretching term, i.e. the production term in Eqn 5.5, takes precedence. Also, as vorticity stretching need not be constrained to be zero as is in a TNTI, it facilitates a mechanism of enstrophy production throughout the entire thickness of the TTI. However, the viscous diffusion and dissipation terms still exist with a similar magnitude for both low and high outer turbulence. This is postulated to be a remnant of the VSL, but the magnitude is lower than the vortex stretching term for most of the VSL. This questions the physical significance of scaling the TTI thickness by the Kolmogorov scale. In our results, the magnitude of vortex stretching cannot be checked as the results are from planar PIV, so in plane vorticity components cannot be obtained.

5.4. DISCUSSION

The coflow can influence the evolution of the turbulent jet through the boundary layer it generates over the jet pipe and the turbulence in coflow. Increasing $U_{\text{coflow}}/U_{\text{jet}}$ leads to larger values of b^* , thereby showing slower jet centerline velocity decay. Also, the half-width is seen to be smaller at the same axial location. This indicates that entrainment

from the surroundings is reduced, and this is also supported by the conditional radial velocity profile, which shows a significantly lower magnitude at the interface than the free jet condition. Upon correct scaling, if the equivalent free jet have a Reynolds number such that they have achieved the mixing transition [147], the centerline decay profiles in Fig 5.9b should collapse on each other for all coflow ratio cases. As this is not the case, this is directly attributed to the "shielding" effect of the boundary layer developed by the coflow around the jet, which reduces turbulent exchange between the two streams. It must be noted that the entrainment and profiles mentioned above are for the scaled jet, i.e., in a normalized form that makes them comparable. According to the entrainment theory [109], the entrainment rate is proportional to the centerline velocity. However, this would be an absolute entrainment that varies even between two free turbulent jets of the same Reynolds numbers but with different diameters and, hence, jet centerline velocities.

In the conditional enstrophy transport equation, the diffusion term (D_f) peak width at the interface, which indicates the VSL structure, remains unchanged for varying coflow ratios, which shows that the low turbulence intensity level of the coflow does not influence the interface structure. However, the boundary layer generated by the coflow over the jet pipe, creates a shielding effect, indicated by a local velocity deficit. This correlates with lower magnitude of enstrophy dissipation (D_s) in the jet core, leading to higher enstrophy and RSS peaks on the jet side of the interface for $U_{\text{coflow}}/U_{\text{jet}} > 0$. This "shielding effect" is the reason why the scaled trends of the jet-centerline decay and half-width do not collapse on the curves of the free turbulent jet and, in fact, indicate lower relative entrainment.

Higher turbulence intensity in the background has been observed to increase the tortuosity/contortion of the interface [128][117]; however, in this study, as the turbulence intensities are too low (<6%), they are unable to influence the interface shape. Thus, the "shielding effect" prevents intense contortion of the interface, leading to lower tortuosity in the jet-in-coflow than in a free jet.

5.5. CONCLUSION

This work aims to study the evolution of a jet-in-coflow in the near-to-intermediate field (NIF) in the presence of low turbulence intensity (<6%) in the coflow. In a practical system such as that of a jet-in-hot-coflow combustion system, the coflow generates a boundary layer over the outer wall of the jet pipe and this may have a significant effect on the evolution of the flow field in the NIF, having an impact on the mixing and other reacting phenomenon. The flow field of a turbulent jet in turbulent coflow was measured by 2D2C PIV in the region $0 \leq x/D \leq 40$ for coflow ratios of 0, 0.09, 0.16, and 0.33. The first point of interest is to see whether a jet-in-coflow may be represented as an effectively slow-moving free jet by applying the appropriate scaling. An overview of the flowfield is presented in terms of the mean axial velocity and turbulence intensity distribution, along with centerline profiles for mean velocity, jet half-width, and jet momentum. The centerline profiles of the scaled jet-in-coflow cases differ from those of a free jet. Increasing the coflow ratio leads to a lower centerline mean velocity decay rate, reduced jet spreading, and a virtual origin shift upstream toward the nozzle compared to a free jet. Further, the turbulent coflow contributes an addition of axial momentum to the tur-

bulent jet along the axis.

To investigate the cause for these deviations, radial profiles of one-point velocity statistics are plotted at $x/D=5, 10, 22,$ and 30 . For cases of higher coflow ratio, there is a clear axial velocity deficit in the interface region. The mean profiles of turbulence intensity and RSS show a higher peak near one halfwidth distance from the jet center. The velocity deficit is attributed to the coflow initial conditions where a boundary layer is formed on the external wall of the pipe producing the jet. To get a better understanding of the interaction between the jet and the turbulent coflow at the interface, conditional statistics are assembled with respect to the instantaneous interface detected in the PIV image frames. The velocity deficit at the interface for the jet-in-coflow is also seen in the conditional axial velocity profiles. This is postulated to originate from the boundary layer generated over the outer wall of the jet pipe. The turbulence of the coflow has little effect on the structure of the interface as is seen from the enstrophy diffusion peak profile, which has a similar structure for the various jet-in-coflow cases and the free jet case. On the other hand, the enstrophy dissipation has a lower magnitude for the jet-in-coflow cases, correlating well with the higher peak levels of RSS and enstrophy on the jet side of the interface, compared to the free jet case. Thus, the higher peaks of turbulence, also seen in the mean radial profiles, is attributed to reduced dissipation in the jet-in-coflow due to the "shielding effect" of the wake of the boundary layer initially formed around the jet pipe. Further, the tortuosity of the interface is found to be lower for the jet-in-coflow compared to the free jet, which shows that the low turbulence intensity of the coflow cannot contort the interface, and the "shielding effect" dampens the contortion that may arise.

This work was motivated by the need to understand the turbulent flow fields in MILD/Flameless combustion systems, but since this was done in an isothermal flow field, it is recommended to verify the applicability of these results under conditions with heat release.



6

CHARACTERIZATION OF A JET-STABILIZED COMBUSTOR

No man was ever wise by chance.

Seneca

A jet-stabilized combustor was operated with CH₄-H₂ fuel mixtures with H₂ varying from 0-100% and with varying equivalence ratios (ϕ). Comprehensive measurements were carried out of the velocity field using Particle Image Velocimetry (PIV), temperature and gas composition by traversing probes in the chamber, and flame topology using chemiluminescence imaging. The flow field in this combustor consists of a jet that undergoes recirculation, generating Central and Peripheral Recirculation Zones (CRZ and PRZ). The recirculation ratio in the PRZ is found to be twice that of the CRZ. Increasing H₂% for the same ϕ leads to higher NO_x. Ultra-low ϕ flames could be stabilized only at H₂ \geq 50%, which in turn leads to low NO_x due to low adiabatic flame temperatures. The combination of temperature, gas composition (CO/NO), and chemiluminescence images is used to identify the extent and location of the reaction zone. Distributed reaction zones, stabilizing at around 30% of the length of the chamber, are achieved at lean conditions, whereas an increase in H₂% makes the reaction zone more compact and shifts upstream towards the burner head. Flame kernels are extracted from the instantaneous chemiluminescence images, and probability distribution functions for their aspect ratio and axial location are constructed. These are used to identify ignition modes (autoignition/flame propagation) for varying fuel H₂% and inlet ϕ based on a hypothesis of flame stabilization mechanisms.

6.1. INTRODUCTION

Hydrogen has emerged as a promising energy carrier for reducing carbon emissions from combustion devices, aligning with global efforts to mitigate climate change [148][149]. However, the direct substitution of conventional fuels with hydrogen presents several technical challenges, including an increased risk of flashback, combustion instabilities, and potentially higher NO_x emissions [150][151]. Moreover, the near-term availability of green hydrogen is projected to be limited, potentially insufficient to meet current energy demands [152]. To address these constraints while still leveraging the benefits of hydrogen, a viable strategy involves blending conventional fuels with hydrogen to incrementally reduce carbon footprints. While hydrogen admixing does reduce the carbon emissions, there is still an issue of high NO_x emissions. The flameless combustion regime is one possible combustion strategy that can be exploited as it has good potential for the reduction of NO_x emissions, which makes it an attractive technology for gas turbine engines[153]. It is also associated with autoignition as the primary stabilization mechanism, as opposed to flame propagation[154][155], which makes it important to analyze the ignition mechanism of different fuel admixtures under varying operating conditions for optimal design.

A jet-stabilized combustor is a configuration within which Flameless/MILD Combustion regime can be achieved in premixed/partially premixed fuel-air mixtures [18], [37], [156]. This configuration consists of reactants entering the combustion chamber through high-velocity jets at speeds that are typically much higher than the turbulent flame speed. These jets are located off the axis of the combustor such that a strong recirculation zone is established, thereby supplying hot combustion products back to the reactant stream, which causes it to ignite and thus stabilize a reaction zone in the chamber. The mixing of reactants and recirculated hot products provides suitable conditions, i.e. high temperature of reactants and dilution of O_2 content by the addition of diluents, leading to Flameless/MILD combustion regime [24] [27]. Studies such as [18] and [37] experimentally analyzed CH_4 - H_2 flames in a jet stabilized combustor, with a maximum H_2 admixture of 40% (by volume) with natural gas. The authors demonstrated the suitability of Flameless combustion at gas turbine conditions by preheating the air and operating at 20 bar. A combination of OH-PLIF and OH* chemiluminescence was used to characterize the reaction zone and emissions were measured at the exhaust using an exhaust gas analyzer. Low NO_x emissions were achieved when the reaction zone was homogeneously distributed over a large volume, and the equivalence ratio (ϕ) was <0.5 . Further, it was postulated that by increasing jet velocity, the mixing between fresh fuel/air and recirculated burnt gases was enhanced and the residence time was reduced. Severin *et al.* [60] investigated the flame stabilization mechanism in a single jet stabilized combustor, operating on a CH_4 air mixture at $\phi=1$, $T_{in}=473\text{K}$, $\text{Re}=5640$. This resulted in a visible, lifted flame which was measured by OH-LIF, PIV, and OH* chemiluminescence, all at 5 kHz, thus yielding time-resolved information of the phenomenon. Vortices were generated in the shear layer, but only on the side where there was enough distance between the jet and the wall. These vortices induce the mixing of the recirculated hot products and fresh reactant stream, leading to a series of events in which the mixture ignites, there is a flame wrap-up, flame expansion, and finally, a merger into the main flame body. While flame propagation was attributed to cause most of the flame

expansion, autoignition could not be ruled out. Autoignition was seen to occur through isolated flame kernels at the bottom of the flame body at high frequency, which had a significant effect on the lift-off height. Although the relative weightage of autoignition and flame propagation was difficult to quantify based on these diagnostics, it was clear that the mixing of hot products of combustion and fresh reactants led to the formation of flame precursors, which may enable both flame propagation and autoignition further downstream. Liu *et al.* [157] investigated the effect of H₂ addition to CH₄ in a mild combustor, which was a jet-stabilized FLOX burner similar to the one in the current study. They explored H₂ mixtures up to 50% (by volume). The authors presented measurement results from direct imaging by DSLR and OH* chemiluminescence to image the flame topology. Further, the exhaust flue gas temperature and composition were measured using a type B thermocouple and an exhaust gas analyzer, respectively. The combustor was also modeled using a Chemical Reactor Network. Ultra-low NO_x (< 5ppm) was reported and the addition of H₂ led to a reduction in reaction zone lift-off height. The authors also found it difficult to stabilize a reaction zone above 50% H₂.

While the above are examples of premixed/partially systems, the literature also encompasses flameless combustion systems wherein the fuel and air are injected through separate streams and interact in the combustion chamber. The operational characteristics of a small-scale combustor were studied by Veríssimo *et al.* [42]. The combustor was non-premixed, with a central air nozzle surrounded by fuel nozzles. Emissions were measured for $\phi \leq 1.0$, and NO_x first increased, peaked at $\phi=0.5$ with a value of 9 ppm, and then decreased. On the other hand, CO first decreases and then increases below this value of ϕ . Further studies were done to assess the effect of inlet air velocity [43], thermal power input [44] and air preheat temperature [45]. The effect of increasing air velocity by changing nozzle diameter, i.e., keeping all mass flows constant, resulted in lowering of NO_x and increasing CO. This is attributed to higher entrainment of fuel and recirculating product gases into the air jet, which helps in the onset of flameless combustion. Increasing thermal power implied increasing velocity of all inlet streams while keeping the equivalence ratio constant. This had a significant effect on residence time, thus higher thermal power cases had lower residence time. This led to higher CO at the exit; however, the NO_x remained constant. This was attributed to the suppression of the thermal NO_x pathway under FC regime and it is stipulated that the N₂O pathway may have a more important role.

Ayoub *et al.* [158] performed measurements on a reverse flow non-adiabatic combustor where all the combusted product gases are recirculated and exhausted through the burner head where fuel and air are injected. There are cooling tubes in the combustor which extract heat to emulate a process load. They performed OH* chemiluminescence imaging and exhaust gas measurements to characterize the reaction zone optically and the resultant net emissions. The furnace was operated with methane as well as methane-hydrogen mixtures by Ferrarotti *et al.* [41], and they observed that NO_x increased with increasing H₂% from 0-100%. Decreasing the fuel injector diameter from 25 to 16 mm led to a reduction of NO_x from 175 ppm at 3% O₂ to 60 ppm at 3% O₂ for 100% H₂. By increasing the length of the fuel lance protruding into the chamber from 0 to 50 mm, the NO_x could be further reduced from 60 to 30 ppm for 100% H₂. This was attributed to the extra residence time available for the air to mix with the exhaust gases before interacting

with the fuel stream. The pure CH_4 case showed negligible levels of NO_x .

The jet-in-hot-coflow (JHC) has emerged as a popular choice to emulate conditions created locally in a flameless/mild combustor in the laboratory while allowing for high-fidelity laser diagnostics. Medwell *et al.* [51] observed that for cases with hot coflow, high levels of formaldehyde (CH_2O) were also seen in the preignition zone, i.e., much upstream of the actual lift-off height. This suggested that MILD combustion conditions lead to a different flame stabilization mechanism. Gordon *et al.* [57] identified a series of temporally successive phenomena based on previous experiments and numerical simulations that indicated the existence of autoignition. The events are:

1. Build up of precursor pool: where the mole fraction of CH_2O increases significantly and that of OH remains low.
2. Initiation of reaction: CH_2O and OH mole fractions reach a maximum in a very short period of time.
3. Formation of a steady flame: CH_2O peak decreases while the OH peak mole fraction does not change.

The authors took simultaneous OH , CH_2O PLIF, and Rayleigh temperature measurements in a flame of methane in vitiated coflow and identified the existence of these events. They concluded that they observed a high percentage of autoignition events at the base of the lifted flame, and thus, it was highly likely to be the stabilization mechanism for such a flame.

Oldenhof *et al.* [48] tracked ignition kernels in the Delft jet-in-hot-coflow and analyzed the lift-off behavior. The trends for the sensitivity of lift-off height to jet Reynolds number were completely different for hot and diluted coflow compared to conventional lifted flames. The addition of higher alkanes and increasing the coflow temperature had similar effects of leading to lower axial location where ignitions first occur, higher ignition frequencies, and reduced lift-off height. A quantitative analysis of entrainment of coflow gases into the central jet [52] revealed that the rate at which oxidizer is transported to the shear layer between the jet and the coflow, where mixing occurs, is critical to flame stabilization. Specifically, in the case of the DJHC, there is a positive radial temperature gradient, and an increase in jet velocity leads to increased entrainment of hot coflow, which leads to the initial drop in lift-off height with jet velocity.

To study autoignition, one must be able to identify and distinguish it from flame propagation, which is the stabilization mechanism for a conventional flame. Several researchers have worked on developing criteria for the same. Gordon *et al.* [61] have developed two indicators based on numerical modelling. The first one is a budget of convection, diffusion, and the reaction of key species wherein it was shown that for a conventional flame, diffusion plays an important role, whereas for autoignition, the convection and reaction terms mostly balance out each other. The second is the build-up of HO_2 prior to autoignition followed by the creation of H , O , and OH , whereas, in conventional premixed flame propagation, all radicals would build up simultaneously. On the other hand, Schulz *et al.* [62] derive an autoignition index solely based on the chemistry. HO_2 is denoted as a critical intermediate specie in the heat release reactions, and it is found that the consumption occurs through two main reactions: $\text{HO}_2 + \text{H} \rightleftharpoons \text{OH} + \text{OH}$

(R6) and $HO_2 + OH \rightleftharpoons H_2O + O_2$ (R8). The relative extent of each reaction turns out to be a good indicator of whether the reaction is stabilized by flame propagation (R6>R8) or autoignition (R8>R6). This criterion is used to identify autoignition events in a turbulent lifted methane-air flame, and it is shown that premixing and opposed mixing mode autoignition are the prominent mechanisms of stabilization in the outer shear layer and at the flame base. Aditya *et al.* [63] extended the Chemical Explosive Mode Analysis (CEMA) to distinguish between autoignition and flame propagation. The ratio of the non-chemical to the chemical source term ($\alpha = \phi_s / \phi_\omega$), projected to the left eigenvector of the Chemical Explosive Mode, indicates the relative importance of diffusion to chemical kinetics. The value of this parameter is used to denote assisted ignition, i.e., flame propagation, where diffusion plays a significant role, autoignition, and local flame extinction. This indicator is used to identify in the DNS of a reheat combustor that most of the fuel is consumed via the autoignition process.

While jet-stabilized combustors are suitable for low NO_x combustion, there have been limited studies on the nature of the flame stabilization mechanism (autoignition/flame propagation) under varying hydrogen admixture conditions. Further, to the best knowledge of the authors, there are no studies of this configuration providing temperature and gas composition within the reaction zone, leaving much of the detailed reaction kinetics to informed extrapolation or entirely derived from simulations.

This study bridges a critical research gap on premixed jet-stabilized combustors operating on CH_4/H_2 fuel admixtures by providing a comprehensive experimental dataset that includes velocity fields, temperature, composition, and flame chemiluminescence for varying equivalence ratios and H_2 content, varying from 0 to 100% H_2 by volume, in the fuel mixture. Our extended PIV measurements cover both Central and Peripheral Recirculation Zones, offering a more complete flow field view, which is used to quantify the recirculation ratio based on the detected interfaces. Detailed temperature and composition measurements in the reaction zone provide unprecedented insight into chemical reaction progress within the chamber. We present an innovative approach to analyzing low-fidelity chemiluminescence data to distinguish between autoignition and flame propagation modes and the mode of ignition and stabilization of the reaction zone is observed to shift based on reactant composition. Integrating these multi-parameter analyses offers a unique characterization of this combustor configuration.

6.2. EXPERIMENT SETUP

6.2.1. SETUP AND OPERATING CONDITIONS

The experiments were conducted in a jet-stabilised combustor, shown in Fig 3.2, the burner head of which consists of 12 nozzles of diameter, $D=6.67$ mm each. Each nozzle has a fuel nozzle of $d=1$ mm inner diameter located upstream in tandem, such that the air and fuel mix in a channel of length $\approx 5D/33d$ before entering the combustion chamber. The combustor was operated with two configurations, the first was with a cylindrical quartz combustion chamber (inner diameter, I.D.=208 mm, thickness, $th=3$ mm), to allow complete optical access and the second was with a stainless steel 304 combustion chamber, which had six access ports, to allow for intrusive temperature and gas composition measurements[78].

The massflow rates of CH_4 , H_2 and pilot burner air were controlled by Bronkhorst El-flow flow controllers which have an accuracy of $\pm 0.5\%$ of reading plus $\pm 0.1\%$ of full scale. The main and cooling air flow rates were controlled by Bronkhorst In-Flow meters with Badger RCV Control valve leading to an accuracy of $\pm 1\%$ of full scale. The combustor was operated for fuel mixtures with $\text{H}_2\%$ from 0 to 100% and equivalence ratio (ϕ) varying from 0.3 to 1.0 at a constant inlet air temperature of 350°C and constant nozzle bulk velocity of $\approx 100\text{ m/s}$.

When operating the facility, a fixed startup procedure was followed; the system was preheated by allowing a nominal main air flow rate, set to a temperature of 350°C , till the temperature registered on the outer wall of the burner head was around 80°C . At this point, the pilot burner was ignited and then the main burner was started at a nominal power of 20 kW at 100% CH_4 , $\phi=0.8$. After the massflow rates and exhaust temperature stabilize, the pilot burner was turned off. The main burner power was slowly increased to 30 kW and the system was allowed to heat up until it reaches a steady state, noted by the temperature of the external wall of the burner head. Once this was achieved, the parameters were set to the desired operation conditions, and the measurements were taken once the system reached a steady state. The facility is designed to be able to operate up to a maximum of 200kW thermal power, however, in this study, it was operated between 30 and 80 kW. Although the pilot burner was turned off, a nominal air flow of 62 lpm was maintained to prevent damage by overheating. This served as a dilution stream in the combustor, thereby altering the effective equivalence ratio.

Detailed settings of the operation conditions are listed in Table 6.1. The $\text{H}_2\%$, equivalence ratio (ϕ), heater temperature (set to 350°C) and thermal power (Q_{in}) were given as inputs to the control system. The value of ϕ specified was that for the main burner. The massflow rate set points were obtained by calculation and the values listed in the table are the average of those that were measured by the massflow controller. The temperatures listed are the average of the uncorrected measured values from Inconel sheathed K-type thermocouples.

Table 6.1: Time averaged operating Conditions

$H_2\%$	ϕ	T_{air} (°C)	T_{fuel} (°C)	T_{mix} (°C)	\dot{m}_{air} (lnpm)	\dot{m}_{CH_4} (lnpm)	\dot{m}_{H_2} (lnpm)	U_{nozzle} (m/s)	Q_{in} (kW)	T_{cool} (°C)	$T_{exhaust}$ (°C)	$\dot{m}_{pilot\ air}$ (lnpm)	$\dot{m}_{cooling\ air}$ (lnpm)
0	0.6	371	19	301	1133.7	71.5	0.0	102.3	42.6	4	519	62	2129.2
0	0.7	378	19	298	1131.5	83.2	0.0	102.4	49.6	4	547	62	2607.4
0	0.8	373	19	294	1131.3	94.8	0.0	102.7	56.6	3	566	62	3088.7
0	0.9	371	19	290	1123.0	106.4	0.0	102.4	63.5	2	581	62	3598.7
0	1	371	19	287	1121.5	117.8	0.0	102.6	70.3	2	590	62	4018.4
10	0.6	363	20	300	1133.3	69.3	7.7	102.5	42.8	4	522	62	2134.1
10	0.7	364	20	296	1127.0	80.6	8.9	102.4	49.7	4	544	62	2548.5
10	0.8	367	20	293	1123.5	91.9	10.1	102.4	56.7	4	563	62	3046.8
10	0.9	366	20	289	1122.1	103.0	11.4	102.7	63.5	3	575	62	3528.1
10	1	372	19	285	1115.9	114.1	12.6	102.5	70.4	2	592	62	4061.9
50	0.35	366	20	307	1050.0	30.8	30.8	95.2	23.9	4	452	62	1166.1
50	0.5	365	20	299	1113.7	46.9	46.9	102.0	36.4	4	496	62	1816.3
50	0.6	366	20	294	1108.5	56.0	56.0	102.2	43.5	3	528	62	2215.3
50	0.7	367	20	289	1103.7	64.9	64.9	102.4	50.4	3	548	62	2636.9
50	0.8	369	20	284	1096.8	73.8	73.8	102.5	57.3	2	564	62	3103.8
50	0.9	372	20	280	1093.0	82.5	82.5	102.8	64.1	2	578	62	3603.0
50	1	371	20	275	1086.5	91.1	91.1	102.8	70.7	2	591	62	4115.2
80	0.3	368	20	303	1110.9	17.5	70.1	102.0	23.1	5	437	62	1130.7
80	0.5	368	20	289	1090.4	28.6	114.4	102.4	37.7	4	503	62	1912.7
80	0.6	367	20	283	1077.9	34.0	135.9	102.4	44.7	4	533	62	2286.4
80	0.7	367	20	276	1064.8	39.2	156.9	102.4	51.6	3	552	62	2698.6
80	0.8	367	20	271	1054.7	44.4	177.5	102.5	58.4	3	562	62	3105.5
80	0.9	365	20	265	1048.9	49.4	197.6	103.0	65.0	3	571	62	3539.1
80	1	363	20	260	1032.4	54.3	217.3	102.6	71.5	3	575	62	3939.6
100	0.3	369	20	293	1082.6	0.0	136.9	102.0	24.6	5	436	62	1238.4
100	0.6	365	20	266	1032.3	0.0	259.6	102.9	46.7	4	535	62	2440.4
100	0.8	368	20	250	993.8	0.0	334.7	102.7	60.2	3	569	62	3316.0
100	1	369	19	237	965.4	0.0	405.0	103.2	72.8	3	582	62	4172.5

6.2.2. MEASUREMENT TECHNIQUES

The velocity field was measured using PIV using the quartz combustion chamber under reacting flow conditions for a mixture of $H_2=0\%$ at a thermal power of 60kW, $T_{air}=350^\circ C$ for $\phi=0.6$ and 0.8. TiO_2 particles of an average particle diameter of $0.5 \mu m$ were used to seed the flow through the fuel stream in the top nozzle of the burner head, as shown in Fig ???. The particles were illuminated with an Evergreen double pulse laser with 200 mJ pulse energy and a pulse width of 9 ns at 532 nm emission, formed into a sheet with an average thickness of 1 mm using a series of optics. Two LaVision Imager sCMOS cameras with Micro Nikkor 105 mm lenses with $f\# 11$ were used in planar two component mode. Each camera had a pixel size of $6.5 \mu m$ and field of view 131 mm as shown in Fig. ??, denoted as FOV_{PIV} . Their frames overlapped by 24.7 mm along the axis of the combustor. Approximately 2000 images were acquired for each case at 15 Hz with a Δt of $3.5 \mu s$ and $6 \mu s$ for the cases of $\phi=0.6$ and 0.8, respectively. The uncertainty, based on Gaussian distribution, of the mean is $4\% \sigma_u$ (σ_u / \sqrt{N}) and of the RMS is $3\% \sigma_u$ ($\sigma_u / \sqrt{2N}$) for 95% confidence interval, where σ_u is the standard deviation of velocity. Polarisation filters were placed in front of the lens to reduce noise from reflections of the laser from the surfaces of the quartz pipe, and a 532 nm bandpass filter was used to minimize background noise and the effect of flame luminescence. The images were processed in DaVis 8.4 using an iterative multi-grid approach such that the final pass was done by a 24×24 pixel window with 75% overlap. This resulted in a vector spacing of $305.6 \mu m$ and a window size of $1222.4 \mu m$. While the resolution is relatively coarse, it is the best possible trade-off to capture the relevant field of view to observe the overall flow field.

The gas analyzer and thermocouple measurements were done using the steel chamber by inserting the probes through access ports P1-P6, shown in Fig ???. Each probe had a bushing such that the probe slid within the inner bore of the bushing while keeping minimal clearance. The inner bore diameter was 0.5 mm larger than the respective probe. Due to the pressure drop across the exhaust duct of the combustor, the pressure within the chamber exceeded that of the surrounding atmosphere. Consequently, gas could have leaked out of the chamber through the gap between the bushing and the probe, while the reverse flow was not possible. This condition ensured that the composition and temperature measurements were not diluted by the surrounding air. The measurements were done by traversing the probe radially at a constant speed such that a distance equal to twice the characteristic length (equal to the diameter of the probe) was traversed while acquiring 100 and 200 samples for the gas analyzer and thermocouple, respectively. The values were spatially averaged to reduce measurement noise by taking a sliding average with a convolution filter of the size of the characteristic length.

An S-type thermocouple with a platinum (10%) sheath was used to probe the temperature within the chamber. The thermocouple measurements in the chamber were corrected using an energy balance equation,

$$\epsilon_{tc}(\sigma \epsilon_g T_g^4 + \sigma \epsilon_{wall} T_{wall}^4) + h(T_g - T_{tc}) - \sigma \epsilon_{tc} T_{tc}^4 = 0, \quad (6.1)$$

where ϵ_{tc} was the emissivity of the thermocouple sheath, ϵ_{wall} the emissivity of the combustor inner wall, ϵ_g the emissivity of the gas around the thermocouple measurement point, T_{tc} the temperature measured by the thermocouple, T_g the temperature of the gas around the thermocouple measurement point and T_{wall} the temperature of the in-

ner wall of the combustor as measured by the thermocouple at $r=0.0$. Details on the parameters used for the corrections can be found in Appendix C.2.1

A suction-based system was used to extract gas samples to measure composition in terms of NO, CO, CO₂, CH₄, and O₂. The probe was an Inconel pipe with an outer diameter of 6 mm and an inner diameter of 3 mm. The temperature just before the heated line of the gas analyzer was measured to ensure that the gases were quenched but not cold enough to allow for the condensation of water vapor. An ABB Limas21 HW process photometer (UV-RAS) (0.1 ppm accuracy) was used to measure NO under hot-wet conditions, i.e., the water vapor was not condensed out of the gas stream. This was ensured by maintaining the heated hose at 180 °C and the Limas21 module at 80 °C. The remaining gases were measured on a dry basis by condensing out the water vapor using a cooler. CO₂, CO, and CH₄ were measured using a Uras26 IR absorption analyzer (0.1% vol/ 10 ppm/ 0.01%vol accuracy), and O₂ was measured in the Magnos28 paramagnetic analyzer (0.1% vol accuracy). The gas analyzer was calibrated daily using Air Liquide calibration bottles with a certified accuracy of 1%. NO was calibrated with a bottle of NO/N₂ (8.46 ppm/balance), CO and CH₄ on a bottle of CO/CH₄/N₂ (801 ppm/3.99%vol/balance), CO₂ on a bottle of CO₂/N₂ (59.8% vol/balance) and O₂ on laboratory air. The respective bottles were used for span calibration, while zero calibration was done using a bottle devoid of the species. Gas composition measurements are corrected to a standard value of 15% O₂ using the equation:

$$\chi_{j@15\%O_2} = \chi_{jmeas} \left[\frac{0.2096 - \frac{15}{100}}{0.2096 - \chi_{O_2}} \right], \quad (6.2)$$

where χ_j is the mole fraction of species 'j' and χ_{O_2} is the measured mole fraction of oxygen.

Chemiluminescence imaging of the flame was done using a Nikon D7500 DSLR and the field of view is shown in Fig 3.2, denoted as FOV_{chem}. The exposure time ranged between 100- 800 μ s, and for $\phi < 0.4$, the value was 2.5 ms due to a fainter signal. The "blue" component of the acquired images, which has a peak around 455 nm and a full width at half max (FWHM) of ~ 100 nm [159], is extracted and used for further processing. This correlates with the CH* emissions (431 nm) for flames with CH₄; however, a significant blue spectrum is also seen for H₂ enriched flames up to 100%, as was characterized by Schefer *et al.* [160]. Flame kernels were identified for the instantaneous fluctuation images using an algorithm based on a combination of the DBSCAN [144] and Otsu thresholding algorithm [69]. The detailed procedure is explained in Section 6.2.3.

6.2.3. FLAME KERNEL DETECTION

The instantaneous fluctuation images were processed to obtain statistics of the flame structures. The motivation for this is depicted in Fig 6.1. The camera requires a certain exposure time to image the kernel. However, during this extended exposure, the kernel will undergo a decay due to the completion of the reaction and simultaneously be transported by the flow. This would result in a blur proportional to the local transport velocity and exposure time, as shown in Fig 6.1a, but the blur should show a decaying intensity. Now, if one considers the occurrence of kernels to be a locally stochastic process such that kernels may pop up in the local region, the blur introduced by all of them combined

over time should look like Fig 6.1b. Thus, taking this average and subtracting it from the instantaneous image would result only in the most intense fluctuating component being revealed, which is a closer indication of the location of the emission peak. However, to ensure this representation, only positive fluctuations are accounted for, i.e., values greater than the mean.

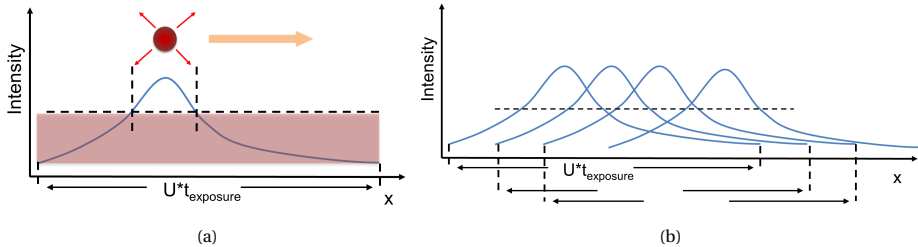


Figure 6.1: Moving Ignition Kernel imaging by chemiluminescence

Figure 6.2 depicts the stages of flame kernel detection, with an example of a single image frame. Flame kernels are extracted from the instantaneous chemiluminescence images (Fig. 6.2a) by subtracting the mean and accounting only for positive values in the result (Fig. 6.2b). They occur in clustered packets with variable spacing between them. They were identified and grouped in clusters based on the density of distribution and space between the structures using the DBSCAN (Density Based Spatial clustering of applications with noise) algorithm[144]. This algorithm can identify densely packed cluster points while distinguishing them from background noise points, i.e., points that may occur sporadically with a few points in the cluster. Figure 6.2c) shows the detected individual clusters identified by the color scale, and the boxes indicate the ones selected for statistical analysis.

The technical implementation of the flame kernel identification procedure is as follows:

1. Image pre-processing: The blue component of images was chosen, converted to grayscale, and then normalized and rescaled to 0-255. The resultant images were downsampled using a pyramid algorithm in OpenCV. This convolves the original

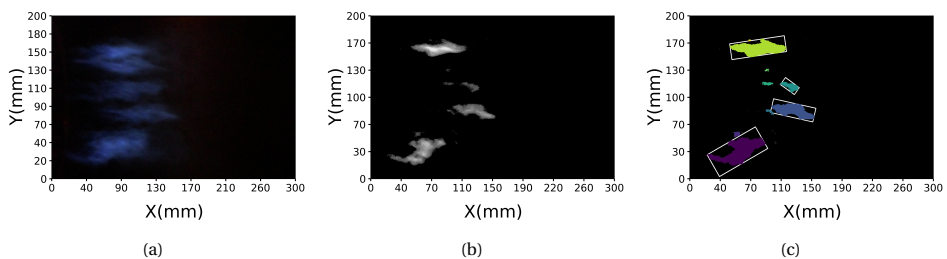


Figure 6.2: Stages of ignition kernel detection (a) Instantaneous (b) Fluctuations(+) (c) Detected kernels with bounding box

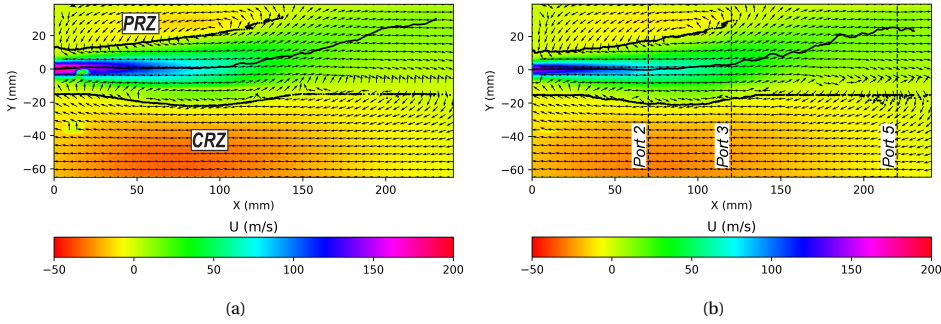


Figure 6.3: Axial velocity contour map with vectors overlaid for $H_2=0\%$, $P=60\text{kW}$, (a) $\phi=0.6$ (b) $\phi=0.8$

image with a Gaussian filter and then removes even numbered rows and columns to reduce the size of the image used while retaining the main features. This process was done twice to downscale the image to $1/16^{\text{th}}$ of the original size. The downscaled image was normalized to have pixel intensity values scaled between 0 and 255.

2. **Thresholding:** The Otsu algorithm was applied to obtain a threshold value that separated the contents of the image into two classes: the foreground and the background. Details of the algorithm can be found in [69]. In the normalized image, pixels above the Otsu threshold were selected and assembled into an array, representing a set of pixels with gaps between them.
3. **Cluster identification:** The DBSCAN algorithm was applied to identify clusters from the thresholded image. The implementation of DBSCAN in the scikit-learn library in Python was used as a basis to write the code. The main parameters were eps and minPts , where a point is considered a core point if at least minPts points are within distance eps of it. For the final statistics, only clusters greater than 33% of the average size of the identified clusters in an image were selected.

LIMITATIONS

This method of flame kernel identification provides an approach to extract more information from relatively simple measurements, however, there are some limitations. If the flames become less turbulent and are positioned in the corrugated flame region or lower, the spatial fluctuation may not be enough to capture through the exposure times used on the DSLR camera. Thus, each frame contains an averaged image, and the variance would be too low to yield anything meaningful. This was seen for 100% H_2 case, and 80% H_2 with $\phi > 0.6$.

6.3. RESULTS AND DISCUSSION

6.3.1. FLOW FIELD

Figure 6.3a and 6.3b show the mean axial velocity field for the reacting flow at 60kW, $H_2=0\%$ with $\phi=0.6$ and 0.8 respectively, to visualize the flow fields of two different noz-

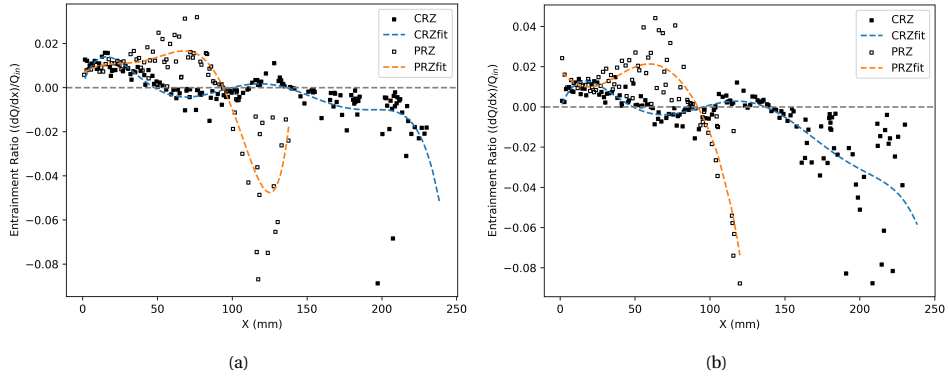


Figure 6.4: Entrainment ratio along the combustor axis at the CRZ and PRZ for $H_2=0\%$, $P=60\text{kW}$, (a) $\phi=0.6$ (b) $\phi=0.8$

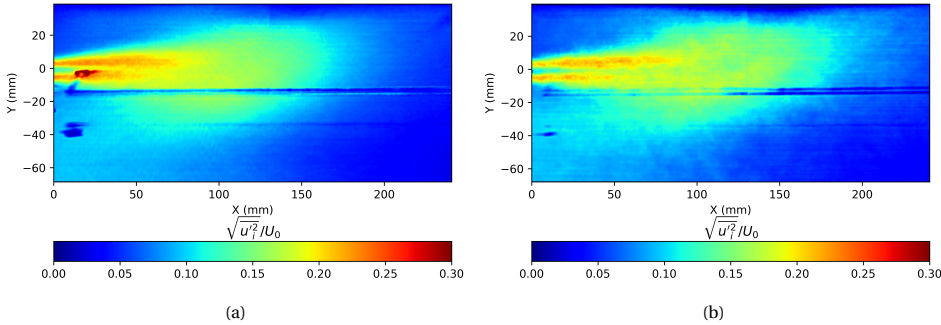
zle bulk velocities and fields of varying levels of temperature due to the influence of ϕ . The high-velocity jet exits the nozzle and forms two recirculation zones, one towards the center of the combustion chamber, the Central Recirculation Zone (CRZ), and one towards the wall, the Peripheral Recirculation Zone (PRZ). The PRZ is a more compact region than the CRZ. The jet flow impinges on the wall at $X \approx 130$ mm ($X/D=19.5$), closing off the PRZ, and continues as a wall-bounded flow with further development of the CRZ downstream. This is a typical feature in wall offset jets parameterized by an offset ratio[161][66].

The jet entrains fluid from the recirculation zones, the extent of which is determined by tracking the inflow at the interface between the jet and the surroundings. This was done by first determining the jet centerline, which was defined as the location of maximum axial velocity for every X-coordinate. Next, the interface was detected, which was defined as the location perpendicular to the centerline where the tangential velocity changed sign. The interface and jet centerline are shown overlaid on the flowfield in Fig. 6.3. Finally, the velocity component perpendicular to the local interface was used to compute the entrained flow. The local entrainment ratio (ER) $((dQ/dx)/Q_{in})$, where dQ/dx was the volume flow entrained per unit length of the interface and Q_{in} is the inlet volume flow at the nozzle) is computed for the CRZ and PRZ as shown in Fig. 6.4a and 6.4b. One can observe that the ER for the CRZ is high in the initial part of the chamber (up to $X \approx 50$ mm) after which it becomes negative, indicating a detrainment. The PRZ, on the other hand, continues to have a positive value up to $X \approx 100$ mm.

The recirculation ratio (RR) is computed as $Q_{entrained}/Q_{inlet}$. The numerator is computed by integrating dQ/dx along the interface and the denominator by integrating volume flow at the nozzle exit. For the PRZ and CRZ individually, the denominator is evaluated as the integral of the volume flow over the upper half and lower half of the nozzle exit, respectively. Thus, the total recirculation ratio (RR) is more of a weighted average of the PRZ RR and CRZ RR. The values are listed in Table 6.2 along with the individual contributions from the PRZ and CRZ. Further, the PRZ contributes more than the CRZ to the recirculation ratio by a factor of 2-2.5.

Table 6.2: Recirculation Ratio and contributions from PRZ and CRZ

Power (kW)	ϕ	Recirculation Ratio (RR)	PRZ RR	CRZ RR
60	0.8	2.56	3.68	1.49
60	0.6	2.52	3.45	1.6

Figure 6.5: Turbulence intensity for $H_2=0\%$, $P=60\text{kW}$, (a) $\phi=0.6$ (b) $\phi=0.8$

This combustor has a high recirculation ratio (~ 2.5) on a volume basis, with a split of ~ 3.5 in the PRZ and ≈ 1.5 in the CRZ. Combining this with the temperature measurement information presented ahead in Section 6.3.2, one can estimate the density ratio of the recirculated products to the incoming reactants. Estimating an average value from the measurements, the products from the PRZ are at 1250 K, from the CRZ are at 1500 K, and the inlet reactants are at 623 K. This results in a density ratio of ≈ 0.5 and 0.4 for the PRZ and CRZ, respectively. Thus, the recirculation ratio on a mass basis is approximately 1.75 for the PRZ and 0.6 for the CRZ, resulting in a total RR of ≈ 1.2 . This would provide conditions for significant dilution of the fresh reactants and raise the temperature, making it suitable for Flameless/MILD combustion.

The turbulence intensity, shown in Fig. 6.5 has a similar distribution and magnitude for both cases. There is a peak value between 25 and 30% closer to the jet exit, while further downstream in the region where recirculation begins, it reduces to around 15%. In the downstream region beyond where the flow impinges on the wall, the value drops to 10% and lower for $\phi=0.6$, while it maintains a higher value, 10-15% for $\phi=0.8$. The lower jet velocity in the latter case may lead to less turbulence dissipation. The central recirculation zone has higher turbulence intensity than the peripheral recirculation zone due to dissipation at the wall. The high turbulence region, $\approx 15\%$ extends as a bulge towards the central recirculation zone in the region of $50 < X < 125$ mm and $-20 < Y < -40$ mm.

The turbulence intensity obtained from PIV is a guideline for estimating the magnitudes under varying operating conditions. The two critical regions where reactive mixtures may be formed are at the interface of the jet and recirculation zones close to the jet exit (T.I.=25%) and further downstream, where the jet slows down and reverses to cir-

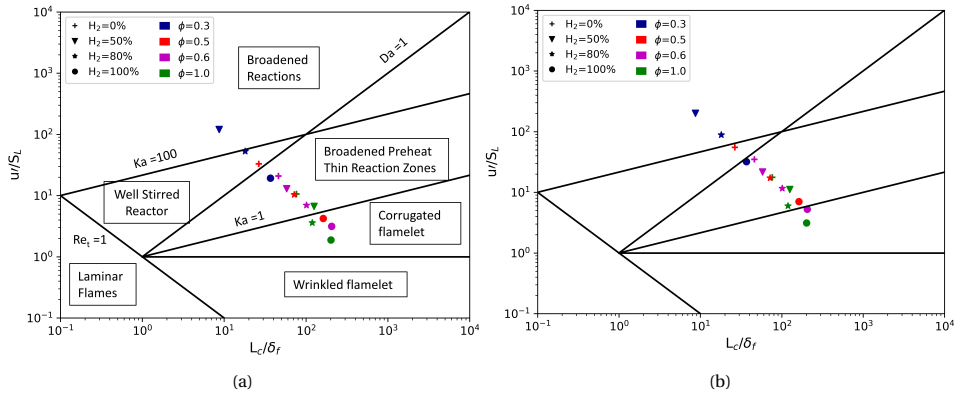


Figure 6.6: H_2 admixture conditions plotted on the Borghi diagram for $u'/U_0 =$ (a) 0.15 (b) 0.25 for a jet of $U_0 = 100$ m/s. The symbols indicate H_2 percentage in the fuel mixture and colours indicate the equivalence ratio.

culate (T.I.=15%). These values are used to plot the operating conditions on the Borghi diagram and predict the behavior of premixed flames under varying inlet composition conditions. The laminar flame speed was calculated using the FreeFlame model in Cantera [89] for a mixture consisting of 50% fresh reactants, by mass, and the remainder being burnt products. The POLIMI_C1C3_HT_NO_x_1412 chemical kinetic mechanism [90, 91] was used (referred to as C1C3 in this article), which is a detailed mechanism of the pyrolysis, partial oxidation, and combustion of hydrocarbon fuels up to 3 C atoms with NO_x. It accounts for 115 species and 2141 reactions. Sabia *et al.* [87] showed that the C1C3 mechanism (also called the Ranzi mechanism in the literature [90, 91]) captured the low-temperature chemistry and Negative Temperature Coefficient (NTC) region of methane-air combustion the best amongst the openly available mechanisms compared in the study. As this study encompasses methane-hydrogen admixtures under vitiated conditions, requiring ignition at moderate temperatures, this mechanism was chosen. The fresh reactants were initiated at a temperature of 623 K and the burnt products were calculated for the fresh reactant mixture using a Perfectly Stirred Reactor (PSR) model. The operating conditions at various turbulence levels are plotted in Fig. 6.6, where it can be seen that most of the points lie in the Broadened Preheat Thin Reaction Zone (BP-TRZ) region. Increasing the percentage of H_2 seems to shift the point towards the bottom right, i.e., more corrugated flamelets. Increasing the turbulence intensity from 15% to 25% pushes the conditions into Broadened Reactions (BR), although this is achieved only under the leanest equivalence ratio conditions with $H_2 = 50\%$ and 80% . The case of 0% H_2 could reach a minimum of $\phi = 0.5$, below which a converged solution was not possible.

6.3.2. TEMPERATURE MEASUREMENTS

The temperature within the combustion chamber was measured by traversing an S-type thermocouple radially through access ports on the wall of the steel chamber. Temperature measurements vs radial location are shown in Fig. 6.7, for $H_2 = 0, 50, 80,$ and 100%

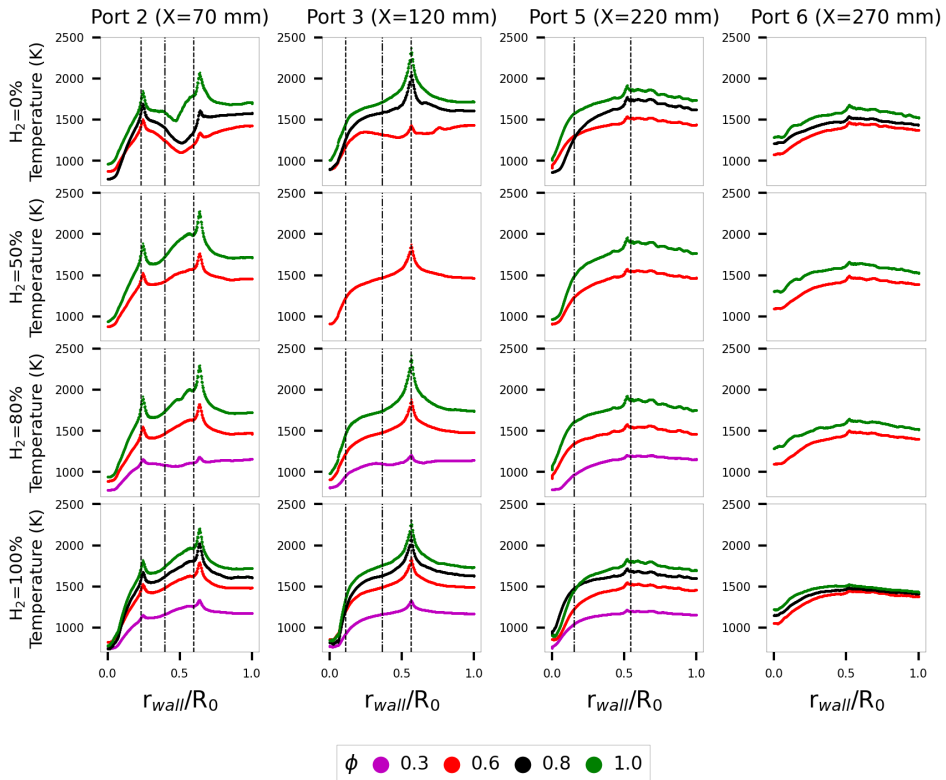


Figure 6.7: Temperature v/s radial location at Port 2, 3, 5 and 6. The vertical lines indicate the local jet center (·-·), PRZ, and CRZ (- · -) on the left and right of the jet centerline, respectively.

at Port 2, 3, 5, and 6, the locations of which are shown in Fig. ???. The radial locations are represented as the distance from the combustion chamber wall, normalized by the radius of the chamber. The measurements have been corrected for radiation and convection based on the velocity field. The vertical lines indicate the radial location of the jet centerline (-) and interface with the recirculation zones (- -), obtained from the flow field presented in Section 6.3.1.

The temperature magnitude increases with equivalence ratio, as expected. The peak values increase from Port 2 to Port 3 and then decrease at Port 5 and 6, which indicates that heat release by combustion primarily occurs up to Port 3, and then further downstream, heat loss dominates. However, for the leanest cases of each H₂%, i.e., H₂=0% $\phi=0.6$, H₂=80% $\phi=0.3$, H₂=100% $\phi=0.3$, this trend differs with peak values increasing from Port 2 to Port 5, indicating a more distributed heat release zone which is shifted further downstream. From the location of the peaks, it seems that the point of highest heat release is concentrated near the interface of the jet and the recirculation zones (PRZ and CRZ). For the CRZ, side, the peak is shifted into the CRZ at Port2 and moves inward towards the jet center at successive Ports. The peak near the PRZ interface is lower than that near the CRZ at Port2 except for in the case of H₂=0% $\phi=0.6$ and H₂=80% $\phi=0.3$. In these exceptions, the lower or almost equal level of peak near the CRZ indicates a delay in ignition on the CRZ side, possibly due to lower entrainment, as shown in Section 6.3.1. Further downstream, at Port 3, the peak near the PRZ vanishes as the interface line shifts closer to the wall, resulting in higher heat loss from the reaction zone. This corresponds to the region where recirculation towards the wall initiates. The flow impinges on the wall around Port 5, where the PRZ interface is no longer present, and the jet centerline is exposed to direct heat loss at the wall. At Ports 5 and 6, even the peak near the CRZ is negligible. There is a steep drop in temperature near the wall ($0 < r_{wall}/R_0 < 0.1 - 0.25$) due to heat losses. Interestingly, the temperature values remain similar for varying H₂ content. This may be due to backflow from the cooling system, which is discussed in detail in Appendix C.1.1

6.3.3. GAS COMPOSITION MEASUREMENT

The gas composition was measured by extracting samples through a probe traversed radially through access ports on the wall of the steel chamber. This provides an overview of the spatial distribution of the reaction zone and NO formation sites. The radial distribution of CO is shown in Fig. 6.8 and that of NO in Fig. 6.9. There are vertical lines, similar to those in the temperature plots, that indicate the location of the local jet center (-) and the interface with the PRZ and CRZ (- -), obtained from the flow field presented in Section 6.3.1.

The typical pathway for combustion of CH₄ is, CH₄ → CH₃ → CH₂O → HCO → CO → CO₂. Thus, in this study, CO measurements are considered a marker of a progressing reaction zone for fuel mixtures ranging from 0-80% H₂. The reader can refer to Appendix C.3.2 for CH₄ and CO₂ to verify the reaction progress. For H₂=0%, there is a high level of CO at Port 2. For $\phi=1.0$, a single peak is seen close to the jet centerline, while $\phi=0.6$ and 0.8 show two peaks. The two peaks in $\phi=0.8$ are less separated than those in $\phi=0.6$ and occur between the jet centerline and the CRZ interface. In the case of $\phi=0.6$, one peak is between the PRZ interface and the jet centerline and the other lies within the CRZ.

Further, the CO peak is higher near the CRZ than the PRZ. This biasing of the peaks may be explained based on the information on the velocity field in Section 6.3.1.

It is observed that the entrainment of fluid into the jet is stronger at the interface on the PRZ side in $0 < X < 100$ mm than the CRZ. This results in more recirculated combustion products at elevated temperatures and containing radicals entering the jet and mixing with fresh reactants on the PRZ side, resulting in more dilution of the fresh reactants and earlier reaction progress. On the CRZ interface side, the ignition and resulting heat release reaction are slower due to less dilution with recirculated hot products, resulting in less reaction progress and higher CO. In the case of $H_2=0\%$ $\phi=0.6$, the CO peak lying in the CRZ suggests that the process is driven by turbulent diffusion at the interface, where some fresh reactant mixes with the hot products, resulting in a low fresh mixture fraction that ignites. This is also the observation at Port 3.

At Port 3 and 5, for $H_2=0\%$ $\phi=0.8$ and 1.0, there is lower CO towards the chamber center, and the value increases near the wall due to a slowing down of reactions because of heat loss, as seen in the temperature profiles in Fig. 6.7. The CO value is comparatively low (<100 ppm) at Port 3 and 5, indicating that most heat release reactions occurred upstream. Thus, the recirculated gases can be considered to be fully burnt products. On the other hand, for $\phi=0.6$, there is a significant CO value at Port 3, thus leading to some unburnt mixture being recirculated in the PRZ. This can also be seen through high CO values in the PRZ at Ports 2 and 3 for this case.

The 50% and 80% H_2 cases with $\phi=0.6$ and 1.0 have a very low level of CO in all Ports with a single peak at Port 2 and the magnitude decreases in Port 3 and 5 successively. This indicates that the reaction initiated and progressed significantly before the axial location of Port 2. For 80% H_2 and $\phi=0.3$, CO has a uniform radial distribution at Port 2, and the value increases at Port 3 and decreases at Port 5, indicating a distributed reaction zone centered around Port 3. The biasing of the CO peak towards the CRZ interface at Port 2 and 3 is also seen for $\phi=0.6$, $H_2=50$ and 80% at Port 3 and $H_2=80\%$ at Port 2. At Port 5, $\phi=1.0$ has higher CO than $\phi=0.6$. This may be due to the CO-CO₂ equilibrium shift in the backward direction due to the lack of excess O₂ and higher adiabatic flame temperature. CO values are higher near the wall due to flame quenching due to heat losses and decrease towards the center due to higher temperatures.

The NO radial distribution at Port 2, 3, and 5 is shown in Fig. 6.9. For the case of 0% H_2 , for $\phi=1.0$ and 0.8, there is a trough in NO at Port 2, the region within the jet. At Ports 3 and 5, the distribution increases from the wall to the chamber center. NO is also higher for higher ϕ . In the cases of 50 and 80% H_2 , the trough at Port 2 is somewhat visible for $\phi=1.0$, but for the rest of the cases and Ports, the values are either increasing from wall to centerline or almost constant. This is opposite to the CO trend but may be expected as the temperature increases towards the centerline. However, the temperature does not rise monotonically and has peaks around the edge of the jet, but the NO profile does not respond accordingly. This may be due to low oxygen levels in the recirculated products and the slow NO formation rate in a fast-moving flow.

The NO, measured at the exhaust of the quartz chamber configuration and compared for all operational conditions, is shown in Fig. 6.10a. Ultra-low levels of NO (<5 ppm) were achieved at extremely lean conditions ($\phi < 0.6$), and these conditions were only achievable, i.e., possible to stabilize in the chamber, with higher levels of H_2 in the

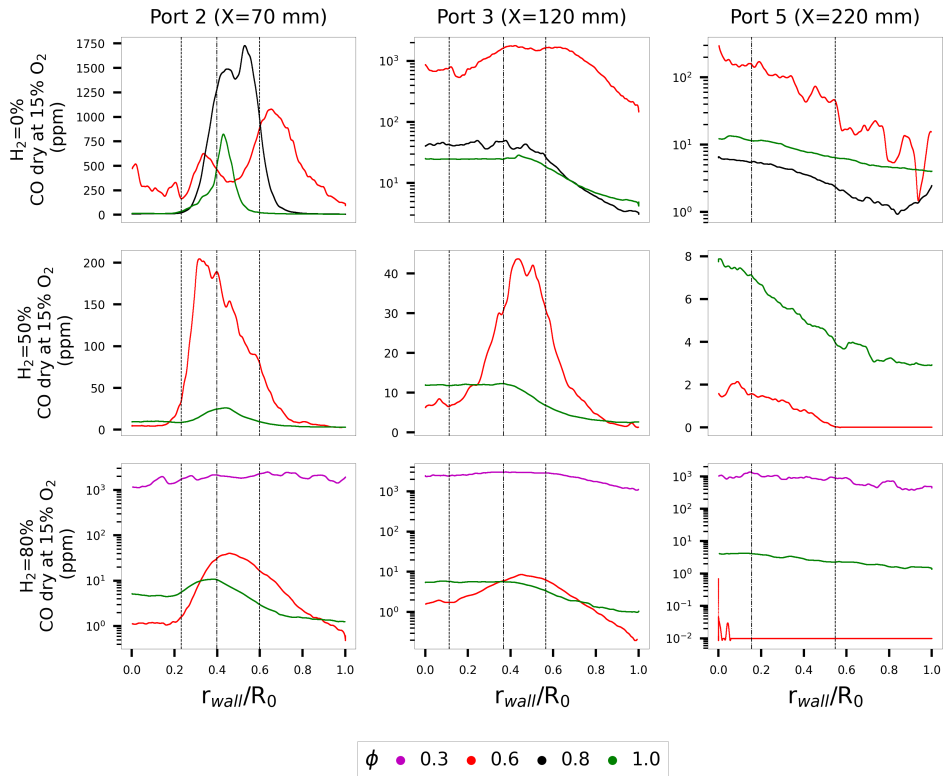


Figure 6.8: CO mole fraction v/s radial location at Port 2, 3, 5. The vertical lines indicate the local jet center (-), PRZ, and CRZ (- - on the left and right of the jet centerline, respectively).

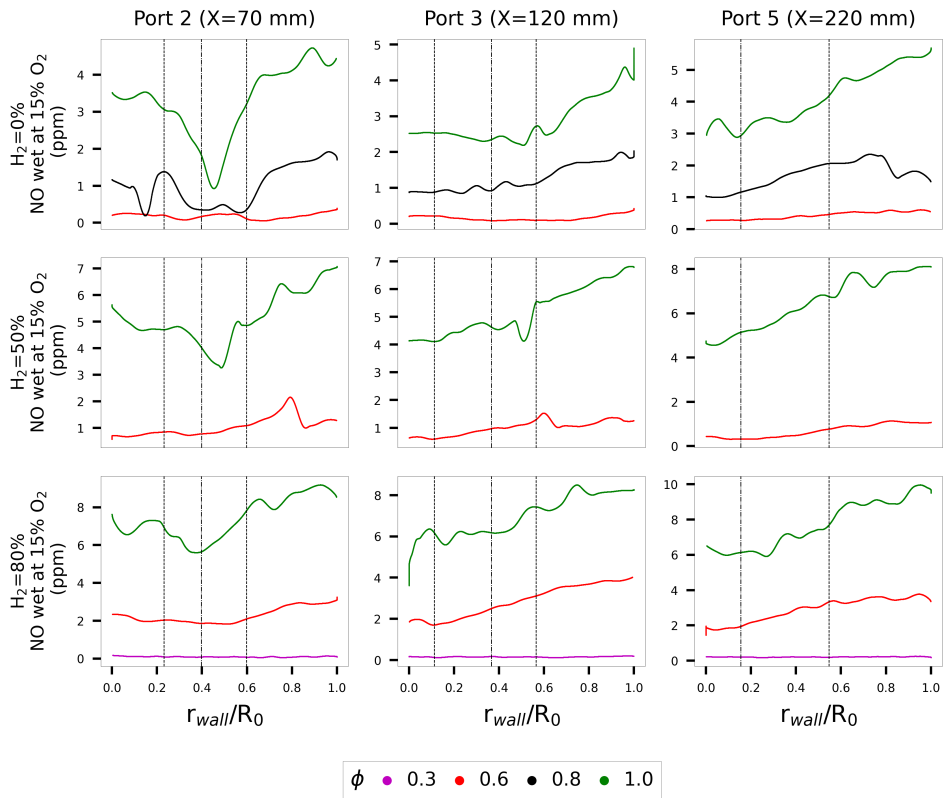


Figure 6.9: NO mole fraction v/s radial location at Port 2, 3 and 5. The vertical lines indicate the local jet center (-), PRZ, and CRZ (- -) on the left and right of the jet centerline, respectively.

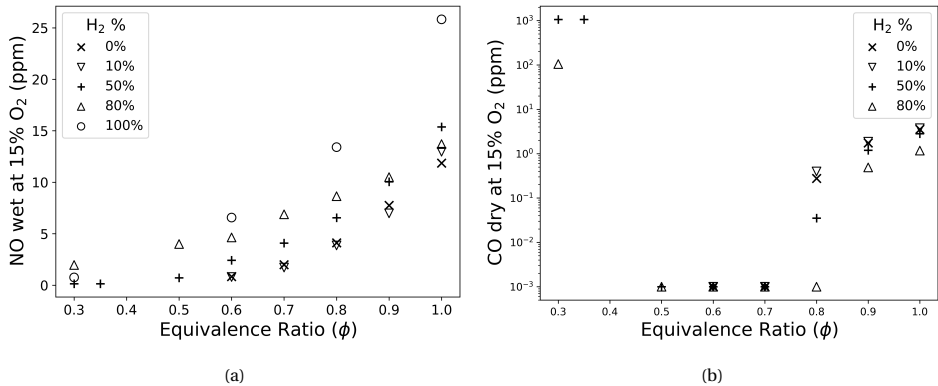
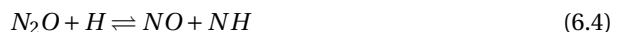


Figure 6.10: NO and CO measured at the exhaust of combustor with the quartz chamber configuration

fuel mixture. However, for $H_2=50\%$ $\phi < 0.4$, the corresponding CO levels are high ≈ 1000 ppm, as shown in Fig. 6.10b. This indicates that for these conditions, a lower jet velocity would be preferred to increase the residence time for CO consumption with possibly minimal impact on NO, which is already ultra-low. NO increases with ϕ and seems generally higher for higher H_2 content in the fuel for the same ϕ . One can also observe that the case of 80% H_2 goes off trend and does show higher NO than the 100% case at $\phi=0.3$ while having lower NO than the 50% case at $\phi=1.0$. If one observes the adiabatic flame temperature of these fuel mixtures in Table C.1, the value is higher for higher H_2 content. However, the difference is minimal, i.e., ≤ 100 K. Thus, other factors may be responsible for the NO trend with respect to $H_2\%$. CO levels at the exhaust increase with equivalence ratio and also increase suddenly at $\phi < 0.4$. The addition of H_2 decreases CO for the same ϕ .

The temperature throughout most radial locations is less than 1800 K, avoiding the typical temperature range of thermal NO_x formation. NO of a similar order of magnitude in the outer and inner recirculation regions may also indicate that although the thermal pathway is subdued, other pathways of NO_x , such as N_2O and NNH pathways, may play an important role, such that they are more dependent on gas composition than temperature. In all of the NO formation pathways, H and OH radicals play an essential role, as shown in the following equations:



In the thermal pathway, OH is responsible for the final production of NO (Eqn 6.3, in the N_2O pathway, the H radical leads to conversion of N_2O to NO (Eqn 6.4) and in the NNH pathway, H radical leads to NNH formation which is later oxidized to NO (Eqn 6.5).

Thus, the increasing concentration of H/OH radicals would aid in NO production, which would be the case for higher H₂% in the fuel mixture.

6.3.4. DSLR RESULTS

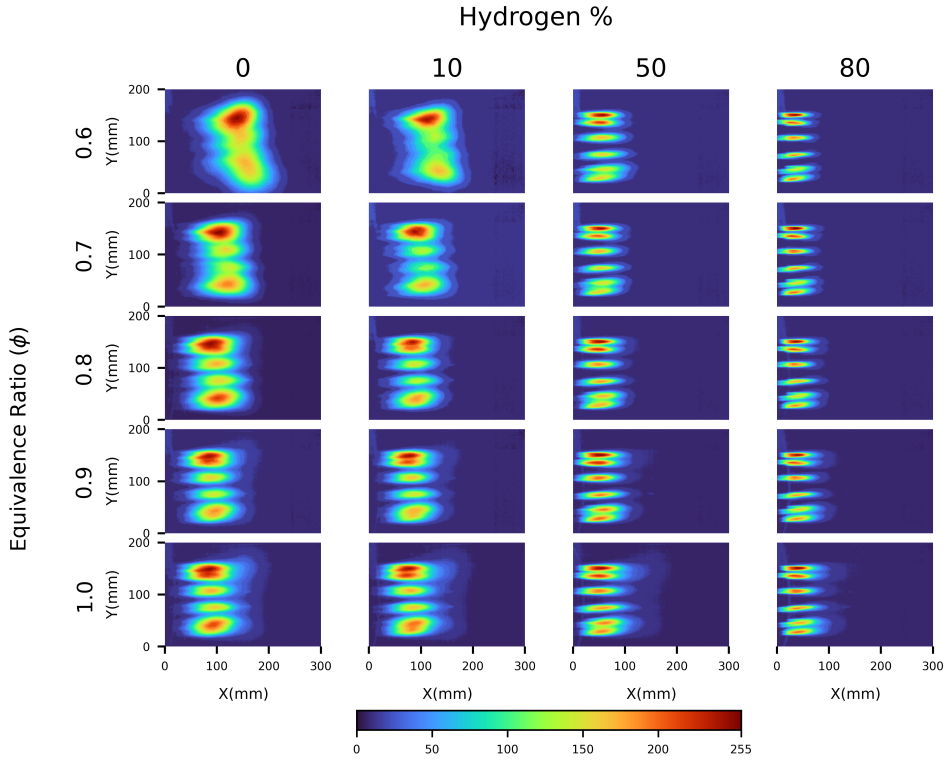


Figure 6.11: Average normalized chemiluminescence images obtained from the blue component of Nikon D7500 RGB sensor.

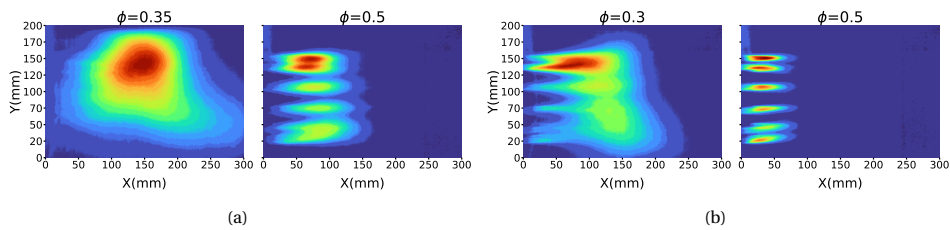


Figure 6.12: Average normalized chemiluminescence images for H₂= (a)50% (b)80%. Colorscale same as in Fig. 6.11.

Figure 6.11 shows the average flame chemiluminescence, where the columns represent the variation of H₂%, from 0-80% in the fuel mixture, while the rows represent dif-

ferent equivalence ratios. The ultra-lean cases of $H_2=50$ and 80% are shown in Fig. 6.12a and Fig. 6.12b, respectively, and the case of $H_2=100\%$ is shown in Appendix C.3.4. The field of view along the X axis ranges from the burner head up to $X=300$ mm, whereas the Y axis ranges over almost the entire diameter of the chamber, leaving out some regions near the wall. For $H_2=0$ and 10% , as ϕ increases from 0.6 to 1.0, the flame zone center shifts upstream towards the burner head, from $X\approx 150$ mm to $X\approx 90$ mm and transitions from spatially distributed to compact. Similarly, increasing H_2 content to 50/80/100% makes the flame more compact and stabilizes upstream at $X\approx 25$ mm. For higher H_2 content, 50/80/100%, the average flame zone is less sensitive to the equivalence ratio due to enhanced reaction rates, which also leads to the flame attaching to the nozzle. The images towards the lean limits, i.e. $\phi=0.6$ at $H_2=0\%$ (Fig 6.11), $\phi=0.35$ at $H_2=50\%$ (Fig 6.12a) and $\phi=0.3$ at $H_2=80\%$ (Fig 6.12b), have the most visually distributed regime. For each of these cases of $H_2\%$, the reaction zone could not be stabilized within the chamber for a lower ϕ at the same nozzle bulk velocity. The case of $\phi=0.3$ and $H_2=80\%$ shows a dual flame nature with a concentrated flame region closer to the nozzle and a distributed flame region further downstream in the chamber. This data shows that the addition of H_2 can enable the stabilization of a reaction zone at significantly leaner equivalence ratios.

FLAME KERNEL STATISTICS

The statistical behavior of instantaneous ignition kernels is captured by detecting clusters in the variance images as explained in Section 6.2.2. The characteristics of these clusters are quantified by assembling probability distribution functions (PDFs) for specific parameters, collected over clustered samples from ~ 200 images. The 100% H_2 PDFs are not constructed as the signal-to-noise ratio of the variance images was too low to identify kernels from the background. The first parameter is the aspect ratio (AR) of the smallest area rectangle enclosing a cluster. Larger AR indicates longer, elliptic flame kernels, while smaller AR indicates more circular ones.

Figure 6.13a shows a comparison of PDFs for $H_2=10\%$ for varying equivalence ratios. Increasing ϕ leads to a shift in the PDF peak from lower aspect ratios to higher values. Further, the PDF tails are also extended to much higher values. Figure 6.13b compares PDFs at $\phi=0.6$ for varying $H_2\%$ along with two ultra-lean cases, which have an in-fill under the curve. Increasing $H_2\%$ leads to a clear increase in aspect ratio with a prominent extension of the tails. In the $H_2=50\%$ case, the leanest condition of $\phi=0.35$ shows a compact PDF with a peak around 1.75, which is lower than the location of the peak for $\phi=0.6$, indicating a shift to rounder flame kernels. In the $H_2=80\%$, the leanest condition of $\phi=0.3$ shows a distributed PDF with two peaks, one around $AR=2$ and the other at $AR=6$. There is certainly a shift in structure from the $\phi=0.6$ case, but it also corroborates well with the observation of a dual flame structure in the mean image in Fig 6.12b. The AR PDF shows that this case has two types of flame kernels and thus indicates a transition case of stabilization mechanism.

Next, PDFs of the axial location of the center of mass of a cluster (X_{COM}) are extracted. This provides information on the probable location of flame kernels along the axial direction of the combustor. A lower value of X_{COM} means that the kernels are stabilizing in the initial regions of the jet where there is a high mean axial velocity and high turbulent fluctuation, and this is only possible if these mixtures have a high consumption

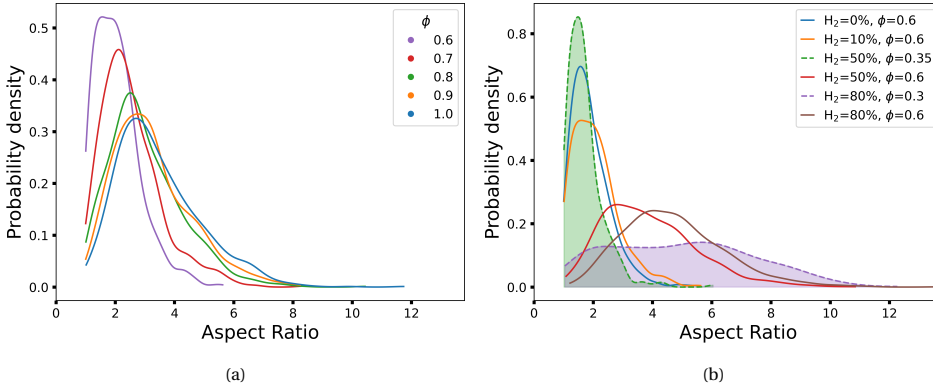


Figure 6.13: PDF of aspect ratio of flame kernels at (a) $H_2=10\%$ (b) varying $H_2\%$ at $\phi=0.6$ and ultra-lean conditions ($\phi<0.5$).

speed or low autoignition delay time. This can be ascertained as the inlet velocity of the nozzle was kept constant across cases. Figure 6.14a compares the PDFs for $H_2=10\%$ at varying ϕ . Reducing ϕ leads to a clear shift in the peak towards a larger X_{COM} . For $\phi=1.0$, the peak occurs at $X_{COM}\approx 40$ mm; for the leanest case of $\phi=0.6$, it moves towards 110 mm. Thus, correlating with the flow field, the higher ϕ cases have kernels distributed in a region dominated by a recirculation inflow from the PRZ and where the jet has a "belly" towards the centerline. The leaner cases stabilize kernels downstream in the region where the jet deviates towards the wall, and there is an outflow into the PRZ from the jet. Thus, the reactants may already be mixed with the recirculated gases in the lean cases and comprise a diluted mixture.

Figure 6.14b compares the PDFs at $\phi=0.6$ for varying $H_2\%$ along with two ultra-lean cases, which have an in-fill under the curve. For constant ϕ , there are clearly two flame stabilization regions. Higher $H_2\%$ cases (50/80%) stabilize upstream indicated by lower X_{COM} (≈ 25 mm) while lower $H_2\%$ cases stabilize downstream (≈ 100 -125 mm) with a wider distribution, indicating a wider spatial region of flame kernel occurrence. The ultra-lean cases, which occur at higher $H_2\%$, show separate characteristics. While the $H_2=80\%$, $\phi=0.3$ case shows a concentrated PDF peak at lower X_{COM} with a long tail having significant area under the curve, the $H_2=50\%$, $\phi=0.35$ shows a peak at around 110-140 mm with a wide distribution similar to the low $H_2\%$ cases.

FLAME STABILIZATION MECHANISM

The recirculating hot products serve as an "igniter" for the fresh reactant jet stream, as shown in Fig 6.15. They interact at a turbulent-turbulent interface. Suppose the gases from the two streams mix completely before igniting. In that case, it leads to the formation of an autoignition kernel that would evolve evenly in all directions, thereby leading to a low aspect ratio (≈ 1) flame kernel. On the other hand, if the ignition occurs by diffusion of heat and radicals across the interface, i.e., flame propagation, the mixture ignites before complete mixing, leading to a flame kernel that would align with the interface, leading to longer, larger aspect ratio kernels. From the observed results, cases with lower

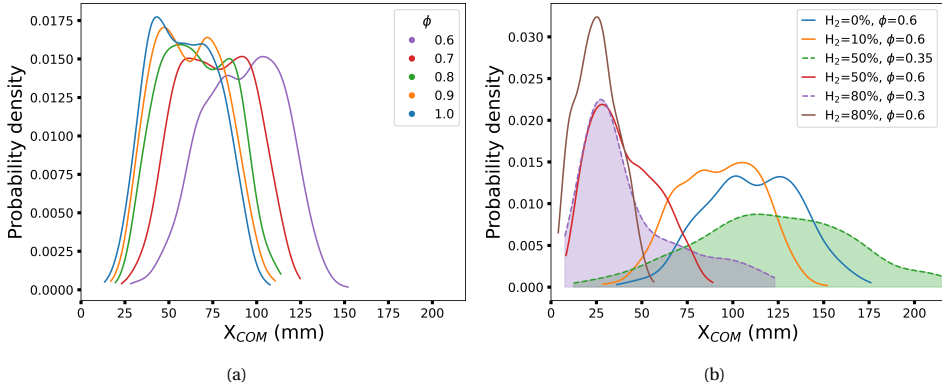


Figure 6.14: PDF of x location of Center of Mass(COM) of flame kernels at (a) $H_2=10\%$ (b) varying $H_2\%$ at $\phi=0.6$ and ultra-lean conditions ($\phi<0.5$).

6

AR tend to have larger X_{COM} and are located near the region where recirculation outflow from the jet begins. In comparison, higher AR are located more upstream, where there is an influx of recirculating gases. Thus, although not a sufficient condition, larger aspect ratio flame kernels indicate a higher probability of flame propagation, while lower aspect ratio kernels indicate autoignition stabilization. Thus, H_2 addition shifts the CH_4 flame from distributed and autoignitive to concentrated, flame propagation dominated stabilized. This is also consistent with Fig. 6.6, where the flame regimes are indicated on the Borghi diagram, where the mixtures tending to flame propagation lie in the lower limits of the BPTRZ region while the autoignition ones lie closer to the WSR/Broadened Reaction region. The case of $H_2=80\%, \phi=0.3$ presents a dual nature, having both flame propagation and autoignition play significant roles in the stabilization. Thus, it represents a transition case where a further reduction in equivalence ratio would push it completely to autoignition stabilization, and an increase in $H_2\%$ would push it towards flame propagation.

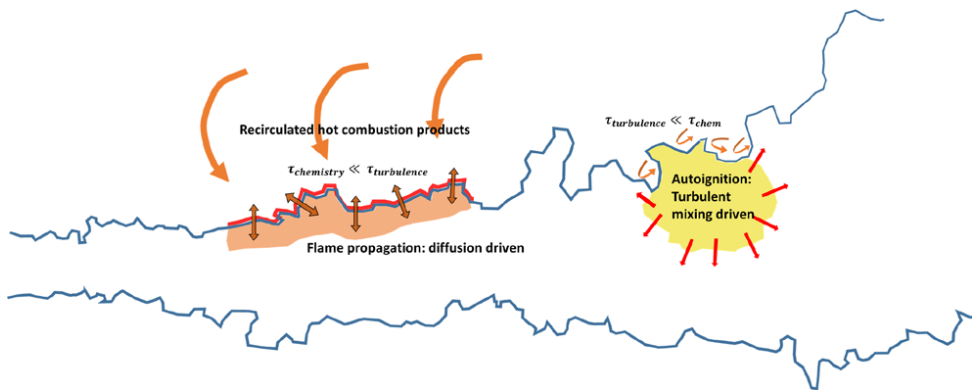


Figure 6.15: Two types of ignition mechanisms

6.4. CONCLUSION

The stabilization of the reaction zone and ensuing emissions in a premixed jet-stabilized combustor were investigated for CH₄-H₂ fuel admixtures. The combustor was operated at constant jet velocity, and air preheat temperature while varying the equivalence ratio (ϕ) and H₂ content in the fuel mixture from 0 to 100%. PIV measurements were done to measure the flowfield; the temperature was measured using an S-type thermocouple, the gas composition was measured by a suction probe attached to a gas analyzer unit, and chemiluminescence imaging was done using a DSLR camera to image the average flame as well as build PDFs of the fluctuating flame kernels.

This paper shows results on the flow field and reaction zone characteristics which can be used as guidelines by engineers while designing a jet-stabilized combustor. The results show that this combustor can stabilize a wide range of CH₄-H₂ mixtures, facilitating fuel-flexible operations. However, to obtain minimum NO_x and CO emissions, the equivalence ratio for each H₂% needs to be specifically chosen. A higher H₂% allowed for stabilizing a leaner fuel-air mixture before lean blowout occurred. Further analysis was done to identify the flame stabilization mechanisms involved in this combustor based on flame kernel properties, which were shown to vary with H₂% and ϕ . The following are the main conclusions:

- (i) The measured flow field of this combustor reveals a jet interacting with a Peripheral and Central Recirculation Zone (PRZ and CRZ) with an overall recirculation ratio estimated to be ~ 1.2 on a mass basis. The PRZ recirculation by volume is about 2 times that of the CRZ. There is a higher entrainment on the PRZ side than on the CRZ side, which leads to a different rate of reaction progress on the two sides of the jet due to variation in the dilution of fresh reactants in the jet by hot products, as is seen by the CO and temperature distributions.
- (ii) The heat loss from the walls influences the temperature and gas composition profiles. Quenching of the flame at the wall leads to higher CO and lower temperature in the PRZ.
- (iii) H₂% and ϕ had a significant effect on the flame stabilization location and mechanism.
 - (a) Theoretically, by plotting the operating conditions on the Borghi diagram, it is seen that most conditions lie in the Broadened Preheat Thin Reaction Zone regime. The addition of H₂ pushes the conditions towards the corrugated flamelet regime while decreasing equivalence ratio pushes them towards the Well Stirred Reactor/Broadened reaction regime. However, for successful stabilization of very lean mixtures, a higher H₂% is required.
 - (b) Chemiluminescence imaging reveals the average flame positions, where the addition of H₂ pushes the flame upstream, towards the nozzle, and makes it compact, while a leaner equivalence ratio leads to one stabilized downstream in a distributed manner.
 - (c) The ignition mechanism is interpreted from the probability distributions of aspect ratio (AR) and axial location (X_{COM}) of the flame kernels identified

from the chemiluminescence images. Higher aspect ratio kernels stabilizing upstream are seen for higher H_2 content and higher equivalence ratios, indicating flame propagation dominant stabilization. On the other hand, lower aspect ratio kernels are seen for lower H_2 content and lower equivalence ratios, indicating an autoignition dominant stabilization mechanism.

(iv) Effect of $H_2\%$ and ϕ on emissions:

- (a) NO levels increase with increasing H_2 in the fuel mixture for the same ϕ . A higher $H_2\%$ leads to a higher concentration of H/OH radicals that enhance the N_2O/NNH pathway and play a role in the final steps of the thermal pathway. Further, longer effective residence time of hot gases due to upstream stabilization of the reaction zone for higher H_2 content leads to higher NO. However, increasing $H_2\%$ allows for the stabilization of a leaner fuel-air mixture, which leads to lower NO at the exhaust.
- (b) Distributed reaction zones are formed at the leanest conditions of each $H_2\%$ case. For $\phi < 0.5$, this leads to ultra-low NO but also high values of CO, even at Port 5 and the exhaust. These cases also tend to have flatter/distributed temperature profiles. In these cases, operating at lower jet velocities might be more suitable for providing a longer residence time to reduce CO.

7

CONCLUSIONS AND RECOMMENDATIONS

यह महान दृश्य है,
चल रहा मनुष्य है,
अश्रु, स्वेद, रक्त से
लथ-पथ, लथ-पथ, लथ-पथ,
अग्निपथ! अग्निपथ! अग्निपथ!

*What greater spectacle,
Than to see such a human walk,
Who in tears, sweat and blood,
Is soaked, covered and coated;
And still walks the Path of fire! Path of fire! Path of fire!*

Harivansh Rai Bachchan

Flameless combustion has the potential to give high combustion efficiency while producing low NO_x emissions. This regime may be produced in jet-stabilized combustors where reactants enter the combustion chamber through high-velocity jets and the confinement results in the formation of recirculation zones. This causes hot burnt products to be fed back to the fresh reactants and mix with them, generating hot-vitiated fuel-oxidizer mixtures.

The current work explores the fundamental phenomenology of such a combustor. This is done by studying the autoignition characteristics of the mixtures generated and the flow physics of a canonical case representing the turbulent interface between hot diluents and fresh reactants in a practical combustor. Finally, the performance of such a combustor with methane-hydrogen admixtures is studied in the context of flame zone stabilization and emissions. The main contributions of this thesis are summarized in Fig 7.1, with the type of contribution mentioned in brackets (I: Phenomenology, II: Methodology, III: Dataset). This chapter presents the main conclusions and puts the overall research in perspective.

Phenomenology of Combustion in a Jet-Stabilized Combustor

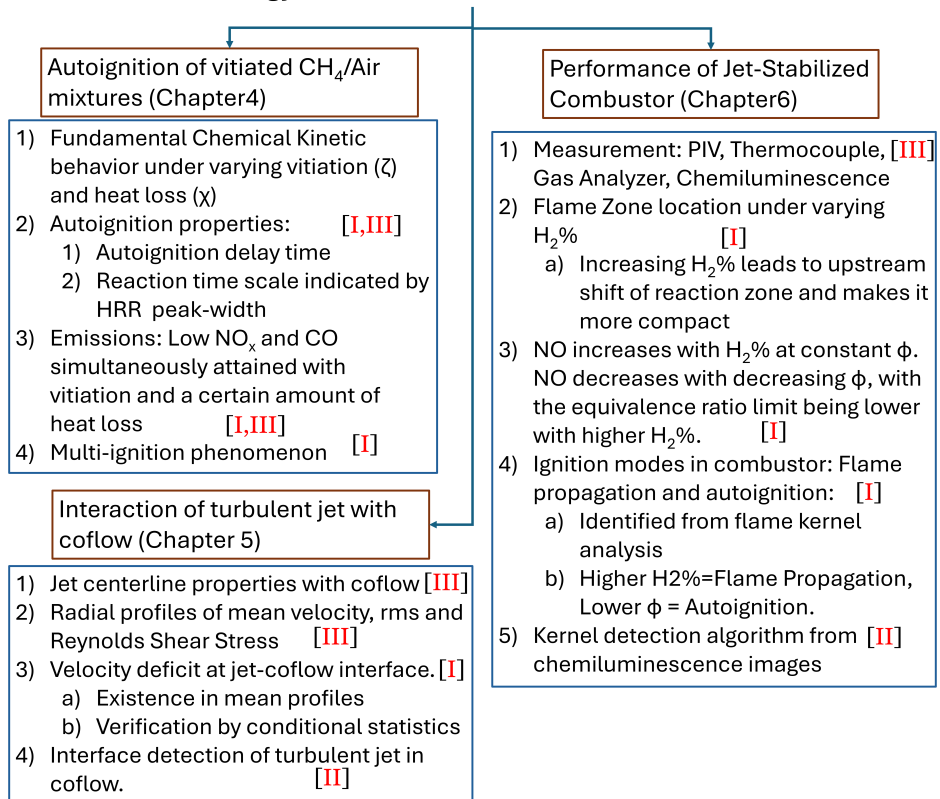


Figure 7.1: Thesis summary and contributions. Type I: Phenomenology, II: Methodology and III: Dataset

7.1. CONCLUSIONS

7.1.1. AUTOIGNITION OF CH₄/AIR MIXTURES VITIATED BY EXHAUST GASES

Jet-Stabilized combustors rely on internally recirculated hot product gases to stabilize a reaction zone. This leads to vitiated mixtures where the fresh reactants, injected in premixed condition, mix with hot products. These hot products contain not only stable species such as CO₂, N₂, H₂O and CO, but also radicals such as OH, H, and O, which occur in equilibrium. The recirculation zones also interact with the walls of the combustor and may thus undergo heat loss. Thus, the effect of vitiation represented as a citation fraction ζ , and the effect of heat loss, represented by a heat loss factor, χ , on the autoignition characteristics and resulting emissions of CH₄/Air mixtures vitiated by hot products of combustion, were investigated. Ignition was identified using the criteria of product of mole fraction of OH and CH₂O, which is used as an indicator of heat release rate (HRR). Simulations were done in a 0-D reactor for $\phi=0.3, 0.55, 0.75$ and ζ χ varied between 0 and 1. Following were the observations and conclusions:

- The autoignition delay time decreases with increasing ζ and increases with increasing χ . For sufficiently high ζ , the autoignition delay for all values of χ attains similar values, which indicates the importance of radicals in determining it.
- The peak-width of HRR peak is used to indicate the reaction time scale. Based on this, the reaction time scale is seen to be almost constant with a slight increase, with increasing vitiation at adiabatic conditions. However, if heat loss is factored in, the timescale first increases with vitiation and then decreases. For ultra-lean mixtures ($\phi=0.3$), at $\chi>0$, a monotonic increase was seen. This shows that the notion of a distributed reaction zone under vitiated conditions may not be very prominent under adiabatic conditions for such mixtures, but with some heat loss, this characteristic is significantly present.
- NO_x emissions are seen to remain nearly constant with increasing vitiation under adiabatic conditions. CO under these conditions shows a slight increase. However, with heat loss, i.e., $\chi>0$, NO_x and CO may be simultaneously reduced. This is attributed to the reduction in mixture temperature, while the increase in radicals ensures complete oxidation of CO. Thus, for premixed conditions, simply increasing vitiation does not lead to low NO_x combustion as expected from the Flameless regime, but instead, the combination with heat loss can cause a significant reduction while maintaining, if not improving combustion efficiency.
- Multi-ignition phenomenon was observed through more than one peak in HRR, which also corresponded to multiple peaks of the gradient of temperature with time. Two peaks were observed; the first one is termed a pre-ignition peak, which does not lead to a significant temperature change but causes a change in the composition, and the second one is called the main ignition peak, where the major temperature rise associated with combustion occurs. The two peak regime was more likely to occur under conditions with moderate vitiation and high heat loss. The pre-ignition peak occurs due to an initial radical pool originating from the hot-product vitiation. The peak is a result of falling OH and rising CH₂O mole

fractions. At sufficient vitiation and heat loss, the initial OH pool leads to CH₂O and HCO formation, and the reduced temperature due to heat loss slows down the OH production pathway. After a significant decline in OH, the reactions slow down, and cumulatively, over time, OH concentration starts rising. This leads up to the main ignition event.

This study shows that the characteristics of the distributed reaction zone and low NO_x commonly associated with Flameless combustion are best achieved with hot-product vitiation and some heat-loss for premixed reactants. Further, there are certain conditions when multi-ignition may occur. This must be taken into account while interpreting experimental and numerical data.

7.1.2. PHYSICS OF THE TURBULENT INTERFACE IN A TWO-STREAM SYSTEM

The flow field in a jet-stabilized combustor comprises a turbulent jet interacting with turbulent recirculation zones. The turbulent/turbulent interface determines the mixing of recirculated hot products with fresh reactants in the jet. The turbulent-jet-in-coflow was chosen as a canonical configuration to study the turbulent interface of a two-stream flow field. Particularly, it was investigated whether a jet-in-coflow could be represented as an equivalent free-jet by appropriate scaling. The flow field was measured using planar PIV in the region $0 \leq x/D \leq 40$ for varying coflow ratios, $U_{\text{coflow}}/U_j = 0, 0.09, 0.16,$ and 0.33 . The jet was maintained at a constant $Re=14000$ and the coflow turbulence intensity was low ($<6\%$). In this case, the coflow ratio was varied to emulate conditions that may be produced to increase the vitiation ratio in a jet-stabilized combustor. In practical systems, the coflow stream produces a boundary layer over the central jet pipe. The Re_θ (Reynolds number based on momentum thickness) was shown to increase with increasing coflow ratio. The main conclusions from this investigation were:

- The centerline trends revealed some differences between a scaled turbulent jet-in-coflow and free turbulent jet. A higher coflow ratio resulted in a reduced mean centerline velocity decay rate, reduced jet spreading, and a shifting of the virtual origin backward. The turbulent coflow is a source of additional axial momentum to the turbulent jet, observed by a rise along the centerline. For a turbulent free jet, this value remains constant.
- The radial profiles revealed an axial velocity deficit at the interface of the jet and coflow. This is attributed to the initial conditions of the coflow where a boundary layer is formed over the external wall of the pipe generating the jet. Further, the turbulence intensity and Reynolds Shear Stress peak within the jet core, as seen in the radial profiles, was higher for higher coflow ratios. The deficit region is not completely filled by momentum transfer, although there is a higher level of turbulence both in the jet and the coflow for higher coflow ratios. This suggests the existence of an isolating layer.
- Mean field statistics may get smeared due to the meandering turbulent interface. To verify and further investigate the mechanism behind the above observation, conditional statistics were extracted. An algorithm was developed to detect the interface from PIV data. This was done by filtering the image using a threshold

vorticity. The threshold value was determined for each frame based on the curve of the area detected for varying threshold values. Due to certain levels of turbulence in the coflow, mere thresholding did not reveal a unique interface; hence the DBSCAN algorithm was used to cluster regions within and outside the jet. The DBSCAN algorithm is an image-processing algorithm used to identify clusters in noisy environments. This method of interface identification has potential applications for detection in flow fields of combustion chambers where two or more turbulent streams interact. Following observations and conclusions were drawn from the conditional profiles:

- The axial velocity deficit and higher Reynolds Shear Stress peak for higher coflow ratios are observed in the conditional profiles, confirming the observations from the mean profiles.
- Coflow turbulence level is so low that it has little effect on the phenomenology. This is seen through the enstrophy diffusion profiles which are nearly identical for the varying coflow ratios.
- The initial boundary layer generates a "shielding effect", which is confirmed by the enstrophy dissipation profile. There was lower dissipation for a higher coflow ratio. This also explains the higher level of turbulence intensity and RSS within the jet core for higher coflow ratios.
- The tortuosity of the interface is lower for higher coflow as it is dominated by the gradient of axial velocity across the interface, which leads to Kelvin-Helmholtz instabilities rather than the rising coflow turbulence levels. This is further evidence that a low turbulence level does not penetrate the viscous superlayer at the turbulent interface.

The "shielding effect" has implications on practical flameless combustion systems with two coflow interacting streams. In the case of low coflow turbulence, there could be the possibility of reduced mixing, affecting the flame characteristics such as lift-off height and stability margin.

7.1.3. REACTION ZONE STABILIZATION AND EMISSIONS FROM A JET STABILIZED COMBUSTOR WITH CH_4/H_2 ADMIXTURES

Hydrogen is poised to be a future energy carrier and can serve towards carbon emission reduction by adoption in combustion devices. This may take place in phases where it is blended with natural gas/ methane due to the limited availability of green hydrogen in the near future. Chapter 6 elucidates the combustion of methane-hydrogen admixtures in a jet-stabilized combustor. A more detailed understanding of reaction zone stabilization and emissions was obtained through experiments and the following conclusions were made:

- PIV measurement of the flow field enabled quantification of recirculation in the Peripheral and Central recirculation zones. The PRZ has twice the recirculation of the CRZ by volume. The overall recirculation ratio was 1.2 by mass.

- An algorithm was developed to identify flame kernels from instantaneous chemiluminescence images. The probability distribution of the properties of these kernels, such as aspect ratio, location, and rotation angle, can be used to gain insights into the phenomenology. A PDF peak at a larger aspect ratio indicates elongated ellipses, which are stabilized by flame propagation, while a peak at a smaller value indicates circular kernels stabilized by autoignition.
- Increasing hydrogen concentration in the fuel admixture leads to a shift of flame stabilization mechanism from autoignition to conventional flame propagation characterized by back diffusion of heat and species. Changing the equivalence ratio from very lean to stoichiometric also has the same effect.
- At constant nozzle velocity conditions, a higher amount of hydrogen in the fuel mixture causes the flame to stabilize upstream.
- Most of the operating points of the jet-stabilized combustor lie in the Broadened Preheat Thin Reaction Zone regime. The addition of H₂ in the fuel mixture at the same ϕ shifts the regime towards the corrugated flamelet regime while reducing ϕ shifts it into the Well Stirred Reactor/ Broadened Reaction regime.
- The addition of hydrogen allows a significantly leaner mixture to stabilize a reaction zone within the chamber.
- The temperature and CO radial measurements reveal the region of the fresh reactant jet and its interaction with the hot recirculation products at the edge of the jet where heat release occurs. Further, the recirculation zones may carry partially burnt product under leaner conditions indicated by higher levels of CO.
- At low ϕ conditions and reducing H₂ content in the fuel, distributed reaction zones are produced. However, in ultra-lean cases, incomplete combustion may occur, as revealed by higher CO values at Port 5. In these cases, it might be better to operate at low jet velocities, which could be obtained, for example, by using nozzles of larger diameter.
- NO at the exhaust rises with increasing H₂ in the fuel mixture due to a higher concentration of H/OH radicals. Further, longer effective residence time due to the flame zone stabilizing further upstream leads to higher cumulative NO.

7.2. DISCUSSION

The jet-stabilized combustor is suitable for Flameless/MILD combustion. In a premixed configuration, as is described in this thesis, significant NO_x reduction, compared to combustion of the mixture in a conventional flame, may only be attained when the process is combined with heat loss. Hydrogen can readily be combusted in the same geometrical configuration of the combustor and burner head used for methane, providing a fuel-flexible device. However, this leads to a shift in flame stabilization and increased NO_x at the same equivalence ratio at constant jet velocity. The jet-stabilized combustor offers a wide stability margin in terms of equivalence ratios for pure methane as well as

methane-hydrogen admixtures up to 100% hydrogen. Thus, low NO_x can be obtained by shifting the operating conditions to leaner equivalence ratios. Adding H_2 to the fuel mixture shifts the flame regime on the Borghi diagram but also moves it upstream due to higher reactivity. This could be used as a parameter to control the flame location and stabilize ultra-lean flames in a jet-stabilized combustor.

The strong recirculation zones produced in this combustor extend the stability margin in terms of the leanest equivalence ratio of mixture that can be combusted by providing a source of hot products with radicals that act as an igniter. This process occurs at the turbulent interface between the fresh reactant jet and the recirculation zones. The interface is the site of the initial mixing of hot products of combustion from the recirculation zones with the fresh reactants of the jet, giving rise to hot vitiated mixtures. The mixing governs the local vitiation fraction, ζ , and thus the autoignition properties. The relative value of turbulence timescales to the reaction timescale of the local mixture may determine whether the reaction zone stabilization is dominated by flame propagation or autoignition. Diffusion-governed flame propagation may be more dominant if the chemical timescales of heat release are smaller than the turbulent mixing time scales. This would lead to a concentration of high ζ pockets at the interface of the recirculation zone and fresh reactant jet, which would have a short ignition delay. This is especially true in the case of a fuel composition with higher H_2 content. If mixing time scales are smaller than or comparable to the heat release chemical timescales, the hot products can mix with the fresh reactants, forming homogeneous moderate ζ pockets, which have a longer ignition delay and autoignite further downstream in the flow. These tend to give more distributed reaction zones, noticed at leaner equivalence ratios and lower H_2 content in a CH_4 - H_2 fuel mixture.

The Peripheral Recirculation Zone (PRZ) is also subject to heat loss at the wall. Thus, the autoignition conditions of the mixtures established with the interaction of the PRZ and the jet would be governed more by the non-adiabatic cases simulated in Chapter 4. The heat loss is essential for producing a low NO_x regime as well as a distributed reaction zone, as is often associated with Flameless combustion, for premixed reactants in such a combustor.

Based on the learnings from a canonical jet-in-coflow flow field in Chapter 5, when the coflow has low turbulence, which would be the recirculation zones in the combustor, the extent of mixing at the jet-recirculation zone interface is governed more by the boundary layer formed around the jet nozzle by the surrounding flow than the turbulence intensity. This is attributed to the limited mixing due to the "shielding effect" of a region of velocity deficit originating upstream from the boundary layer generated by the surrounding flow over the nozzle structure. Thus, the mixing may be manipulated by experimenting with varying nozzle shapes and profiles at the burner head to control this boundary layer.

7.3. RECOMMENDATIONS FOR FUTURE WORK

This work encompassed a variety of numerical and experimental methods to arrive at conclusions about the phenomenology of a jet-stabilized combustor. However, there are limitations to the methodology and results, which give rise to recommendations for future research. The following are the limitations along with the corresponding recom-

recommendations:

- The hot vitiation considered in the 0D reactor simulations was from equilibrium state of combustion products. In a jet-stabilized combustor, there may be partially burnt mixtures that mix back with the fresh reactants. This can be simulated by defining a degree of completion of the reaction, such as a progress variable, and a corresponding design of experiments can be done.
- The phenomenon of multi-ignition is seen in numerical simulations but there is no experimental evidence. Specific experiments should be designed to observe this and verify its existence.
- The current work on turbulent-jet-in-turbulent-coflow reports results only for a low level of turbulence (<6%). Experiments should be performed at higher coflow turbulence intensities.
- Higher coflow ratios should be explored to observe the phenomenon in the limit of transition from jet to wake.
- The interface detection algorithm in Chapter 5 works in the canonical case but has not been shown on the flow field of a jet-stabilized combustor. This should be done and conditional statistics should be used to derive the entrainment ratio and compared with one obtained directly from the mean field.
- The quartz chamber and steel chamber have different levels of heat loss at the wall and thus may introduce a systematic error in the state for the same operating conditions. CFD analysis can be used to verify the influence of this on the flame state.
- The phenomenology of the ignition kernels is observed through chemiluminescence which is a line-of-sight approach. This should be validated with planar techniques such as PLIF and an intensified camera should be used to reduce the exposure time and hence the blur induced in the frame.
- The performance of the combustor was evaluated at constant jet velocity. It would be useful to conduct experiments with $\text{CH}_4\text{-H}_2$ admixtures at varying jet velocities, which would change the flow timescales, and verify if that leads to a shift in flame stabilization mechanism.
- NO_2 measurements were not possible due to the influence of water condensation due to the maximum temperature of the gas analyzer being 80°C . The only way to prevent condensation is by diluting the sample with a known amount of inert gas such as N_2 and then correcting the measurement for it. This should be done to get a total NO_x measurement as opposed to only NO .
- The probe measurements are intrusive and, hence, may affect the flow field. Further, traversing the gas probe radially could lead to varying quenching distances of the sample as different amounts of the probe are in the hottest parts of the combustor at different radial locations. Similarly, the temperature distribution on the

thermocouple sheath would also vary with radial location. These limitations may be checked and overcome by performing laser-based diagnostics such as CARS.

- The cylindrical nature of the chamber prevented the use of Schlieren imaging, which could have been powerful in identifying flame kernels. As opposed to the chemiluminescence signal, which grows fainter in the FC regime, this can be controlled by the artificial light source. It may be worthwhile to develop a chamber with flat windows such as a 4 or 8-sided one, keeping in mind the viewing planes required to perform PIV on the corresponding flow field.



BIBLIOGRAPHY

- [1] IPCC, *Climate Change 2023: Synthesis Report. Contribution of Working Groups I, II and III to the Sixth Assessment Report of the Intergovernmental Panel on Climate Change*, Tech. Rep. (2023).
- [2] UNFCCC, *The Paris Agreement*, in *Paris Climate Change Conference, COP 21* (2015).
- [3] UNFCCC, *Conference of the Parties serving as the meeting of the Parties to the Paris Agreement- Outcome of the first global stocktake. UNFCCC (United Nations Framework Convention on Climate Change)*, Tech. Rep. December (2023).
- [4] IEA, *Renewables 2023*, Tech. Rep. (IEA, Paris, 2024).
- [5] IEA, *Managing Seasonal and Interannual Variability of Renewables*, Tech. Rep. (IEA, Paris, 2023).
- [6] IEA, *Share of renewable electricity generation by technology, 2000-2028*, .
- [7] IEA, *Tracking Clean Energy Progress 2023*, Tech. Rep. (IEA, Paris, 2023).
- [8] S. Rosanka, C. Frömming, and V. Grewe, *The impact of weather patterns and related transport processes on aviation's contribution to ozone and methane concentrations from NO_x emissions*, *Atmospheric Chemistry and Physics* **20**, 12347 (2020).
- [9] V. Grewe, S. Matthes, and K. Dahlmann, *The contribution of aviation NO_x emissions to climate change: are we ignoring methodological flaws?* *Environmental Research Letters* **14**, 14 (2019).
- [10] J. Maruhashi, V. Grewe, C. Frömming, P. Jöckel, and I. C. Dedoussi, *Transport patterns of global aviation NO_x and their short-term O₃ radiative forcing - a machine learning approach*, *Atmospheric Chemistry and Physics* **22**, 14253 (2022).
- [11] European Council, *Directive 2010/75/EU Industrial Emissions*, *Official Journal of the European Union* **L334**, 17 (2010).
- [12] O. F. T. H. E. Council, *DIRECTIVE (EU) 2015/2193 OF THE EUROPEAN PARLIAMENT AND OF THE COUNCIL of 25 November 2015 on the limitation of emissions of certain pollutants into the air from medium combustion plants*, **2015** (2020).
- [13] U.S. EPA, *Epa-456/F-99-006R*, Tech. Rep. November (Clean Air Technology Center, U.S. Environmental Protection Agency, 1999).
- [14] L. D. Smoot, S. C. Hill, and H. Xu, *NO_x control through reburning*, *Progress in Energy and Combustion Science* **24**, 355 (1998).

- [15] Y. Liu, X. Sun, V. Sethi, D. Nalianda, Y. G. Li, and L. Wang, *Review of modern low emissions combustion technologies for aero gas turbine engines*, Progress in Aerospace Sciences **94**, 12 (2017).
- [16] S. Samuelson, *Rich burn, quick-mix, lean burn (RQL) combustor*, The gas turbine handbook, 227 (2006).
- [17] R. Stickles and J. Barrett, *TAPS II Combustor Final Report*, U.S. Department of Transportation - Federal Aviation Administration (2014).
- [18] R. Luckerath, W. Meier, and M. Aigner, *FLOX[®] Combustion at High Pressure With Different Fuel Compositions*, Journal of Engineering for Gas Turbines and Power **130**, 011505 (2008).
- [19] Y. Levy, V. Erenburg, V. Sherbaum, and I. Gaissinski, *Flameless Oxidation Combustor Development for a Sequential Combustion Hybrid Turbofan Engine*, in *Volume 4B: Combustion, Fuels and Emissions* (ASME, 2016) p. V04BT04A055.
- [20] F. Güthe, J. Hellat, and P. Flohr, *The Reheat Concept: The Proven Pathway to Ultralow Emissions and High Efficiency and Flexibility*, Journal of Engineering for Gas Turbines and Power **131**, 1 (2009).
- [21] M. R. Bothien, A. Ciani, J. P. Wood, and G. Fruechtel, *Toward Decarbonized Power Generation with Gas Turbines by Using Sequential Combustion for Burning Hydrogen*, Journal of Engineering for Gas Turbines and Power **141**, 1 (2019).
- [22] Y. Levy and T. Reichel, *AHEAD Deliverable 2.7: Feasibility of the hybrid combustion concept*, , 1 (2014).
- [23] J. Wunning, *FLOX-Flameless Combustion*, in *Thermprocess Symposium*, Vol. 80 (2003).
- [24] J. Wunning, *Flameless oxidation to reduce thermal NO_x formation*, Progress in Energy and Combustion Science **23**, 81 (1997).
- [25] J. G. Wunning, *FLAMELESS COMBUSTION AND ITS APPLICATIONS*, , 1.
- [26] M. Oberlack, R. Arlitt, and N. Peters, *On stochastic Damköhler number variations in a homogeneous flow reactor*, Combustion Theory and Modelling **4**, 495 (2000).
- [27] A. Cavaliere and M. de Joannon, *Mild Combustion*, Progress in Energy and Combustion Science **30**, 329 (2004).
- [28] M. De Joannon, A. Saponaro, and A. Cavaliere, *Zero-dimensional analysis of diluted oxidation of methane in rich conditions*, Proceedings of the Combustion Institute **28**, 1639 (2000).
- [29] B. Zhou, M. Costa, Z. Li, and M. Aldén, *Characterization of the reaction zone structures in a laboratory combustor using optical diagnostics : from flame to flameless combustion*, Proceedings of the Combustion Institute **36**, 4305 (2017).

- [30] A. A. Perpignan, A. Gangoli Rao, and D. J. Roekaerts, *Flameless combustion and its potential towards gas turbines*, *Progress in Energy and Combustion Science* **69**, 28 (2018).
- [31] G. Sorrentino, P. Sabia, M. De Joannon, A. Cavaliere, and R. Ragucci, *The Effect of Diluent on the Sustainability of MILD Combustion in a Cyclonic Burner*, *Flow, Turbulence and Combustion* **96**, 449 (2016).
- [32] G. Sorrentino, P. Sabia, P. Bozza, R. Ragucci, and M. de Joannon, *Impact of external operating parameters on the performance of a cyclonic burner with high level of internal recirculation under MILD combustion conditions*, *Energy* **137**, 1167 (2017).
- [33] G. Sorrentino, P. Sabia, M. de Joannon, P. Bozza, and R. Ragucci, *Influence of pre-heating and thermal power on cyclonic burner characteristics under mild combustion*, *Fuel* **233**, 207 (2018).
- [34] G. Sorrentino, U. Göktolga, M. De Joannon, J. Van Oijen, A. Cavaliere, and P. De Goey, *An experimental and numerical study of MILD combustion in a Cyclonic burner*, *Energy Procedia* **120**, 649 (2017).
- [35] P. Sabia, G. Sorrentino, P. Bozza, G. Ceriello, R. Ragucci, and M. De Joannon, *Fuel and thermal load flexibility of a MILD burner*, *Proceedings of the Combustion Institute* **37**, 4547 (2019).
- [36] G. Battista, G. Sorrentino, R. Ragucci, M. De, and P. Sabia, *Ammonia / Methane combustion : Stability and NO_x emissions*, *Combustion and Flame* **241**, 112071 (2022).
- [37] R. Sadanandan, R. Lückcrath, W. Meier, and C. Wahl, *Flame Characteristics and Emissions in Flameless Combustion Under Gas Turbine Relevant Conditions*, *Journal of Propulsion and Power* **27**, 970 (2011).
- [38] O. Lammel, H. Schutz, G. Schmitz, R. Luckerath, M. Stohr, B. Noll, M. Aigner, M. Hase, and W. Krebs, *FLOX® Combustion at High Power Density and High Flame Temperatures*, *Journal of Engineering for Gas Turbines and Power* **132**, 121503 (2010).
- [39] M. Severin, O. Lammel, H. Ax, R. Lückcrath, W. Meier, M. Aigner, and J. Heinze, *High Momentum Jet Flames at Elevated Pressure: Detailed Investigation of Flame Stabilization With Simultaneous Particle Image Velocimetry and OH-LIF*, *Journal of Engineering for Gas Turbines and Power* **140**, 041508 (2017).
- [40] M. Ferrarotti, M. Fürst, E. Cresci, W. De Paepe, and A. Parente, *Key Modeling Aspects in the Simulation of a Quasi-industrial 20 kW Moderate or Intense Low-oxygen Dilution Combustion Chamber*, *Energy and Fuels* **32**, 10228 (2018).
- [41] M. Ferrarotti, W. De Paepe, and A. Parente, *Reactive structures and NO_x emissions of methane/hydrogen mixtures in flameless combustion*, *International Journal of Hydrogen Energy* **46**, 34018 (2021).

- [42] A. S. Veríssimo, A. M. A. Rocha, and M. Costa, *Operational, Combustion, and Emission Characteristics of a Small-Scale Combustor*, *Energy & Fuels* **25**, 2469 (2011).
- [43] A. Veríssimo, A. Rocha, and M. Costa, *Experimental study on the influence of the thermal input on the reaction zone under flameless oxidation conditions*, *Fuel Processing Technology* **106**, 423 (2013).
- [44] A. Veríssimo, A. Rocha, and M. Costa, *Importance of the inlet air velocity on the establishment of flameless combustion in a laboratory combustor*, *Experimental Thermal and Fluid Science* **44**, 75 (2013).
- [45] A. S. Veríssimo, A. M. A. Rocha, P. J. Coelho, and M. Costa, *Experimental and Numerical Investigation of the Influence of the Air Preheating Temperature on the Performance of a Small-Scale Mild Combustor*, *Combustion Science and Technology* **187**, 1724 (2015).
- [46] R. Cabra, T. Myhrvold, J. Y. Chen, R. W. Dibble, A. N. Karpetis, and R. S. Barlow, *Simultaneous laser raman-rayleigh-lif measurements and numerical modeling results of a lifted turbulent H₂/N₂ jet flame in a vitiated coflow*, *Proceedings of the Combustion Institute* **29**, 1881 (2002).
- [47] B. Dally, A. Karpetis, and R. Barlow, *Structure of turbulent non-premixed jet flames in a diluted hot coflow*, *Proceedings of the Combustion Institute* **29**, 1147 (2002).
- [48] E. Oldenhof, M. J. Tummers, E. H. V. Veen, and D. J. E. M. Roekaerts, *Ignition kernel formation and lift-off behaviour of jet-in-hot-coflow flames*, *Combustion and Flame* **157**, 1167 (2010).
- [49] P. R. Medwell and B. B. Dally, *Experimental observation of lifted flames in a heated and diluted coflow*, *Energy and Fuels* **26**, 5519 (2012).
- [50] E. Oldenhof, M. J. Tummers, E. H. V. Veen, and D. J. E. M. Roekaerts, *Ignition kernel formation and lift-off behaviour of jet-in-hot-coflow flames*, *Combustion and Flame* **157**, 1167 (2010).
- [51] P. R. Medwell, P. A. M. Kalt, and B. B. Dally, *Imaging of diluted turbulent ethylene flames stabilized on a Jet in Hot Coflow (JHC) burner*, **152**, 100 (2008).
- [52] E. Oldenhof, M. J. Tummers, E. H. van Veen, and D. J. E. M. Roekaerts, *Role of entrainment in the stabilisation of jet-in-hot-coflow flames*, *Combustion and Flame* **158**, 1553 (2011).
- [53] P. R. Medwell, P. A. M. Kalt, and B. B. Dally, *Simultaneous imaging of OH, formaldehyde, and temperature of turbulent nonpremixed jet flames in a heated and diluted coflow*, **148**, 48 (2007).
- [54] Y. Minamoto, N. Swaminathan, R. S. Cant, and T. Leung, *Reaction zones and their structure in MILD combustion*, *Combustion Science and Technology* **186**, 1075 (2014).

- [55] Y. Minamoto, N. Swaminathan, S. R. Cant, and T. Leung, *Morphological and statistical features of reaction zones in MILD and premixed combustion*, *Combustion and Flame* **161**, 2801 (2014).
- [56] P. R. Medwell, D. L. Blunck, and B. B. Dally, *The role of precursors on the stabilisation of jet flames issuing into a hot environment*, *Combustion and Flame* **161**, 465 (2014).
- [57] R. L. Gordon, A. R. Masri, and E. Mastorakos, *Simultaneous Rayleigh temperature, OH- and CH₂O-LIF imaging of methane jets in a vitiated coflow*, *Combustion and Flame* **155**, 181 (2008).
- [58] R. L. Gordon, *A Numerical and Experimental Investigation of Autoignition*, August 2007 (2008).
- [59] X. Huang, *Measurements and model development for flameless combustion in a lab-scale*, Ph.D. thesis (2018).
- [60] M. Severin, O. Lammel, and W. Meier, *Laser diagnostic investigation of a confined premixed turbulent jet flame stabilized by recirculation*, *Combustion and Flame* , 112061 (2022).
- [61] R. L. Gordon, A. R. Masri, S. B. Pope, and G. M. Goldin, *A numerical study of autoignition in turbulent lifted flames issuing into a vitiated co-flow*, *Combustion Theory and Modelling* **11**, 351 (2007).
- [62] O. Schulz, T. Jaravel, T. Poinso, B. Cuenot, and N. Noiray, *A criterion to distinguish autoignition and propagation applied to a lifted methane-air jet flame*, *Proceedings of the Combustion Institute* **36**, 1637 (2017).
- [63] K. Aditya, A. Gruber, C. Xu, T. Lu, A. Krisman, M. R. Bothien, and J. H. Chen, *Direct numerical simulation of flame stabilization assisted by autoignition in a reheat gas turbine combustor*, *Proceedings of the Combustion Institute* **37**, 2635 (2019).
- [64] M. D. Joannon, G. Sorrentino, and A. Cavaliere, *MILD combustion in diffusion-controlled regimes of Hot Diluted Fuel*, *Combustion and Flame* **159**, 1832 (2012).
- [65] D. C. Vaz, *Towards the application of flameless combustion to micro gas turbines*, , 298 (2007).
- [66] M. Agelin-Chaab and M. F. Tachie, *Characteristics and structure of turbulent 3D offset jets*, *International Journal of Heat and Fluid Flow* **32**, 608 (2011).
- [67] M. Raffel, C. E. Willert, S. T. Wereley, and J. Kompenhans, *Particle Image Velocimetry A Practical Guide* (Springer, 2007).
- [68] T. T. Paschal, M. A. Turner, P. Parajuli, E. L. Petersen, and W. D. Kulatilaka, *High-speed oh^* And ch^* Chemiluminescence imaging and oh planar laser-induced fluorescence (Plif) studies in spherically expanding flames*, *AIAA Scitech 2019 Forum* , 1 (2019).

- [69] N. Otsu, P. L. Smith, D. B. Reid, C. Environment, L. Palo, P. Alto, and P. L. Smith, *Otsu 1979 Otsu Method*, IEEE Transactions on Systems, Man, and Cybernetics C, 62 (1979).
- [70] M. Ester, H.-P. Kriegel, J. Sander, and X. Xu, *A Density-Based Algorithm for Discovery Clusters in Large Spatial Databases with Noise*, in *Proceedings of 2nd International Conference on Knowledge Discovery and Data Mining* (1996).
- [71] G. Eula and A. Ivanov, *Theoretical and Experimental Investigations of an Opto-Pneumatic Detector*, Journal of Dynamic Systems, Measurement and Control 122, 1 (2000).
- [72] B. Worthington and H. von Hoersten, *Novel Differential Ultra-Violet Resonance Absorption Gas Analyzer for NOx Measurements in Continuous Emission Monitoring Systems*, Tech. Rep.
- [73] ABB, *Advance optima continuous gas analyzers AO2000 series Operator's Manual*, (2009).
- [74] ABB, *Magnos28*, Tech. Rep. November (2017).
- [75] K. Jasek and M. Pasternak, *Paramagnetic Sensors for the Determination of Oxygen Concentration in Gas Mixtures*, ACS Sensors 7, 3225 (2022).
- [76] J. Warnatz, U. Maas, and R. W. Dibble, *Combustion: Physical and Chemical Fundamentals, Modeling and Simulation, Experiments, Pollutant Formation* (2006) pp. 1–378, arXiv:arXiv:1011.1669v3 .
- [77] A. V. Perpignan, A. Gangoli, and D. J. E. M. Roekaerts, *Flameless combustion and its potential towards gas turbines*, 69 (2018), 10.1016/j.peccs.2018.06.002.
- [78] R. Sampat, N. Goselink, F. Schrijer, and A. Gangoli Rao, *Operating Characteristics of a Flameless Combustor Obtained By Experiments Informed Modelling*, in *Volume 3A: Combustion, Fuels, and Emissions* (American Society of Mechanical Engineers, 2022).
- [79] P. Sabia, M. Lubrano Lavadera, P. Giudicianni, G. Sorrentino, R. Ragucci, and M. de Joannon, *CO2 and H2O effect on propane auto-ignition delay times under mild combustion operative conditions*, Combustion and Flame 162, 533 (2015).
- [80] S. Garnayak, A. M. Elbaz, O. Kuti, S. K. Dash, W. L. Roberts, and V. M. Reddy, *Auto-Ignition and Numerical Analysis on High-Pressure Combustion of Premixed Methane-Air mixtures in Highly Preheated and Diluted Environment*, Combustion Science and Technology 194, 3132 (2022).
- [81] P. Sabia, M. de Joannon, A. Picarelli, and R. Ragucci, *Methane auto-ignition delay times and oxidation regimes in MILD combustion at atmospheric pressure*, Combustion and Flame 160, 47 (2013).

- [82] P. Sabia, G. Sorrentino, A. Chinnici, A. Cavaliere, and R. Ragucci, *Dynamic behaviors in methane MILD and oxy-fuel combustion. Chemical effect of CO₂*, *Energy and Fuels* **29**, 1978 (2015).
- [83] A. C. Lipardi, P. Versailles, G. M. Watson, G. Bourque, and J. M. Bergthorson, *Experimental and numerical study on NO_x formation in CH₄-air mixtures diluted with exhaust gas components*, *Combustion and Flame* **179**, 325 (2017).
- [84] P. Hui-Sheng and Y. Tian-Hang, *Investigating the Effects of H, CH₃, and C₂H₅ Radicals on the Kinetics of Ignition for Methane/Air Mixtures*, *Journal of Energy Resources Technology* **145**, 1 (2023).
- [85] J. Sidey, E. Mastorakos, and R. L. Gordon, *Simulations of autoignition and laminar premixed flames in methane/air mixtures diluted with hot products*, *Combustion Science and Technology* **186**, 453 (2014).
- [86] S. K. Gupta and V. K. Arghode, *Characteristics of Premixed Flames of Hot and Diluted Mixtures*, *Combustion Science and Technology* **00**, 1 (2022).
- [87] P. Sabia, M. D. Joannon, A. Picarelli, A. Chinnici, and R. Ragucci, *Modeling Negative Temperature Coefficient region in methane oxidation*, *Fuel* **91**, 238 (2012).
- [88] J. B. Michael, T. L. Chng, and R. B. Miles, *Sustained propagation of ultra-lean methane/air flames with pulsed microwave energy deposition*, *Combustion and Flame* **160**, 796 (2013).
- [89] D. G. Goodwin, R. L. Speth, H. K. Moffat, and B. W. Weber, *Cantera: An Object-oriented Software Toolkit for Chemical Kinetics, Thermodynamics, and Transport Processes*, (2021).
- [90] E. Ranzi, C. Cavallotti, A. Cuoci, A. Frassoldati, M. Pelucchi, and T. Faravelli, *New reaction classes in the kinetic modeling of low temperature oxidation of n-alkanes*, *Combustion and Flame* **162**, 1679 (2015).
- [91] G. Bagheri, E. Ranzi, M. Pelucchi, A. Parente, A. Frassoldati, and T. Faravelli, *Comprehensive kinetic study of combustion technologies for low environmental impact: MILD and OXY-fuel combustion of methane*, *Combustion and Flame* **212**, 142 (2020).
- [92] V. P. Zhukov, V. A. Sechenov, and A. Y. Starikovskii, *Autoignition of a lean propane-air mixture at high pressures*, *Kinetics and Catalysis* **46**, 319 (2005).
- [93] P. H. Paul and H. N. Najm, *Planar laser-induced fluorescence imaging of flame heat release rate*, *Symposium (International) on Combustion* **27**, 43 (1998).
- [94] S. Bockle, J. Kazenwadel, T. Kunzelmann, D. I. Shin, C. Schulz, and J. Wolfrum, *Simultaneous single-shot laser-based imaging of formaldehyde, OH and temperature in turbulent flames*, *International Symposium on Combustion Abstracts of Accepted Papers* **28**, 29 (2000).

- [95] R. Balachandran, B. O. Ayoola, C. F. Kaminski, A. P. Dowling, and E. Mastorakos, *Experimental investigation of the nonlinear response of turbulent premixed flames to imposed inlet velocity oscillations*, *Combustion and Flame* **143**, 37 (2005).
- [96] B. O. Ayoola, R. Balachandran, J. H. Frank, and E. Mastorakos, *Spatially resolved heat release rate measurements in turbulent premixed flames*, **144**, 1 (2006).
- [97] R. L. Gordon, A. R. Masri, and E. Mastorakos, *Heat release rate as represented by $[OH] \times [CH_2O]$ and its role in autoignition*, **7830** (2009), 10.1080/13647830902957200.
- [98] P. Sabia, M. Lubrano Lavadera, G. Sorrentino, P. Giudicianni, R. Ragucci, and M. De Joannon, *H₂O and CO₂ Dilution in MILD Combustion of Simple Hydrocarbons*, *Flow, Turbulence and Combustion* **96**, 433 (2016).
- [99] A. A. Konnov, A. Mohammad, V. R. Kishore, N. I. Kim, C. Prathap, and S. Kumar, *A comprehensive review of measurements and data analysis of laminar burning velocities for various fuel+air mixtures*, *Progress in Energy and Combustion Science* **68**, 197 (2018).
- [100] U. o. C. a. S. D. Mechanical and Aerospace Engineering(Combustion Research), *Chemical Kinetic Mechanisms for Combustion Applications*, .
- [101] R. Cabra, J. Y. Chen, R. W. Dibble, A. N. Karpetis, and R. S. Barlow, *Lifted methane-air jet flames in a vitiated coflow*, *Combustion and Flame* **143**, 491 (2005).
- [102] C. G. Ball, H. Fellouah, and A. Pollard, *The flow field in turbulent round free jets*, *Progress in Aerospace Sciences* **50**, 1 (2012).
- [103] I. Wygnanski and H. Fiedler, *Some measurements in the self-preserving jet*, *Journal of Fluid Mechanics* **38**, 577 (1969).
- [104] N. R. Panchapakesan and J. L. Lumley, *Turbulence Measurements in Axisymmetric Jets of Air and Helium. Part 2. Helium Jet*, *Journal of Fluid Mechanics* **246**, 225 (1993).
- [105] H. J. Hussein, S. P. Capp, and W. K. George, *Velocity measurements in a high-Reynolds-number, momentum-conserving, axisymmetric, turbulent jet*, *Journal of Fluid Mechanics* **258**, 31 (1994).
- [106] G. Xu and R. A. Antonia, *Effect of different initial conditions on a turbulent round free jet*, *Experiments in Fluids* **33**, 677 (2002).
- [107] R. A. Antonia and R. W. Bilger, *An experimental investigation of an axisymmetric jet in a co-flowing air stream*, *Journal of Fluid Mechanics* **61**, 805 (1973).
- [108] T. B. Nickels and A. E. Perry, *An experimental and theoretical study of the turbulent coflowing jet*, *Journal of Fluid Mechanics* **309**, 157 (1996).

- [109] B. R. Morton, T. Geoffrey, and J. S. Turner, *Turbulent Gravitational Convection from Maintained and Instantaneous Sources*, in *Proceedings of the Royal Society of London. Series A, Mathematical and Physical*, Vol. 234 (1956) pp. 1–23.
- [110] S. Gaskin and I. Wood, *The axisymmetric and the plane jet in a coflow*, *Journal of Hydraulic Research* **39**, 451 (2001).
- [111] C. Or, K. Lam, and P. Liu, *Potential core lengths of round jets in stagnant and moving environments*, *Journal of Hydro-environment Research* **5**, 81 (2011).
- [112] P. C. K. Chu, J. H. Lee, and V. H. Chu, *Three-Dimensional Salinity Simulations of*, *Journal of Hydraulic Engineering* **125**, 193 (1999).
- [113] M. Uddin and A. Pollard, *Self-similarity of coflowing jets: The virtual origin*, *Physics of Fluids* **19**, 068103 (2007).
- [114] M. Moeini, B. Khorsandi, and L. Mydlarski, *Effect of Coflow Turbulence on the Dynamics and Mixing of a Nonbuoyant Turbulent Jet*, *Journal of Hydraulic Engineering* **147**, 1 (2021).
- [115] S. J. Gaskin, M. McKernan, and F. Xue, *The effect of background turbulence on jet entrainment : An experimental study of a plane jet in a shallow coflow*, *Journal of Hydraulic Research* **42**, 533 (2004).
- [116] B. Khorsandi, S. Gaskin, and L. Mydlarski, *Effect of background turbulence on an axisymmetric turbulent jet*, *Journal of Fluid Mechanics* **736**, 250 (2013).
- [117] R. Sahebjam, K. F. Kohan, and S. Gaskin, *The dynamics of an axisymmetric turbulent jet in ambient turbulence interpreted from the passive scalar field statistics*, *Physics of Fluids* **34** (2022), 10.1063/5.0071023.
- [118] S. Corrsin and A. L. Kistler, *NACA-TR*, Tech. Rep. (1955).
- [119] J. Westerweel, C. Fukushima, J. M. Pedersen, and J. C. Hunt, *Momentum and scalar transport at the turbulent/non-turbulent interface of a jet*, *Journal of Fluid Mechanics* **631**, 199 (2009).
- [120] K. Chauhan, J. Philip, C. M. De Silva, N. Hutchins, and I. Marusic, *The turbulent/non-turbulent interface and entrainment in a boundary layer*, *Journal of Fluid Mechanics* **742**, 119 (2014).
- [121] D. Mistry, J. Philip, J. R. Dawson, and I. Marusic, *Entrainment at multi-scales across the turbulent/non-turbulent interface in an axisymmetric jet*, *Journal of Fluid Mechanics* **802**, 690 (2016).
- [122] C. B. Da Silva and R. J. Dos Reis, *The role of coherent vortices near the turbulent / non-turbulent interface*, *Philosophical Transactions of the Royal Society of London. Series A: Physical and Engineering Sciences* **368**, 738 (2011).

- [123] C. B. Da Silva and R. R. Taveira, *The thickness of the turbulent/nonturbulent interface is equal to the radius of the large vorticity structures near the edge of the shear layer*, *Physics of Fluids* **22** (2010), 10.1063/1.3527548.
- [124] C. B. da Silva and J. C. Pereira, *Invariants of the velocity-gradient, rate-of-strain, and rate-of-rotation tensors across the turbulent/nonturbulent interface in jets*, *Physics of Fluids* **20** (2008), 10.1063/1.2912513.
- [125] C. B. Da Silva, J. C. Hunt, I. Eames, and J. Westerweel, *Interfacial layers between regions of different turbulence intensity*, *Annual Review of Fluid Mechanics* **46**, 567 (2014).
- [126] R. R. Taveira and C. B. da Silva, *Characteristics of the viscous superlayer in shear free turbulence and in planar turbulent jets*, *Physics of Fluids* **26** (2014), 10.1063/1.4866456.
- [127] G. Balamurugan, A. Rodda, J. Philip, and A. C. Mandal, *Characteristics of the turbulent non-turbulent interface in a spatially evolving turbulent mixing layer*, *Journal of Fluid Mechanics* **894** (2020), 10.1017/jfm.2020.241.
- [128] K. S. Kankanwadi and O. R. Buxton, *Turbulent entrainment into a cylinder wake from a turbulent background*, *Journal of Fluid Mechanics* (2020), 10.1017/jfm.2020.755.
- [129] K. S. Kankanwadi and O. R. Buxton, *On the physical nature of the turbulent/turbulent interface*, *Journal of Fluid Mechanics* **942**, 1 (2022).
- [130] J. Chen and O. R. Buxton, *Spatial evolution of the turbulent/turbulent interface geometry in a cylinder wake*, *Journal of Fluid Mechanics* **969**, 1 (2023), arXiv:2301.04959 .
- [131] K. F. Kohan and S. J. Gaskin, *On the scalar turbulent/turbulent interface of axisymmetric jets*, *Journal of Fluid Mechanics* **950**, 1 (2022).
- [132] R. R. Taveira and C. B. da Silva, *Kinetic energy budgets near the turbulent/nonturbulent interface in jets*, *Physics of Fluids* **25** (2013), 10.1063/1.4776780.
- [133] D. K. Bisset, J. C. Hunt, and M. M. Rogers, *The turbulent/non-turbulent interface bounding a far wake*, *Journal of Fluid Mechanics* **451**, 383 (2002).
- [134] M. Khashehchi, A. Ooi, J. Soria, and I. Marusic, *Evolution of the turbulent/non-turbulent interface of an axisymmetric turbulent jet*, *Experiments in Fluids* **54**, 1449 (2013).
- [135] T. Watanabe, X. Zhang, and K. Nagata, *Turbulent/non-turbulent interfaces detected in DNS of incompressible turbulent boundary layers*, *Physics of Fluids* **30** (2018), 10.1063/1.5022423.
- [136] W. Dahm and R. Dibble, *Combustion stability limits of coflowing turbulent jet diffusion flames*, in *26th Aerospace Sciences Meeting* (American Institute of Aeronautics and Astronautics, Reston, Virginia, 1988).

- [137] B. Ganapathisubramani, K. Lakshminarasimhan, and N. T. Clemens, *Determination of complete velocity gradient tensor by using cinematographic stereoscopic PIV in a turbulent jet*, Experiments in Fluids **42**, 923 (2007).
- [138] A. Roshko, *NACA-TR*, Tech. Rep. (NACA, 1954).
- [139] G. Vita, H. Hemida, T. Andrienne, and C. C. Baniotopoulos, *Generating atmospheric turbulence using passive grids in an expansion test section of a wind tunnel*, Journal of Wind Engineering and Industrial Aerodynamics **178**, 91 (2018).
- [140] T. Kurian and J. H. Fransson, *Grid-generated turbulence revisited*, Fluid Dynamics Research **41** (2009), 10.1088/0169-5983/41/2/021403.
- [141] T. Watanabe, Y. Sakai, K. Nagata, Y. Ito, and T. Hayase, *Turbulent mixing of passive scalar near turbulent and non-turbulent interface in mixing layers*, Physics of Fluids **27** (2015), 10.1063/1.4928199.
- [142] G. E. Elsinga, R. J. Adrian, B. W. Van Oudheusden, and F. Scarano, *Three-dimensional vortex organization in a high-Reynolds-number supersonic turbulent boundary layer*, Journal of Fluid Mechanics **644**, 35 (2010).
- [143] R. R. Prasad and K. R. Sreenivasan, *Scalar interfaces in digital images of turbulent flows*, Experiments in Fluids **7**, 259 (1989).
- [144] E. Schubert, J. Sander, M. Ester, H. P. Kriegel, and X. Xu, *DBSCAN revisited, revisited: Why and how you should (still) use DBSCAN*, ACM Transactions on Database Systems **42** (2017), 10.1145/3068335.
- [145] G. Bradski, *The OpenCV Library*, Dr. Dobb's Journal of Software Tools (2000).
- [146] X. Zhang and R. C. Chin, *A Numerical Study of the Effects of the Velocity Ratio on Coflow Jet Characteristics*, Journal of Fluids Engineering, Transactions of the ASME **142**, 1 (2020).
- [147] P. E. Dimotakis, *The mixing transition in turbulent flows*, Journal of Fluid Mechanics **409**, 69 (2000).
- [148] International Energy Agency, *The Future of Hydrogen*, Tech. Rep. (IEA, Paris, 2019).
- [149] I. Staffell, D. Scamman, A. Velazquez Abad, P. Balcombe, P. E. Dodds, P. Ekins, N. Shah, and K. R. Ward, *The role of hydrogen and fuel cells in the global energy system*, Energy & Environmental Science **12**, 463 (2019).
- [150] Y. Huang and V. Yang, *Dynamics and stability of lean-premixed swirl-stabilized combustion*, Progress in Energy and Combustion Science **35**, 293 (2009).
- [151] K. Göckeler, O. Krüger, and C. Oliver Paschereit, *Laminar burning velocities and emissions of hydrogen–methane–air–steam mixtures*, Journal of Engineering for Gas Turbines and Power **136**, 031508 (2014).

- [152] International Renewable Energy Agency, *Green Hydrogen Cost Reduction: Scaling up Electrolysers to Meet the 1.5°C Climate Goal*, Tech. Rep. (IRENA, Abu Dhabi, 2020).
- [153] A. A. V. Perpignan, M. G. Talboom, Y. Levy, and A. G. Rao, *Emission Modeling of an Interturbine Burner Based on Flameless Combustion*, *Energy & Fuels* **32**, 822 (2018).
- [154] R. L. Gordon, A. R. Masri, S. B. Pope, and G. M. Goldin, *A numerical study of auto-ignition in turbulent lifted flames issuing into a vitiated co-flow*, *Combustion Theory and Modelling* **11**, 351 (2007).
- [155] R. L. Gordon, A. R. Masri, S. B. Pope, and G. M. Goldin, *Transport budgets in turbulent lifted flames of methane autoigniting in a vitiated co-flow*, *Combustion and Flame* **151**, 495 (2007).
- [156] O. Lammel, M. Stohr, P. Kutne, C. Dem, W. Meier, and M. Aigner, *Experimental Analysis of Confined Jet Flames by Laser Measurement Techniques*, *Journal of Engineering for Gas Turbines and Power* **134**, 041506 (2012).
- [157] Z. Liu, Y. Xiong, Z. Zhu, Z. Zhang, and Y. Liu, *Effects of hydrogen addition on combustion characteristics of a methane fueled MILD model combustor*, *International Journal of Hydrogen Energy* **47**, 16309 (2022).
- [158] M. Ayoub, C. Rottier, S. Carpentier, C. Villermaux, A. M. Boukhalfa, and D. Honoré, *An experimental study of mild flameless combustion of methane/hydrogen mixtures*, *International Journal of Hydrogen Energy* **37**, 6912 (2012).
- [159] O. Skorcka, P. Kane, and R. Ispasoiu, *Color Correction for RGB Sensors with Dual-Band Filters for In-Cabin Imaging Applications*, *Electronic Imaging* **31**, 1 (2019).
- [160] R. W. Schefer, W. D. Kulatilaka, B. D. Patterson, and T. B. Settersten, *Visible emission of hydrogen flames*, *Combustion and Flame* **156**, 1234 (2009).
- [161] M. Miozzi, F. Lalli, and G. P. Romano, *Experimental investigation of a free-surface turbulent jet with Coanda effect*, *Experiments in Fluids* **49**, 341 (2010).
- [162] accessed on 02/03/2017.
- [163] Nist, *NIST Chemical Kinetics Database, NIST Standard Reference Database 17, Version 7.0 (Web Version), Release 1.6.8, Data version 2015.12, National Institute of Standards and Technology, Gaithersburg, Maryland, 20899-8320*. accessed on 01/03/2017.
- [164] J. Santner, S. F. Ahmed, T. Farouk, and F. L. Dryer, *Computational Study of NO_x Formation at Conditions Relevant to Gas Turbine Operation: Part 1*, *Energy and Fuels* **30**, 6745 (2016).
- [165] J. A. Miller and C. T. Bowman, *Mechanism and modeling of nitrogen chemistry in combustion*, *Progress in Energy and Combustion Science* **15**, 287 (1989).

- [166] J. WARNATZ, *Concentration-, Pressure-, and Temperature-Dependence of the Flame Velocity in Hydrogen-Oxygen-Nitrogen Mixtures*, *Combustion Science and Technology* **26**, 203 (1981).
- [167] C. P. Fenimore, *Formation of nitric oxide in premixed hydrocarbon flames*, Symposium (International) on Combustion **13**, 373 (1971).
- [168] J. W. Bozzelli and A. M. Dean, *O + NNH: A Possible New Route for NO_x formation in flames*, *International Journal of Chemical Kinetics* **27**, 1097 (1995).
- [169] P. C. MALTE and D. T. PRATT, *The Role of Energy-Releasing Kinetics in NO_x Formation: Fuel-Lean, Jet-Stirred CO-Air Combustion*, *Combustion Science and Technology* **9**, 221 (1974).
- [170] Y. A. Çengel and A. J. Ghajar, *Heat and Mass Transfer: Fundamentals & Applications*, Asia Higher Education Engineering/Computer Science Mechanica (McGraw Hill Education, 2015).
- [171] D. Bradley and A. G. Entwistle, *Determination of the emissivity, for total radiation, of small diameter platinum-10% rhodium wires in the temperature range 600-1450°C*, *British Journal of Applied Physics* **12**, 708 (1961).
- [172] F. Cassol, R. Brittes, F. H. França, and O. A. Ezekoye, *Application of the weighted-sum-of-gray-gases model for media composed of arbitrary concentrations of H₂O, CO₂ and soot*, *International Journal of Heat and Mass Transfer* **79**, 796 (2014).



A

EMISSIONS PATHWAY

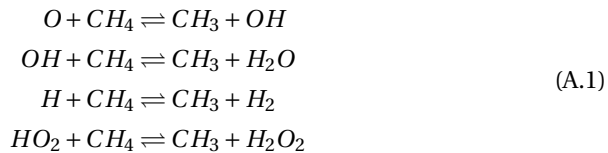
A.1. CARBON MONOXIDE

Carbon Monoxide(CO) can be poisonous if inhaled as it forms a complex compound with the hemoglobin in blood and reduces the capability of oxygen absorption for biological energy production and metabolic activity. It could lead to unconsciousness, nausea and death[162].

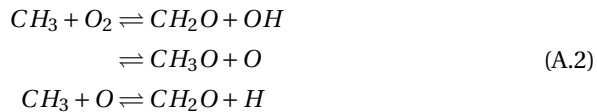
A.1.1. FORMATION

In order to understand the formation of CO, it is necessary to understand the process of combustion of a hydrocarbon. The explanation is provided using methane as a fuel and in successive steps.

1. Combustion at high temperatures(>1000K) relies on radicals to react with fuel molecules. The important radicals are O, OH, H and HO₂. These radicals are produced during ignition or by pyrolysis in the preheat zone. These radicals attack fuel molecules and cause them to dissociate, in this case from CH₄ to CH₃.



2. Next, the intermediate, CH₃ oxidizes to form CH₂O.



CH₂O by itself doesn't cause further chain branching, but is responsible for the production of H atoms, which in turn, take part in chain branching reactions as

shown in Equation A.3, as part of the hydrogen oxidation mechanism, that sustains the combustion reactions by the radicals hence produced.



3. CH₂O undergoes further oxidation and dissociation to produce CO, i.e



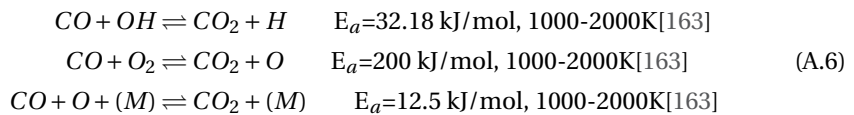
4. CO in turn oxides through several reactions to form CO₂ which is the end product of complete combustion. This step is also the major source of heat release in the combustion process.

Although the above process has been presented specifically for methane oxidation, the process is quite similar for higher hydrocarbons as during their oxidation, the fuel molecules first break down into simpler alkyls and undergo a similar process.

The global reaction for the oxidation of CO is as given in Equation A.5



The main elementary reactions involved in this conversion are given in Equation A.6



The reactions in Equation A.6 are relatively slow, which makes it possible for some of the CO produced to not be oxidized to CO₂ before it leaves the combustion chamber, often due to lower temperatures or low residence time. Thus CO emissions obtained at the combustion chamber exhaust are due incomplete oxidation.

A.2. NITROGEN OXIDES

NO_x, which is a combination of NO, N₂O and NO₂, has been found to cause photochemical smog, acid rain and generate ozone¹ by chemical reaction in the troposphere. In the stratosphere NO_x chemically reacts with ozone, hence depleting the ozone layer leaving the earth's surface vulnerable to the excess ultraviolet radiation from the sun. Consequently, NO_x reduction has become one of the primary focus of advances towards cleaner gas turbine combustion[76].

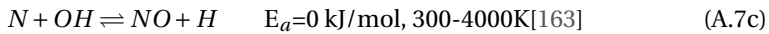
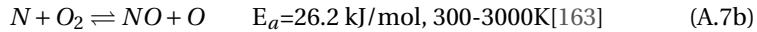
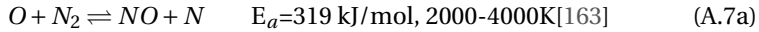
¹Tropospheric ozone is considered a pollutant which can cause stunted growth in crops as well as be poisonous to humans.

A.2.1. FORMATION MECHANISMS

NO_x has been found to be formed by the Thermal Pathway, Fenimore mechanism, NNH mechanism, N_2O route and Fuel NO_x pathway[164].

1. Thermal NO_x :

Its formation is described by the extended Zeldovich mechanism[165]. It is governed by the following equations:



The triple bond in the Nitrogen molecule is very strong and hence Equation A.7a has a high activation energy (319 kJ/mol). It is the rate limiting step in the Zeldovich mechanism and has a high reaction rate above 2000K, which gives it the name 'Thermal NO_x '.

A common way of calculating the NO concentration is to assume that the N atoms are in a quasi steady state. This is because Equation A.7b and Equation A.7c have been found to be much faster than Equation A.7a, thus the N atoms which are a product of Equation A.7a are almost instantly consumed. So the concentration of NO is expressed as,

$$\frac{d[\text{NO}]}{dt} = k_1[\text{O}][\text{N}_2] + k_2[\text{N}][\text{O}_2] + k_3[\text{N}][\text{OH}] \quad (\text{A.8})$$

$$\frac{d[\text{N}]}{dt} = k_1[\text{O}][\text{N}_2] - k_2[\text{N}][\text{O}_2] - k_3[\text{N}][\text{OH}]$$

$$\frac{d[\text{N}]}{dt} = 0 \quad (\text{A.9})$$

$$\therefore k_1[\text{O}][\text{N}_2] = k_2[\text{N}][\text{O}_2] + k_3[\text{N}][\text{OH}]$$

$$\therefore \frac{d[\text{NO}]}{dt} = 2k_1[\text{O}][\text{N}_2]$$

The value of $[\text{N}_2]$ can be measured by probes or calculated by equilibrium analysis, but $[\text{O}]$ has been shown to be under-predicted by an equilibrium assumption[166] as it is an unstable species.

$$[\text{O}] = \frac{k_{\text{H}+\text{O}_2} \cdot k_{\text{OH}+\text{H}_2} \cdot [\text{O}][\text{H}_2]}{k_{\text{OH}+\text{O}} \cdot k_{\text{H}+\text{H}_2\text{O}} \cdot [\text{H}_2\text{O}]} \quad (\text{A.10})$$

A more reliable prediction can be obtained by a partial equilibrium calculation as shown in Equation A.10. It is calculated using the concentrations of O_2 , H_2 and H_2O which can be better predicted by calculations or measurements as they are stable species[76]. The most accurate method would be to perform the calculation without any assumptions of equilibrium and derive the concentrations of the concerned species from a chemical kinetic mechanism.

2. Prompt/Fenimore NO:

Prompt NO_x is formed by the following rate limiting reaction,

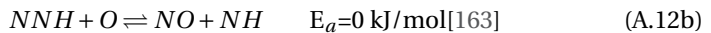
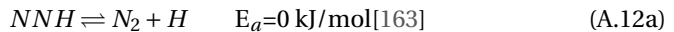


The CH radical is formed by a precursor, C_2H_2 , which is formed in fuel rich conditions. This mechanism has a much lower activation energy than the thermal pathway and is hence formed at lower temperatures (<2000K)[76]. In the presence of oxygen, the N atoms produced react to form NO.

The mechanism was discovered by experiments by Fenimore [167]. He measured the NO concentrations in the post flame and primary reaction zones. The measurements indicated the formation of NO in the primary reaction zone which was contrary to the prediction from the Zeldovich mechanism, according to which NO_x should be found only in the post flamezone due to the high temperature requirements for the reaction. Thus in [167] it is concluded that the Prompt NO_x may be a significant contributor to the total NO_x especially under fuel rich reaction conditions.

3. NNH mechanism:

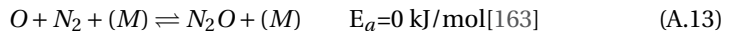
This deals with the reaction of dissociation of NNH to H and N_2 . The reactions involved are:



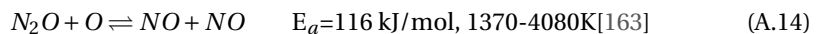
The forward reaction rate of Equation A.12a is found to be more or less independent of temperature but the reverse reaction rate increases especially at high temperature conditions in flames due to the increase of H species concentration. The pathway can lead to increase of NO concentration by an order of magnitude in a methane/air flame at 1800K[168]. The reverse reaction of Equation A.12a is rapid enough to establish equilibrium of NNH, which results in NNH concentrations to be high enough to be important in bimolecular reactions such as the NO producing Equation A.12b.

4. N_2O mechanism:

This is similar to the thermal mechanism, wherein O attacks N_2 molecules, but in this case it occurs in the presence of a third molecule M and leads to the formation of N_2O in Equation A.13.



This reaction is promoted at high pressures as it is a three body reaction and has a low activation energy, making it an important contributor to NO_x under lean premixed gas turbine combustor conditions. This is because Thermal NO_x is reduced due to lower temperatures and Prompt NO_x by lean conditions[169]. Subsequently the reaction in Equation A.14 produces NO.



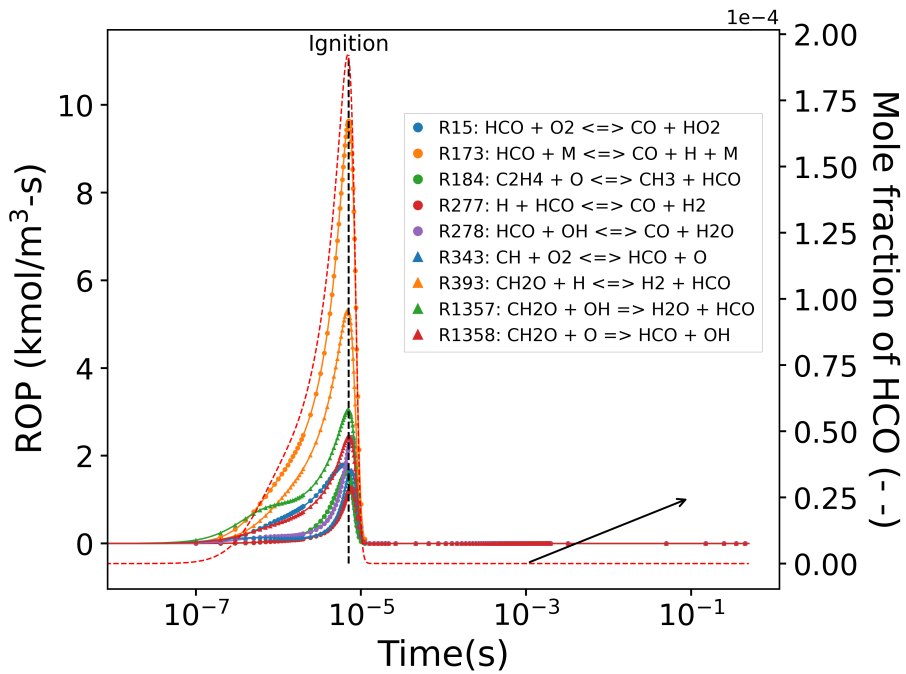
5. Fuel NO_x:

This is formed by the reaction of fuel bound nitrogen found in fuels such as coal. This is less relevant from a gas turbine perspective which employs cleaner hydrocarbon fuels such as natural gas and kerosene compared to coal and biomass.



B

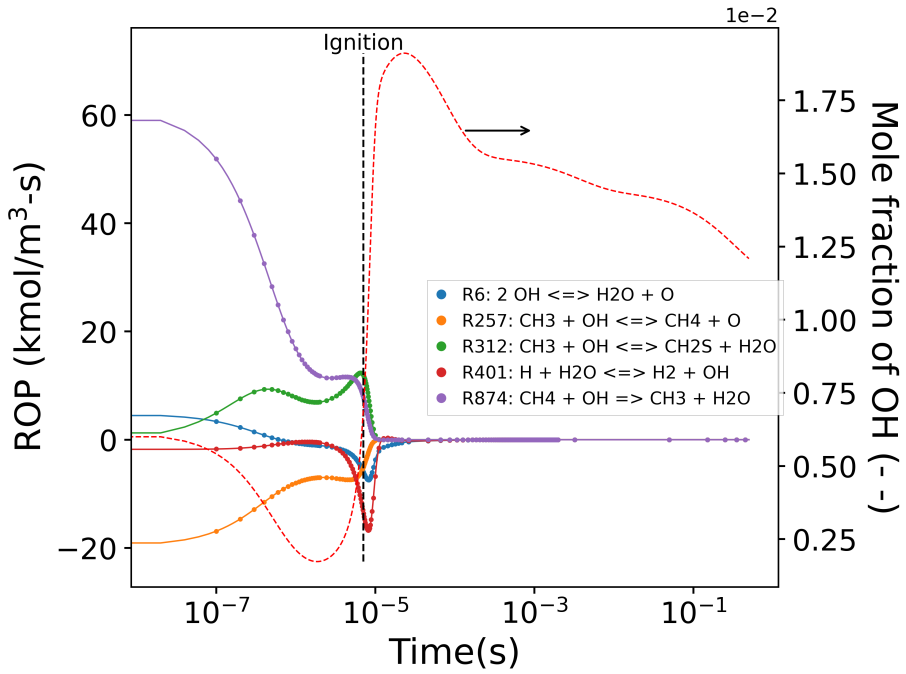
MULTI-IGNITION ROP AND MOLE FRACTION



(a) HCO

Figure B.1: Rate of Progress of reactions related to HCO and its mole fraction at $\phi=0.75$, $\zeta=0.5$, $\chi=0.0$.

B



(a) OH

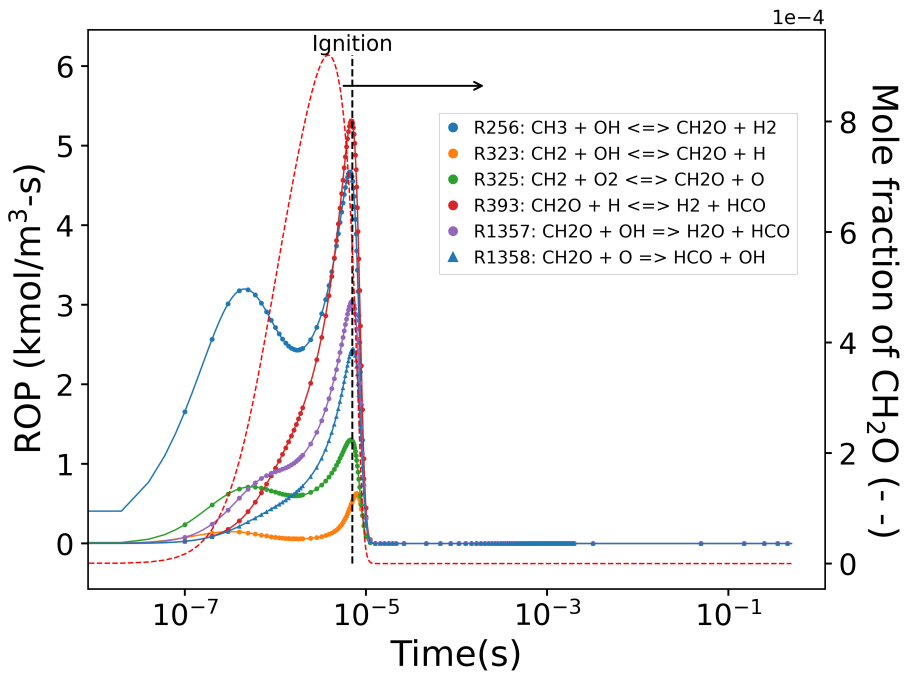
(b) CH_2O

Figure B.2: Rate of Progress of reactions related to OH and CH_2O and their mole fractions at $\phi=0.75$, $\zeta=0.5$, $\chi=0.0$

C

CHARACTERIZATION OF A JET-STABILIZED COMBUSTOR

C.1. COMBUSTION SETUP AND OPERATION CONDITIONS

C.1.1. BACKFLOW FROM EXHAUST

Although there is a contraction section at the exhaust to accelerate the flow, there is a noticeable backflow of cooling air into the system due to the low-pressure region created along the centerline of the combustor by the intense recirculation zones. This is seen by the O_2 measurements at the exhaust and comparing it to the expected values calculated using a PSR model, in Cantera, for inlet gas composition, presented in Table C.1. The $O_2\%$ is calculated and measured on a dry basis and is done including the air flow through the pilot burner. The measured value, as expected, reduces with increasing equivalence ratio for lean mixtures and increases with $H_2\%$ for the same ϕ . However, for the same ϕ , the variation is smaller for cases of varying $H_2\%$. The measured O_2 at the exhaust deviates from the calculated value, and the deviation increases for higher equivalence ratios. The exhaust cooling system maintains a specified temperature in the exhaust duct by diluting the hot combustion products with cooling air. This system is necessary to ensure the integrity of the exhaust duct and is thus programmed to be below $600\text{ }^\circ\text{C}$. As the adiabatic flame temperature ($T_{\text{flame adiabatic}}$) of the mixture increases with ϕ , more cooling air is required to maintain a low enough temperature. This results in more excess O_2 being transported upstream and a larger deviation for calculated O_2 for higher ϕ , which also correspond to higher $T_{\text{flame adiabatic}}$. The backflow issue would be present in any atmospheric pressure rig of this type. This effect may be eliminated by a significant pressure drop along the entire diameter of the exhaust, such as by a honeycomb, or the exhaust needs to be choked, leading to a pressurized combustion chamber.

Table C.1: Exhaust Conditions

H ₂ %	ϕ	$\dot{m}_{air,pilot}$ (lnpm)	ϕ_{eq}	O ₂ at inlet (%)(calc)	O ₂ dry at outlet (%)(calc)	O ₂ dry at outlet (%)(measured)	T _{flame adiabatic} (K)(calc)
0	0.6	0.57	62	19.82	8.96	10.10	1883.5
0	0.8	0.76	62	19.46	4.60	6.68	2184.7
0	1	0.95	62	19.10	1.04	4.09	2358.8
10	0.6	0.57	62	19.73	8.99	10.19	1886.6
10	0.8	0.76	62	19.34	4.63	7.05	2188.0
10	1	0.95	62	18.96	1.06	4.03	2362.4
50	0.35	0.33	62	19.90	14.35	14.78	1434.7
50	0.8	0.76	62	18.63	4.75	7.35	2209.5
50	1	0.94	62	18.12	1.14	4.37	2383.9
80	0.3	0.28	62	19.54	15.55	15.72	1354.5
80	0.8	0.76	62	17.52	4.87	7.75	2250.3
80	1	0.94	62	16.83	1.21	5.36	2420.9
100	0.3	0.28	62	18.76	16.02	16.14	1382.1
100	0.8	0.75	62	15.95	4.97	8.19	2318.5
100	1	0.94	62	15.06	1.24	5.76	2484.3

C.2. MEASUREMENT PROCESSING

C.2.1. THERMOCOUPLE CORRECTION

The convective heat transfer coefficient, h , was calculated from the Nusselt number as $Nu = hD/k$, where D was the probe diameter and k was the thermal conductivity of the burnt product gases. The Nusselt number was determined from correlations for cylinders in cross-flow [170],

$$\begin{aligned}
 Nu &= 0.989Re^{0.33}Pr^{0.33} & 0.4 \leq Re < 4 \\
 Nu &= 0.911Re^{0.385}Pr^{0.33} & 4 \leq Re < 40 \\
 Nu &= 0.683Re^{0.466}Pr^{0.33} & 40 \leq Re < 4000 \\
 Nu &= 0.193Re^{0.618}Pr^{0.33} & 4000 \leq Re < 40000 \\
 Nu &= 0.027Re^{0.805}Pr^{0.33} & 40000 \leq Re < 400000
 \end{aligned} \tag{C.1}$$

The emissivity of the Pt10%Rh sheathed thermocouple is taken from [171] where the emissivity was determined for a range 600 °C to 1450 °C from 0.1287 to 0.2243. A fixed value of 0.175 was used in the present work. The emissivity of the gas phase was calculated using the Weighted Sum of Gray Gases (WSGG) method [172]. This model segregates the emittance of a species into discrete gray gases to represent the spectral emittance such that each gray gas has its own spectral absorption coefficient.

$$\epsilon_\chi = \sum_{j=1}^{J_\chi} a_{\chi j}(T) [1 - \exp(-\kappa_{P_{\chi j}} P_\chi X)] \tag{C.2}$$

The temperature dependent coefficients, $a_{\chi j}$, are evaluated by a polynomial equation,

$$a_{\chi j}(T) = \sum_{k=1}^{K_\chi} b_{\chi, j, k} T^{k-1} \tag{C.3}$$

The WSGG coefficients are taken from [172], which were obtained by fitting total emittance data computed by line-by-line integration of spectral absorption lines generated from HITEMP2010. The number of gray gases used was 4 for both, H₂O and CO₂, and a 4th order polynomial was used to represent the temperature-dependent coefficients. The coefficients were evaluated for each species and the quantities for the mixture were calculated as:

$$\kappa_{m, j_m}(x) = p_w(x)\kappa_{p, w, j} + p_c(x)\kappa_{p, c, j} \tag{C.4}$$

$$a_{m, j_m}(x) = a_{w, j_w}(x) \times a_{c, j_c}(x) \tag{C.5}$$

C.3. SUPPLEMENTARY DATA

C.3.1. FLOW FIELD REYNOLDS STRESSES

Figure C.1a and C.1b show the normalized Reynolds shear stress (RSS) for the cases of reacting flow for H₂=0% at 60kW with $\phi=0.6$ and 0.8, respectively. There is a high magnitude at the interface between the jet and the recirculation zone, and the case of $\phi=0.6$ has a higher magnitude of peak RSS than $\phi=0.8$. The RSS is highest at the nozzle exit

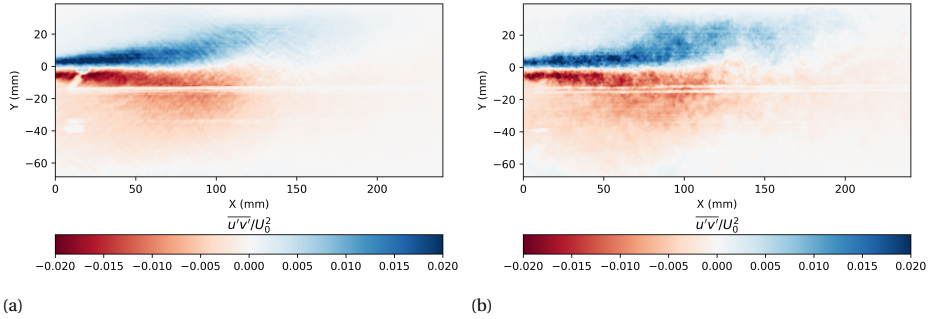


Figure C.1: Reynolds Shear Stress contour for $H_2=0\%$, $P=60\text{kW}$, (a) $\phi=0.6$ (b) $\phi=0.8$

and reduces to a value between 35-50% at the PRZ. The value further downstream and at the point where the jet flow starts forming the CRZ ($X \approx 150$ mm) is much lower, almost 10% of the original. However, in the recirculation zones, both PRZ and CRZ, closer to the jet exit where the flow is entrained into the jet, the magnitude is higher, $\approx 25\%$ of the maximum. For a jet flow, the RSS also indicates the amount of momentum transferred in the perpendicular direction. This quantity directly impacts the turbulent transport of material across the interface, which affects the interaction of burnt products with fresh reactants in the jet.

C.3.2. GAS COMPOSITION PLOTS

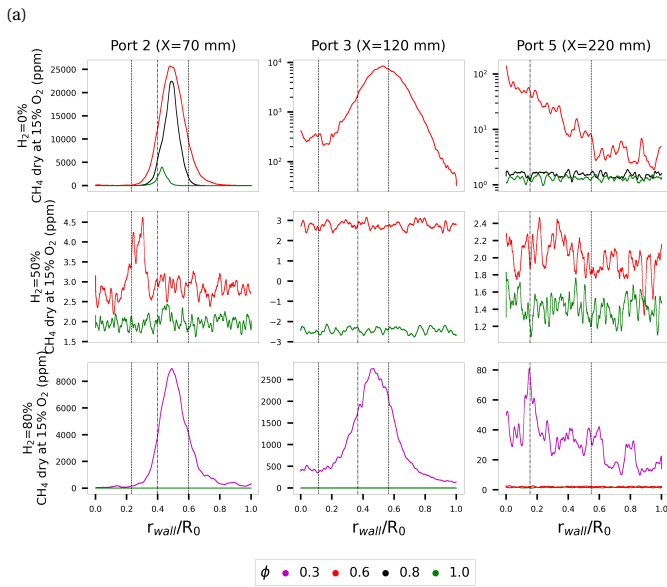
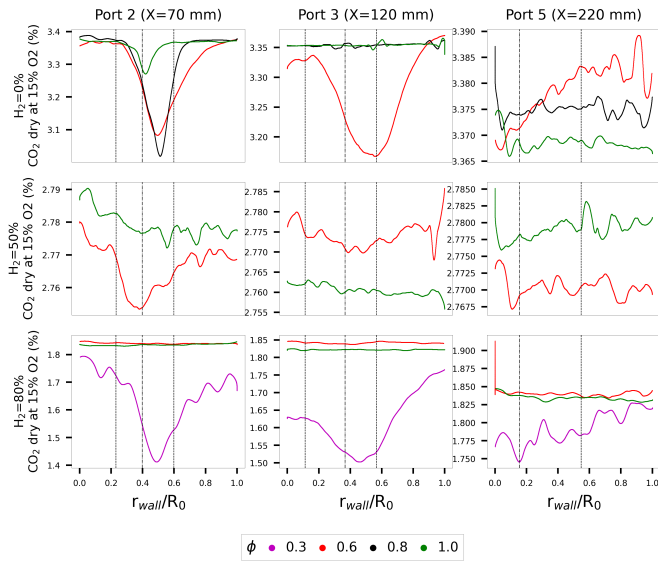
Figure C.3 shows the development of NO and CO along the length of the combustor by plotting the NO value measured at Port 2,3 and 5 at the jet centerline and the exhaust. There is a rise along the chamber length, and cases with $\phi \geq 0.8$ have similar trends. The NO level within the chamber is significantly lower than that at the exhaust. This effect is reduced for lower equivalence ratios. The in-chamber measurements are up to 220 mm, but the exhaust measurement is 546 mm from the nozzle. The velocity field data in Section 6.3.1 shows that in the latter half of the chamber, the jet flow expands into the cross-sectional area of the chamber and takes on more of a pipe-flow kind of velocity distribution. Thus, the axial velocity downstream is lower, providing more residence time for NO formation and CO consumption. Thus, based on these measurements, even lower exhaust NO could have been achieved by having a shorter combustion chamber; however, in the distributed flame cases, that would lead to higher CO. The CO development along the chamber is either a monotonic decrease, indicating a flame zone stabilized closer to the burner head, or first increase and then decreases, indicating one centered around the probed Ports with a distributed nature as in the leanest cases of $H_2=0\%$ and 80%.

C.3.3. RAW TEMPERATURE MEASUREMENTS

The raw, uncorrected thermocouple measurements are shown in Fig C.4.

C.3.4. CHEMILUMINESCENCE $H_2=100\%$

Chemiluminescence images for $H_2=100\%$, $\phi=0.3, 0.6, 0.8$ and 1.0 in Fig C.5.



(b)

Figure C.2: CO₂ and CH₄ mole fraction v/s radial location at Port 2, 3 and 5. The vertical lines indicate the local jet center (-), PRZ, and CRZ (- -) on the left and right of the jet centerline, respectively.

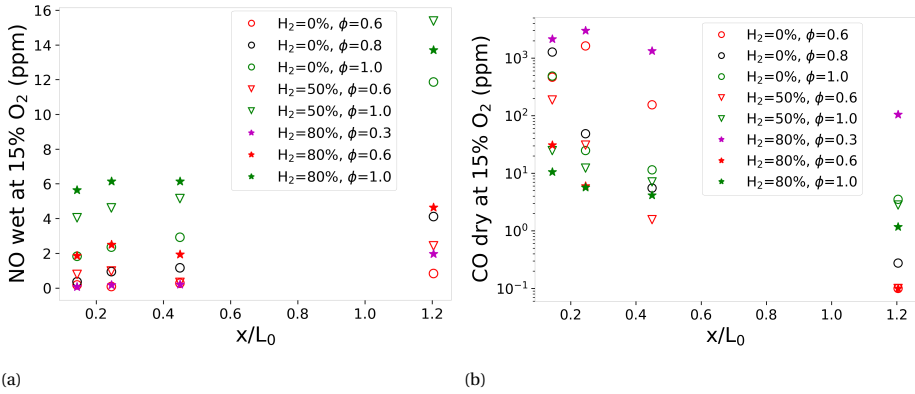


Figure C.3: NO and CO mole fraction along the length of the chamber, measured at Port 2, 3 and 5 at jet centerline as shown in Fig. 6.3b and the exhaust.

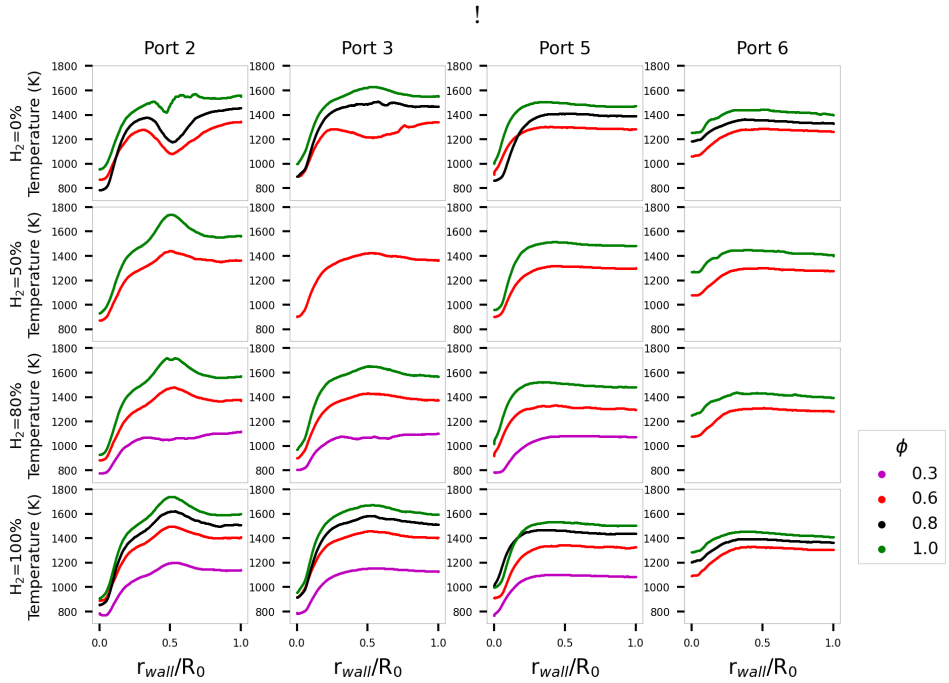


Figure C.4: Temperature v/s radial location at Port 2, 3, 5 and 6. This is raw, uncorrected data obtained from the thermocouple.

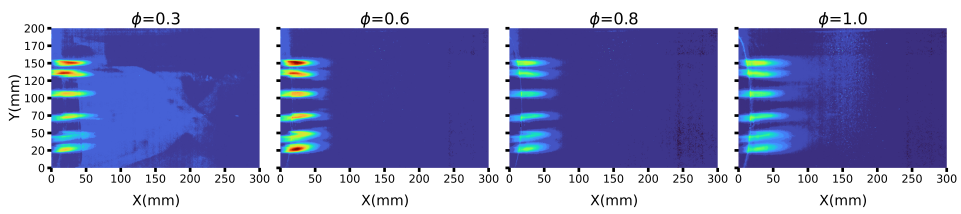


Figure C.5: Average normalized chemiluminescence images for $H_2=100\%$. Colorscale same as in Fig. 6.11, Section 6.3.4



D

COMBUSTOR P&ID

ACKNOWLEDGEMENTS

The PhD journey has been a long one, with several ups and downs. However, the culmination of hard work and mental grit has led to this dissertation, and it would not have been possible without the help and support of many people.

First and foremost, I would like to express my deepest gratitude to my promoter, Prof. Dr. Arvind Gangoli Rao, for giving me the opportunity to embark on this journey. I am incredibly thankful for the many lessons that have helped me grow both as a researcher and as a person. I appreciate the opportunities he provided, the freedom to explore various research and development paths, and, most importantly, his guidance as both a mentor and a friend.

I would also like to extend my sincere thanks to my co-promoter, Dr. Ferry Schrijer, whose expertise and insights have significantly contributed to my research. I have learned a lot from his invaluable guidance in fluid mechanics, experimental techniques, and scientific writing. Despite combustion not being his primary field, he took a keen interest in my work and supported me wholeheartedly, for which I am truly grateful.

A special acknowledgment goes to Jos, the true hero of the combustion lab. His unwavering dedication and technical expertise have played a pivotal role in shaping the lab as it stands today. His contributions to machining, assembly, and installation have been instrumental in the success of this PhD. I am deeply appreciative of his manufacturing insights and the hands-on learning experience I gained through our collaboration.

Several key aspects of this PhD research, as well as some published papers, were made possible through the hard work and dedication of MSc students. I would like to express my gratitude to Niek Goselink for his work on the Flameless Combustor and his patience in spending countless hours in the lab with me. I also sincerely thank Thimo for his outstanding efforts in building and commissioning the Enclosed Jet-in-Hot-Coflow setup—though not featured in this thesis, our collaboration was extremely valuable. Additionally, I appreciate the contributions of other MSc students I had the privilege of supervising: Simon, Maaïke, Pratik, Yoram, Justin—their dedication and enthusiasm made for a great research experience. Special thanks to Simon for helping out during the jet-in-coflow experiments.

When I began my PhD, the combustion group was still in its early stages, but over the years, it has grown into a dynamic and exciting research team. I am fortunate to have worked alongside like-minded individuals who share a deep passion for combustion science and technology. I deeply appreciate the insightful discussions and camaraderie of my fellow "pyromaniacs": Kaushal, Turhan, Gioele, Marisa, Alessandro Porcarelli, Sarah, Ivan, and Francesca. A special thanks to Kaushal for being a great sounding board for both professional and personal discussions. Special thanks to Turhan for helping out during some of the experiments and being a good friend to hang out with.

I am also grateful to the technical staff and engineers who provided invaluable support in bringing to life the various experimental setups I worked on. Special thanks to

Dennis, Gert-Jan, Frits, Peter and Henk-Jan from the High Speed Lab for their technical work in realizing several experiments. I would like to acknowledge the work of our colleagues at DEMO, Rajeev, Martijn, Jos, and Gerard, for their contributions to building various aspects of the combustor, namely the software and control system, electrical hardware and mechanical hardware.

During my early days in the lab, several colleagues helped me get up to speed with experimental techniques, particularly with PIV and the DaVis ecosystem. Many thanks to Biaggio and Alessandro de Agnano for their help.

A PhD is not just about research; it is also about the environment and the people who make the journey enjoyable. I have been fortunate to be surrounded by an amazing group of colleagues and friends with whom I have shared countless coffee breaks, procrastination sessions, and venting over beers. A big thank you to my fellow office mates and partners in crime: Nitish, Killian, Martijn, Francesco Tosto, Daaman, Ramon, Francesco Neri, Alessandro Cappiello, Matteo, Federica, Nikki, Floyd, Wessel, Ruben, Alessio—your support and friendship made this experience truly special. Special thanks to Nitish for being the go to guy for many life related questions and being the initiator of many social activities. I also acknowledge friends from my early PhD days who welcomed me into their social circle and made me feel at home: Andre, Adam, Nitish Anand, Sumit, Sebastian, Lucia, Marco, Kushagra.

Finally, I would like to express my deepest appreciation to my family, whose unwavering support and confidence in me made this achievement possible. My heartfelt thanks go to my mother, whose sacrifices and relentless efforts ensured that I received a good education, even under the most challenging circumstances. Her resilience and strength have been a constant source of inspiration, and my hope to make her proud drives me to do well in my pursuits. I am also grateful to my father for his steadfast support in all my endeavors. Last but not least, my dear little sister, thank you for always believing in me and for your occasional pep talks that lifted me up during tough times. Your encouragement kept me going even in my darkest moments.

This dissertation is the result of the collective efforts, support, and kindness of many individuals, and I am truly grateful to each and every one of you.

CURRICULUM VITÆ

Rishikesh Pankaj SAMPAT

18-09-1993 Born in Dubai, United Arab Emirates.

EDUCATION

- 2011–2015 Bachelors of Technology in Mechanical Engineering
National Institute of Technology Tiruchirappalli, India
- 2015–2018 Masters of Science in Aerospace Engineering
Delft University of Technology, The Netherlands
Thesis: Automatic Generation of Chemical Reactor Networks for Combustion Simulations
Promotor: Dr. A. Perpignan, Prof. A. Gangoli Rao
- 2018–2024 PhD. in Aerospace Engineering
Delft University of Technology, The Netherlands
Thesis: Phenomenology of COmbustion in a Jet-Stabilized Combustor
Promotor: Dr. ir. F. F. J. Schrijer, Prof. A. Gangoli Rao

EXPERIENCE

- 2022–2024 Research Associate, Delft University of Technology
Combustion characterization of Sustainable Aviation Fuels (SAF) derived from hydrogenated Fast Pyrolysis Bio-oil (FPBO) through experiments and simulation.
- June 2016–
Nov 2016 Intern, Mitsubishi Turbochargers and Engines Europe B.V.
Design and testing of Combustion Rig for a Micro Gas turbine as Range Extender.
- May 2014–July
2015 Intern, Indian Institute of Science.
Fluid-Structure Interaction simulation of a flexible wing.



LIST OF PUBLICATIONS

JOURNALS

1. A.A.V Perpignan, **R. Sampat**, A. Gangoli Rao, Modelling pollutant emissions of Flameless Combustion with a joint CFD and Chemical Reactor Network approach, *Frontiers in Mechanical Engineering* 5, 63, 2019
2. T. van den Berg, **R. Sampat**, A. Gangoli Rao, Flow field and emission characterisation of a novel enclosed jet-in-hot-coflow canonical burner, *Applications in Energy and Combustion Science*, 100298, 2024
3. **R. Sampat**, FFJ. Schrijer, A. Gangoli Rao, Evolution of turbulent-jet-in-coflow, *Flow Turbulence and Combustion* (accepted)
4. **R. Sampat**, N. Goselink, K. Dave, F. Schrijer, A. Gangoli Rao, Stabilization and Emissions Characteristics of CH₄-H₂ blends in a premixed jet stabilized combustor, *Fuel* (accepted)
5. **R. Sampat**, FFJ. Schrijer, A. Gangoli Rao, Effects of vitiation and heat loss on ignition and emissions characteristics of methane-air mixtures, *Combustion Theory and Modelling* (under review)

CONFERENCES

1. **R. Sampat**, FFJ. Schrijer, A. Gangoli Rao, Turbulent interaction of Jet with Coflow, 55th 3AF International Conference on Applied Aerodynamics, 2020
2. **R. Sampat**, N. Goselink, F. Schrijer, A. Gangoli Rao, Operating Characteristics of a Flameless Combustor Obtained By Experiments Informed Modelling, ASME Turbo Expo: Power for Land, Sea, and Air, 2022
3. **R. Sampat**, F. Schrijer, A. Gangoli Rao, Scalar quantities obtained by post processing velocity fields measured by PIV using Chemical Reactor Networks, Combura, 2022
4. **R. Sampat**, F. Schrijer, A. Gangoli Rao, Stabilisation and Emissions Characteristics of CH₄-H₂ blends in a premixed Jet stabilised Combustor, European Combustion Meeting, 2023
5. **R. Sampat**, F. Schrijer, A. Gangoli Rao, Identification of ignition kernels from Chemiluminescence imaging in a Flameless Combustor, International Symposium on Flow Visualization, 2023